

DIGITAL ACCESS TO SCHOLARSHIP AT HARVARD
DASH.HARVARD.EDU

HARVARD LIBRARY


Water and Phase Transitions in Rocky Planetary Interiors

Citation

Dong, Junjie. 2023. Water and Phase Transitions in Rocky Planetary Interiors. Doctoral dissertation, Harvard University Graduate School of Arts and Sciences.

Link

https://nrs.harvard.edu/URN-3:HUL.INSTREPOS:37375828

Terms of use

This article was downloaded from Harvard University's DASH repository, and is made available under the terms and conditions applicable to Other Posted Material (LAA), as set forth at

https://harvardwiki.atlassian.net/wiki/external/NGY5NDE4ZjgzNTc5NDQzMGIzZWZhMGFlOWI2M2EwYTg

Accessibility

https://accessibility.huit.harvard.edu/digital-accessibility-policy

Share Your Story

The Harvard community has made this article openly available.
Please share how this access benefits you. Submit a story

HARVARD UNIVERSITY
Graduate School of Arts and Sciences



DISSERTATION ACCEPTANCE CERTIFICATE

The undersigned, appointed by the

Department of Earth and Planetary Sciences

have examined a dissertation entitled

"Water and Phase Transitions in Rocky Planetary Interiors"

presented by Junjie Dong

candidate for the degree of Doctor of Philosophy and hereby certify that it is worthy of acceptance.

Signature _____

Typed name: Prof. Rebecca Fischer

Signature _____

Typed name: Prof. Jerry Mitrovica

Signature _____

Typed name: Prof. Robin Wordsworth

Signature _____

Typed name: Prof. Lars Stixrude

Signature _____

Typed name: Prof. David Johnston

Date: April 10, 2023

Page left intentionally blank.

Water and Phase Transitions in Rocky Planetary Interiors

A dissertation presented

by

Junjie Dong

to the

Department of Earth and Planetary Sciences

in partial fulfillment of the requirements

for the degree of

Doctor of Philosophy

in the subject of

Earth and Planetary Sciences

Harvard University

Cambridge, Massachusetts

April 2023

© 2023 Junjie Dong All rights reserved.

Dissertation Advisor: Rebecca A. Fischer Junjie Dong

Water and Phase Transitions in Rocky Planetary Interiors

Abstract

This dissertation explores two fundamental aspects of rocky planetary interiors: water and phase transitions. The first two chapters investigate the deep water cycles in Earth and Mars. The research provides an estimate of the bulk water storage capacity of their mantles as a function of mantle potential temperature using thermodynamic modeling, and examines its implications for the hydrosphere of early Earth through isostatic modeling. In the third chapter, a machine learning framework is introduced for determining high-pressure phase diagrams, with a specific focus on the post-spinel transition in Mg_2SiO_4. The resulting nonlinear Clapeyron slope of the post-spinel transition is then used to estimate its lateral variation at the base of the Earth's transition zone.

Contents

Title Page

Copyright

Abstract **iii**

List of Figures **viii**

List of Tables **xii**

Acknowledgments **xv**

Dedication **xx**

1 Introduction: A Personal Account of the Research Process **1**

2 Constraining the Volume of Earth's Early Oceans With a Temperature-Dependent Mantle Water Storage Capacity Model **15**

2.1 Introduction 17

2.2 Methods 19

2.2.1 Water Storage Capacities in Olivine, Wadsleyite, and Ringwoodite . 19

2.2.2 Water Storage Capacity in Bridgmanite and Other Lower Mantle NAMs 23

2.2.3 Phase Equilibria of Earth's Solid Mantle and Its Bulk Water Storage Capacity 24

2.2.4 Uncertainties in Mantle Water Storage Capacity From Monte Carlo Sampling . . . 27
2.2.5 Isostatic Equilibrium and Flooding of Early Continents . . . 29
2.3 Results and Discussion . . . 31
2.3.1 Parameterization of the Water Storage Capacity Model in Olivine, Wadsleyite, and Ringwoodite . . . 31
2.3.2 A Comparison of Bridgmanite Water Storage Capacity Between the Temperature-Dependent Mantle Water Storage Capacity Model and Experiments . . . 33
2.3.3 Temperature-Dependent Mantle Water Storage Capacity . . . 39
2.3.4 Minimum Volume of Earth's Early Archean Oceans . . . 45
2.3.5 Implications for the Flooded Fraction of Early Continents . . . 51
2.4 Summary and Conclusions . . . 58

3 Water Storage Capacity of the Martian Mantle Through Time 60

3.1 Introduction . . . 61
3.2 Methods . . . 64
3.2.1 Equilibrium Phase Assemblages of the Martian Mantle . . . 64
3.2.2 Bulk H_2O Storage Capacity of Martian Mantle Rocks . . . 65
3.2.3 The Effects of Iron on Solid Mantle H_2O Storage Capacity . . . 68
3.3 Results and Discussion . . . 72
3.3.1 Depth-dependent Profiles of the Solid Martian Mantle H_2O Storage Capacity and the Effects of Fe . . . 72
3.3.2 Estimates of the Solid Martian Mantle H_2O Storage Capacity as a Function of Mantle T_p . . . 80
3.3.3 Comparing the Solid Mantle H_2O Storage Capacities of Mars and Earth and Their Evolution Through Time . . . 85
3.3.4 Possible Sources and Sinks for Water in the Martian Mantle Through Time . . . 89
3.4 Summary and Conclusions . . . 90

4 Nonlinearity of the Post-spinel Transition and Its Expression in Slabs and Plumes Worldwide 93

4.1 Introduction . . . 95

4.2 New In Situ Experimental Dataset on the Mg_2SiO_4 Phase Diagram . . . 97

4.2.1 Synchrotron X-Ray Diffraction Experiments . . . 97

4.2.2 Phase Boundary Detection . . . 98

4.3 In Situ Phase Stability Observations in Mg_2SiO_4 Compiled From Literature and Their Pressure and Temperature Corrections . . . 101

4.4 Global Analysis of Phase Stability Observations in Mg_2SiO_4 . . . 103

4.4.1 Multi-Class Logistic Model for High Pressure Phase Diagram Determination . . . 103

4.4.2 Toward a Nonlinear Post-spinel Transition in Mg_2SiO_4 . . . 106

4.4.3 Machine Learned Phase Diagram of Mg_2SiO_4 At Transition Zone Conditions . . . 116

4.5 Mantle Expression of Nonlinear Postspinel Boundary in Slabs and Plumes Worldwide . . . 121

4.6 Summary and Conclusions . . . 126

5 Afterword: A Critical Reflection 129

5.1 The Case for a Flooded Early Earth . . . 129

5.2 A Wider View of Water Worlds . . . 133

5.3 The Philosophy of Drawing a Phase Boundary . . . 137

A Supplementary Materials for Chapter 2 143

A.1 Thermodynamic Model of Water Storage Capacities in Nominally Anhydrous Minerals . . . 143

A.2 Selection and Correction of Experimental Data on Water Storage Capacities in NAMs . . . 145

A.3 Parametrization of the Earth's Hypsometric Curve . . . 148

B Supplementary Materials for Chapter 3 **173**

B.1 Density–Pressure Profiles for the Martian Mantle 173

C Supplementary Materials for Chapter 4 **204**

C.1 Experimental Procedures 204

C.2 Phase Identification and Phase Boundary Detection 206

C.3 Selection of Phase Stability Observations From Literature 208

C.4 Supervised Learning Procedures 208

C.5 A Brief Review of Previous Data and Their Comparison With This Study . 210

C.6 A Composite Mantle Temperature Model for the "660-km" Discontinuity . 213

References **283**

List of Figures

1.1 Literature data on the partitioning of iron between bridgmanite and melt as a function of pressure 4

1.2 An example of an early data set on water content in hydrous ringwoodite under water-saturated conditions, taken from Ohtani et al. (2000). 5

1.3 Estimated thickness of mantle transition zone for a Mg_2SiO_4 Composition . 7

1.4 Experimental data for wadsleyite (wd), ringwoodite (rw), and bridgmanite (bm) + periclase (pe) from literature 9

2.1 Water storage capacities in olivine, wadsleyite, and ringwoodite at high pressure and temperature. 21

2.2 Bulk water storage capacity map of the pyrolitic mantle up to 27 GPa. . . 28

2.3 Adiabatic geotherms and water storage capacity profiles at mantle potential temperatures of T_p = 1550–1950 K. 37

2.4 Temperature–dependent water storage capacity in the Earth's solid mantle. 40

2.5 Minimum volume of early Archean oceans as a function of T_p and present-day mantle water content. 47

2.6 Minimum flooded fraction of early Archean continents as a function of T_p and present-day mantle water content from isostatic modeling. 53

3.1 Workflow for the "bagging" method. 71

3.2 Effects of Fe content on the water storage capacities of olivine, wadsleyite, and ringwoodite at selected pressures and temperatures. 73

3.3 Water storage capacity diagrams of Martian and terrestrial mantle assemblages between 3 and 22 GPa. 74

3.4 Water storage capacity of the solid Martian mantle. 77

3.5 Sensitivity of bulk mantle water storage capacity to mantle composition at 1600 K and 1900 K. 83

3.6 Summary of the Martian water reservoirs in the surface, crust, and mantle, as well as the estimates of the lost surface water potentially associated with morphological features on Mars. 87

4.1 In situ phase stability observations in Mg_2SiO_4 collected in LH-DAC experiments with synchrotron XRD from this study. 99

4.2 Machine learned phase diagram of Mg_2SiO_4 at transition zone conditions. . 108

4.3 Model selection and evaluation for the Mg_2SiO_4 phase diagram. 112

4.4 Temperature-dependent Clapeyron slope in the post-spinel transition in Mg_2SiO_4. 114

4.5 Global mapping of mantle temperature and post-spinel Clapeyron slope at the "660-km" discontinuity with superimposed subducting slabs and plume-fed hotspots locations. 119

A.1 Water storage capacity profiles for T_p = 1550–1950 K generated from the Monte Carlo sampling. 150

A.2 Distributions and differences in bulk mantle water storage capacities for T_p = 1550–1950 K generated from the Monte Carlo sampling. 152

A.3 Distributions and differences in lower mantle water storage capacities for T_p = 1550–1950 K generated from the Monte Carlo sampling. 153

A.4 Isostacy schematic for the continental freeboard modeling 154

B.1 Adiabatic temperature gradients of the "T13" Martian mantle computed with HeFESTo. 175

B.2 Examples of calculated phase assemblages for the "T13" Martian mantle along the 1600 K and 1900 K adiabats. 177

B.3 Examples of calculated phase assemblages for the "LK19 (EH+L)" Martian mantle along the 1600 K and 1900 K adiabats. 178

B.4 Examples of calculated phase assemblages for the "LK19 (EL+H)" Martian mantle along the 1600 K and 1900 K adiabats. 179

B.5 Examples of calculated phase assemblages for the "YM20" Martian mantle along the 1600 K and 1900 K adiabats. 180

B.6 Examples of calculated phase assemblages for the "K22" Martian mantle along the 1600 K and 1900 K adiabats. 181

B.7 Pressure or temperature effects on the water storage capacities of olivine, wadsleyite, and ringwoodite at selected P–T conditions. 182

B.8 Best-fit water storage capacity profiles along mantle adiabats for five BSM compositions at $T_{\mathrm{p}} = 1600$ K and $T_{\mathrm{p}} = 1900$ K. 184

C.1 Difference between pressures calculated based on the W scale and pressures based on the KCl scale. 215

C.2 Flow chart of machine learning procedure. 216

C.3 Benchmarks on the $rw \leftrightarrow bm + pe$ post-spinel transition with the simple binary logistic model for each literature dataset. 217

C.4 Benchmarks on the $wd \leftrightarrow bm + pe$ transition with the simple binary logistic model for each literature dataset. 219

C.5 Benchmarks on the $wd \leftrightarrow rw$ transition with the simple binary logistic model for each literature dataset. 220

List of Tables

2.1 Bulk Water Storage Capacity in Earth's Solid Mantle 45

2.2 Minimum flooded fraction of early Archean continents at $T_p = 1900$ K . . 52

2.3 Maximum Present-Day Mantle Water Content Permitted for Constant Freeboard at $T_p = 1900$ K (OM) 56

A.1 Summary of experimental data on water storage capacity in olivine. 155

A.2 Summary of experimental data on water storage capacity in wadsleyite at temperatures above 1673 K. 163

A.3 Summary of experimental data on water storage capacity in ringwoodite at temperatures above 1673 K. 168

A.4 Coefficients and covariance matrices of parameterizations for the water storage capacity model, as applied to olivine, wadsleyite, and ringwoodite at high pressure and temperature. 171

A.5 Tabulated parameters for water partition coefficient calculations in Eq. 2.2 172

B.1 Bulk Silicate Mars composition based on Taylor (2013) 185

B.2 Bulk Silicate Mars composition based on Liebske and Khan (2019) ("EH+L") 186

B.3 Bulk Silicate Mars composition based on Liebske and Khan (2019) ("EL+H") 187

B.4 Bulk Silicate Mars composition based on Yoshizaki and McDonough (2020) 188

B.5 Bulk Silicate Mars composition based on Khan et al. (2022) 189

B.6 Bulk water storage capacity in the solid Martian mantle with the "T13" composition 190

B.7 Bulk water storage capacity in the solid Martian mantle with the "LK19 (EH+L)" composition 191

B.8 Bulk water storage capacity in the solid Martian mantle with the "LK19 (EL+H)" composition 192

B.9 Bulk water storage capacity in the solid Martian mantle with the "YM20" composition 193

B.10 Bulk water storage capacity in the solid Martian mantle with the "K22" composition 194

B.11 Additional literature data on the water storage capacity of olivine, an update to the compilation of Dong et al. (2021) 195

B.12 Additional literature data on the water storage capacity of wadsleyite, an update to the compilation of Dong et al. (2021) 200

B.13 Additional literature data on the water storage capacity of ringwoodite, an update to the compilation of Dong et al. (2021) 202

C.1 New in situ experimental dataset on the Mg_2SiO_4 phase diagram. 222

C.2 In situ phase stability observations in Mg_2SiO_4 compiled from literature with corrected pressures and temperatures. 234

C.3 In situ phase stability observations in Mg_2SiO_4 compiled from literature with uncorrected pressures and temperatures. 257

C.4 Model selection results. 276

C.5 Subducting slabs and their T660 and $\gamma_{\text{post-spinel}}$. 277

C.6 Hotspot-associated plumes and their T660 and $\gamma_{\text{post-spinel}}$. 280

Acknowledgments

I express my deepest gratitude to my Ph.D. advisor, Rebecca Fischer, who has guided every aspect of my graduate studies at Harvard. Working with Rebecca has been incredibly motivating and empowering because she trusts my ability to do things more than I trust myself. I have needed her enthusiasm and criticism at every stage of the work presented in this dissertation. I am also grateful for the maximum flexibility she has given me to work on whatever else interests me, both within and beyond mineral physics. To Rebecca, I owe not only what I have learned but also who I have become.

I also owe a great debt of gratitude to the other members of my dissertation committee, including Lars Stixrude at UCLA, and Robin Wordsworth and Jerry Mitrovica here at Harvard. I admire Lars for his unfailing erudition and the lucid clarity with which he answered all my questions. Robin inspired me with the breadth of his interests in geophysics and planetary science, and I also appreciate his calm demeanor, which always puts me at ease. Jerry introduced me to the fascinating world of sea-level modeling, encouraged me to incorporate it into my own work, and provided invaluable feedback at various stages of its development.

In addition, I would like to express my gratitude to Nadja Drabon, Roger Fu, Andy Knoll, Charlie Langmuir, and Stein Jacobsen at Harvard, and Carolina Lithgow-Bertelloni at UCLA, who, while not directly supervising my dissertation, enriched my academic exploration with their vast knowledge and expertise. I would also like to thank Ann Pearson and John Shaw, the department chairs, and David Johnston, director of graduate studies, for their timely responses and helpful guidance during my advisor's leave of absence. I must also mention my undergraduate mentor, Jackie Li at Michigan,

whose friendship has encouraged me in all my academic and personal endeavors.

I would like to express my heartfelt appreciation to the friends who soundtracked my time at EPS. Each of them possesses a unique character, and their high caliber has constantly inspired me to see the bigger picture in life. I admire Matt Brennan for his efficient time management skills as a scientist and his stoic ethics and fortitude as a man. I am immensely grateful to Zach Eriksen for his warmth, positivity, and thoughtfulness in checking in on me and asking if I was having a good time everywhere we went together. Jesse Gu is the person I've argued with the most. Although we don't always agree on everything, he has always shown forgiveness and a patient, thoughtful perspective. Jesse exudes a quiet intelligence that I have always loved about him. I was also touched by Peter Sherman's kind and humble nature, and he treated me not only as a friend, but as part of his family. Kait Loftus has an infectious laugh and is someone I believe we were once the same person in one of our past lives. She shared my enthusiasm for collecting books and debating Catholic theology. Zhuo Yang would always find me in my office at the end of the day and drive me to my favorite restaurants while listening to my endless blather about my broken codes and failed experiments. He never complained and was like a father figure to me at EPS. Ned Kleiner was always willing to engage me in a random conversation about anything and everything, and at times he crushed my contrarian arguments with precision. Alec Brenner inspires me with his uncanny ability to find any rock he wants and build anything from scratch to suit his needs. He is the reason I hold the profession of geology in such high regard. Camille Hankel was the best ally for our shared passion for the history of science at EPS. Ted Amdur inspired me with his altruistic spirit and sense of service by helping those in need in his community. Last but not least, I worked with an exceptional Harvard student, Darius Mardaru,

during the last two years of my Ph.D. Darius was my first mentee and I consider him a friend. He has a relentless thirst for knowledge and his motivation is truly inspiring. When I look at him, I see a younger version of myself, but more confident and capable.

I am also grateful for the wonderful hours I spent discussing various topics related or unrelated to my dissertation with other members of the Fischer group, including, Kate Turner, Kierstin Daviau, Terry-Ann Suer, Mike Volk, Riko Iizuka-Oku, Chiara Chung-Halpern, Jack Sheehan, and other solid earth colleagues, such as Hao Cao, Hairuo Fu, Jocelyn Fuentes, Eugenia Hyung, Katherine Keller, Heather Kirkpatrick, Stephanie Klinger, Yarui Ku, Anna Mittelholz, Haley Olson, Linda Pan, Chris Pareno, Tamara Pico, Judy Pu, Sarah Steele, Natasha Toghramadjian, Laila Yu, Congcong Yuan, and Li Zeng. Moreover, I have enjoyed and benefited from conversations with my dear friends on the fluid earth side who have graciously crossed the aisle and reached out to me, including Mark Baum, Eimy Bonilla, Stephen Bourguet, Ju Chulakadabba, Jess Cmiel, Minmin Fu, Colleen Golja, Jack Hensley, Ethan Manninen, Elise Penn, Jon Proctor and Hannah Nesser. These wonderful people at EPS, who shared most of my 20s with me and saw me vacillate between narcissistic self-absorption and existential despair, have my gratitude, and I will never forget them.

I would like to thank my friends outside of the EPS department who have patiently supported me throughout my Ph.D. years. First, I would like to thank one of my roommates, Susana Hoyos, for her sweet and uplifting presence that kept me sane at home while I was finishing the last mile of my Ph.D. Second, I am immensely grateful to Andrew Provencher for revealing a secret beach in Wellfleet, and to Brent Jacobs for taking me on late night museum visits. I would also like to thank my friends, whom I have known since my teenage years–Chen Zhong, Cheng Chui, Minjie Shen, and Yi

Wang, who continue to share their lives with me even as they move in very different directions, and from whom I have learned a great deal about making iPhones, building a low-carbon house, splurging on Michelin-starred restaurants in New York, and swearing in French. My life in Cambridge has also been enriched by Yuxuan Yang's commitment to bringing a healthy dose of skepticism to everything I do, Si Wu's dedication to feminism in China, Siheng Chen's passion for getting free flights, and Allie Pickard's world-famous comforting hugs.

During the last three years of my Ph.D., I also spent a significant fraction of my time at the Department of the History of Science. I am immensely thankful for my other mentor there, Ben Wilson. Without his sympathetic interest and constant encouragement, I doubt I could have explored the intricacies of the history of geophysics. Ben's willingness to take time out of his own book project to talk with me for hours every two weeks was a gift beyond measure.

My appreciation also extends to the other professors in the HoS department, including Eram Alam, Peter Galison, Matt Hersch, and Alisa Bukolich at BU Philosophy, whose inspiration was invaluable in my pursuit of a secondary field in the history of science. I am grateful for the welcoming environment provided by my colleagues and friends in the history and philosophy of science, including Umar Agha, Rory Brinkmann, Ben Maldonado, Francis Newman, Tiffany Nichols, Jane Zhang here at Harvard, the Φ-Geo group at BU, and Miguel Ohnesorge at the other Cambridge. We spoke about eras, history, and world creation—both in their materialistic and metaphysical sense—and their insights have been an endless source of enlightenment for me.

I would like to acknowledge two important aspects of my life in Cambridge: the

Harvard Film Archive, which provided endless hours of cinematic bliss, and WZBC, which offered radical politics at noon, witty banter at night, and an eclectic mix of tunes throughout the day. My Ph.D. years would have been far less enjoyable and more mundane without them, and for that, I am eternally grateful.

Receiving the James Miller Fellowship from the Graduate School of Arts and Sciences at Harvard has been a tremendous help and honor.

Above all, I would like to thank my parents, Qiuling Wang and Baohong Dong, and my grandparents, Peiyu Wang and Yinsun Wang, for a million things, but most of all, for their endless and unconditional love. Any good character I possess I owe entirely to them, and the responsibility for my foibles rests solely on my shoulders.

To those who uplifted me to reach for the stars.

Chapter 1

Introduction: A Personal Account of the Research Process

Not only do scientists' statements create problems for historical elucidation; they also systematically conceal the nature of the activity which typically gives rise to their research reports. In other words, the fact that scientists often change the manner and content of their statements when talking to outsiders causes problems—both for outsiders' reconstruction of scientific events and for an appreciation of how science is done. It is therefore necessary to retrieve some of the craft character of scientific activity through in situ observations of scientific practice. More specifically, it is necessary to show through empirical investigation how such craft practices are organised into a systematic and tidied research report.

—Bruno Latour and Steve Woolgar, *Laboratory Life*

To begin my dissertation, I've chosen a quote from "Laboratory Life" by Bruno Latour and Steve Woolgar (Latour and Woolgar 1986). The book argues that scientific knowledge is not something that simply waits to be discovered. Instead, it's created through a complex web of social interactions, negotiations, and power relations among scientists, their instruments, and their research subjects. Although I'm not a big fan of Latour's philosophy and have mixed feelings about his ahistorical views on how scientific knowledge is constructed, I do appreciate his innovative approach to studying science ethnographically and his insightful comments about what is often left out of research reports. Scientific journals and peer review can systematically obscure the nature of scientific activities, preventing readers from understanding how research intentions and motivations evolve over time, and how related activities are carried out, frustrated, or even sometimes abandoned.

The three main chapters of my dissertation were copied and pasted directly from two previously published articles (Dong et al. 2021, 2022b)and a preprint on arXiv (Dong et al. 2022a). As Latour correctly notes, they don't provide enough context by themselves. To help outsiders understand scientific events and appreciate how science is done, Latour suggests using in-situ observations of scientific practice. This allows observers to gain insight into the craftsmanship of scientific activity. Since my work isn't significant enough for an philosopher like Latour to spend months observing and writing about, I will personally provide an account of my research process ex-situ. I hope that by sharing this, readers will gain some insight into how I transform a small part of the natural world that interests me into something that can be observed, measured, and analyzed.

In this dissertation, I present three chapters that, as the title suggests, can be

broadly divided into two topics: water and phase transitions. Although these two topics may not seem closely related, they both originated from the same idea I had early on in graduate school.

At the beginning of my graduate studies in 2017, I sat down with my advisor, Rebecca Fischer, to discuss potential projects. My initial interest was to work with Rebecca on melt-solid partitioning in mantle silicates, a topic that had yielded conflicting results in previous experimental work (Fig. 1.1, Nomura et al. 2011; Andrault et al. 2012; Tateno et al. 2014). Together we planned to extend existing experimental constraints to the megabar range using the 8-color spectrometry system she was building. This would allow us to map the pressure and temperature dependence of iron partitioning between the solid and liquid phases as silicate melts between the solidus and liquidus. The original members of the Fischer group, including Rebecca, Matt, and myself, later joined by Terry-Ann and Kierstin, worked for about two years to complete the laser heating part of the system. However, to provide a reliable temperature map, we still needed to complete the 8-color system, which was halted by the pandemic in early 2020. By the time we returned to the lab and resumed construction of the 8-color system in 2022, Matt had graduated and Kierstin and Terry-Ann had left for their new jobs. With only about a year left in my Ph.D., it became impractical for me to continue the partitioning project, and these experiments I had designed and planned for my Ph.D. never materialized.

Both Rebecca and I anticipated the uncertainty and slow progress of the experimental work, so at the beginning of my Ph.D. we decided to work on a petrological modeling project. This ensured that even if the experiments did not work out, we would still have some research output. I still remember the day I had that conversation with Rebecca.

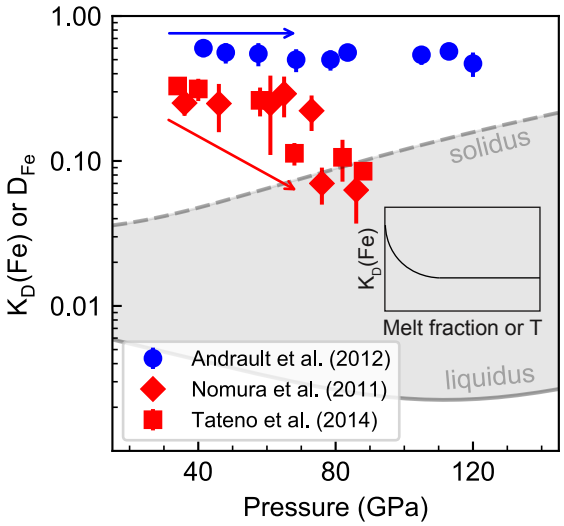


Figure 1.1: **Literature data on the partitioning of iron between bridgmanite and melt as a function of pressure.** The published data on iron partitioning between bridgmanite and melt show significant differences and inconsistencies. One possible explanation for these discrepancies is that the value of K_D(Fe) depends on the degree of partial melting and therefore on temperature. To investigate this, it may be helpful to create a temperature map of the sample that correlates temperature with chemical composition. This map could provide insight into how K_D(Fe) changes with temperature during melting. This figure was made in 2020 for my NASA FINESST grant application.

She asked me, "What projects would you like to do? You can try to come up with your own, or I can introduce you to some of my ideas." Eager to try something on my own, I suggested spending a few weeks brainstorming ideas to see how far I could go. She gave the green light to this "experiment" of mine.

We explored several ideas, and the most well-developed ones were in areas that I had been exposed to during my undergraduate research; and one of them was water in the transition zone. I worked on several multi-anvil experiments with Feng Zhu,

a postdoc in Jackie's lab, and we studied the reaction between iron and water-rich wadsleyite (Zhu et al. 2019). This was the first time I learned that water could be stored in planetary interiors. At that time, prior to 2017, most of the literature on this topic focused on Earth's transition zone today. Many experimental studies of the water storage capacity of nominally anhydrous minerals in the mantle had been conducted, but these experiments could only be reliably performed at relatively low temperatures (lower than today's mantle temperatures). As multi-anvil techniques advanced, experimental temperatures reached as high as 1900 K, with some groups reaching 2200–2300 K (e.g., Fig. 1.2; Ohtani et al. 2000). With present-day temperatures at 1900 K, we finally had a constraint on water storage capacity in the present-day mantle transition zone.

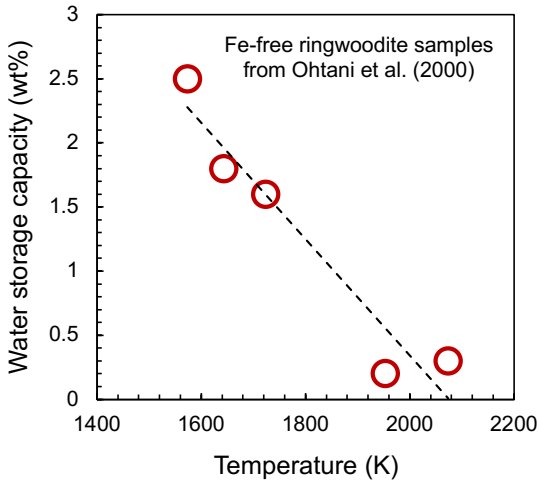


Figure 1.2: **An example of an early data set on water content in hydrous ringwoodite under water-saturated conditions, taken from Ohtani et al. (2000).** This study is one of the earliest to point out the potential temperature dependence of water storage capacity in nominally anhydrous minerals, such as ringwoodite. The figure was made in the fall of 2017, when Rebecca and I were first exploring the topic of water in the transition zone.

As I examined the data, I found the temperature dependence intriguing. Conceptually, the temperature axis in the plot also represents the cooling history of the planet, and the decreasing trend with temperature could easily be interpreted as a change in water storage over Earth's history. To constrain the total mantle water capacity of a cooling planet, we needed to understand how the water storage capacities of each mantle mineral change with pressure and temperature, as well as their proportions relative to each other and how they change with temperature. Although the Earth's mantle is a multiphase system with over 40 minerals other than olivine and its polymorphs, for simplicity we started with only wadsleyite and ringwoodite in the Mg_2SiO_4 composition. I plotted the thickness of the two parts of the transition zone and was fascinated by the results (Fig. 1.3). If all the simplifications we made were true, ringwoodite would disappear at the base of the transition zone, and since ringwoodite is one of the largest potential water reservoirs on Earth, this would have a significant impact on our estimate of water capacity.

Of course, the mantle is composed of minerals other than olivine, and a detailed description of the mantle mineral assemblaged and their proportions is not a trivial task. To understand how the proportions of each phase change over time as the planet cools, we have to rely on thermodynamic modeling. At the time, the widely available thermodynamic code was "Perple_X," which my labmate Matt had used in his Mars paper (Brennan et al. 2020). I experimented with it, but was not entirely happy with the numerical instability it sometimes produced. The other code I was aware of was "HeFESTo", created by Lars Stixrude and Carolina Lithgow-Bertelloni Stixrude and Lithgow-Bertelloni (2011, 2005, 2022). Since the code was not publicly available, I sent Lars a cold email, and he replied a month later, agreeing to meet and share their results.

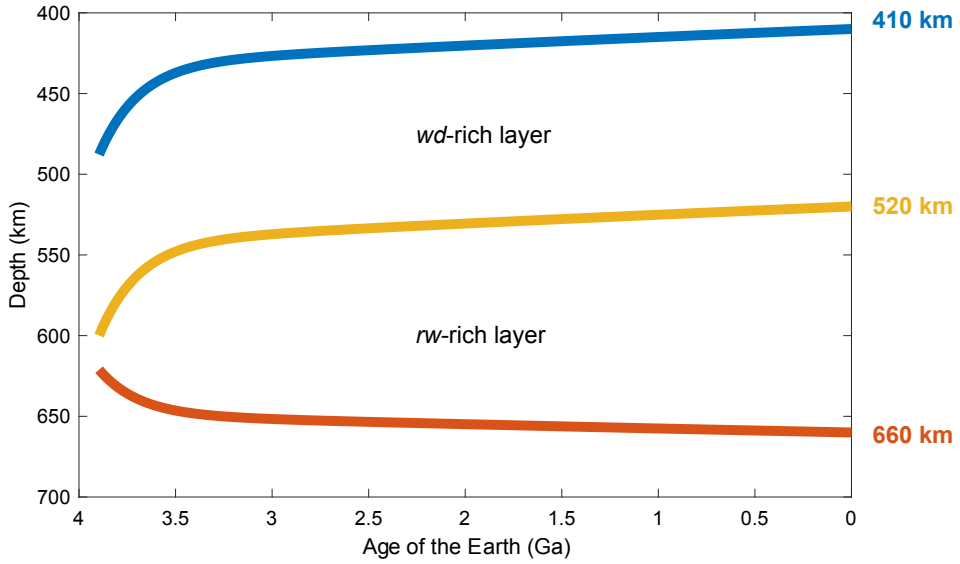


Figure 1.3: **Estimated thickness of mantle transition zone for a Mg_2SiO_4 Composition.** A figure produced in December 2017 from a back-of-the-envelope calculation, showing the plotted thickness of the mantle transition zone for a simplified Mg_2SiO_4 composition. The thinning of the ringwoodite layer, a potential water reservoir, would significantly affect the estimation of Earth's mantle water capacity.

Being relatively new to modeling and unfamiliar with Linux and Fortran, I asked Rebecca if I could visit Lars and Carolina in London. She agreed and even covered my $400 expedited visa fee! On my way to London I brought an incomplete set of water storage capacity data with an exponential fit. While visiting Lars, I coded several hundred lines that later became the central part of my project. Although we spent another year building detailed thermodynamic models for water and running Monte Carlo sampling for sensitivity tests, and this work was not published until 2021, by the end of my London trip in 2018 we already had a rough idea of the Archean water world for my first paper.

I recall having separate, independent conversations with both Rebecca and Lars in which I expressed my doubts. I asked them if the excess water, given that the water storage capacity in the mantle was much less than the actual water content today, would end up on the surface, resulting in a larger Archean ocean. Was this a crazy idea? Both responded with something along the lines of "why not". With the blessing of both Lars and Rebecca, this little pet project I started to fill in the gaps between building our laser heating system and eventually became the bulk of my Ph.D. thesis. Two papers on this project have been published (Dong et al. 2021, 2022b) and are included in this dissertation as Chapters 2 and 3.

The connection between the water project and the phase transition project arises when calculating the proportion of each phase in the mantle. For those who have seen a pseudosection of the Earth's mineral assemblage, the first thing they notice are the stability fields of the mineral assemblages. Each stability field defines a unique combination of minerals whose proportions change with pressure and temperature. Pseudosections are the ultimate atlas of the Underworld. Thermodynamically, they are constructed from each end member component and require input on the phase relations of the end members. The phase relations of the end members may appear well defined, but the cleanliness of their phase boundaries can sometimes be quite deceptive. An example is Mg_2SiO_4, arguably the most fundamental phase diagram for the Earth's interior. When the existing experimental data are superimposed on the phase boundary we draw for the transition, the transition does not appear to be constrained by the data at all (Fig. 1.4).

Intrigued by such discrepancies in the data, I went to Argonne to do XRD diffraction experiments. First, we tried the membrane cell, which supposedly could precisely

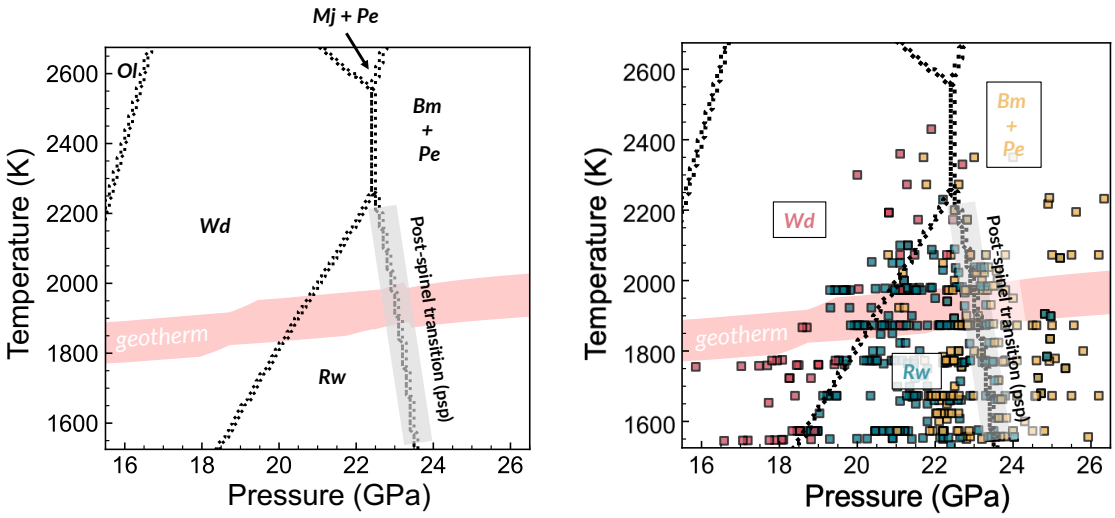


Figure 1.4: **Experimental data for wadsleyite, ringwoodite, and bridgmanite + periclase from literature, plotted in red, blue, and yellow, respectively.** Notably, the post-spinel boundary appears to be unconstrained by the available data. The dashed lines in the plot represent the computational results obtained from HeFESTo. This figure was initially created in 2018 for our beamtime application to GSECARS 13 ID-D at APS.

control the pressure during heating. This technique would have the advantage of providing a tight bracket at a relatively pressure-independent phase boundary. The practical challenge is that the membrane cell does not work as perfectly as intended. It has very little ability to reduce pressure incrementally, making reverse experiments impossible. In addition, compressing the cell during heating often causes the sample to move, misaligning the X-ray and heated spots, which could be fatal to observing phase stability. Therefore, we returned to the conventional short symmetric cell. Even with heating alone, identifying phase transitions between these patterns is a tricky business. Wadsleyite and bridgmanite have relatively low symmetry, resulting in many overlapping peaks, while ringwoodite has relatively high symmetry and its peaks are mostly buried

by those of wadsleyite and bridgmanite. This makes triple point identification very difficult.

All of these experimental efforts took place in 2018 and 2019. However, I was unable to complete the data analysis, partly due to the distraction of the water project and partly due to the practical challenges I have described. When faced with an X-ray pattern with a large number of peaks, the human cognitive system fails completely. I went through the data twice, manually fitting the peaks and identifying the first appearance of the new phase. However, I couldn't convince myself that the pattern I found was the actual appearance of the first new peaks. I was frustrated by the possibility that my personal biases, or those of another experimenter, had crept into the data. Perhaps we were using an outdated JCPDS file that didn't give a good prediction of the temperature dependence of the peaks, or we missed important bridgmanite or ringwoodite peaks, or we simply mislabeled the phase when we was tired. As a result, I ended up constructing my own EoS for all relevant phases and implementing some rudimentary peak search functions. Although the code never worked perfectly and the fitting procedure sometimes broke down, viewing the pattern with a waterfall figure and the unique peak search allowed me to feel more confident that the pattern I identified could be the first appearance of the new phase.

Building my own peak identification workflow took a couple of months, and I thought that was essentially it for the project. However, I was just beginning the most difficult part of the project - determining how to draw a boundary/line from my phase stability observations. Most of the experimenters before me produced their own results, drew a line by hand, and considered it acceptable. They were often very selective with their data, discarding any inconsistent runs and finding reasons to justify excluding

them from the analysis. While this practice isn't necessarily "wrong," since it represents personal judgment based on expert experience, the problem arises when experts draw many different lines for a single phase boundary—so which one should I trust?

I began to consider an alternative, more "mechanical" method of finding the phase boundary, as opposed to the conventional expert judgment approach, which may suffer from a posteriori bias based on the experimenter's idiosyncratic judgment. Unfortunately, there are few readily available inversion schemes in the literature. "HeFESTo" has an inversion code based on linear discriminant analysis implemented by Lars, but this requires careful selection of a minimal set of observations. Consequently, linear discriminant analysis, like human vision, performs poorly when faced with conflicting evidence (Stixrude and Lithgow-Bertelloni 2011). When I visited Lars after he moved to UCLA, I asked him about the inversion strategy. He referred me to a book chapter by Abby Kavner that presented a probability analysis of phase stability observations based on logistic regression (Kavner et al. 2000). This was something he was interested in implementing in HeFESTo, but had limited time to fully develop. I took a quick look at the article but couldn't fully understand the paper, so this direction came to a standstill.

At EPS, every graduate student is required to take two math or statistics classes. At the time, I was one class away from fulfilling this requirement. So I decided to enroll in an introductory data science class with Matt and Zack, not realizing that the core of such a class would revolve around classification—essentially, drawing boundaries for multidimensional data. Throughout the course, I was systematically introduced to a variety of classification algorithms, from logistic regression to random forests to neural networks.

This course helped me develop the technical skills needed to implement Lars' suggestion to try logistic regression. Building on Abby's article, the advantage of this approach is the introduction of supervised learning, which helps avoid overfitting. Machine learning may be a more brutal approach compared to the fine-tuned expert judgment we are familiar with, but it offers an alternative perspective that contrasts with traditional methods that are often highly selective in their results and thus more susceptible to a posteriori bias.

Over the course of five years, almost the entirety of my Ph.D., this phase transition project progressed from our initial experiments on Mg_2SiO_4 to the development of a global inversion strategy for phase stability data. A preprint of an improved Mg_2SiO_4 phase diagram generated using a novel global inversion strategy was posted to arXiv in 2022 (Dong et al. 2022a). This journey taught me the hard lesson that data analysis is often as important as data collection. However, in the mineral physics community, data analysis currently seems to receive far less epistemic credit than the production of primary data, even when the published primary data was accompanied by potentially flawed interpretations. Thanks to the challenges I encountered during my experimental efforts, I was motivated to delve into this exploding field of data science and machine learning, which not only opened up a whole new direction for my research, but also provided a fresh perspective on the existing data that the mineral physics community has been collecting for decades.

Now, let me give you a preview of what's to come. In Chapters 2 and 3, I will take you on a journey exploring the deep water cycle and surface water stability of Earth and Mars using a thermodynamic model of water storage capacity in nominally anhydrous minerals. With these findings, I will demonstrate how the water storage capacity of the

solid mantles of these planets generally increases with decreasing temperature due to secular cooling. Surprisingly, the water capacity in the early, hot mantle of Earth is probably smaller than in the present-day mantle water content, indicating that the extra water in today's mantle would have existed on the early surface, forming a water world with little exposed land. Additionally, I will explore the relationship between an early global ocean, the geological record, and the habitats of early life.

In Chapter 4, I will introduce you to a machine learning approach that infers high pressure phase transitions from experimental data on Mg_2SiO_4 and addresses the nonlinearity of the post-spinel transition. I will explain how this nonlinear transition affects mantle convection and its expression in slabs and plumes worldwide. Through my results, you will see that in the present-day mantle, the average post-spinel Clapeyron slope in plumes is about three times more negative than that in slabs.

Recently, I have been working to develop reference P–T phase diagrams for the major mantle oxides and iron using the global inversion strategy presented in Chapter 4. This project has the potential to synthesize existing experimental and simulated data up to multi-megabar pressures, and the resulting phase diagrams will serve as a roadmap for exploration of planetary interiors. However, the preliminary results need further refinement and are incomplete. As a result, I have decided not to include them in this dissertation, but hope to refine and publish these results in the next few years.

In the Afterword, I offer a more detailed consideration of two types of water worlds. The first is a terrestrial world with all its continents submerged in water, and the second is an exoplanet with a thick water envelope. I then discuss how my interest in this topic has evolved from one type of water world to the other, and how this evolution

has reflexively shaped my research goals for the future. I also discuss my attempt to draw an "objective" phase boundary, and how this challenge sparked my interest in the philosophy of science and the concept of objectivity.

As I wrap up this introduction, I'd also like to emphasize my interest in the history of geophysics, which occupied most of my time during the last few years of my Ph.D. when I wasn't debugging code or running experiments. I came across a wealth of fascinating archival materials related to Francis Birch, one of the founders of solid earth science. These materials have the potential to reveal the early history of mineral physics and the connection between the Manhattan Project and Birch's model of the Earth's interior. Unfortunately, I have not devoted as much attention to discussing my historical research as I have to my scientific work in this dissertation. Nevertheless, I remain optimistic that I'll soon be able to put these archival materials into a narrative and bring them to light.

Chapter 2

Constraining the Volume of Earth's Early Oceans With a Temperature-Dependent Mantle Water Storage Capacity Model

Water, water, every where,

And all the boards did shrink.

—Samuel Taylor Coleridge, *The Rime of the Ancient Mariner*

Abstract*

The water content in Earth's mantle today remains poorly constrained, but the bulk water storage capacity in the solid mantle can be quantified based on experimental data and may amount to a few times the modern surface ocean mass (OM). An appreciation of the mantle water storage capacity is indispensable to our understanding of how water may have cycled between the surface and mantle reservoirs and changed the volume of the oceans through time. In this study, we parameterized high pressure-temperature experimental data on water storage capacities in major rock-forming minerals to track the bulk water storage capacity in Earth's solid mantle as a function of temperature. We found that the mantle water storage capacity decreases as mantle potential temperature (T_p) increases, and its estimated value depends on the water storage capacity of bridgmanite in the lower mantle: 1.86–4.41 OM with a median of 2.29 OM for today (T_p = 1600 K), and 0.52–1.69 OM with a median of 0.72 OM for the early Earth's solid mantle (for a T_p that was 300 K higher). An increase in T_p by 200–300 K results in a decrease in the mantle water storage capacity by $1.19^{+0.9}_{-0.16}$–$1.56^{+1.1}_{-0.22}$ OM. We explored how the volume of early oceans may have controlled sea level during the early Archean (4–3.2 Ga) with some additional assumptions about early continents. We found that more voluminous surface oceans might have existed if the actual mantle water content today is >0.3–0.8 OM and the early Archean T_p was ≥1900 K.

*This chapter includes modified content from my previously published article, "Constraining the Volume of Earth's Early Oceans With a Temperature-Dependent Mantle Water Storage Capacity Model," which appeared in *AGU Advances* in 2021.

2.1 Introduction

Water was delivered to the Earth during accretion and/or soon afterward (Morbidelli et al. 2000). This was followed by vigorous outgassing of possibly oxidized volcanogenic gases, including H_2O (Hirschmann et al. 2012), from the early Earth's mantle, which may have led to the formation of primordial oceans (Elkins-Tanton 2008). Sometime after the onset of plate tectonics, mantle rehydration by subduction (Rüpke et al. 2004; Iwamori 2007; van Keken et al. 2011) began to change the relative water contents of the surface and internal reservoirs.

Extensively preserved eustatic sea-level records indicate that the continental freeboard has been approximately constant throughout the Phanerozoic (541 Ma to the present) (Miller et al. 2005). However, the subaqueous and subaerial proportions of the Earth's surface may have been quite different before the Phanerozoic, especially in the early Archean, approximately from the Eoarchean to the Paleoarchean (4–3.2 Ga). Though they are sparse, isotopic records from the early Archean may be used to indirectly constrain the size of the early oceans (Kurokawa et al. 2018; Pope et al. 2012; Johnson and Wing 2020). One such constraint is the deuterium-depleted hydrogen isotopic signature (D/H) recorded in serpentinized oceanic crust from the ca. 3.8 Ga Isua Supracrustal Belt in Greenland. This low D/H ratio of the Eoarchean ocean could be explained by the preferential loss of hydrogen from the deuterium-depleted early oceans to the mantle through subduction over geologic time, which suggests more voluminous oceans in the early Archean (Kurokawa et al. 2018; Pope et al. 2012).

Previous studies showed that surface water may have been continuously transported beyond the volcanic front to contribute to the deeper mantle's possible water-rich regions

(Hacker 2008; van Keken et al. 2011). The exact value of the present-day global net water flux into the deep mantle is still under debate, especially in terms of uncertainties associated with the contribution of (nonmagmatic) updip transport of water (e.g., Bebout 1996) and the hydration (serpentinization) of oceanic mantle (e.g., Korenaga et al. 2017). The current estimates on the present-day value are on the order of 10^{11}–10^{12} kg/year (Korenaga et al. 2017; Schmidt and Poli 2014; van Keken et al. 2011). Furthermore, the onset and efficiency of early subduction, and hence the total net water flux in the past, remains even less constrained (e.g., van Hunen and Moyen 2012). If the recycled water flux were larger than the outgassed water flux over the age of the Earth, then possibly several tens of percent to a few times the Earth's present-day ocean mass (OM) could have been returned into the deep mantle van Keken et al. (2011).

Numerous geodynamical studies have investigated the coupled evolution of Earth's interior and surface oceans in hydrous mantle convection, implying that the volume of the surface oceans evolves with time over billion-year timescales (e.g., Crowley et al. 2011; Korenaga et al. 2017; Nakagawa and Iwamori 2019; Price et al. 2019; Sandu et al. 2011). However, most of the existing geodynamical models did not take into account the mineral physics constraints on mantle water storage; some assumed that the solid mantle is a water reservoir with infinite storage capacity. In reality, Earth's solid mantle has a finite water storage capacity (e.g., Bercovici and Karato 2003). Melting of mantle rocks and hence the release of water will occur when the mantle water content exceeds its storage capacity (the maximum amount of water that mantle mineral assemblages can hold structurally) near its solidus. The coevolution of water in Earth's interior and surface reservoirs may have been further regulated by the bulk water storage capacity in the solid mantle; however, this particular perspective remains virtually unexplored.

In mineral physics, water storage capacities in major rock-forming minerals of Earth's mantle have been studied individually by high pressure (P) and temperature (T) experiments and/or ab initio molecular dynamic simulations (Tables A.1–A.3). In particular, due to the strong negative effect of temperature on water storage capacities in nominally anhydrous minerals (NAMs), the mantle water storage capacity would have increased over geologic time as a result of secular planetary cooling. Although these individual water storage capacities have been measured over ranges in temperature and pressure that encompass much of the present-day and early mantle conditions, a detailed, quantitative estimate of the bulk mantle water storage capacity is not yet available. This study estimated the bulk water storage capacity in Earth's solid mantle at different mantle potential temperatures (T_{p}) and demonstrated that the bulk solid mantle water storage capacity was smaller in the hotter mantle of the early Earth relative to that of the present-day. In addition, we applied this temperature-dependent water storage capacity model to constrain the volume of the surface oceans and explore its implications on long-term sea-level change.

2.2 Methods

2.2.1 Water Storage Capacities in Olivine, Wadsleyite, and Ringwoodite

To quantify the P–T effects on water storage capacities in major NAMs of Earth's mantle, we compiled and parameterized high-pressure mineral physics data on water storage capacities (Tables A.1–A.3; Fig. 2.1) and partition coefficients of the NAMs

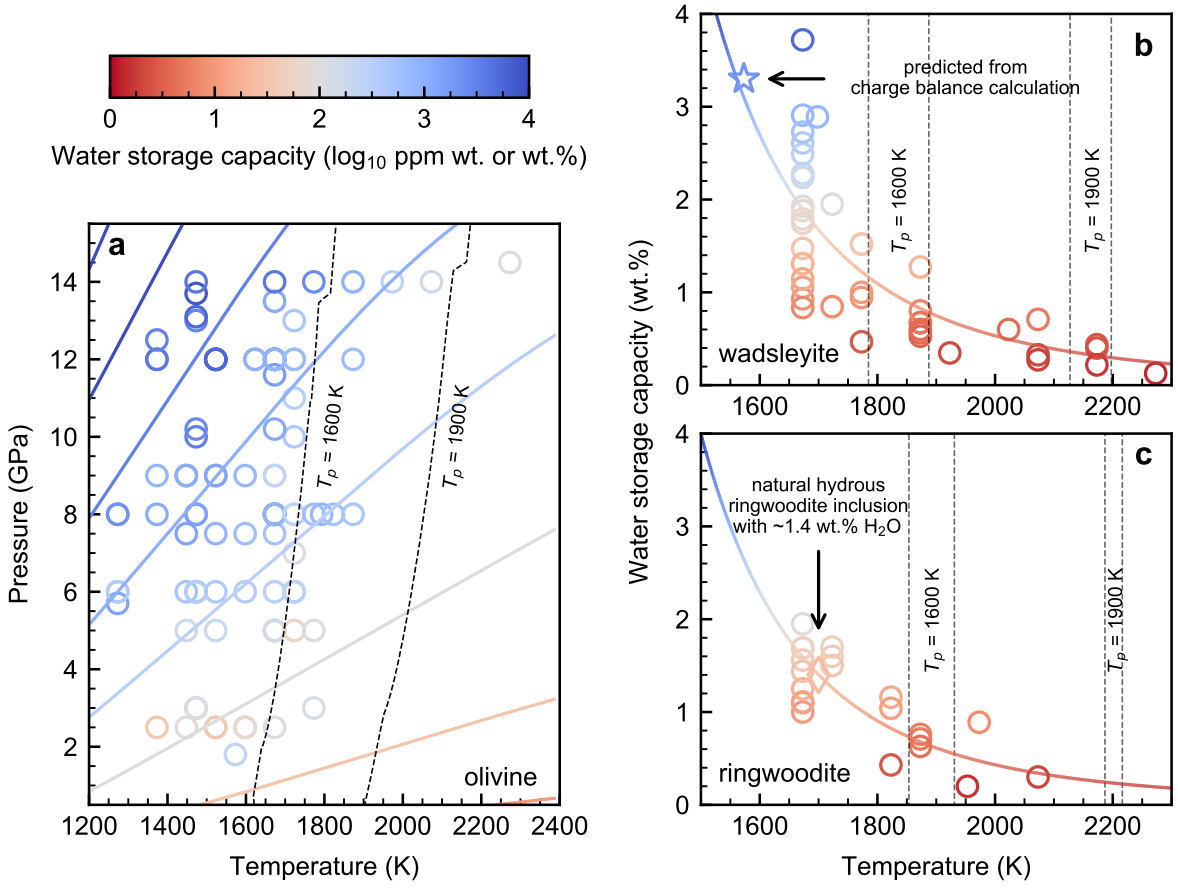
(Table S4). Hydrogen enters these NAMs through crystal defects and forms hydroxyl groups. The water storage capacity in a mineral under H_2O-saturated conditions can be expressed as (see Appendix A.1):

$$\ln(c_{\mathrm{H_2O}}) = \ln(\frac{1}{2\mathrm{n}}) + \mathrm{a} + \frac{\mathrm{n}}{2} \cdot \ln(f_{\mathrm{H_2O}}) + \frac{\mathrm{b} + \mathrm{c} \cdot P + \mathrm{d} \cdot X_{Fe}}{T} \tag{2.1}$$

with T in kelvin (K), P in gigapascals (GPa), $f_{\mathrm{H_2O}}$ (water fugacity) in GPa, and X_{Fe} (iron content) in mole fraction. The parameters a, b, c, d, and n are obtained from an nonlinear robust regression to the compiled experimental data for olivine, wadsleyite, and ringwoodite. We quantified the water storage capacities in other abundant NAMs in the upper mantle and transition zone using their water partition coefficients (see Section 2.3).

In selecting experimental data to include in the fitting, we have established the following criteria: 1) At least one liquid phase has to be present in the recovered phase assemblage to ensure that the coexisting NAMs were most likely saturated with water (when the water concentration equals the water storage capacity). 2) Only water storage capacities measured by direct quantitative analytical methods (Fourier transform infrared spectroscopy [FTIR], secondary ionization mass spectrometry [SIMS], and elastic recoil detection analysis [ERDA]) were used. In contrast, those based on more qualitative estimation methods (e.g., water content estimated from lattice parameters) were excluded. More details on data selection are described in Appendix A.2.

Figure 2.1 *(following page)*: **Water storage capacities in olivine (a), wadsleyite (b), and ringwoodite (c) at high pressure and temperature.** The colored open circles are experimentally determined water storage capacity data from Tables A.1–A.3. The colored lines correspond to the fits to the data, with the regression parameters provided in Table A.4. Symbol and line colors indicate water storage capacities in log ppm wt. (olivine) or wt. (wadsleyite and ringwoodite). In (a), the black dotted lines indicate the present-day geotherm ($T_\mathrm{p} = 1600$ K) and the early Archean geotherm ($T_\mathrm{p} = 1900$ K). In (b), the star is a theoretical estimate of water storage capacity in wadsleyite at 1573 K and 15.5 GPa, based on a charge balance calculation (Kudoh et al. 1996). In (b and c), the dashed rectangular boxes indicate the temperature ranges inclusion containing ∼1.4 wt.% H_2O (Pearson et al. 2014) is indicated by an arrow. Its water content corresponds to formation at up to ∼1690 K, consistent with its cold origin in a subducting slab.


0
1
2
3
4
Water storage capacity ($\log_{10}$ ppm wt. or wt.%)
a
Pressure (GPa)
Temperature (K)
T_p = 1600 K
T_p = 1900 K
olivine
b
predicted from
charge balance calculation
wadsleyite
c
natural hydrous
ringwoodite inclusion
with ~1.4 wt.% H_2O
ringwoodite
Water storage capacity (wt.%)

2.2.2 Water Storage Capacity in Bridgmanite and Other Lower Mantle NAMs

Experimental constraints on water storage capacities in lower mantle NAMs are inconsistent and insufficient to fit the thermodynamic model presented above. The synthesis of large, high-quality hydrous single crystals of lower mantle phases and measurements of their water contents will likely remain technically difficult for a long time to come.

This study focused on the temperature effect on solid mantle storage capacity, so we investigated a temperature-dependent scenario: different values for bridgmanite's water storage capacity are calculated based on the temperature-dependent water storage capacity in ringwoodite (Figure 1c) and the experimentally determined partition coefficient between ringwoodite and bridgmanite ($D_{rw/bdg} = 15 \pm 8$; Inoue et al. 2006). The partition coefficient values used here are in good agreement with the ab initio simulation performed by Hernández et al. (2015), where they found a partition coefficient of about 15 for the Fe-bearing system. This scenario resembles a pyrolitic mantle where ringwoodite and bridgmanite coexist. Bridgmanite makes up more than half the mass of the mantle, so uncertainties in bridgmanite's water storage capacity are by far the most important consideration in evaluating constraints on whole-mantle storage capacity.

Therefore, we performed a series of Monte Carlos simulations to examine the combined uncertainties of the thermodynamic models for olivine, wadsleyite, and ringwoodite, and the water storage capacity in bridgmanite calculated from the partition coefficient (Section 2.4). We also estimated the bulk water storage capacity associated with each experimental constraint on bridgmanite (Section 3.2) and demonstrated that

our stated uncertainty range encompasses the full range of water storage capacities reported by previous experimental studies on bridgmanite (see data compilations in Kaminsky 2018; Fu et al. 2019).

The water storage capacity in postperovskite is calculated based on the computationally determined, temperature-dependent partition coefficient between bridgmanite and post-perovskite ($D_{bdg/ppv}$ = 2–18; Townsend et al. 2016), with 10 ppm wt. prescribed for both calcium silicate perovskite and ferropericlase. Calcium silicate perovskite may have a higher water storage capacity (Chen et al. 2020), especially at the P–T conditions of the uppermost lower mantle (Muir and Brodholt 2018). However, this high-pressure mineral converts to an amorphous phase upon pressure release, so its water storage capacity has not been quantitatively constrained (Chen et al. 2020; Németh et al. 2017). The water storage capacity in ferropericlase is likely to be relatively low throughout the lower mantle (Bolfan-Casanova et al. 2002; Litasov 2010).

2.2.3 Phase Equilibria of Earth's Solid Mantle and Its Bulk Water Storage Capacity

Using the thermodynamic code HeFESTo and the self-consistent thermodynamic data set contained therein (Stixrude and Lithgow-Bertelloni 2011), phase proportions for the pyrolite mantle were computed along a series of geothermal adiabats at various mantle potential temperatures (T_{p}) from 1550 K to 1950 K, with consideration of the influence of phase transformations on the mantle's thermal structure. Melting was not included in the phase equilibria computation. The simplified bulk composition of pyrolite (Workman and Hart 2005) (in mole%) includes six chemical components: SiO_2 (38.71%), MgO

(49.85%), FeO (6.17%), CaO (2.94%), Al_2O_3 (2.22%), and Na_2O (0.11%), which form 21 distinct mantle phases. An equilibrium phase diagram of Earth's pyrolite mantle was computed up to 27 GPa (Figure 2), and phase assemblages above the anhydrous solidus curve (Herzberg et al. 2000) were truncated.

In calculating the Earth's solid mantle bulk water storage capacity, the water storage capacities in individual mantle minerals at each pressure and temperature were evaluated and summed. The water storage capacity models for olivine, wadsleyite, ringwoodite, and bridgmanite are described in Sections 2.1 and 2.2. The water storage capacities in the rest of the abundant mantle silicates (j), including orthopyroxene, clinopyroxene, garnet, and high-pressure clinoenstatite, were estimated based on their water partition coefficients ($D^{\frac{i}{j}}_{H_2O}$) relative to a major silicate phase (i):

$$c^j_{H_2O} = \frac{c^i_{H_2O}}{D^{\frac{i}{j}}_{H_2O}(T, P, X_{Fe}, X_{Al})} \tag{2.2}$$

The partitioning behavior of water is a function of T, P, X_{Fe}, and X_{Al}. Here, we consider temperature, pressure, and compositional dependences for the water partition coefficients of orthopyroxene, clinopyroxene, and garnet relative to olivine, which have been parameterized based on previous studies (Hauri et al. 2006; Keppler and Bolfan-Casanova 2006):

$$D^{\frac{i}{j}}_{H_2O}(T, P, X_{Fe}, X_{Al}) = \frac{c^i_{H_2O}}{c^j_{H_2O}} = \frac{A_i}{A_j} \cdot f^{n_i - n_j}_{H_2O} \cdot e^{\frac{(\Delta H^{1\ bar}_i - \Delta H^{1\ bar}_j) + (\Delta V^{solid}_i - \Delta V^{solid}_j)\cdot P}{RT}} \tag{2.3}$$

The water storage capacities in the literature compilations (Hauri et al. 2006; Keppler and Bolfan-Casanova 2006) used in the partition coefficient calculations were based on uncorrected experimental data (see Appendix A.2), but they are self-consistent and hence provide the P–T dependences of the partition coefficients.

Here, to obtain their water partition coefficients at different P–T conditions and Al contents, we used the previously published and tabulated parameters for the water storage capacities in olivine, orthopyroxene, clinopyroxene, and garnet (Table A.5) in Eq. 2.3. The water storage capacities in orthopyroxene, clinopyroxene, and garnet used here were based on the water storage capacity in olivine and the partition coefficients calculated from Equations 2 and 3. The water partition coefficient of high-pressure clinoenstatite relative to olivine can be approximated as a constant ($D_{\mathrm{H_2O}}^{ol/hcp} \approx 0.8$; Withers et al., 2007).

The total solid mantle water storage capacity was then taken as the sum of the water storage capacities in individual mantle minerals based on the relative abundances of the thermodynamically stable phases that are present at that P–T condition:

$$c_{\mathrm{H_2O}}^{\mathrm{mantle}} = (c_{\mathrm{H_2O}})_i \cdot (X_i + \sum_j (X_j \cdot D_{\mathrm{H_2O}}^{\frac{i}{j}})) \tag{2.4}$$

where $X_{i,j}$ is the mole fractions of minerals i (*olivine* and its polymorphs) and j (other mantle minerals) in pyrolite. Water storage capacity profiles as a function of depth were quantified along a series of geotherms and integrated to produce total water storage capacities of the pyrolitic mantle as a function of mantle potential temperature.

The nominally anhydrous phase assemblage of the pyrolite mantle between 3 and 27 GPa computed from HeFESTo (Fig. 2.2) is consistent with the experimentally determined phase relations for a CMAS-pyrolite with 2 wt.% H_2O (Litasov and Ohtani 2002), where all hydrous minerals are unlikely to be stable along the geotherms of the ambient mantle, especially in the early Archean when T_{p} was 200–300 K higher (Herzberg et al. 2010). The effects of water on melting (Hirschmann et al. 2009) and solid-state phase transformations (Frost and Dolejs 2007), likely to be relatively small

under nominally anhydrous conditions, were not considered in the computation.

2.2.4 Uncertainties in Mantle Water Storage Capacity From Monte Carlo Sampling

The temperature-dependent mantle water storage capacity model described above involves a number of input parameters with associated uncertainties, assumed to be normally distributed, including the experimentally determined partition coefficient between ringwoodite and bridgmanite (Inoue et al. 2006) and fitted regression parameters (Table A.4).

To obtain a statistically significant estimate of mantle water storage capacity and investigate the propagation of the uncertainties associated with all parameters, we used a Monte Carlo sampling method to explore the full parameter space. Each Monte Carlo simulation is based on 10^4 combinations of randomly sampled parameters from their normal distributions. Parameters for upper mantle and transition zone minerals are given in Table A.4. For bridgmanite, $D_{rw/bdg} = 15 \pm 8$ (Inoue et al. 2006). The mantle water storage capacity reported for each potential temperature corresponds to the median of one representative set of 10^4 simulations. Two-sided uncertainties in mantle water storage capacity at each T_p were used, corresponding to the 5th and 95th percentiles of the distribution; the interquartile range (IQR) of each distribution, between the 25th and 75th percentiles, is also presented. The Monte Carlo sampling occasionally generated unphysical water storage capacities in bridgmanite (i.e., negative values or 4 wt.%), due to the considerable uncertainty in $D_{rw/bdg}$. These extreme values are less than 0.5 % of the total sampled parameters and have been removed. The distribution of the simulation

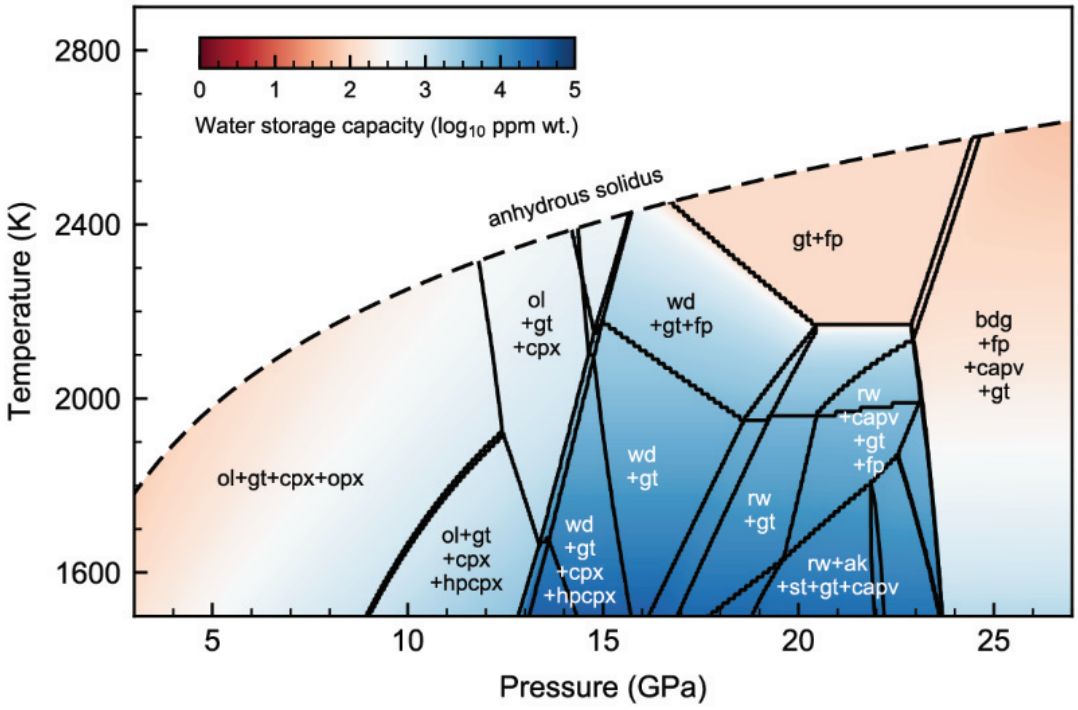


Figure 2.2: **Bulk water storage capacity map of the pyrolitic mantle up to 27 GPa.** The bulk water storage capacities were calculated based on the relative abundances and water storage capacities of NAMs at each P—T (Tables A.1–A.5). The stable phase assemblages of a pyrolitic mantle were computed using the thermodynamic code HeFESTo. Mantle phases are labeled as: *ol*: olivine, *wd*: wadsleyite, *rw*: ringwoodite, *bdg*: bridgmanite, *fp*: ferropericlase, *cpx*: clinopyroxene, *opx*: orthopyroxene, *hpcpx*: high-pressure clinopyroxene, *ak*: akimotoite, *st*: stishovite, and *capv*: $CaSiO_3$-perovskite.

results is close to log-normal but with long tails, likely due to the large uncertainty associated with the water storage capacity in bridgmanite.

2.2.5 Isostatic Equilibrium and Flooding of Early Continents

The estimated water storage capacity in the early Archean mantle and the possible range of present-day mantle water contents, were then used to calculate minimum volumes of the early Earth's oceans (Section 3.3). The implications for flooding of the continents were investigated, with the isostatic balance between continents and oceans parameterized as (Figure S4; Flament et al. 2008; Korenaga et al. 2017):

$$eqn - ch2 - 5\rho_{\mathrm{w}} \cdot (h + d_0) + \rho_{\mathrm{oc}} \cdot h_{\mathrm{oc}} + \rho_{\mathrm{ol}} \cdot h_{\mathrm{ol}} + \rho_{\mathrm{om}} \cdot h_{\mathrm{om}} = \rho_{\mathrm{om}} \cdot \max(0, h) + \rho_{\mathrm{cc}} \cdot h_{\mathrm{cc}} + \rho_{\mathrm{cl}} \cdot h_{\mathrm{cl}} \tag{2.5}$$

where h is the sea level difference relative to the present-day value and d_0 is the depth of mid-ocean ridges. ρ_i and h_i denote the densities and thicknesses, respectively, of the various components i in the isostatic balance, namely water (w), oceanic crust (oc), depleted oceanic lithospheric mantle (ol), oceanic asthenospheric mantle (om), continental crust (cc), and continental lithospheric mantle (cl).

The present-day hypsometry curve (continental elevation relative to sea level) was approximated by fitting the ETOPO1 Global Relief Model (Amante and Eakins 2009), where ∼27.5% of the present-day continents are submerged under water. The vertical scale of hypsometry was defined as a variable to describe its likely reduction due to the weaker lithosphere in the Archean (Rey and Coltice 2008). Both cases with and without reduction in the hypsometry were tested (Section 3.4). The bathymetry curve was calculated based on Flament et al. (2008), and the details are described in Appendix

A.3.

The densities and thicknesses of oceanic crust and depleted mantle ($\rho_{\rm oc}$, $\rho_{\rm ol}$, $h_{\rm oc}$, and $h_{\rm ol}$) can be parameterized as functions of mantle potential temperature, based on a decompression melting model (Korenaga 2006) in which a hotter mantle in the Archean would generate thicker oceanic crusts ($h_{\rm oc}$) and depleted mantle residues ($h_{\rm ol}$). The density of oceanic asthenospheric mantle ($\rho_{\rm om}$) can also be parameterized as a function of mantle potential temperature (Korenaga et al. 2017):

$$\rho_{\rm om}(T_{\rm p}) = \rho_{\rm om}(T_{\rm p,0}) \cdot (1 - \alpha \cdot (T_{\rm p} - T_{\rm p,0})) \tag{2.6}$$

where $\rho_{\rm om}(T_{\rm p,0})$ is 3300 kg/m^3 and the thermal expansion coefficient α is 3.5 $\times$ 10^{-5} K^{-1} (Bouhifd et al. 1996). The density and thickness of continental crust are assumed to be independent of potential temperature and are taken to be $\rho_{\rm cc}$ = 2890 kg/m^3 (Korenaga et al. 2017) and $h_{\rm cc}$ = 34 km (Huang et al. 2013), respectively. The average density of continental crust is assumed to be constant through time based on recent studies suggesting that the Archean continental crust was dominated by felsic rocks (e.g., Greber and Dauphas 2019; Guo and Korenaga 2020; Ptáček et al. 2020). However, the possibility of a more mafic early continental crust, which would have been denser, cannot be ruled out (e.g., Tang et al. 2016). The average Archean continental lithospheric mantle was likely highly depleted compared to its oceanic counterpart (Servali and Korenaga 2018). To describe how buoyant the continents would have been in the early Archean, we introduced a buoyancy correction, $\Delta\rho^A_{\rm cl}$ = –5 kg/m$_3$, similar to Korenaga et al. (2017). The density $\Delta\rho^A_{\rm cl}$ = –5 kg/m$_3$ is hence expressed as $\rho_{\rm om}(T_{\rm p})$ + $\Delta\rho^A_{\rm cl}$ = –5 kg/m^3. The compensation depth is taken as the base of the continental lithosphere (200 km), which is used to determine the thicknesses of the oceanic asthenospheric mantle

(h_{om}) and continental lithosphere (h_{cl}) in the model (Fig. A.4).

With the final topographic profile governed by oceanic and continental buoyancy, bathymetry, and hypsometry, the integral of the ocean volume over the submerged area was calculated. The convergence of sea level (h) was obtained by iteratively computing the ocean volume at various h until the desired ocean volume at the relevant mantle potential temperature T_{p} was reached, using the bisection method with a step size in h of 10^{-4} km. The ocean volume of the present-day Earth was benchmarked to be 1.45×10^{21} kg, which agrees with the ocean volume calculated from ETOPO1 (OM = 1.335×10^{21} kg) (Eakins and Sharman 2010) within <12%.

2.3 Results and Discussion

2.3.1 Parameterization of the Water Storage Capacity Model in Olivine, Wadsleyite, and Ringwoodite

The five parameters a, b, c, d, and n were fitted to the data on water storage capacity in olivine (Table A.1) using a robust regression with bisquare weighting of the residuals. Constants a, c, and d were found to be statistically insignificant (p-values > 0.05; no significant compositional dependence within the range Mg# = $\frac{X_{\mathrm{Mg}}}{X_{\mathrm{Mg}}+X_{\mathrm{Fe}}} \cdot 100$ = 81–100, and pressure affects water storage capacity only through $f_{\mathrm{H_2O}}$), which yields the equation (Fig. 2.1a; Table A.4):

$$\ln(c_{\mathrm{H_2O}}) = \frac{\mathrm{n}}{2} \cdot \ln(f_{\mathrm{H_2O}}) + \frac{\mathrm{b}}{T} \tag{2.7}$$

The fitted value of n may represent the average number of hydroxyls through multiple substitution mechanisms over the wide range of pressure and water concentration for olivine (Ferot and Bolfan-Casanova 2012; Otsuka and Karato 2011). Temperature dependence of the water storage capacity in olivine ($\frac{b}{T}$) can be attributed to the decrease in the activity of the H_2O component in the aqueous fluid or silicate melt with increasing temperature (Mibe et al. 2002; Stalder et al. 2001).

Similarly, the five parameters were fitted to the data on water storage capacity in wadsleyite and ringwoodite (Tables A.2 and A.3), and n, c, and d were found to be statistically insignificant (p-values > 0.05; i.e., no significant water fugacity, pressure, or compositional dependence). Therefore, with the fits of a and b from a robust regression (Figures 2.1b and 2.1c; Table A.4), the water storage capacities in wadsleyite and ringwoodite can be expressed in a simplified form of Eq. 2.1:

$$\ln(c_{H_2O}) = a + \frac{b}{T} \tag{2.8}$$

Under pressures and temperatures beyond upper mantle conditions (>5 GPa), aqueous fluids and silicate melts are completely miscible and become one single liquid phase (Mibe et al. 2002). Increasing miscibility between silicate melts and hydrous fluids may provide a physical explanation for the lack of statistical significance of the water fugacity term in Equation 8 (when f_{H_2O} can no longer be approximated by the equation of state of pure water at these conditions), and leaves three degrees of freedom in the system MgO–SiO_2–H_2O. Even at a fixed pressure and temperature (two degrees of freedom), the water storage capacity can only be strictly defined and unique if one additional coexisting phase is present. In practice, however, measurements of the water storage capacities in wadsleyite and ringwoodite remain approximately the

same regardless of the speciation, even in the presence of an additional buffering phase (Litasov et al. 2011). Therefore, experimental data in the literature may be used to fit the model (Eq. 2.8) regardless of the experiments' buffering phases.

Since wadsleyite and ringwoodite are stable over a narrower range of pressure than olivine, no significant pressure effect was observed experimentally (Demouchy et al. 2005). Water storage capacities in Fe-bearing wadsleyite (Mg# = 87–96) were shown to be comparable to those in Fe-free wadsleyite (Litasov and Ohtani 2008). Temperature is the only variable shown experimentally to directly affect water storage capacities in both wadsleyite and ringwoodite (Demouchy et al. 2005; Litasov and Ohtani 2008; Ohtani et al. 2000). Although thermodynamic interpretations of the fitted parameters n, a, and b remain challenging, the water storage capacity parameterizations (Eqs. 2.7 and 2.8; Table A.4) describe the experimental observations adequately (Fig. 2.1; Tables A.1–A.3).

2.3.2 A Comparison of Bridgmanite Water Storage Capacity Between the Temperature-Dependent Mantle Water Storage Capacity Model and Experiments

To model the temperature-dependent water storage capacity in bridgmanite, we used the partition coefficient of water between ringwoodite and bridgmanite. Both the mineral physics experiments of Inoue et al. (2010) and the first-principles simulation of Hernández et al. (2015) suggest $D_{rw/bdg} \approx 15 \pm 8$. In the model, this choice of $D_{rw/bdg}$ leads to 370^{+1240}_{-180} ppm wt. (IQR = 270–570 ppm wt.) in bridgmanite at $T_\mathrm{p} = 1600$ K and 170^{+570}_{-95} ppm wt. (IQR = 110–270 ppm wt.) at $T_\mathrm{p} = 1900$ K. With 10 ppm wt. each in calcium silicate perovskite and ferropericlase, the bulk water storage capacity in the

lower mantle is 290^{+950}_{-140} ppm wt. at $T_{\rm p}$ = 1600 K (IQR = 210–440 ppm wt.) and 130^{+440}_{-70} ppm wt. (IQR = 90–210 ppm wt.) at $T_{\rm p}$ = 1900 K.

Existing measurements on the water storage capacity in bridgmanite are still in disagreement, with quantitative reports ranging from less than a few ppm wt. (Bolfan-Casanova et al. 2003), to a few hundred ppm wt. (e.g., Meade et al., 1994; Litasov et al., 2003 [Al-free]; Inoue et al., 2010; Fu et al., 2019 [FTIR]), to 1,000–1,500 ppm wt. (Litasov et al., 2003 [Al-bearing]; Fu et al., 2019 [SIMS]), to >2,000 ppm wt. (Murakami et al. 2002).

Inoue et al. (2010), referred to hereafter as "In10," synthesized coexisting mineral assemblages of ringwoodite with 0.63–0.76 wt.% H_2O and bridgmanite with 300–700 ppm wt. H_2O at 23–23.2 GPa and 1873 K, with a starting composition of $(Mg_{0.8}Fe_{0.2})_2SiO_4$ plus 15.8 wt.% H_2O. The water contents in the ringwoodite phase have reached the storage capacity of ringwoodite (∼0.68 wt.%, predicted from our ringwoodite model in Section 2.3.1), while a significant amount of water still remained in the bridgmanite phase; both phases are expected to have reached their storage capacities with 15.8 wt.% H_2O in the starting bulk composition. Use of the bridgmanite storage capacity based on In10 has the significant advantage of constraining the temperature dependence through use of the partition coefficient and a temperature-dependent model for ringwoodite.

Two earlier studies by Meade et al. (1994) (Me94) and Litasov et al. (2003) (Li03) reported slightly lower water storage capacities in the Mg-endmember of bridgmanite $MgSiO_3$: in Me94, the FTIR measurements showed 105(25) ppm wt. H_2O at 27 GPa and 2103 K; in Li03, the FTIR measurements indicated 104(14) ppm wt. H_2O, while the SIMS measurements showed 300(100) ppm wt. H2O, in bridgmanite synthesized

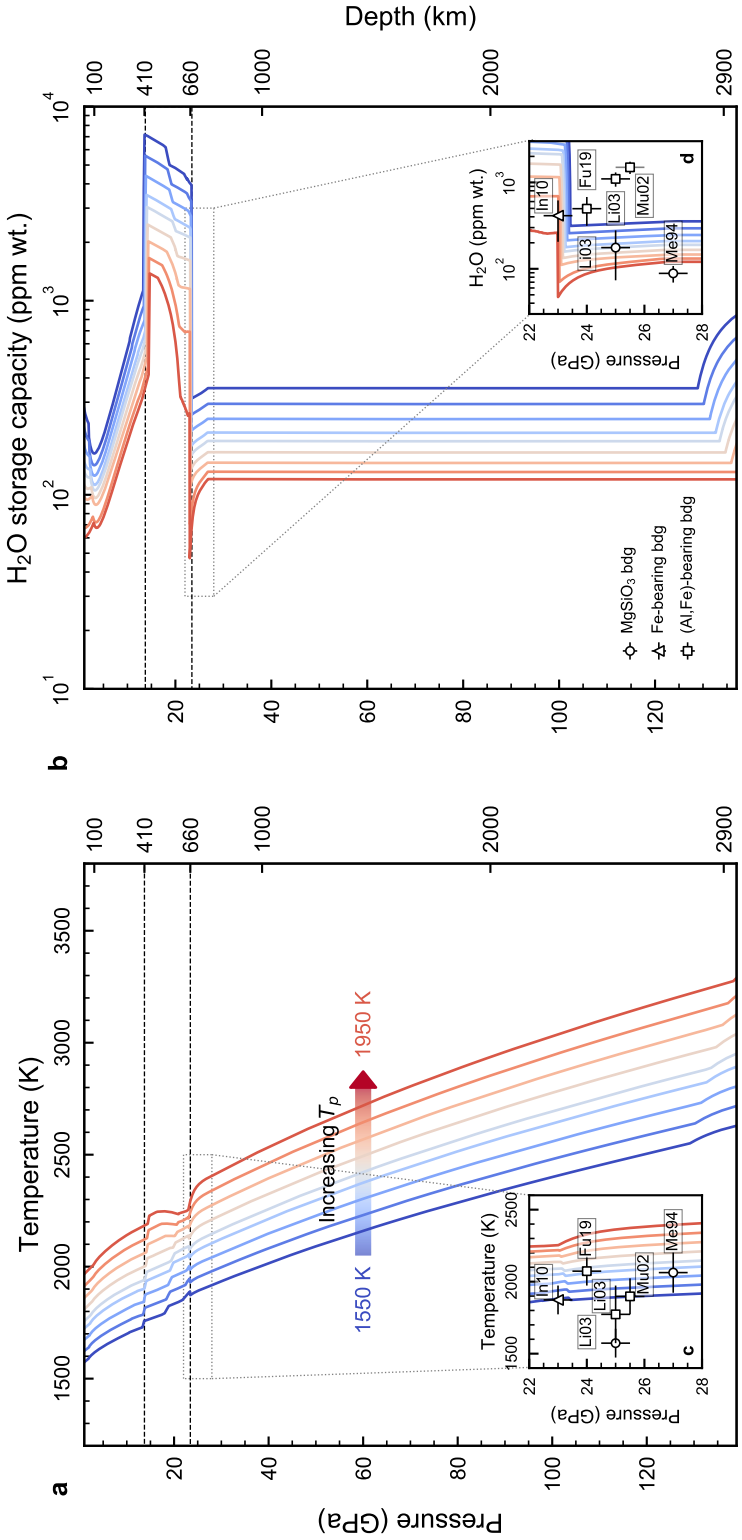
at 25 GPa and 1500 K. Unlike other silicate phases such as olivine, wadsleyite, and ringwoodite (Tables S1–S3), there is an evident discrepancy between the FTIR and SIMS measurements for bridgmanite. The prevalence and cause of this discrepancy between the two analytical methods remain unclear. The most recent study by Fu et al. (2019) (Fu19) showed a similar discrepancy and reported a water concentration in bridgmanite of 596–731 ppm wt. (FTIR) and 1005–1031 ppm wt. (NanoSIMS), where (Al,Fe)-bearing bridgmanite single crystals were synthesized from a hydrous melt containing 6.7 wt.% water at 24 GPa and 2073 K. Compared with the Mg-endmember, the presence of (Al,Fe) may have slightly enhanced the water storage capacity in bridgmanite through a variety of possible substitution mechanisms (Walter et al., 2015), as similar effects have been observed in olivine (Hauri et al. 2006; Withers et al. 2011).

As discussed above, the majority of the existing measurements on water storage capacity in bridgmanite, except for Murakami et al. (2002) (Mu02) and Bolfan-Casanova et al. (2003) (Bo03), are in agreement with the predicted range at $T_{\mathrm{p}} = 1600$ K (190–1570 ppm wt.). Bo03 reported that bridgmanite could contain only a few ppm wt., near or less than the detection limit, while Mu02 reported 1,900–2,400 ppm wt. H_2O in their (Al,Fe)-bearing samples. Both the extremely low (<10 ppm wt.) and high (>2000 ppm wt.) water storage capacities have been suggested to result from the presence of tiny inclusions of hydrous phases in their mineral assemblages (Fu et al. 2019; Schmandt et al. 2014). In Bo03, brucite, $Mg(OH)_2$, and ringwoodite with 0.14–0.21 wt.% water were formed along with dry bridgmanite (1–2 ppm wt.) from a bulk H2O content of 6 wt.% that was likely undersaturated. The water content in its ringwoodite phase was well below the expected storage capacity based on our model (∼1.59 wt.%), also suggesting that the sample was synthesized in water-undersaturated conditions. Brucite

and ringwoodite in Bo03 may have devoured the water in the system and made the amount of water dissolved in their bridgmanite samples much smaller than the storage capacity of bridgmanite coexisting only with hydrous melt (Fu et al. 2019). In Mu02, the high water content based on FTIR may include a contribution from the brucite phase, which is associated with a sharp peak at 3680 cm^{-1} that is present in their FTIR spectra (Fu et al. 2019; Schmandt et al. 2014). The formation of nanoscale, intergranular inclusions of the hydrous phase remains the main challenge in synthesizing hydrous bridgmanite. As yet, only Fu19 successfully measured the water capacity in high-quality, inclusion-free (Al,Fe)-bearing bridgmanite single crystals (596–731 ppm wt. from FTIR and 1005–1031 ppm wt. from NanoSIMS). This measurement may be more robust than previous studies because it avoids the primary source of uncertainty arising from the presence of intergranular hydrous inclusions (Fu et al. 2019). Though no temperature dependence can be derived directly from the Fu19 study based on their bridgmanite single crystals, it does imply that the water storage capacity in bridgmanite is within the ranges of our model results for bridgmanite within the 5th and 95th percentiles (e.g., 190–1610 ppm wt. at T_p = 1600 K; 75–740 ppm wt. at T_p = 1900 K).

We also estimated the bulk water storage capacities that Earth's lower mantle would have based on each experimentally measured bridgmanite water storage capacity (Fig. 2.3). The top of the lower mantle would have a storage capacity of 70–110 ppm wt. and 70–280 ppm wt. based on the $MgSiO_3$ samples from Me94 and Li03, respectively; 310–680 ppm wt. and 890–1300 ppm wt. based on (Al,Fe)-bridgmanite single crystals in Fu19 and (Al,Fe)-bridgmanite in complex assemblages in Li03, respectively; 1250–1740 ppm wt. based on (Al,Fe)-bridgmanite with inclusions of hydrous phases from Mu02. If the absolute water contents in bridgmanite from In10 are used, the bulk lower

Figure 2.3 *(following page)*: **Adiabatic geotherms and water storage capacity profiles at mantle potential temperatures of T_p = 1550–1950 K.** In (a), geothermal profiles are shown with a spacing of 50 K in T_p. The adiabatic curves are deflected at phase transformations according to the Verhoogen effect, where the magnitudes of the temperature discontinuities are related to the latent heat of the pertinent phase transformations. Phase assemblages of the pyrolitic mantle vary slightly for different T_p. In (b), the storage capacity profiles are shown. The mineral assemblages at transition zone pressures (with wadsleyite and ringwoodite) have the largest water storage capacities, but the storage capacity of this region drops by ∼2/3 from T_p = 1600 K–1900 K. The changes in the shapes of the profiles with temperature are due to changes in the stable phase assemblage. The *P*–*T* conditions of the existing experimental constraints on bridgmanite's water storage capacity and estimates of the bulk water storage capacity associated with them at the top of the lower mantle are plotted in the inserts (c and d), respectively. Details can be found in Section 2.3.2


Depth (km)
100
410
660
1000
2000
2900
H_2O storage capacity (ppm wt.)
10^1
10^2
10^3
10^4
b
20
40
60
80
100
120
Pressure (GPa)
H_2O (ppm wt.)
10^2
10^3
d
Li03
Fu19
Mu02
Me94
In10
22
24
26
28
$MgSiO_3$ bdg
Fe-bearing bdg
(Al,Fe)-bearing bdg
Temperature (K)
1500
2000
2500
3000
3500
a
Increasing T_p
1550 K
1950 K
c

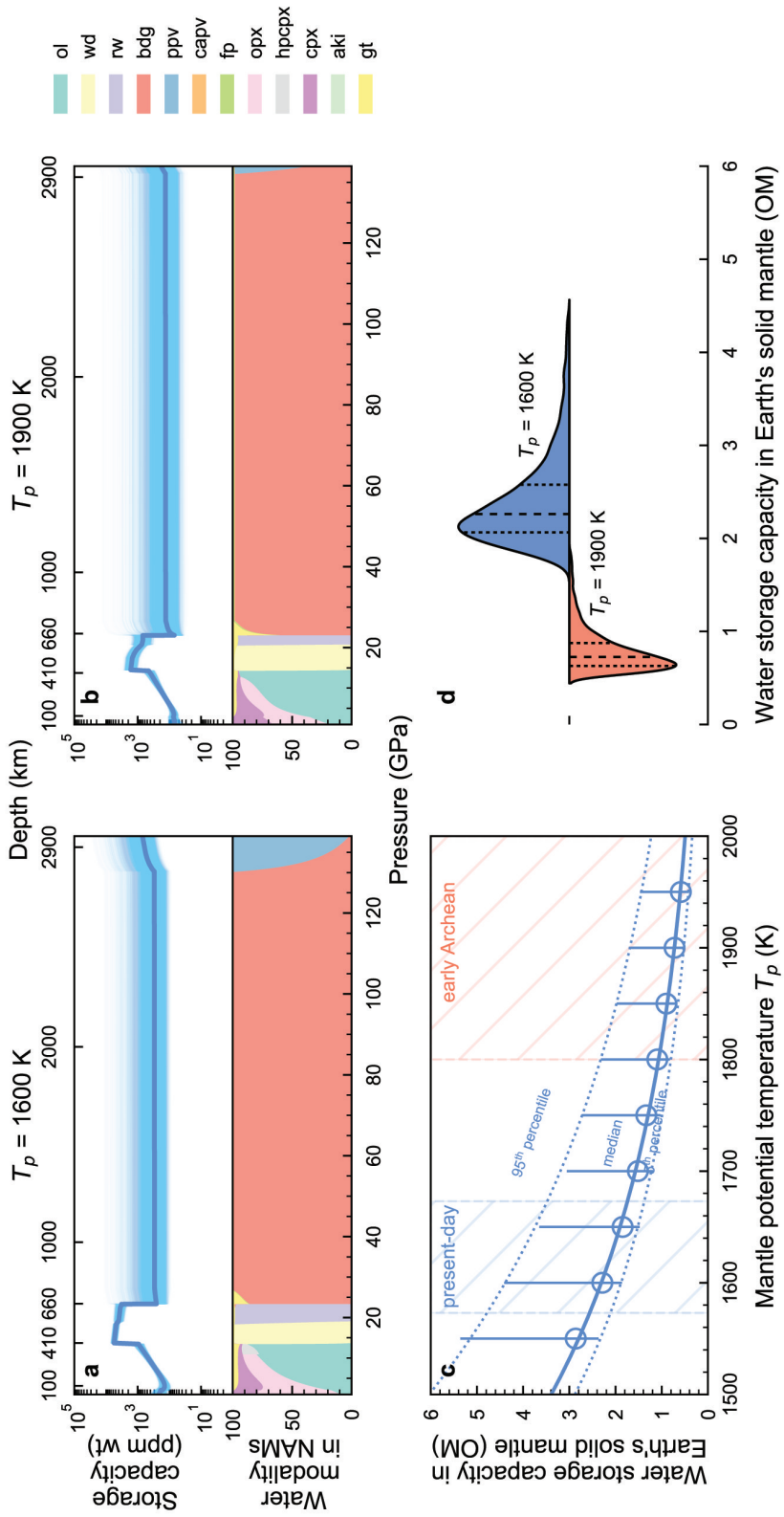
mantle storage capacity is 210–620 ppm wt. H_2O. However, some of these bridgmanite samples were synthesized at temperatures that are much lower than a realistic geotherm, so these values are, to some extent, upper bounds. Even without the Monte Carlos simulations, our model results (Fig. 2.3) are already consistent with the majority of bulk mantle water storage capacities derived from experimental data on bridgmanite and are slightly lower than those based on the (Al,Fe)-bearing samples embedded in complex mineral assemblages reported in Mu02 and Li03. With the Monte Carlos simulations, the estimated uncertainties of our model results between the 5th and 95th percentiles (e.g., 190–1610 ppm wt. at T_p = 1600 K) encompass the full range of the existing measurements of bridgmanite's water storage capacity (Figs. 2.5a and 2.4b).

2.3.3 Temperature-Dependent Mantle Water Storage Capacity

We computed the mantle water storage capacity at each P–T point based on the relative abundances of minerals and their water storage capacities up 27 GPa (Figure 2), and calculated water storage capacity profiles along the different geotherms, then integrated them throughout the entire mantle (Fig. 2.3). The water storage capacity in an upper mantle mineral assemblage increases significantly with pressure, but at the base of the upper mantle it is still about 7 times smaller than that of the transition zone (1210 ppm wt. at 13.5 GPa and 1800 K, vs. 8060 ppm wt. at 14.0 GPa and 1800 K).

For the entire Earth's mantle, we obtained a storage capacity of $2.29^{+2.21}_{-0.43}$ OM (OM = 1.335×10^{21} kg) at present with T_p = 1600 K (IQR = 2.07–2.65 OM), and $0.72^{+0.97}_{-0.20}$ OM in the early Archean with T_p = 1900 K (IQR = 0.62–0.90 OM) (Figs. 2.4, A.1, A.2; Table 2.1). While the uncertainties (5th–95th percentiles) are somewhat

Figure 2.4 *(following page)*: **Temperature–dependent water storage capacity in the Earth's solid mantle.** (a, b) In the upper panels, the thick blue curves correspond to the bulk water storage capacity profiles along a mantle geotherm at (a) $T_{\rm p} = 1600$ K and (b) $T_{\rm p} = 1900$ K, which were calculated with the combination of the best fit parameters listed in Tables A.4 and A.5. The light blue curves correspond to 10^4 samples in a representative set of Monte Carlo simulations. In the lower panels, the contributions of individual NAMs to bulk water storage capacity are shown. (c) Water storage capacity of the Earth's mantle as a function of $T_{\rm p}$. Open blue circles and thick blue curve correspond to the medians of 10^4 Monte Carlo simulations for bulk mantle water storage capacities at each $T_{\rm p}$. The error bars represent the 5th and 95th percentiles of each distribution. The dashed rectangles correspond to the estimated ranges of present-day (blue) and early Archean (red) mantle potential temperatures. The mantle water storage capacity decreases significantly as $T_{\rm p}$ increases, due to the strong temperature dependence of water storage capacities in mantle NAMs. (d) Distributions and differences in mantle water storage capacities generated from the Monte Carlo sampling (within 5th and 95th percentiles) are drawn as violin plots. Each histogram shows the statistical distribution of the sampled bulk water storage capacities. The vertical dashed and dotted lines represent the medians and interquartile ranges, respectively, for $T_{\rm p} = 1600$ K (upper, blue) or $T_{\rm p} = 1900$ K (lower, red).


ol
wd
rw
bdg
ppv
capv
fp
opx
hpcpx
cpx
aki
gt
T_p = 1600 K
T_p = 1900 K
Depth (km)
Pressure (GPa)
Storage capacity (ppm wt)
Water modality in NAMs
a
b
c
d
present-day
early Archean
95th percentile
median
5th percentile
Water storage capacity in Earth's solid mantle (OM)
Mantle potential temperature T_p (K)

large due to the uncertainties in bridgmanite, the negative temperature effect is very robust because the uncertainties at different T_p are highly correlated, and the median bulk water storage capacity of Earth's mantle increases significantly with decreasing mantle potential temperature (secular cooling). For example, a lower storage capacity in bridgmanite would decrease the calculated bulk water storage capacity at present, but it would similarly decrease the calculated bulk water storage capacity in the early Archean (Figure S3). During the early Archean, the higher temperatures would have caused significantly lower water storage capacities in most rock-forming NAMs, narrowed the width of the transition zone, and possibly caused the breakdown of wadsleyite into garnet and ferropericlase, which store much less water (Figs. 2.2 and 2.3). These temperature effects result in a significantly lower water storage capacity for the mantle of the young planet: the storage capacity in an early, hotter mantle (T_p = 1800–1900 K, ΔT_p = +200–300 K) is $1.19^{+0.90}_{-0.16}$–$1.56^{+1.16}_{-0.22}$ OM smaller than at present.

A critical source of uncertainty is the pressure-temperature effect on the water storage capacities in lower mantle NAMs. The pressure-temperature effect on these water storage capacities, as well as their water partition coefficients above mid-mantle pressures (>30 GPa), have not been constrained experimentally. The temperature effect would likely give rise to a smaller bulk water storage capacity in the lower mantle when T_p is higher, as seen in other NAMs. Conversely, we may conjecture that the storage capacities will increase at higher pressures, as this is the case for olivine and pyroxene for which have been studied over a significant range of pressures (Figs. 2.3 and 2.4). Such a pressure dependence for wadsleyite and ringwoodite is not evident in their regressions, perhaps because those phases are not stable over a sufficient range of pressures. If the pressure effect surpasses the temperature effect at greater depth, our upper bound on

the bulk water storage capacity may need to be revised upwards.

Another important source of uncertainty is that water storage capacities are not strictly additive for complex rocks. The pyrolite mantle is likely to have a lower storage capacity than the sum of its individual minerals, as demonstrated experimentally (Ardia et al. 2012; Ferot and Bolfan-Casanova 2012; Tenner et al. 2012). Our current model could be improved if experiments that were conducted with complex mineral assemblages were used. Unfortunately, there is not enough literature data on the P–T effects on the actual storage capacity of the full complex pyrolite assemblage. At some conditions, such as in the lower mantle, experiments with complex assemblages are simply not available, in which case the storage capacities in individual minerals have to be used. Thus, these calculated water storage capacities may only represent an upper bound on the storage capacity profile of the upper mantle, transition zone, and possibly lower mantle as well.

Furthermore, a variety of hydrous phases, such as phase D (Frost and Fei 1998; Shieh et al. 1998), phase H (Nishi et al. 2014; Ohtani et al. 2014), δ-phase (Yuan et al. 2019), and possibly hydrous silica (Lin et al. 2022) as well as free aqueous fluid (Tschauner et al. 2018), carried by or derived from cold subducted slabs, may provide additional water storage in the present-day mantle. However, these phases are stable only at relatively low temperatures, so most of them may only remain thermally stable for less than 300 Ma after subduction (van der Meer et al. 2010) before slab materials become thermally equilibrated with the surrounding mantle. The additional water storage capacity from hydrous phases would also be limited by the total amount of water available in the cold subducting slab. Petrological analyses suggest that the fraction of Earth's deep mantle comprised of recycled crust is $\sim$20% (Sobolev et al. 2007; Xu et al. 2008). If subducted slab materials are cold enough to retain water for a maximum of 300

Ma (van der Meer et al. 2010) and subduction has been operating for ∼4,000 Ma, then ∼300 Ma/4,000 Ma = 7.5% of this subducted material remains cold enough to stabilize hydrous materials (7.5% × 20% = 1.5% of the total deep mantle). If slabs contain an average of 2 wt.% water, with an upper bound of 1/3 of this water retained beyond the volcanic arc to be subducted (van Keken et al. 2011), this would amount to 0.3 OM stored in the present-day mantle in hydrous phases of subducted slabs. This upper bound is significantly lower than the storage capacity of NAMs in the present-day mantle and would have been considerably lower in the hotter early mantle, so their presence in the mantle today only increases the difference between the storage capacities of the early and modern Earth. Although the residence time for water in hydrous minerals (<300 Ma; van der Meer et al. 2010) is short, and the storage capacity in hydrous minerals is relatively small compared with that in NAMs, these slab-derived hydrous minerals and their breakdown reactions are key intermediates of the deep water cycle toward long-term stable water storage in the NAMs of Earth's mantle.

In this study, we focus on the early period of the Archean Eon (4–3.2 Ga) that includes the Eoarchean (4–3.6 Ga) and the Paleoarchean (3.6–3.2 Ga). Rock records from this period are scanty or lacking; Earth's mantle had cooled enough to remain mostly solid, and water delivery from impacts had waned, making the total water budget in the Earth more stable. The ambient mantle T_{p} for the early Earth is thought to have been higher than in the present-day mantle (T_{p} = 1600 K), though estimates of the mantle T_{p} in the early Archean (4–3.2 Ga) vary from $\Delta T_{\mathrm{p}} = +200$ to $\Delta T_{\mathrm{p}} = +300$ K, depending on conflicting interpretations of petrological constraints (Aulbach and Arndt 2019; Condie et al. 2016; Ganne and Feng 2017; Herzberg 2019; Herzberg et al. 2010). The classical heat flow scaling predicts that mantle temperature decreases monotonically but would

lead to a thermal runaway if the present-day Urey ratio is adopted; alternatively, a different thermal history model presented by Korenaga and others (e.g., Herzberg et al. 2010; Korenaga 2006) suggests that the Earth's thermal evolution switched from initially warming up to cooling down around 3 Ga. Other resolutions to the thermal runaway include different modes of tectonics or a weaker temperature effect on viscosity. All of the studies discussed above maintain, however, that the mantle potential temperature in the early Archean (4–3.2 Ga) was 1800–2000 K ($\Delta T_{\rm p}$ = +200–300 K).

Table 2.1:: Bulk Water Storage Capacity in Earth's Solid Mantle (OM)

$T_{\rm p}$ (K)	5-th %tile	25-th %tile	50-th %tile	75-th %tile	95-th %tile
1550	2.37	2.62	2.86	3.3	5.36
1600	1.86	2.07	2.29	2.65	4.41
1650	1.48	1.66	1.85	2.16	3.65
1700	1.19	1.35	1.52	1.79	3.05
1750	1.03	1.18	1.34	1.58	2.73
1800	0.83	0.96	1.1	1.32	2.32
1850	0.66	0.78	0.9	1.09	1.98
1900	0.52	0.62	0.72	0.9	1.69
1950	0.41	0.5	0.59	0.74	1.47

2.3.4 Minimum Volume of Earth's Early Archean Oceans

The present-day mantle water content is not necessarily equal to its storage capacity. The total amount of water in the oceans plus the mantle may have remained approximately

constant since the early or mid-Archean; exchange between the ocean and mantle reservoirs redistributed water over geological time (van Keken et al. 2011). If the mantle today holds more water than its water storage capacity during the early Archean (e.g. $0.72^{+0.97}_{-0.2}$ OM at $T_{\rm p}$ = 1900 K, IQR = 0.62–0.90 OM), more voluminous surface oceans must have existed in the past. If 1 or 2 OM water are stored in the mantle today, the early Earth with a water-saturated mantle at $T_{\rm p}$ = 1900 K should have had surface oceans with a minimum volume of $1.27^{+0.20}_{-0.96}$ OM (IQR = 1.10–1.38 OM) or $2.27^{+0.20}_{-0.96}$ OM (IQR = 2.10–2.38 OM), respectively (Fig. 2.4). The exact prediction depends on the amount of water in the mantle today and the early Archean mantle $T_{\rm p}$.

Alternatively, with 0.5 OM stored in the mantle today, the minimum volume of the early Archean oceans is $0.77^{+0.20}_{-0.77}$ OM (IQR = 0.60–0.88 OM), smaller than the surface oceans today. In this particular scenario, the volume of the early oceans becomes less constrained without a detailed knowledge of the water flux. If a more voluminous Archean ocean can be excluded through an improved understanding of the geologic record in the future, this would indicate that the bulk water content of the present-day mantle is lower than its early water storage capacity $0.72^{+0.97}_{-0.20}$ OM at $T_{\rm p}$ = 1900 K.

To place constraints on the volume of the early oceans, the bulk water content in the present-day Earth's mantle is a key piece of information. One standard method to estimate the mantle H2O content is to use the roughly constant H_2O/Ce ratio in oceanic basalts and the Ce concentration in the bulk silicate Earth (BSE). Estimates of the actual mantle water content today based on H_2O/Ce ratios in oceanic basalts typically span 0.5–2 OM (Dauphas and Morbidelli 2014; Hirschmann 2018). The latest estimate with a rigorous error analysis by Hirschmann (2018) implies that the present-day water content is between 0.55 and 0.95 OM, which is at the lower end of this range. However,

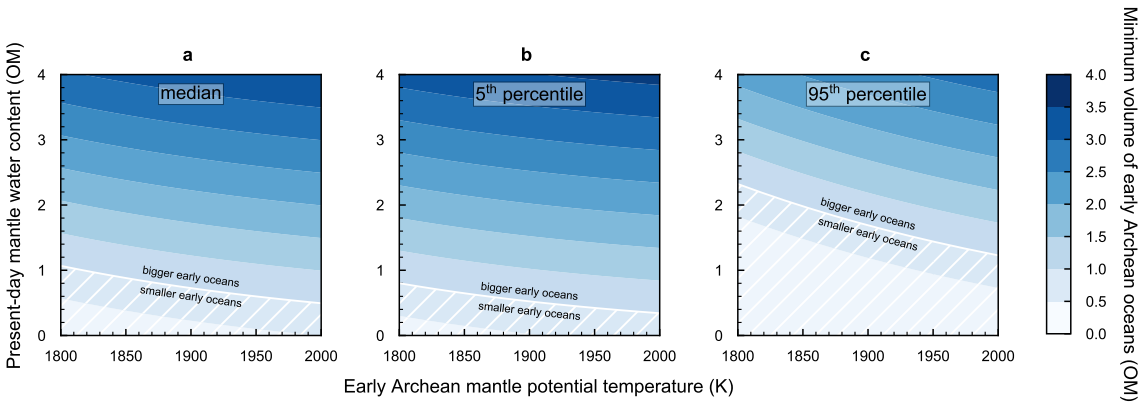


Figure 2.5: **Minimum volume of early Archean oceans as a function of T_{p} and present-day mantle water content (a, median; b, 5-th percentile; c, 95-th percentile).** With a water-saturated mantle at $T_{\mathrm{p}} = 1900$ K and a present-day mantle water content of 1–2 OM, the early Archean Earth should have had surface oceans of $1.27^{+0.21}_{-0.96}$ OM (IQR = 1.10–1.38 OM) to $2.27^{+0.21}_{-0.96}$ OM (IQR = 2.10–2.38 OM). Alternatively, with a present-day mantle water content of 0.5 OM, the minimum volume of the early Archean oceans is $0.77^{+0.21}_{-0.77}$ OM (IQR = 0.60–0.88 OM), smaller than the surface oceans today. The white solid lines correspond to the volume of present-day oceans (1 OM), delineating the boundary between necessarily bigger early oceans and possibly smaller early oceans.

the assumption underlying this H_2O/Ce method, that all geochemical reservoirs with different H_2O/Ce have been sampled by the full spectrum of oceanic basalts that have been analyzed, may not hold if there exist large regions of the mantle with H_2O/Ce ratios higher than the bounds constrained from a typical mid-ocean ridge basalt or ocean island basalt source. Recent studies have found some modern localities with elevated H_2O/Ce ratios, such as the islands of Bermuda (Mazza et al. 2019), and suggest that some deeper water-enriched mantle reservoirs with distinct H_2O/Ce may not be represented in the suite of oceanic basalts that have been analyzed previously. In particular, Bermuda may sample the water-enriched transition zone underneath it, in which wadsleyite and ringwoodite can theoretically store up to a few weight percent of water in their structures. Geophysical and geochemical constraints also suggest that the transition zone is at least locally water-enriched, based on the water concentration measured in a diamond-hosted hydrous ringwoodite inclusion (Pearson et al. 2014), as well as geophysical inferences from electrical conductivity (Kelbert et al. 2009), viscosity (Fei et al. 2017), and possibly shear wave velocities (Schulze et al. 2018; Wang et al. 2019). If modern localities like Bermuda with elevated H_2O/Ce ratios represent a significant fraction of the mantle, such as the transition zone, the current best estimate based on H2O/Ce (0.55–0.95 OM) may be an underestimate. However, it is perhaps unlikely that the hundreds of oceanic basalt localities that have been studied in the literature (compared to only a few with elevated H_2O/Ce ratios) somehow fail to sample the majority of the mantle. Therefore, the upper bound on the present-day mantle water content likely does not exceed 2 OM; at the same time, a present-day water content of <0.5 OM would be contradictory to observations of deep water-enriched reservoirs (e.g., Mazza et al. 2019) and the predicted global flux of H2O to the deep mantle over geological time (e.g., Korenaga et al. 2017;

van Keken et al. 2011).

Some estimates of the bulk water content in the present-day Earth's mantle span 10–50 OM from cosmochemical arguments (e.g., Abe et al. 2000; Dreibus and Wänke 1989; Righter and Drake 1999). The cosmochemical constraints are often based on the expected water contents of the primitive planetesimals that formed the Earth. The efficiency of water delivery and retention during accretion, however, remains highly controversial. Based on this temperature-dependent mantle water storage capacity model, the possible range for present-day mantle water storage capacity (with T_{p} = 1550–1650 K) is 1.85–2.86 OM (medians), and at most 5.36 OM (the 95th percentile at 1550 K), with the possible addition of up to 0.3 OM stored in hydrous phases. Therefore, the Earth's solid mantle is physically unable to accommodate more than 5–6 OM today. If the total amount of water that was delivered to the Earth was tens of OMs, the excess water may have been either devolatilized and lost upon impact, lost to space, or partitioned into the core during or shortly after the end of accretion (Wu et al. 2018).

Here, we conservatively consider only the minimum surface ocean volume under the assumptions that the early mantle was water-saturated and the total water budget of the mantle plus ocean was constant through time. This results in a lower bound on early ocean volume because these assumptions are unlikely to be strictly correct. Though it has been observed that some primordial water was retained in the Earth's mantle (Hallis et al. 2015), processes associated with magma ocean solidification and overturn would have degassed the primordial mantle significantly and made its actual water content much lower than its storage capacity (e.g., Elkins-Tanton 2008; Tikoo and Elkins-Tanton 2017). Recent models based on noble gas constraints suggest that the early Earth may have been dominated by net degassing from the interior, with net regassing (re-hydration) not

becoming prevalent until sometime later (Marty et al. 2019; Parai and Mukhopadhyay 2018), though the exact timing of the switch is model-dependent, possibly sensitive to continental growth (Guo and Korenaga 2020). In addition, we assumed that the total water budget of the Earth system became stable by the early or mid-Archean (Morbidelli et al. 2000; Zahnle et al. 2019) and remained approximately constant to the present, with no significant H2O loss to space. The validity of this assumption strongly depends on atmospheric composition (Wordsworth and Pierrehumbert 2013), and the hydrogen escape rate might have been significant throughout the Archean (Zahnle et al. 2019) if the early Archean atmosphere was N_2 poor and/or H_2 rich. If the early mantle were undersaturated with water and/or if a considerable amount of water was lost to space since that time, the early surface oceans would have been even larger than these predicted volumes.

Alternatives to water having resided on the surface include possible reservoirs of water in the deep Earth, such as the core or partial melts in the mantle. However, these possibilities are less likely. The water content of the core remains controversial (e.g., Clesi et al. 2018; Hirose et al. 2019; Iizuka-Oku et al. 2017; Li et al. 2020; Okuchi 1997; Terasaki et al. 2012; Yuan and Steinle-Neumann 2020), but it is most likely not decreasing over time, making it an unlikely source of an increase in mantle water. Possible hydrous partial melts in the early mantle would have likely been too buoyant to remain gravitationally stable at depth (Mookherjee et al. 2008) and would have erupted to release their water onto the surface. To maintain neutral buoyancy of a hydrous melt layer at the top of the transition zone, even along the present-day geotherm, its water content would be limited to ∼8 wt.% (Sakamaki et al. 2006). With a 10 km thick melt layer above the transition zone (Bercovici and Karato 2003), the additional water

storage capacity contributed from this stable hydrous melt layer would amount to ∼1 OM. Seismic signatures of another possible melt layer at the base of the transition zone have only been reported in a few localities around the globe (Schmandt et al. 2014), so that the possible contribution from this layer should be several orders of magnitude smaller. In addition, it has been suggested that a neutrally buoyant hydrous layer could be present at the core-mantle boundary (Sakamaki et al. 2006), but there is no direct seismic evidence of this on a global scale. Even if it exists, most of its water should have had been lost to the core, which has a greater affinity for hydrogen (O'Rourke and Shim 2019).

2.3.5 Implications for the Flooded Fraction of Early Continents

Besides the volume of early oceans, the nature and tempo of continental growth play a critical role in the modeling of the early Archean surface environment, which involves a number of parameters without direct observational constraints, including the nature of early continental and oceanic plates as well as surface topography (Section 2.2.4). In particular, the total amount of emergent continents during the early Archean could have been anywhere between ∼10% and 100% (e.g., Korenaga et al. 2017). The parameter space of the sea level model has been explored in the earlier studies (Flament et al. 2008; Korenaga et al. 2017), without consideration of the finite mantle water storage capacity. However, it remains difficult to assess the degree to which different sets of parameters can satisfy the observational constraints on the early Archean Earth. Therefore, unlike for the volume of the early oceans, we did not perform a full uncertainty analysis on the combined effects of these parameters (e.g., Seales and Lenardic 2020). In this study,

Table 2.2:: Minimum flooded fraction of early Archean continents at $T_{\rm p}$ = 1900 K‡

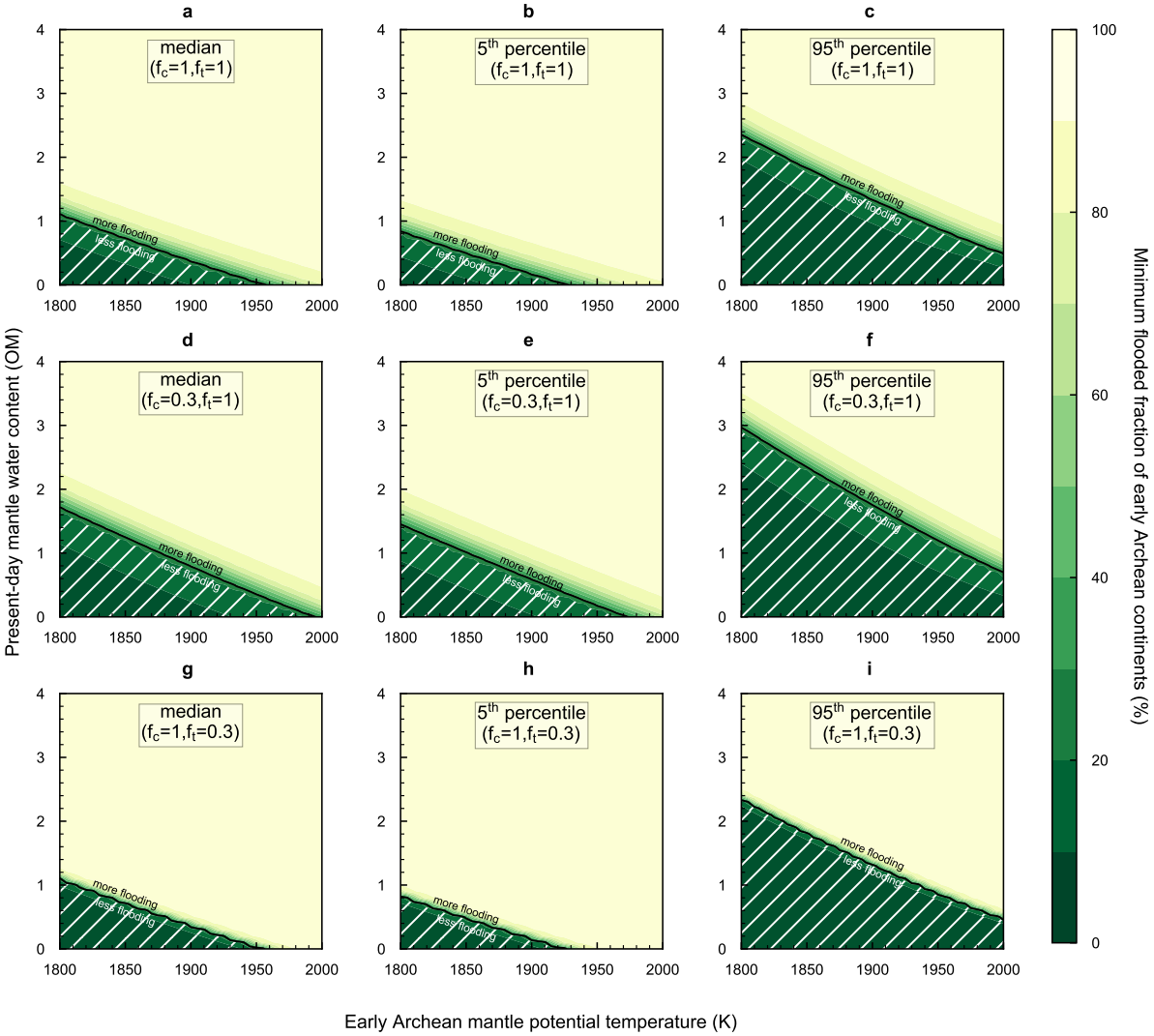
Present-day mantle water content (OM)	$f_{\rm c}$*	$f_{\rm t}$†	**5-th %tile**	**25-th %tile**	**50-th %tile (median)**	**75-th %tile**	**95-th %tile**
0.5	1	1	84	74	54	*19*	*0*
	0.3	1	*19*	*17*	*15*	*12*	*0*
	1	0.3	96	94	88	*16*	*0*
1	1	1	95	94	92	89	*11*
	0.3	1	86	79	64	33	*6*
	1	0.3	100	100	100	98	*0*
2	1	1	99	99	99	98	93
	0.3	1	98	97	97	96	70
	1	0.3	100	100	100	100	100

* $f_{\rm c}$ = 1 represents 100% of the present-day size of the continents.

† $f_{\rm t}$ = 1 represents 100% of the present-day height of the continents.

‡ Results with possibly less flooded early Archean continents relative to present-day (∼27.5%) are italicized.

Figure 2.6 *(following page)*: **Minimum flooded fraction of early Archean continents as a function of T_p and present-day mantle water content from isostatic modeling.** Three explorative cases with an early Archean continental configuration of $f_\mathrm{c} = 1$ and $f_\mathrm{t} = 1$, $f_\mathrm{c} = 0.3$ and $f_\mathrm{t} = 1$, and $f_\mathrm{c} = 1$ and $f_\mathrm{t} = 0.3$ are plotted in (a–c), (d–f), and (g–i), respectively. With a greater volume of surface oceans at $T_\mathrm{p} \geq 1900$ K for the early Archean mantle and >0.3–0.8 OM (medians) water stored in the mantle today, the early continents may have been excessively flooded. The exact fraction of submerged continents is dependent on model parameters. The black solid lines correspond to the flooded fraction of present-day continents (∼27.5%), delineating the boundary between necessarily more flooding than at present and possibly less flooding.


a
median
(fc=1,ft=1)
b
5th percentile
(fc=1,ft=1)
c
95th percentile
(fc=1,ft=1)
d
median
(fc=0.3,ft=1)
e
5th percentile
(fc=0.3,ft=1)
f
95th percentile
(fc=0.3,ft=1)
g
median
(fc=1,ft=0.3)
h
5th percentile
(fc=1,ft=0.3)
i
95th percentile
(fc=1,ft=0.3)
more flooding
less flooding
Present-day mantle water content (OM)
Early Archean mantle potential temperature (K)
Minimum flooded fraction of early Archean continents (%)

the primary goal is to explore how our estimated volumes of the early oceans may have influenced early Archean sea level. Therefore, we present three representative cases with a continental configuration of (1) 100% of its present-day size (f_c) and height (f_t), f_c = 1 and f_t = 1; (2) f_c = 0.3 and f_t = 1; and (3) f_c = 1 and f_t = 0.3 (Fig. 2.6; Tables 2.2 and 2.3). For example, given the geochemical estimates of 1 OM stored in the mantle at present and an early Archean T_p = 1900 K, with (1) $f_c = f_t = 1$, the early continents were likely at least 92^{+3}_{-81}% flooded (IQR = 89%–94%); with (2) f_c = 0.3 and f_t = 1, at least 64^{+22}_{-58}% flooded (IQR = 33%–79%); and with (3) f_c = 1 and f_t = 0.3, 100^{+0}_{-100}% flooded (IQR = 98%–100%). More specifically, the boundaries between less flooding and more flooding relative to present-day sea level are shown as solid black lines in Figures 2.6a—2.6i. For the early Archean Earth at T_p = 1900 K with $f_c = f_t = 1$, the early continents would have been more flooded than today if the present-day mantle water content is $> 0.4^{+0.5}_{-0.2} OM$ (IQR = 0.3–0.5 OM); with f_c = 0.3, f_t = 1, $> 0.8^{+0.9}_{-0.2}$OM (IQR = 0.7–1.0 OM); and with f_c = 1, f_t = 0.3, $> 0.4^{+1.0}_{-0.2}$ OM (IQR = 0.2–0.5 OM).

In general, increasing the volume of early continental crust or decreasing its topography (height) increases the flooded fraction for a given T_p. If the early oceans were more than twice as voluminous as in the present day with an early Archean T_p $\geq$ 1900 K, the continents were possibly covered entirely by water, with only a small number of subaerial landmasses protruding above sea level due to hot spot volcanism and/or oceanic plateaus. In contrast, if we assume a present-day mantle water content of 0.5–1 OM or less, the minimum volume of the early oceans may be smaller than that of the modern ocean (Fig. 2.6). In these scenarios, the majority of the early continents would have been above sea level. It has been argued recently (Korenaga et al., 2017) that the greater buoyancy of continental lithosphere relative to oceanic lithosphere was

enhanced in the early Archean (e.g., $\Delta\rho_{\rm cl}^{\rm A} = -5$ kg/m^3; see Section 2.2.4), which suggests that having an early Archean sea level similar to present-day requires a larger volume of surface oceans, even if early continents are 100% of their present-day size.

This model's major caveat is that plate tectonics, with oceanic and continental plates of different densities, is assumed to have been operating during the early Archean, which may or may not have been the case (e.g., Brown et al. 2020; Cawood et al. 2018; Korenaga 2013). Alternatively, the early crust could have been a more uniform lithosphere with a single density (e.g., Moore and Webb 2013), which would have inhibited the positive topography in isostatic equilibrium, hence requiring a smaller ocean volume to achieve the same flooded fraction of the early Earth's surface.

Table 2.3:: Maximum Present-Day Mantle Water Content Permitted for Constant Freeboard at $T_{\rm p} = 1900$ K (OM)‡

$f_{\rm c}$*	$f_{\rm t}$†	**5-th %tile**	**25-th %tile**	**50-th %tile (median)**	**75-th %tile**	**95-th %tile**
1	1	0.2	0.3	0.4	0.5	0.9
0.3	1	0.6	0.7	0.8	1	1.7
1	0.3	0.1	0.2	0.3	0.5	1.3

* $f_{\rm c} = 1$ represents 100% of the present-day size of the continents.

† $f_{\rm t} = 1$ represents 100% of the present-day height of the continents.

‡ Constant continental freeboard indicates that the submerged fraction of the continents was ∼27.5%.

Most of the model results suggest a largely flooded early Archean Earth (Table 2.2). Though extremely sparse, the geologic records from the early Archean (before 3.2 Ga) are consistent with a global surface ocean with little or no land (a "water world"). A number of recent isotope studies on Earth's early surface environment (hydrogen isotopes: Pope et al., 2012; Kurokawa et al., 2018; oxygen isotopes: Bindeman et al., 2018; Johnson & Wing, 2020) suggest more voluminous early oceans with largely flooded continents. The stable isotope signatures are consistent with observations that almost all large igneous province volcanism was subaqueous before the Archean (e.g., Arndt and Nisbet 2012; Kump and Barley 2007). Additionally, Earth's earliest thick and laterally extensive platform sedimentary successions were deposited only in the late Archean (Windley 1996), which could not have been created without continents becoming exposed at that time.

A largely water-covered early Earth would have had a lower albedo than at present, which may have moderated surface temperatures during this period of reduced solar influx (Rosing et al. 2010) when early life may have been emerging. It might also have induced the deep hydration of primitive oceanic lithosphere via thermal cracking and subsequent serpentinization, helping to facilitate the onset of plate tectonics (Korenaga 2007). Additionally, increasing the ocean volume while decreasing the subaerial land area may have significantly reduced tidal dissipation in the early oceans, possibly responsible for the necessarily low lunar recession rate in the early history of the Earth-Moon system (e.g., Hansen 1982; Motoyama et al. 2020).

However, interpretations for these early geologic records may not be unique. If excessively flooded early continents and deeper oceans can be excluded through an improved understanding of the geologic record in the future, then the present-day mantle

water content would have to be <0.3–0.8 OM, and most likely much less than this range since the early mantle was likely water-undersaturated.

2.4 Summary and Conclusions

We fitted a thermodynamic model to the experimental data on water storage capacities in olivine, wadsleyite, and ringwoodite and quantified the pressure-temperature effects. We also calculated the possible water storage capacity in bridgmanite at different T_{p} based on the partition coefficient of water between ringwoodite and bridgmanite. Combined with the mantle phase assemblages and their mineral proportions calculated from HeFESTo, we established a temperature-dependent water storage capacity model for the Earth's solid mantle.

The bulk water storage capacity of the Earth's solid mantle was significantly affected by secular cooling due to its constituent minerals' temperature-dependent storage capacities. The mantle's water storage capacity today is 1.86–4.41 OM, with a median of 2.29 OM (T_{p} = 1600 K). This value is consistent with the geochemical estimates of the present-day water content (0.5–2 OM). For the early Earth's solid mantle (T_{p} = 1900 K), the water storage capacity was only 0.52–1.69 OM, with a median of 0.72 OM. The uncertainties in our bulk water storage capacity estimates of Earth's mantle are dominated by uncertainties in the water storage capacities of lower mantle NAMs, especially bridgmanite, which is an important target for future experimental studies.

Nevertheless, due to correlations in the uncertainties at different T_{p}, we robustly find that the early (hotter) mantle's water storage capacity would have been significantly

lower than at present, by $1.19^{+0.90}_{-0.16}$–$1.56^{+1.16}_{-0.22}$ OM. If the actual water content of today's mantle is greater than its storage capacity was in the early Archean, then the early Archean oceans must have been larger than at present, possibly causing excessive flooding of the surface. Alternatively, if in the future an improved understanding of the early Archean geological record rules out the possibility of larger oceans, then the present-day mantle water content is constrained to be <0.3–0.8 OM, and likely much less than this range.

Acknowledgments

J. Dong was supported by a James Mills Peirce Fellowship from the Graduate School of Arts and Sciences at Harvard University. R. A. Fischer was supported by the Henry Luce Foundation. L. P. Stixrude was supported by the European Research Council under Advanced Grant 291432 MoltenEarth (FP7) and by the National Science Foundation (EAR-1853388). C. R. Lithgow-Bertelloni was supported by research funding from the Louis B. and Martha B. Slichter Endowed Chair in the Geosciences at University of California Los Angeles and by the National Science Foundation (EAR-1900633). We thank Jun Korenaga, Adrian Lenardic, and two anonymous reviewers for their helpful feedback, and the editor for handling our manuscript. In addition, we thank several anonymous reviewers for their detailed comments on previous versions of the manuscript, which improved it considerably. We also thank Matthew Brennan, John Brodholt, Marc Hirschmann, Andrew Knoll, Jerry Mitrovica, Francis Nimmo, and Feng Zhu for helpful discussions.

Chapter 3

Water Storage Capacity of the Martian Mantle Through Time

Water, water, every where,

Nor any drop to drink.

—Samuel Taylor Coleridge, *The Rime of the Ancient Mariner*

Abstract*

Water has been stored in the Martian mantle since its formation, primarily in nominally anhydrous minerals. The short-lived early hydrosphere and intermittently flowing water on the Martian surface may have been supplied and replenished by magmatic degassing

*This chapter includes modified content from my previously published article, "Water Storage Capacity of the Martian Mantle Through Time," which appeared in *Icarus* in 2022.

of water from the mantle. Estimating the water storage capacity of the solid Martian mantle places important constraints on its water inventory and helps elucidate the sources, sinks, and temporal variations of water on Mars. In this study, we applied a bootstrap aggregation method to investigate the effects of iron on water storage capacities in olivine, wadsleyite, and ringwoodite, based on high-pressure experimental data compiled from the literature, and we provide a quantitative estimate of the upper bound of the bulk water storage capacity in the FeO-rich solid Martian mantle. Along a series of areotherms at different mantle potential temperatures ($T_{\rm p}$), we estimated a water storage capacity equal to $9.0^{+2.8}_{-2.2}$ km Global Equivalent Layer (GEL) for the present-day Martian mantle at $T_{\rm p}$ = 1600 K and $4.9^{+1.7}_{-1.5}$ km GEL for the initial Martian mantle at $T_{\rm p}$ = 1900 K. The water storage capacity of the Martian mantle increases with secular cooling through time, but due to the lack of an efficient water recycling mechanism on Mars, its actual mantle water content may be significantly lower than its water storage capacity today.

3.1 Introduction

Unlike Earth, which has vast oceans on its surface, Mars is primarily cold and dry today. The majority of its surface water at present likely lies in the polar-layered deposits (PLD) and in shallow ground ice. Melting the PLD and ground ice reservoirs would produce an H2O layer with an estimated thickness of 20–40 m if it were spread evenly over the Martian surface (Carr and Head, 2015), referred to as a Global Equivalent Layer (GEL). Early Mars may have had a much larger surface water reservoir, as suggested by its geomorphology (e.g., Carr 1996) and abundance of ancient clay minerals (e.g.

Ehlmann and Edwards 2014). The high D/H ratio of the present Martian atmosphere (at least 5–7 times higher than the terrestrial value, e.g., Villanueva et al. 2015) can also be interpreted as the result of loss of early surface water reservoirs (Chassefiere et al. 2013; Kurokawa et al. 2014; Scheller et al. 2021). The current size of the Martian surface water reservoir is the result of a complex history of crustal hydration, atmospheric escape, and mantle outgassing since its formation (Jakosky 2021).

Water, which has been stored in the Martian mantle rocks since its formation, can lower their viscosity and affect the thermal evolution of the Martian interior, which further alters melting in the mantle and hence controls crustal formation as well as water outgassing onto the Martian surface (e.g., Hauck and Phillips 2002; Fraeman and Korenaga 2010; Grott et al. 2011; Morschhauser et al. 2011; Sandu and Kiefer 2012; Ruedas et al. 2013a,b; Breuer et al. 2016; Ogawa 2021). For a better understanding of how the water budget of the Martian surface and interior reservoirs have evolved through geologic time, quantitative constraints on water in the Martian mantle are indispensable.

Current geochemical estimates of the Martian mantle water content are often based on our existing Martian meteorite archives, and their estimated water contents fall in the range 14–250 ppm wt H_2O (summarized in Filiberto et al. 2019, and references therein). However, these meteorite-based estimates have two major drawbacks (Filiberto et al. 2019): (1) the water content derived from one or a few meteorite samples may only represent their source regions instead of the average mantle; and (2) several secondary processes, including shock, magmatic degassing upon cooling, and terrestrial contamination may have altered the original water contents of these meteorites. Alternatively, as observational constraints on Martian mantle structure continue to improve (e.g., Mocquet and Menvielle 2000; Civet and Tarits 2014; Johnson

et al. 2020; Ruedas and Breuer 2021; Stahler et al. 2021), the mantle water content may be constrained by geophysical observables such as seismic velocities and attenuation and electrical conductivity in the future (Verhoeven and Vacher 2016; Ruedas and Breuer 2021).

In this study, we present a mineral physics approach to put constraints on the amount of water in the Martian mantle. On a microscopic level, water is stored in the form of structurally-bound hydroxyl groups (OH) in the nominally anhydrous minerals (NAMs), which comprise the bulk of the Martian mantle. Instead of being infinite water reservoirs, individual mantle NAMs have finite OH solubilities, also known as their water storage capacities. Numerous mineral physics studies (cf. Dong et al. 2021, and references therein) have investigated the water storage capacities in major NAMs common to the mantles of terrestrial planets. The experimental data on the major NAMs' water storage capacities available in the literature were used in this study to model the bulk water storage capacity of the Martian mantle based on its stable mineral assemblages (Tables S11–S13). An analogous calculation for the Earth indicates that the terrestrial mantle today has an estimated bulk water storage capacity of 2.3 times the modern surface ocean mass (Dong et al. 2021). The Martian mantle is expected to be primarily composed of olivine (ol) and its high-pressure polymorphs, wadsleyite (wd) and ringwoodite (rw), as well as pyroxene (px) and garnet (gt), similar to Earth's mantle at the same pressures (Bertka and Fei 1997). However, the bulk water storage capacity of the Martian mantle could be quite different from that of the Earth, due to the smaller planetary size of Mars, the different Martian mantle potential temperature, and the potentially more iron-rich composition of the Martian mantle. Here we first quantified the effects of iron on the water storage capacities of major mantle NAMs, and

then built a bulk water storage capacity model for the solid Martian mantle and tracked its evolution along mantle adiabats as a function of T_{p}.

3.2 Methods

3.2.1 Equilibrium Phase Assemblages of the Martian Mantle

We computed a series of adiabatic temperature gradients (areotherms) of a simplified Martian mantle composition as a function of pressure for T_{p} from 1500 to 1900 K, using the thermodynamic code HeFESTo and the self-consistent parameter set contained therein Stixrude and Lithgow-Bertelloni (2005, 2011) (Fig. B.1). The equilibrium mineral assemblages along these adiabats were calculated to constrain the mineralogical evolution of the Martian mantle with secular cooling over geologic time (Figs. B.2–B.6). Conversion from pressure to depth was performed using a thin shell calculation (Supplementary Text S1). The simplified bulk silicate Mars (BSM) composition in our model was a six-component system of Na_2O–CaO–FeO–MgO–Al_2O_3–SiO_2, with abundances primarily based on Taylor (2013) ("T13", Table B.1). In addition, a pseudosection for the T13 composition was calculated between 3 and 22 GPa and between 1500 K and 2500 K to explore how Martian mantle equilibrium mineral assemblages vary with pressure (P) and temperature (T). We also included another four BSM compositions, from Liebske and Khan (2019) ("LK19", Tables B.2–B.3), Yoshizaki and McDonough (2020) ("YM20", Table B.4) and Khan et al. (2022) ("K22", Table B.5) to test the sensitivity of our calculations to mantle composition (Fig. S2–S6, Section 3.3.2). At least 25 mantle phases (e.g., *ol*, *wd*, *rw*) with 47 endmember species (e.g.,

fo–fa) are likely to be stable over the P–T conditions of terrestrial planetary mantles and have been considered here (cf. Table A1 in Stixrude and Lithgow-Bertelloni 2011). The phase stability predictions of HeFESTo are generally consistent with the experimental results based on a BSM composition similar to T13 (Bertka and Fei 1997; Khan et al. 2022). For the full description of the thermodynamic method of HeFESTo, see Stixrude and Lithgow-Bertelloni (2005, 2011).

3.2.2 Bulk H_2O Storage Capacity of Martian Mantle Rocks

In calculating the bulk water storage capacity of the solid Martian mantle, the water storage capacities of individual NAMs at each pressure and temperature were estimated and summed. The water storage capacities of the major NAMs in the Martian mantle (*ol*, *wd*, and *rw*) can be parameterized as:

$$\ln(c_{\mathrm{H_2O}}) = \ln(\frac{1}{2n}) + \mathrm{a} + \frac{\mathrm{n}}{2} \cdot \ln(f_{\mathrm{H_2O}}) + \frac{\mathrm{b} + \mathrm{c} \cdot P + \mathrm{d} \cdot X_{\mathrm{Fe}}}{T} \tag{3.1}$$

with T in kelvin (K), P in gigapascals (GPa), $f_{\mathrm{H_2O}}$ (water fugacity) in GPa, and X_{Fe} (iron content) in mole fraction (see more details in Dong et al., 2021). The constants a, b, and c are related to the changes in entropy, enthalpy, and volume of the hydration reaction, respectively; d expresses the effect of iron (as FeO); and n is the fugacity exponent. We did not include the effects of oxygen fugacity, $f_{\mathrm{O_2}}$), because its influence on the water storage capacities of *ol*, *wd*, and *rw* is likely negligible (*ol*: Withers and Hirschmann (2008); Gaetani et al. (2014); *wd*: Druzhbin et al. (2021); *rw*: Fei and Katsura (2020)). The presence of trace elements may enhance water incorporation in NAMs such as olivine at low pressures (< 3 GPa) and low temperatures (< 900 °C) (Padrón-Navarta and Hermann 2017). However, the effects of trace elements diminish

at the adiabatic Martian mantle conditions we are interested in here, and hence were not included in the calculation. For simplification, we merged two constant terms, $\ln(\frac{1}{2n})$ and a, in Eq. 3.1 of Dong et al. (2021) into the constant a (Eq. 3.1) of this study.

To fit Eq. 3.1 for each NAM, we used a compilation of high-pressure mineral physics data on NAM water storage capacities (in *ol*, *wd*, and *rw*) from Dong et al. (2021), in which all water measurements based on Fourier transform infrared spectroscopy (FTIR) were corrected to the same calibration (*ol*: Withers et al. (2012); *wd*/*rw*: Bolfan-Casanova et al. (2018)). For this study, we made several improvements to the Dong et al. (2021) data compilation: (1) a number of iron-rich samples ($X_{\mathrm{Fe}} = 0.19$–0.44) have been added to investigate how water storage capacities in NAMs may be different from terrestrial values in the FeO-rich mantle of Mars. The newly-added data can be found in Tables S11–13 of this study. (2) We excluded experimental data obtained from complex rock compositions (e.g., a peridotitic or pyrolitic composition) because the water storage capacity model is thermodynamically-derived for individual NAM phases. (3) We excluded experimental data with <1 wt initial water content for olivine and those with <5 wt for wadsleyite and ringwoodite to avoid water-undersaturated experiments. (4) We excluded experimental data for olivine that equilibrated with excess ferropericlase, (Mg,Fe)O, because a) the water storage capacities in these excess (Mg,Fe)O olivine samples are likely different from those equilibrated with excess SiO_2 at low pressures (Fei and Katsura 2020), and hence they contribute additional uncertainty to the analysis; and b) the run products of these excess (Mg,Fe)O experiments do not resemble the mineral assemblages of the upper mantles of either Earth or Mars.

The bulk water storage capacity of Martian mantle rocks, $c_{\mathrm{H_2O}}^{\mathrm{mantle}}$, can be approximated by a weighted average (by their proportions X) of the water storage

capacities of individual stable mantle phases at each P–T, including olivine or its polymorphs (i) and the coexisting mantle NAMs (j):

$$c_{\mathrm{H_2O}}^{\mathrm{mantle}} = (c_{\mathrm{H_2O}}^{\mathrm{NAM}})_i \cdot (X_i + \sum_j X_j \cdot D_{\mathrm{H_2O}}^{\frac{i}{j}}) \tag{3.2}$$

where $D_{\mathrm{H_2O}}^{\frac{i}{j}}$ is the water partition coefficient between i and j, $(c_{\mathrm{H_2O}}^{\mathrm{NAM}})_i$ is the water storage capacity of olivine or its polymorphs, and $(c_{\mathrm{H_2O}}^{\mathrm{NAM}})_j = (c_{\mathrm{H_2O}}^{\mathrm{NAM}})_i \cdot D_{\mathrm{H_2O}}^{\frac{i}{j}}(T, P, X_{\mathrm{Al}})$ is the water storage capacity of coexisting mantle NAMs. We used several literature compilations of uncorrected water storage capacity data (Hauri et al. 2006; Keppler and Bolfan-Casanova 2006) to calculate $D_{\mathrm{H_2O}}^{\frac{i}{j}}$ from the quotient of their uncorrected water storage capacities, $\frac{(c_{\mathrm{H_2O}}^{\mathrm{NAM}})_i}{(c_{\mathrm{H_2O}}^{\mathrm{NAM}})_j}$. Because the water storage capacity data for olivine (i, numerator) and its coexisting mantle NAMs, orthopyroxene, clinopyroxene, and garnet (j, denominator), require similar correction factors, the quotient $D_{\mathrm{H_2O}}^{\frac{i}{j}}$ is virtually unaffected regardless of whether the numerator and denominator are corrected or not, as long as the treatment is consistent. The effects of iron on the water partition coefficients (but not the water storage capacities) are negligible compared with the effects of aluminum (Withers et al. 2011) and hence are not included in the parameterizations. Details of the parameterizations for these partition coefficients as a function of temperature, pressure, and aluminum content, X_{Al}, can be found in Dong et al. (2021). In addition, individual NAM water storage capacities are not strictly additive for complex rocks. Solid mantle rocks may have lower storage capacities than the sums of their individual minerals (e.g., Ardia et al. 2012; Tenner et al. 2012). Thus, the calculated water storage capacities for the solid Martian mantle mineral assemblages, $c_{\mathrm{H_2O}}^{\mathrm{mantle}}$, represent upper bounds.

3.2.3 The Effects of Iron on Solid Mantle H_2O Storage Capacity

In our previous study that focused on Earth's mantle (Dong et al. 2021), we explored the effects of iron on the water storage capacities of *ol*, *wd*, and *rw*, but with an experimental data compilation that only included NAMs with $X_{\mathrm{Fe}} < 0.19$. We found that the compositional dependence d in Eq. 3.1 was statistically insignificant ($p > 0.01$) for all experimental data with $X_{\mathrm{Fe}} < 0.19$. However, the significance threshold for p-values ($p = 0.01$) is established by convention (Wasserstein and Lazar 2016), and this finding for $X_{\mathrm{Fe}} < 0.19$ (Dong et al. 2021) does not necessarily mean an absence of iron effects in these minerals at higher X_{Fe}. A $\frac{\mathrm{d}\cdot X_{\mathrm{Fe}}}{T}$ term with a p-value slightly greater than 0.01 only indicates that the iron effect cannot be readily resolved due to the resolution of the data for $X_{\mathrm{Fe}} < 0.19$.

The Martian mantle is typically estimated to be rich in iron, with a bulk silicate Mg# ($= 100 \times \frac{X_{\mathrm{Mg}}}{X_{\mathrm{Mg}}+X_{\mathrm{Fe}}}$, molar) of ∼75 (e.g., Taylor, 2013) compared to the bulk silicate Earth's Mg# of ∼89 (e.g. Workman and Hart 2005). The range of X_{Fe} (in mole fraction) calculated for major NAMs throughout the Martian mantle (*ol*, *wd*, and *rw*) span approximately 0.2–0.4 for the T13 bulk composition (depending on specific P–T conditions as well as the mineral assemblages along adiabats with $T_{\mathrm{p}} = 1600$–1900 K; Figs. B.2–B.6).

From a thermodynamic point of view, the Gibbs free energy of NAM hydration may be approximated as a linear function of X_{Fe} (Schmalzried 1994):

$$\Delta G^{*}\left(P, T, X_{\mathrm{Fe}}\right) \sim \Delta G^{*}\left(P, T\right) + X_{\mathrm{Fe}} \cdot \Delta G^{*}\left(P, T\right)' + \text{high-order terms} \qquad (3.3)$$

where $X_{\mathrm{Fe}} \cdot \Delta G^{*}\left(P, T\right)'$ represents the deviation of the Gibbs free energy of hydration from that of the Mg endmember due to the presence of iron. The water concentration

c_{H_2O} is expected to change exponentially with X_{Fe} (Zhao et al. 2004):

$$c_{H_2O} \propto e^{\frac{X_{Fe}}{RT} \cdot \Delta G^*(P,T)'} \tag{3.4}$$

Therefore, the effects of iron on the water storage capacities of *ol*, *wd*, and *rw* may become significant at $X_{Fe} = 0.2$–0.4, even though they are currently not resolvable for $X_{Fe} < 0.19$ using a robust nonlinear regression (Dong et al. 2021). In the context of an iron-rich Martian mantle for this study, we included additional experimental data with $X_{Fe} > 0.19$ from the literature (Tables B.11–B.13) to fit the $\frac{d \cdot X_{Fe}}{T}$ term (Equation 1) and to extrapolate the water storage capacities of NAMs to $X_{Fe} = 0.2$–0.4. Previous experiments demonstrate that the water storage capacity of ol increases by a factor of ∼2–3 as its X_{Fe} is increased from 0.2 to 0.4 at 3–6 GPa (Withers et al. 2011), so at least for olivine, iron has noticeable effects on water storage capacity at $X_{Fe} > 0.2$. However, no experimental study has systematically investigated the effects of iron on the water storage capacities of wd and rw with $X_{Fe} > 0.2$. If we directly fit Equation 1 to the compiled experimental dataset with the $\frac{d \cdot X_{Fe}}{T}$ term, the scarcity and imbalance of iron-rich samples, in particular for *wd* and *rw*, may cause an overfitting of d.

To avoid overfitting d, while also incorporating all experimental measurements into our estimate of the Martian bulk mantle water storage capacity and its uncertainty, we applied a statistical method called "bootstrap aggregation" or "bagging" (Fig. 3.1). The "bagging" method averages a large number (N) of the bulk mantle water storage capacity models, M_1, M_2, …, M_n. These models are predicted based on different bootstrapped/resampled datasets and their regressions of Eq. 3.1, with each model having a variance σ^2. This method reduces variance embedded in the fitted X_{Fe} coefficients by generating a model-averaged prediction, $\bar{M}$, with a variance of $\frac{\sigma^2}{N}$ (James

et al., 2013). In other words, we quantified the uncertainty in the $\frac{d \cdot X_{Fe}}{T}$ terms based on experimental data including only limited data at high iron contents ($X_{Fe} > 0.19$), and then we incorporated the uncertainties associated with the extrapolations in X_{Fe} directly as part of the uncertainty in the bulk mantle water storage capacity.

For the "bagging" method, we first resampled the literature data with replacement and created 104 copies of the bootstrapped dataset (Step 1 in Fig. 3.1). We then fit a separate set of water storage capacity models (for each of *ol*, *wd*, and *rw*; Eq. 3.1) to each resampled copy of the dataset (Step 2 in Fig. 3.1), resulting in 10^4 mantle water storage capacity profiles along each adiabat for T_p = 1500–1900 K (Step 3 in Fig. 3.1). All regressions were unweighted due to the lack of inter-laboratory standard practices of error analyses. Finally, we aggregated the 104 water storage capacity profiles as a function of depth for each T_p and obtained the best-fit profiles by model averaging (mean) (Step 4 in Fig. 3.1). We integrated each water storage capacity profile as a function of depth to obtain the bulk mantle water storage capacity for each T_p. To quantify the uncertainty associated with this model, we report the mean bulk mantle water storage capacities as the best-fit values, along with medians as well as 90/10, 95/5 and 99/1 confidence intervals in Table B.6. We use the 95/5 confidence intervals as the error bars throughout the text for consistency. This "bagging" method, unlike the Monte Carlo method used in Dong et al. (2021), considers all of the existing iron-rich NAM samples without presupposing the effects of iron. The trade-off is that the "bagging" method does not allow us to report a single set of regression parameters for each NAM explicitly, because the bulk mantle water storage capacity is based on the average of 10^4 regressions for each NAM (3×10^4 regressions in total). Despite this different approach, the average effects of pressure and temperature found by these regressions are consistent

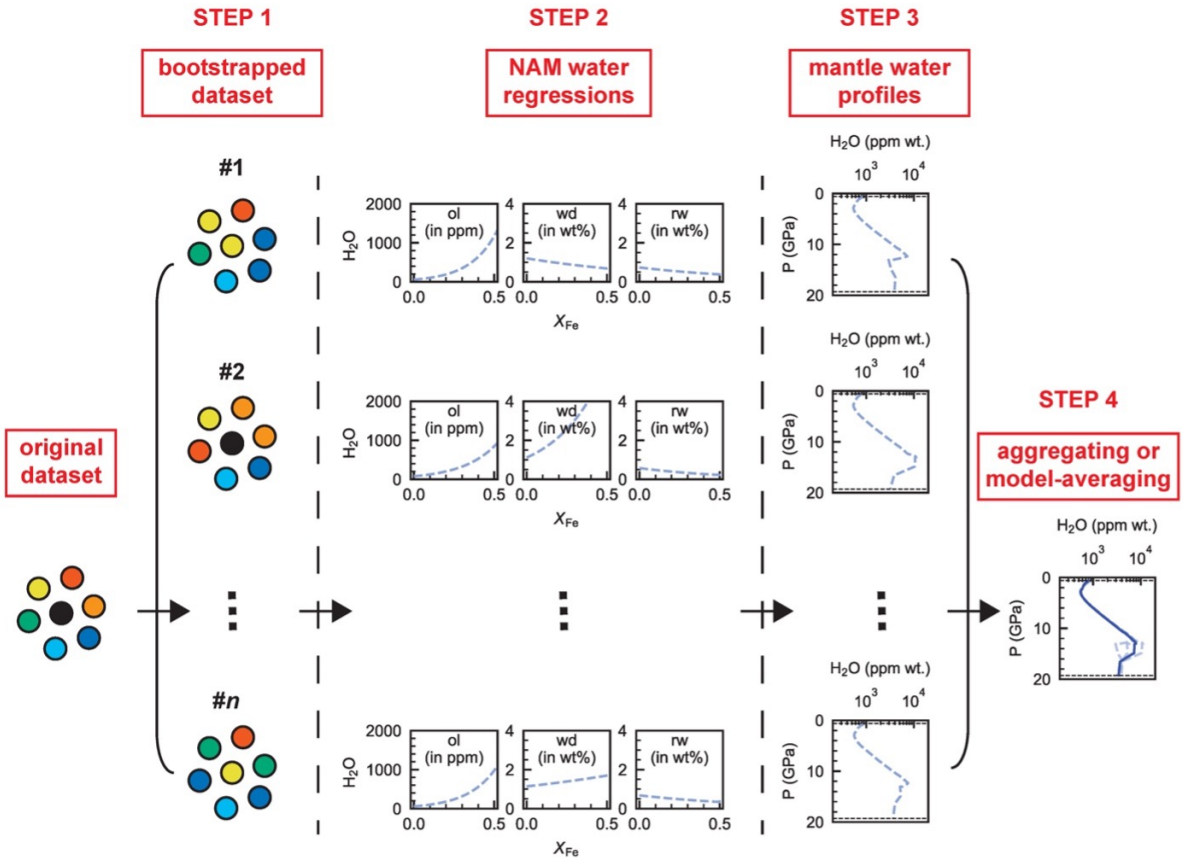


Figure 3.1: **Workflow for the "bagging" method.** Step 1: resampling from the original datasets for *ol*, *wd*, and *rw* (compiled in this study) with replacement. Step 2: fitting the T, P, and X_{Fe} dependence for each mineral for each of n resampled datasets. Step 3: calculating n bulk water storage capacity profiles based on varying T, P, X_{Fe}, and phase proportions along a specific areotherm at each Tp. Step 4: averaging all n profiles to obtain the best-fit bulk water storage capacity profile for T_{p}. NAMs are labeled as: *ol*: olivine, *wd*: wadsleyite, *rw*: ringwoodite.

with those in Dong et al. (2021) (Fig. B.7).

In addition, the uncertainties in the models of the Martian internal structure (e.g., crust thickness, core radius) and mantle chemistry (e.g., bulk silicate Mars composition) are not included in the error analysis. The bulk silicate Mars composition from Taylor (2013) (based on a volatile-depleted CI chondritic composition and element correlations in Martian meteorites) was used as the primary Martian mantle composition in this study. The effects of using other bulk silicate Mars compositions are discussed in Section 3.3.2. The crustal thickness and the core–mantle boundary (CMB) depth were assumed to be 50 km (e.g., Knapmeyer-Endrun et al. 2021) and 1600 km (e.g., Stahler et al. 2021), respectively, based primarily on InSight data as well as recent Martian internal structure models (e.g., Brennan et al. 2020).

3.3 Results and Discussion

3.3.1 Depth-dependent Profiles of the Solid Martian Mantle H_2O Storage Capacity and the Effects of Fe

Using this bootstrapping approach, we found that iron generally increases the water storage capacity of *ol* (Fig. 3.2a). The uncertainty in the regression increases at high pressures and temperatures due to a scarcity of experimental data at higher P–T conditions. For *wd*, we found that the resampling of the experimental data typically produces a positive effect of iron on the *wd* water storage capacity; however, a significant number of regressions produce either negative or no effect of iron on the *wd* water storage capacity (Fig. 3.2b), which is due to inconsistencies in water measurements

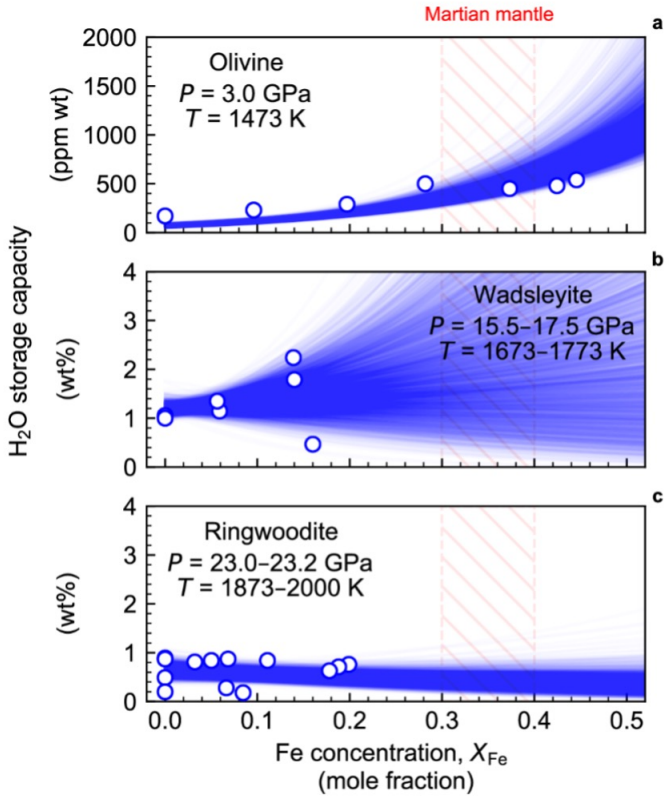
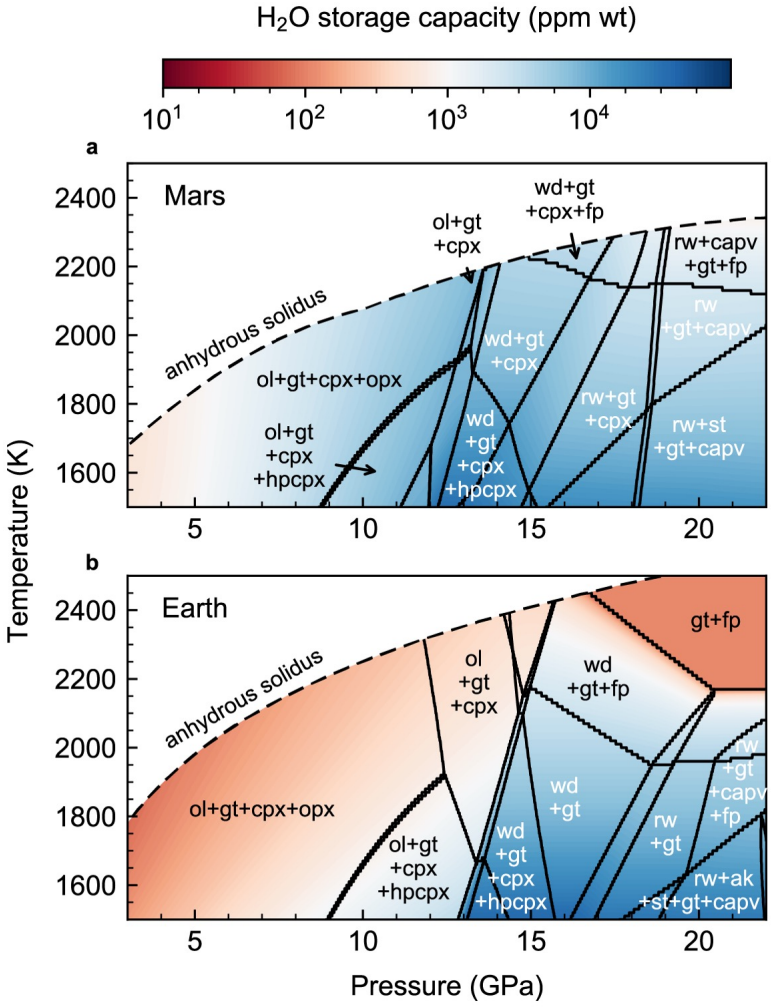


Figure 3.2: **Effects of Fe content on the water storage capacities of (a) olivine, (b) wadsleyite, and (c) ringwoodite at selected pressures and temperatures.** The open circles are experimentally-determined water storage capacity data from the narrow range of P–T conditions shown in the text of each figure for comparison to our models (Tables B.11–B.13 and references therein); their associated uncertainties are not shown for clarity. The blue curves correspond to the water storage capacities predicted at the same P–T conditions for each mineral from the regressions of 10^4 sets of bootstrapped data (Section 2.3). The red hatched regions indicate the approximate range of X_{Fe} expected for olivine, wadsleyite, and ringwoodite in the solid Martian mantle.

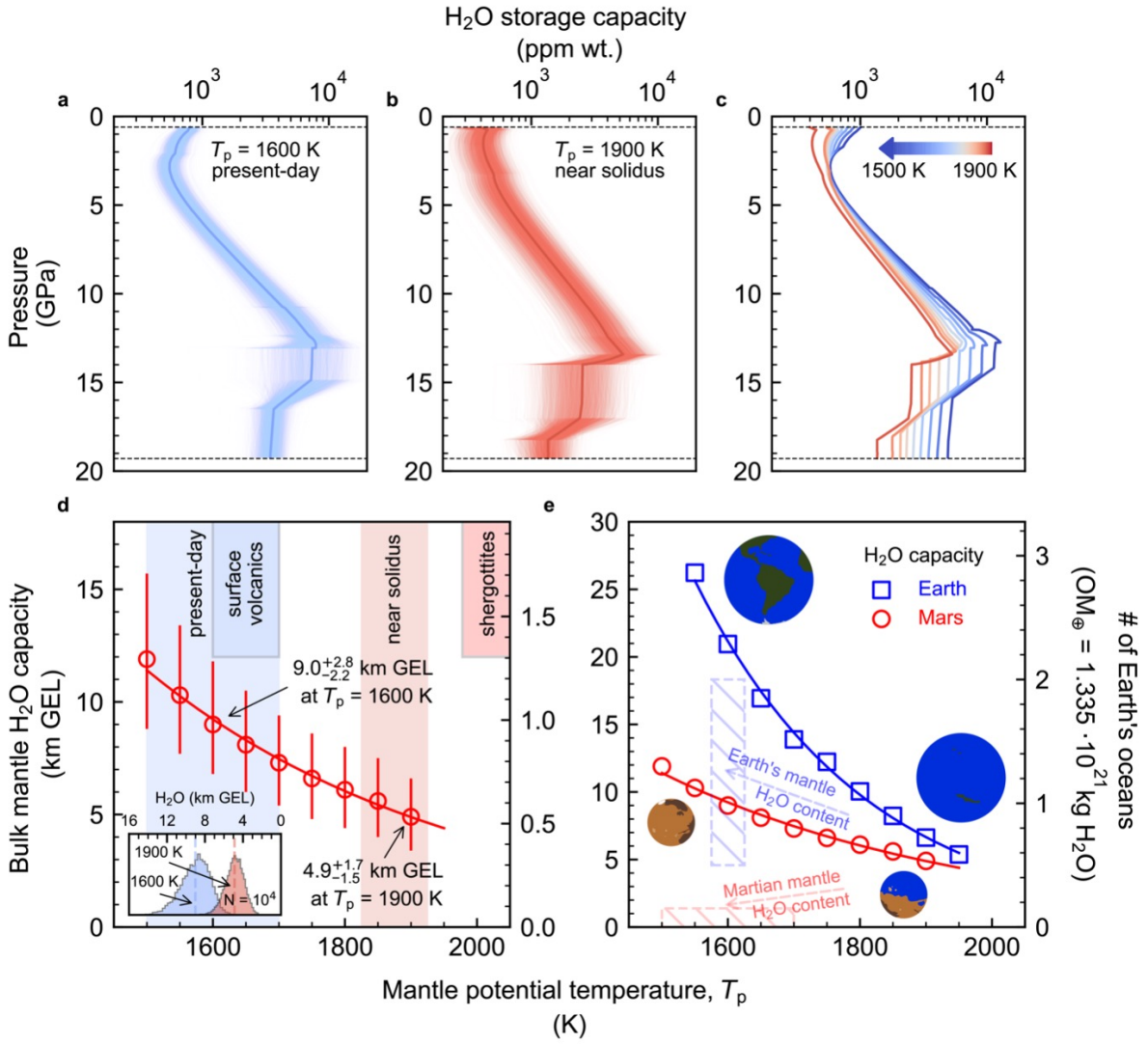
Figure 3.3 *(following page)*: **H_2O storage capacity diagrams of Martian (a; model-averaged estimate from this study) and terrestrial (b Dong et al. 2021) mantle assemblages between 3 and 22 GPa.** The bulk H_2O storage capacities at each P–T were estimated from the H_2O storage capacities of the stable phases and their relative abundances. The thermodynamically-stable mantle assemblages were calculated for a bulk silicate Mars composition (Taylor 2013) and a terrestrial depleted MORB mantle composition (Workman and Hart 2005) using the thermodynamic code HeFESTo (Stixrude and Lithgow-Bertelloni 2005, 2011). The anhydrous mantle solidi for Mars and Earth are from Duncan et al. (2018) and Herzberg et al. (2010), respectively. Mantle phases are labeled as: *ol*: olivine, *wd*: wadsleyite, *rw*: ringwoodite, *fp*: ferropericlase, *cpx*: clinopyroxene, *opx*: orthopyroxene, *hpcpx*: high-pressure clinopyroxene, *ak*: akimotoite, *st*: stishovite, and *capv*: $CaSiO_3$-perovskite.


H2O storage capacity (ppm wt)
10^1
10^2
10^3
10^4
a
Mars
anhydrous solidus
ol+gt+cpx+opx
ol+gt
+cpx
+hpcpx
ol+gt
+cpx
wd+gt
+cpx+fp
wd+gt
+cpx
wd
+gt
+cpx
+hpcpx
rw+gt
+cpx
rw+capv
+gt+fp
rw
+gt+capv
rw+st
+gt+capv
b
Earth
anhydrous solidus
ol+gt+cpx+opx
ol
+gt
+cpx
ol+gt
+cpx
+hpcpx
wd
+gt+fp
wd
+gt
wd
+gt
+cpx
+hpcpx
rw
+gt
gt+fp
rw
+gt
+capv
+fp
rw+ak
+st+gt+capv
Temperature (K)
Pressure (GPa)
2400
2200
2000
1800
1600
5
10
15
20

in the available literature data on *wd*. Fei and Katsura (2021) show that at similar temperatures, the water storage capacity in Fe-bearing *wd* is indeed higher than that in Fe-free *wd*, but they also noted that there is no experimentally-resolvable effect of iron within the Fe-bearing samples with Mg# $\sim$ 88, consistent with the regression results in Dong et al. (2021). This relatively high variation in the extrapolation of the iron effect for *wd* is well characterized in the 10^4 regressions of bootstrapped datasets (Fig. 3.2b) and is taken into account in the estimates of the bulk solid mantle water storage capacity in Section 3.3.2. For *rw*, we found that the regressions of bootstrapped datasets suggest a slightly negative effect of iron on water storage capacity, which is in good agreement with experimental data at 1900–2000 K (Fei and Katsura 2020, Fig. 3.2c).

We computed 10^4 P–T water storage capacity diagrams based on a representative set of bootstrapped regression parameters. Aggregating these results by model averaging, we constructed a best-fit water storage capacity P–T diagram for the Martian mantle (Fig. 3a) as well as water storage capacity profiles along its adiabats (Fig. 4a–c). We found that the maximum water storage capacity along Martian adiabats is often reached in wd within the ol–wd transition region (0.5–1.3 wt%, Fig. 4a–c), where the lower temperatures and higher X_{Fe} in *wd* give rise to a higher water storage capacity (iron preferentially partitions into wd within the *ol–wd* transition region, Fig. S2). Other abrupt changes in the profiles are consequences of phase transformations in the Martian mantle. The relatively large uncertainties in the extrapolation of the iron effect on the *wd* water storage capacity (Fig. 2b) are manifested in the increased variations in the water storage capacity profiles of the deeper Martian mantle (*wd*-dominated layers) in Fig. 4a–b.

Figure 3.4 *(following page)*: **Water storage capacity of the solid Martian mantle.** In the upper panels, the bold lines are the best-fit water storage capacity profiles along mantle adiabats at (a) T_p = 1600 K, (b) T_p = 1900 K, and (c) T_p = 1500–1900 K, in increments of 50 K. The light curves in (a) and (b) are 10^4 profiles from a representative set of "bagging" sampling. In the lower panels, the red open circles are the bulk water storage capacities for the solid Martian mantle at each T_p, which were calculated as the medians of 10^4 "bagging" samples; the blue open squares are the bulk water storage capacities for the solid Earth's mantle estimated by Dong et al. (2021) In (d), the error bars represent the 5th and 95th percentiles of each distribution; the shaded areas are the estimated ranges for the Martian mantle T_p (Table B.6); and the boxes are the T_p ranges estimated for different Martian basalt suites (Filiberto et al. 2019) In the inset of (d), two distributions of "bagging" samples are shown, for T_p = 1600 K (blue) and T_p = 1900 K (red). The vertical dashed lines are the best-fit (model average) bulk water storage capacity for each T_p. In (e), the hatched rectangular regions correspond to geochemical estimates of the actual mantle water contents of Mars (red, 14–250 ppm wt or 80–1460 m GEL Filiberto et al. 2019) and Earth (blue, 0.5–2 OM or 5–19 km GEL Dauphas and Morbidelli 2014; Hirschmann 2018)


H2O storage capacity
(ppm wt.)
a
b
c
Tp = 1600 K
present-day
Tp = 1900 K
near solidus
1500 K
1900 K
Pressure
(GPa)
d
e
present-day
surface
volcanics
near solidus
shergottites
9.0+2.8−2.2 km GEL
at Tp = 1600 K
4.9+1.7−1.5 km GEL
at Tp = 1900 K
H2O (km GEL)
1900 K
1600 K
N = 10^4
Bulk mantle H2O capacity
(km GEL)
H2O capacity
Earth
Mars
Earth's mantle
H2O content
Martian mantle
H2O content
of Earth's oceans
(OM⊕ = 1.335 ·10^21 kg H2O)
Mantle potential temperature, Tp
(K)

The depth-dependent profiles (Figs. 3.4a–c) and P–T water storage capacity diagram (Fig. 3.3a) show that the Martian mantle water storage capacity varies with depth, but a depth-dependent profile in water storage capacity does not necessarily imply a heterogeneous distribution of actual water content with depth. Instead, the water storage capacity in the solid mantle only indicates the maximum water content as a saturation limit for dehydration melting (Bercovici and Karato 2003), which is not necessarily equivalent to the actual mantle water content. It has been suggested that the water distribution in the Earth's mantle is heterogeneous due to the presence of advection, such as partial melting upon transport to a region with a lower water storage capacity (Karato et al. 2020). Due to the lack of a sharp water storage capacity discontinuity in the Martian mantle, however, the associated partial melting mechanism would be less effective at maintaining a heterogeneous water distribution in Mars.

A recent Martian hydrogen isotope study (Barnes et al. 2020) characterized the D/H ratios of the Martian crust between 3.9 and 1.5 Ga based on ALH 84001 and NWA 7034 (D/H = 2.68–5.73 $\times$ 10^{-4}). That study argued that to produce such D/H ratios for the crust using mixing models, at least two isotopically-distinct mantle water reservoirs with different water contents are required, implying that the Martian mantle has almost always been heterogeneous. If so, we cannot use Martian meteorite samples to infer the bulk mantle water content, because they may only represent the source regions where their parental magmas were generated (e.g., olivine-phyric shergottites were likely generated at 3–5 GPa or 255–425 km Filiberto and Dasgupta 2011). However, we may directly compare the water content in the mantle source regions of the Martian meteorites (15–23 ppm wt in the depleted shergottite source and 36–72 ppm wt in the enriched shergottite source; McCubbin et al., 2016) with the mantle water storage capacity at

the same depth (480–650 ppm wt at T_p = 1500–1900 K) to infer the hydration state of the source region (expressed as a percentage of the bulk water storage capacity at this depth), which yields 2–5 and 6–15 hydration for the depleted and enriched sources, respectively.

3.3.2 Estimates of the Solid Martian Mantle H_2O Storage Capacity as a Function of Mantle T_p

The total water storage capacity integrated over depth for the solid Martian mantle was calculated for each T_p from 1500 K to 1900 K (Fig. 3.4d–e and Table B.6). For the present-day Martian mantle with T_p = 1600 K, the bulk mantle water storage capacity is $9.0^{+2.8}_{-2.2}$ km GEL. If the Martian mantle was 100–200 K hotter at the beginning of the Noachian (∼4.1 Ga; Filiberto, 2017), its mantle water storage capacity would have been $7.3^{+2.1}_{-1.9}$ km GEL and $6.1^{+1.9}_{-1.7}$ km GEL for T_p = 1700 K and 1800 K, respectively. These water storage capacities for the early Noachian (T_p = 1700–1800 K) are approximately 1.7–2.9 km GEL smaller than the present-day water storage capacity (T_p = 1600 K). The water storage capacity for the initial Martian mantle with T_p = 1900 K can also be estimated to be $4.9^{+1.7}_{-1.5}$ km GEL.

To date, the scarcity of Martian rock samples has not allowed for a robust reconstruction of the planet's thermal history. Based on orbital spectroscopy of the Martian surface, the estimated mantle T_p associated with its major volcanic provinces is ∼1600–1650 K during the Amazonian (∼3–0 Ga) and ∼1650–1700 K during the Hesperian (∼3.7–3 Ga) (Baratoux et al. 2011). Geochemical analyses of Noachian basalts in Gusev Crater, Gale Crater, and Meridiani Planum (∼4.2–3.7 Ga), as well as

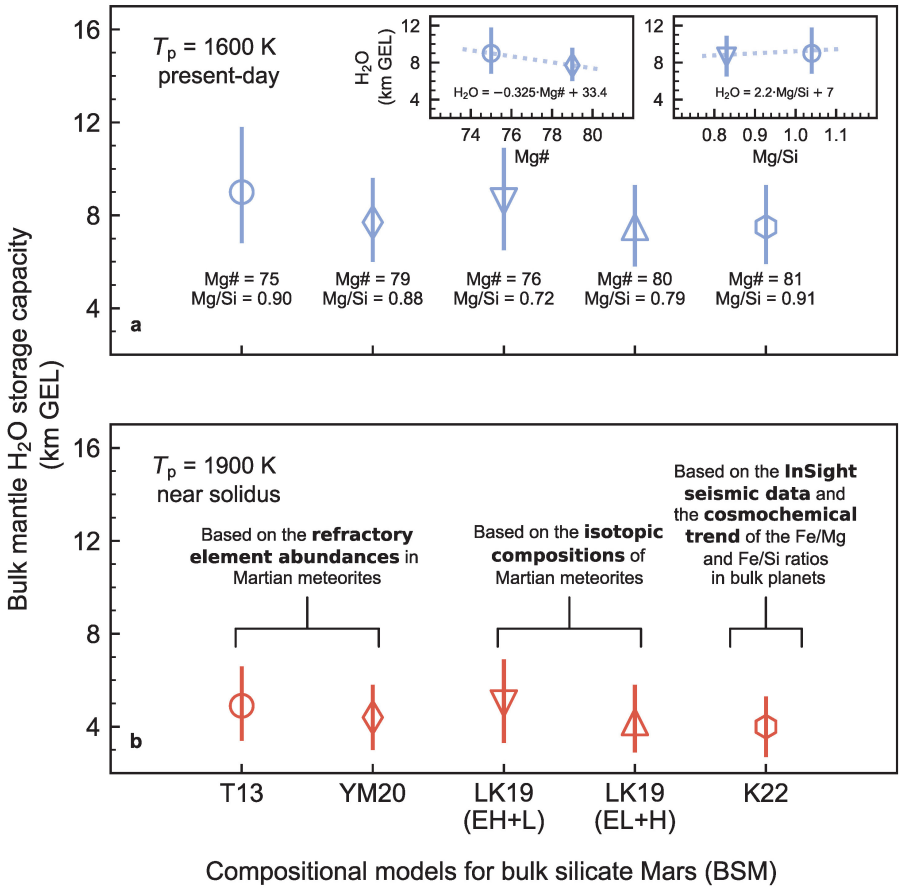
clasts in the Martian meteorite NWA 7034 (pre-Noachian, ∼4.4 Ga), suggest a range of average early mantle T_p of 1600–1800 K (Filiberto and Dasgupta 2015; Filiberto 2017). Some ol-phyric shergottites indicate a much higher mantle T_p of 1800–2000 K, but these samples might only represent a regional temperature anomaly (Filiberto 2017). Therefore, we consider T_p = 1600 K and 1800 K to be pertinent to the average Martian mantle today and at the beginning of the Noachian period (∼4.1 Ga), respectively, with an estimated uncertainty of ±100 K. T_p = 1900 K is prescribed as the highest Tp corresponding to a mostly solidified Martian mantle, because the adiabatic areotherms at $T_p > 1900$ K are significantly above the nominally anhydrous Martian mantle solidus (see Fig. B.1 and references therein) and hence would cause extensive melting of the Martian upper mantle.

We adopted T_p as a simple proxy for the Martian mantle thermal state and took the adiabats as a first-order approximation to the temperature gradient in the Martian mantle. This assumption is likely unrealistic for early Mars because its temperature gradients may have deviated from adiabats in the solid shallow mantle where they exceeded the solidus, causing partial melting (Fig. S1 Rey 2015). From the depths where the adiabats exceed the solidus to the base of the crust (∼50 km), therefore, we only include the unmelted portion of the shallow mantle in our bulk mantle water storage capacity calculation. Consideration of a moderate temperature deviation of ∼100 K (e.g., between the solid mantle adiabats and the melt adiabats, Fig. S1) in the shallow mantle contributes a small error to the water storage capacity of < 9 m GEL, which is negligible compared to the mantle H_2O storage capacities. However, such a simple shift from the adiabats may not be sufficient to reflect the actual lithospheric temperature deviation through time; conductive cooling from the surface leads to the formation of a

lithospheric lid that thickens with time. The thickening of a much cooler lithospheric lid may result in a considerable temperature deviation of a few hundred kelvins and hence contribute a moderate error of tens of meters GEL to our bulk mantle water storage capacity estimates (at least 1–2 order of magnitude smaller than ∼9 km GEL at T_p = 1600 K). If water-saturated (with several wt% H_2O), a number of dense hydrous magnesium silicates (DHMSs) would stabilize at Martian mantle pressures (Ganskow and Langenhorst 2014), especially within a much cooler lithospheric mantle (Wade et al. 2017). However, without efficient recycling of water back to the interior, Martian mantle assemblages would be water-undersaturated and primarily composed of NAMs only. Therefore, a thicker and cooler lithosphere does not substantially change our results.

In this study, we used the canonical bulk silicate Mars (BSM) model from Taylor (2013) (T13), but we do not mean to imply that the BSM composition is well-constrained at present. The differences between some recently-published BSM models (e.g., Taylor 2013; Liebske and Khan 2019; Yoshizaki and McDonough 2020; Khan et al. 2022) are another potential source of uncertainty in our calculation. Two main parameters of the BSM models that affect their bulk mantle water storage capacities are Mg# (molar) and Mg/Si (in wt%) (Fig. 3.5 and Tables B.6–B.10). For example, with similar Mg#, the BSM model derived from mixing of meteoritic isotopic compositions (e.g., "EH+L" from LK19) has a lower Mg/Si ratio than T13, resulting in less olivine and more pyroxene in the Martian mantle (Fig. B.3), which lowers the bulk mantle water storage capacity by 0.4 km GEL (<5%) at T_p = 1600 K (Fig. 3.5). Alternatively, with the same Mg/Si, YM20 proposed an FeO-poor BSM model with a higher bulk silicate Mg# of 79, in contrast to the T13 model, with a bulk silicate Mg# of 75. As discussed in Section 3.3.1, the effects of Fe on *ol* and *wd* are typically positive, and the effect of iron on *rw* is

Figure 3.5 *(following page)*: **Sensitivity of bulk mantle water storage capacity to mantle composition at (a) 1600 K (blue) and (b) 1900 K (red).** T13 and LK19 (EL+H) with an Mg of 75–76 are more enriched in FeO than YM20, LK19 (EH+L), and K22 with an Mg of 79–81. T13, YM20, and K22 have an Mg/Si of 1.04–1.05, similar to Earth. In contrast, two LK19 compositions have a lower Mg/Si of 0.83 and 0.91, leading to lower olivine and higher pyroxene abundances in the calculated Martian mantle assemblages (Figs. 3.2–3.6). The canonical T13 composition and the other four compositions represent the entire possible range of the bulk Mg and Mg/Si for the Martian mantle. Within this range, the bulk H2O storage capacity of the Martian mantle decreases slightly with increasing bulk Mg and increases slightly with increasing bulk Mg/Si (insets, a), but in general it varies by less than ∼13–17% (Tables B.6–B.10). Hence, our estimates based on T13 in Fig. 3.4 are reasonable first-order approximations.


Bulk mantle H2O storage capacity (km GEL)
16
12
8
4
Tp = 1600 K
present-day
H2O (km GEL)
H2O = −0.325·Mg# + 33.4
Mg#
H2O = 2.2·Mg/Si + 7
Mg/Si
Mg# = 75
Mg/Si = 0.90
Mg# = 79
Mg/Si = 0.88
Mg# = 76
Mg/Si = 0.72
Mg# = 80
Mg/Si = 0.79
Mg# = 81
Mg/Si = 0.91
a
Tp = 1900 K
near solidus
Based on the refractory element abundances in Martian meteorites
Based on the isotopic compositions of Martian meteorites
Based on the InSight seismic data and the cosmochemical trend of the Fe/Mg and Fe/Si ratios in bulk planets
b
T13
YM20
LK19 (EH+L)
LK19 (EL+H)
K22
Compositional models for bulk silicate Mars (BSM)

negligible or slightly negative, so the bulk mantle water storage capacity based on YM20 is lower than that based on T13 by 1.3 km GEL (<15%) at T_p = 1600 K (Fig. 3.5). The five different BSM models we selected represent the full possible range of bulk silicate Mg# and Mg/Si. We tested the sensitivity of our bulk mantle water storage capacity estimates to BSM composition at T_p = 1600 K and 1900 K (Fig. 3.5, B.8 and Tables B.6–B.10) and found the effects of mantle composition contribute an error of < 5–15% (Fig. 3.5, B.8). A detailed discussion of the effects of bulk composition on Martian mantle mineralogy and areotherms is beyond the scope of this study.

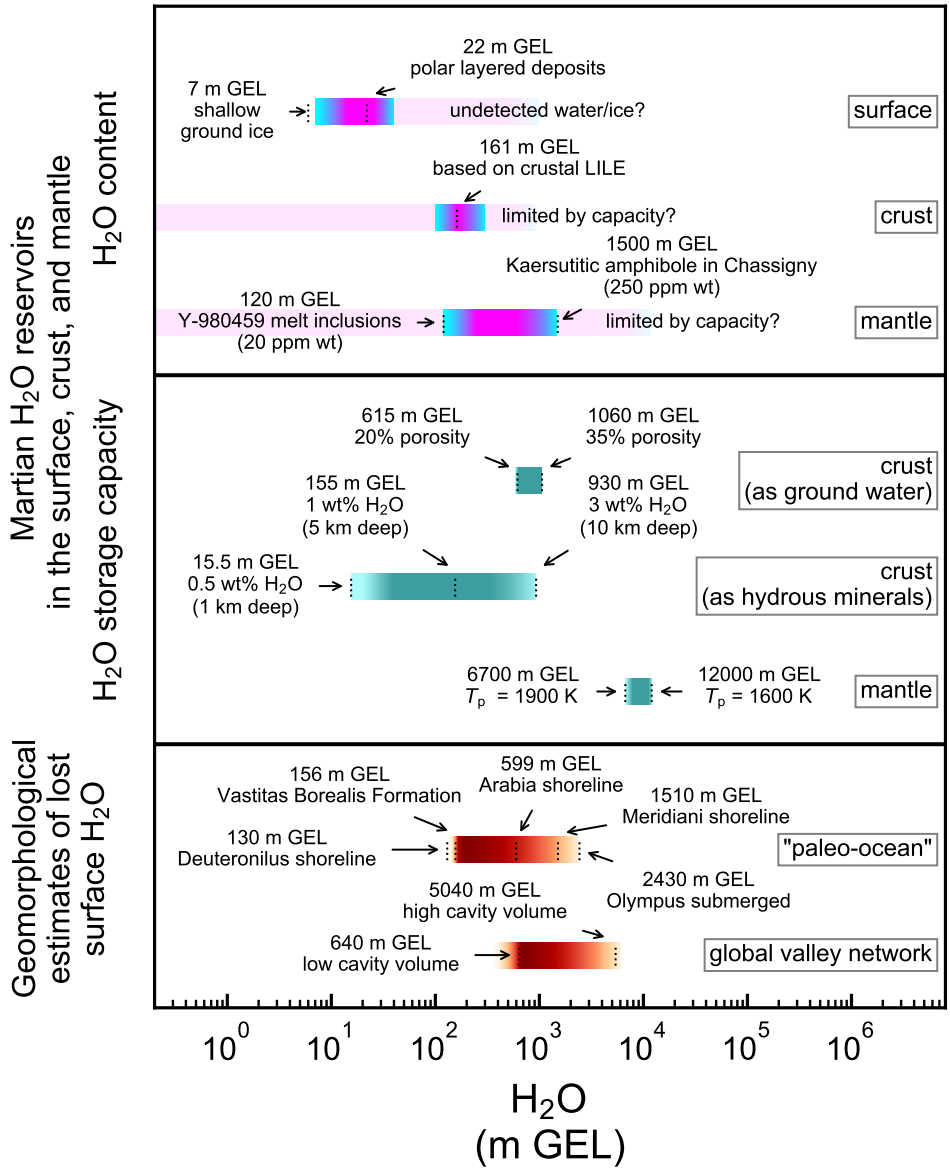
3.3.3 Comparing the Solid Mantle H_2O Storage Capacities of Mars and Earth and Their Evolution Through Time

For Earth's mantle with a bulk silicate Mg# of ∼89, the water storage capacity of the ol-dominated upper mantle remains ∼4–6 orders of magnitude lower than that of the wd-dominated transition zone at similar *P*–*T* conditions where *ol* and *wd* coexist (∼13–15 GPa), forming a sharp water storage capacity increase at the 410-km discontinuity of Earth's mantle (Fig. 3.3b Dong et al. 2021). In contrast, the ol-dominated upper portion of the Martian mantle (bulk silicate Mg# ≈ 75) (Fig. 3.3a) can incorporate much more water than Earth's upper mantle (bulk silicate Mg# ≈ 89) due to the positive effect of Fe on olivine water storage capacity. The water storage capacity of the Martian mantle *ol*-dominated layer can reach and even exceed that of the *wd*-dominated layer (Fig. 3.4a–c). Even though the increased abundance of Fe in rw does not change its water storage capacity significantly, the bulk water storage capacity in the lowermost Martian mantle (*rw*-dominated layer) can be much higher than that in the Earth at

similar pressures when the temperature is high. This is because the equilibrium phase assemblage of the Earth's mantle is mostly comprised of gt and ferropericlase (*fp*) above 2100 K at 20 GPa (Fig. 3.3b), and *gt* + *fp* has a much lower water storage capacity than *rw*. In contrast, the high Fe content of the Martian mantle stabilizes *rw* up to the solidus, with no *gt* + *fp* field present in the equilibrium phase diagram (Fig. 3.3a).

The bulk water storage capacity of the Martian mantle increases with decreasing T_{p} (Fig. 3.4), as in the Earth (Dong et al. 2021), which mainly results from the negative effects of temperature on the water storage capacities of *ol*, *wd*, and *rw*. The evolution of bulk water storage capacity in Mars and Earth as a function of T_{p} during secular cooling are compared in Fig. 3.4e. On the one hand, with T_{p} = 1600 K (present-day), the bulk water storage capacity of the Earth's mantle (∼2.3 OM, where OM is the modern surface ocean mass on Earth, 1.335 × 10^{21} kg H_2O) is only a factor of ∼ 2.3 larger than that of Mars (∼1.0 OM), despite the volume of Earth's mantle (∼9.1×10^{11} km^3) being nearly ∼6.5 times larger than that of Mars (∼1.4×10^{11} km^3). This difference arises primarily from the Fe enrichment in the Martian mantle. On the other hand, the bulk water storage capacities of Earth and Mars converge at higher T_{p} (Fig. 3.4e, 0.4–0.6 Earth's ocean masses at T_{p} = ∼1950 K), because 1) the effects of temperature on the water storage capacities of NAMs outcompete the effects of iron at high T_{p}, and 2) contributions of Earth's lower mantle to its bulk mantle water storage diminish significantly at high T_{p}. Last but not least, though the evolution of mantle water storage capacities in Earth and Mars follows the same increasing trend with secular cooling (Fig. 3.4e), mantle rehydration by subduction (e.g., van Keken et al. 2011) may have been increasing Earth's actual mantle water content since the onset of plate tectonics (light blue dashed arrow in Fig. 3.4e). In contrast, Mars lacks efficient water recycling

Figure 3.6 *(following page)*: **Summary of the Martian water reservoirs in the surface, crust, and mantle (water content in blue/pink and water storage capacity in blue-green), as well as the estimates of the lost surface water potentially associated with morphological features on Mars (red/orange).** The gradients in color represent the qualitative uncertainty for each bar. In general, these estimates are subject to considerable uncertainty, but their orders of magnitude are much more robust. Estimates from: Carr and Head (2015) (polar layered deposits and shallow ground ice), Barnes et al. (2020) (crustal H2O content based on enriched shergottite mantle and large ion lithophile elements (LILE) crustal abundance), Filiberto et al. (2019) (mantle source region H_2O content based on Yamato 980459 melt inclusions and Kaersutitic amphibole in Chassigny), Clifford et al. (2010) (pore water volumes of the crust for different porosities), Mustard (2019) (hydrated minerals for different depths of crust), this study (bulk mantle water storage capacity), Carr and Head (2003) (volumes of ocean contained by putative shorelines for different elevations), Rosenberg et al. (2019); Luo et al. (2020) (volume of water required to carve the Martian valley networks for different cavities).


Martian H2O reservoirs
in the surface, crust, and mantle
H2O content
H2O storage capacity
Geomorphological
estimates of lost
surface H2O
22 m GEL
polar layered deposits
7 m GEL
shallow
ground ice
undetected water/ice?
surface
161 m GEL
based on crustal LILE
limited by capacity?
crust
1500 m GEL
Kaersutitic amphibole in Chassigny
(250 ppm wt)
120 m GEL
Y-980459 melt inclusions
(20 ppm wt)
limited by capacity?
mantle
615 m GEL
20% porosity
1060 m GEL
35% porosity
155 m GEL
1 wt% H2O
(5 km deep)
930 m GEL
3 wt% H2O
(10 km deep)
crust
(as ground water)
15.5 m GEL
0.5 wt% H2O
(1 km deep)
crust
(as hydrous minerals)
6700 m GEL
Tp = 1900 K
12000 m GEL
Tp = 1600 K
mantle
156 m GEL
Vastitas Borealis Formation
599 m GEL
Arabia shoreline
1510 m GEL
Meridiani shoreline
130 m GEL
Deuteronilus shoreline
"paleo-ocean"
2430 m GEL
Olympus submerged
5040 m GEL
high cavity volume
640 m GEL
low cavity volume
global valley network
10^0
10^1
10^2
10^3
10^4
10^5
10^6
H2O
(m GEL)

mechanisms such as long-term subduction-driven plate tectonics (Nimmo and Tanaka 2005), so its actual mantle water content may have remained relatively low to the present (light red dashed arrow in Fig. 3.4e).

3.3.4 Possible Sources and Sinks for Water in the Martian Mantle Through Time

During accretion, Mars acquired its primordial H_2O/H_2 from chondritic materials (Brasser 2013) and/or the solar nebula (Olson and Sharp 2018). Some fraction of this primordial water was retained in the Martian mantle upon solidification of the magma ocean (e.g., Elkins-Tanton 2008; Kurokawa et al. 2021). Subsequently, volcanic outgassing continued to release water onto the surface (e.g., Craddock and Greeley 2009; Phillips et al. 2001). The initial water content in the newly-solidified mantle was limited by its bulk water storage capacity of $>$ 5 km GEL at T_p = 1900 K. Assuming that the early Martian hydrosphere was supplied by outgassing only, the amount of water estimated for the putative early oceans ($\sim$0.1–2.4 km GEL) (e.g., Carr and Head 2003; Sholes et al. 2021, Fig. 3.6) requires the initial Martian mantle reservoir to outgas $>$2–48% of its water, and to fill up all global valley networks of $\sim$0.6–1.8 km GEL (e.g., Rosenberg et al. 2019; Luo et al. 2020, Fig. 3.6) would require the initial Martian mantle reservoir to outgas $>$12–36% of its water.

The early hydrosphere initially outgassed from the mantle was lost either to space through atmospheric escape (e.g., Kurokawa et al. 2014) or to the crust through serpentinization (e.g., Chassefiere et al. 2013), or, most likely, to both (e.g., Scheller et al. 2021). A return flux of water into the crust is estimated to be $\sim$0.1–1.5 km GEL

H_2O based on Martian surface D/H (Chassefiere et al. 2013; Scheller et al. 2021), which is comparable either to the storage capacity of ∼0.2–0.9 km GEL H2O in the top 5–10 km of hydrated minerals in the Martian crust (e.g., Mustard 2019; Wernicke and Jakosky 2021, Fig. 3.6) or to the storage capacity of 0.1–1.0 km GEL H2O in the available pore space of the permeable Martian crust to a depth of ∼26.5 km (e.g., Clifford and Parker 2001; Clifford et al. 2010, Fig. 3.6). Such a return flux would be insufficient to hydrate the lower crust and hence return water back to rehydrate the mantle, despite the relatively large water storage capacity estimated for Martian basaltic materials at shallow mantle conditions (Wade et al. 2017).

O'Rourke and Shim (2019) proposed that water stored in the *rw*-dominant layer at the base of the Martian mantle may react with and enter the core as FeH_x. However, the nominally anhydrous *rw* layer in direct contact with the Fe-rich core would soon become enriched in FeO and convert into a layer of dry iron-rich fp and stishovite (st) if the core was reacting with the base of the mantle (Matsuzaka et al. 2000), which would impede any further hydrogenation of the core. Therefore, a significant exchange of water between the Martian mantle and core since their formation remains unlikely.

3.4 Summary and Conclusions

In this study, we applied a bootstrap aggregation method to model the effects of Fe on the water storage capacities of major terrestrial mantle NAMs, *ol*, *wd*, and *rw*, based on high-pressure mineral physics data in the literature. We assessed the variations of our parameterization of the Fe effects based on the errors in the experimental data on water measurements in NAMs. We found that our bootstrapped resampling typically indicates

that iron increases the water storage capacities of *ol* and *wd* and has no/little effect on the water storage capacity of *rw*.

We presented depth-dependent water storage capacity profiles for the Martian mantle and found that the water storage capacity of the more Fe-rich Martian mantle is in general higher than that of Earth at similar P–T, due to iron increasing the water storage capacities of *ol* and *wd* as well as expanding the *rw* stability field to higher temperatures. We also calculated the bulk water storage capacity of the solid Martian mantle as a function of mantle T_{p}. As the mantle cooled, its water storage capacity would have increased by 4.1 km GEL, from 4.9 km GEL ($T_{\mathrm{p}} = 1900$ K, initial mantle) to 9.0 km GEL ($T_{\mathrm{p}} = 1600$ K, present-day). We tested the sensitivity of those estimates to BSM composition and found the effects of mantle composition contribute an error of $<$ 5–15%. Despite an increase in its water storage capacity through time, the actual water content in the Martian mantle today is lower than what it was in the pre-Noachian with a net water loss to the surface, due to lack of an efficient deep-water recycling mechanism on Mars.

Acknowledgments

We thank the editor, Elizabeth Rampe, for handling our manuscript, and we thank the reviewers, Thomas Ruedas and J. Brian Balta, for constructive comments and the former for his generous checking of our equations and text; responsibility for any remaining errors rests solely with the authors. We also thank Robin Wordsworth for helpful advice and Sam Klug (The Fellowships and Writing Center at Harvard) for improving the writing of this manuscript. This work is derived from a final project prepared by J.

Dong and Z.T. Eriksen for a Harvard seminar course taught by R.A. Fischer in Fall 2018 (E-PSCI 248: Topics in Mineral Physics and Chemistry: Volatiles in the Deep Earth), and it benefited from the seminar discussions. The preliminary results of this work were presented at the 2019 Goldschmidt conference with the support of a planetary science travel grant from the National Aeronautics and Space Administration. J. Dong was supported by a James Mills Peirce Fellowship from the Graduate School of Arts and Sciences at Harvard University. R.A. Fischer was supported by the Henry Luce Foundation. L. P. Stixrude was supported by the European Research Council under Advanced Grant 291432 MoltenEarth (FP7) and by the National Science Foundation (NSF) (EAR-1853388). C.R. Lithgow-Bertelloni was supported by research funding from the Louis B. and Martha B. Slichter Endowed Chair in the Geosciences at University of California Los Angeles and by the NSF (EAR-1900633). M.C. Brennan was supported by an NSF Graduate Research Fellowship (DGE-1745303).

Chapter 4

Nonlinearity of the Post-spinel Transition and Its Expression in Slabs and Plumes Worldwide

Michelangelo was once asked how he had carved his marble masterpiece. The sculptor apocryphally responded that nothing could be simpler; all one needed was to remove everything that was not David. In this respect the laboratory is not so different from the studio. As the artistic tale suggests, the task of removing the background is not ancillary to identifying the foreground—the two tasks are one and the same. [...] When the background could not be properly circumscribed, the demonstration had to remain incomplete, like Michelangelo s St. Matthew, in which the artist was unable to "liberate" his sculpture from its "marble prison."

—Peter L. Galison, *How Experiments End*

Abstract*

At the interface of Earth's upper and lower mantle, the post-spinel transition boundary controls the dynamics and morphologies of downwelling slabs and upwelling plumes, and its Clapeyron slope is hence one of the most important constraints on mantle convection. In this study, we reported a new in situ experimental dataset on phase stability in Mg_2SiO_4 at mantle transition zone pressures from laser-heated diamond anvil cell experiments, along with a compilation of corrected in situ experimental datasets from the literature. We presented a machine learning framework for high-pressure phase diagram determination and focused on its application to constrain the location and Clapeyron slope of the post-spinel transition: ringwoodite $\leftrightarrow$ bridgmanite + periclase. We found that the post-spinel boundary is nonlinear and its Clapeyron slope varies locally from $-2.3^{+0.6}_{-1.4}$ MPa/K at 1900 K, to $-1.0^{+1.3}_{-1.7}$ MPa/K at 1700 K, and to $0.0^{+1.7}_{-2.0}$ MPa/K at 1500 K. We applied the temperature-dependent post-spinel Clapeyron slope to estimate its lateral variation across the "660-km" seismic discontinuity in subducting slabs and hotspot-associated plumes worldwide, as well as the ambient mantle. We found that, in the present-day mantle, the average post spinel Clapeyron slope in the plumes is three times more negative than that in slabs, and we then discussed the effects of a nonlinear post-spinel transition on the dynamics of Earth's mantle.

*This chapter includes modified content from my preprint titled "Nonlinearity of the Post-spinel Transition and Its Expression in Slabs and Plumes Worldwide," which was previously posted on *arXiv* in 2022.

4.1 Introduction

The pressure-induced, endothermic breakdown of ringwoodite (rw) into bridgmanite and ferropericlase ($bm + fp$) in the iron-bearing system $(Mg,Fe)_2SiO_4$, typically referred to as the post-spinel transition, coincides with a global scale seismic discontinuity in the Earth's mantle at approximately 660 km in depth (e.g., Deuss et al. 2013). Significant changes in temperature, rheology, and buoyancy accompany the post-spinel transition and influence mantle circulation through interaction with cold downwelling (slabs) and hot upwelling (plumes). The reaction pressure of the post-spinel transition in $(Mg,Fe)_2SiO_4$ is nearly independent of the presence of iron in small amounts (e.g., <0.01 GPa at 1700 K, corresponding to <250 m in the mantle Ishii et al. 2019). Hence, the pressure (P) and temperature (T) conditions and Clapeyron slope of the $rw \leftrightarrow bm$+periclase (pe) boundary in the iron-free system Mg_2SiO_4, can be used as a proxy to investigate the interactions of the mantle transition zone with slabs and plumes.

Several generations of experimentalists have studied the location and Clapeyron slope of the $rw \leftrightarrow bm + pe$ post-spinel transition, along with other solid-solid phase transitions/reactions in Mg_2SiO_4 at transition zone pressures: wadsleyite (wd) $\leftrightarrow rw$ and $wd \leftrightarrow bm + pe$, using ex situ (quench) or in situ experiments in multi-anvil (MA) press (Ito and Takahashi 1989; Irifune et al. 1998; Suzuki et al. 2000; Hirose 2002; Katsura et al. 2003; Fei et al. 2004; Inoue et al. 2006; Ishii et al. 2011; Ghosh et al. 2013) as well as in situ experiments in laser-heated diamond anvil cell (DAC) (Shim et al. 2001; Chudinovskikh and Boehler 2001). Despite several decades of experimental focus on one phase diagram, there is not yet a global analysis of phase stability observations in Mg_2SiO_4 that provides a statistically-optimized Mg_2SiO_4 phase diagram and

determines its phase boundaries and their uncertainties self-consistently. Furthermore, the post-spinel boundary has historically been conceived as a linear boundary, but a recent experimental dataset reported by Chanyshev et al. (2022) suggests that the post-spinel boundary is not linear based on free-hand drawing. A robust assessment of the nonlinearity of the post-spinel boundary therefore becomes indispensable for more realistic morphological and dynamical interpretation of slabs and plumes.

In this paper, we first reported a new set of the Mg_2SiO_4 phase diagram data (Section 4.2). This dataset covers the P–T range (16–28 GPa, 1573–2723 K) for all three phase transitions at transition zone pressures and includes the high temperature area between the triple point and the Mg_2SiO_4 solidus ($>\sim$2000 K) that has not been well constrained by previous studies. Then, we proposed a machine learning framework for high-pressure phase diagram determination. In combination with previously published experimental datasets (Section 4.3), we applied this novel analytical methodology to determine the locations and Clapeyron slopes of these phase transitions in Mg_2SiO_4 and the corresponding triple point (Section 4.4). Most importantly, we obtained a robust estimate on the nonlinearity of the post-spinel transition Clapeyron slope and its associated uncertainty, and then estimated the lateral variation of the post-spinel Clapeyron slope in subducting slabs, hotspot-associated plumes, as well as the ambient mantle at the base of the transition zone (Section 4.5).

4.2 New In Situ Experimental Dataset on the Mg_2SiO_4 Phase Diagram

4.2.1 Synchrotron X-Ray Diffraction Experiments

Our experimental dataset on the Mg_2SiO_4 phase diagram was collected in laser-heated DAC experiments (LH-DAC) with in situ X-ray diffraction (XRD) at high pressure and high temperature. Short symmetric cells and a gas-membrane cell were used to generate high pressure. Double-sided laser heating and synchrotron XRD measurements were performed at beamline 13-ID-D of GeoSoilEnvrio Center for Advanced Radiation Sources (GSECARS) (Shen et al. 2005; Prakapenka et al. 2008), and beamline 16-ID-B, High Pressure Collaborative Access Team (HPCAT) (Meng et al. 2015) at the Advanced Photon Source (APS), Argonne National Laboratory (ANL). Starting materials were powdered synthetic forsterite Mg_2SiO_4 mixed with tungsten (W). The mixed sample was sandwiched between two potassium chloride (KCl) layers and loaded in a sample chamber pre-dilled in a rhenium (Re) gasket. The KCl layers served as the pressure medium, thermal insulator, and the primary pressure scale while the W powder was used as a laser absorber and a secondary pressure scale. Both W and KCl have melting temperatures higher than those of Mg_2SiO_4 Zhou et al. (2020); Errandonea (2005) and are chemically inert at the relevant pressure and temperature range. More details of our experimental setup can be found in Appendix C.1.

Sample temperatures ($T_{\text{meas.}}$) were measured spectroradiometrically, and temperatures of the KCl layers (T_{KCl}) were estimated from the mean temperatures between the sample ($T_{\text{meas.}}$) and the diamond anvil culets, whose surface temperatures

are 295 K (Campbell et al. 2009). Sample pressures P_{W} and P_{KCl} were determined based on the equation of state (EoS) of W with T_{meas} (Sokolova et al. 2016) and the EoS of KCl with T_{KCl} (Tateno et al., 2019, cross-calibrated with Sokolova et al., 2016), respectively. The estimated P_{W} deviates from P_{KCl} significantly at high temperatures (Fig. C.1), likely due to lack of thermal EoS data on W at $>\sim$1673 K (Litasov et al. 2013; Sokolova et al. 2016). Therefore, we chose KCl as our primary pressure scale, and all pressures reported in the main text are based on the EoS of KCl from Tateno et al. (2019). The unit cell parameters of both KCl and W and their estimated pressures can be found in Table C.1.

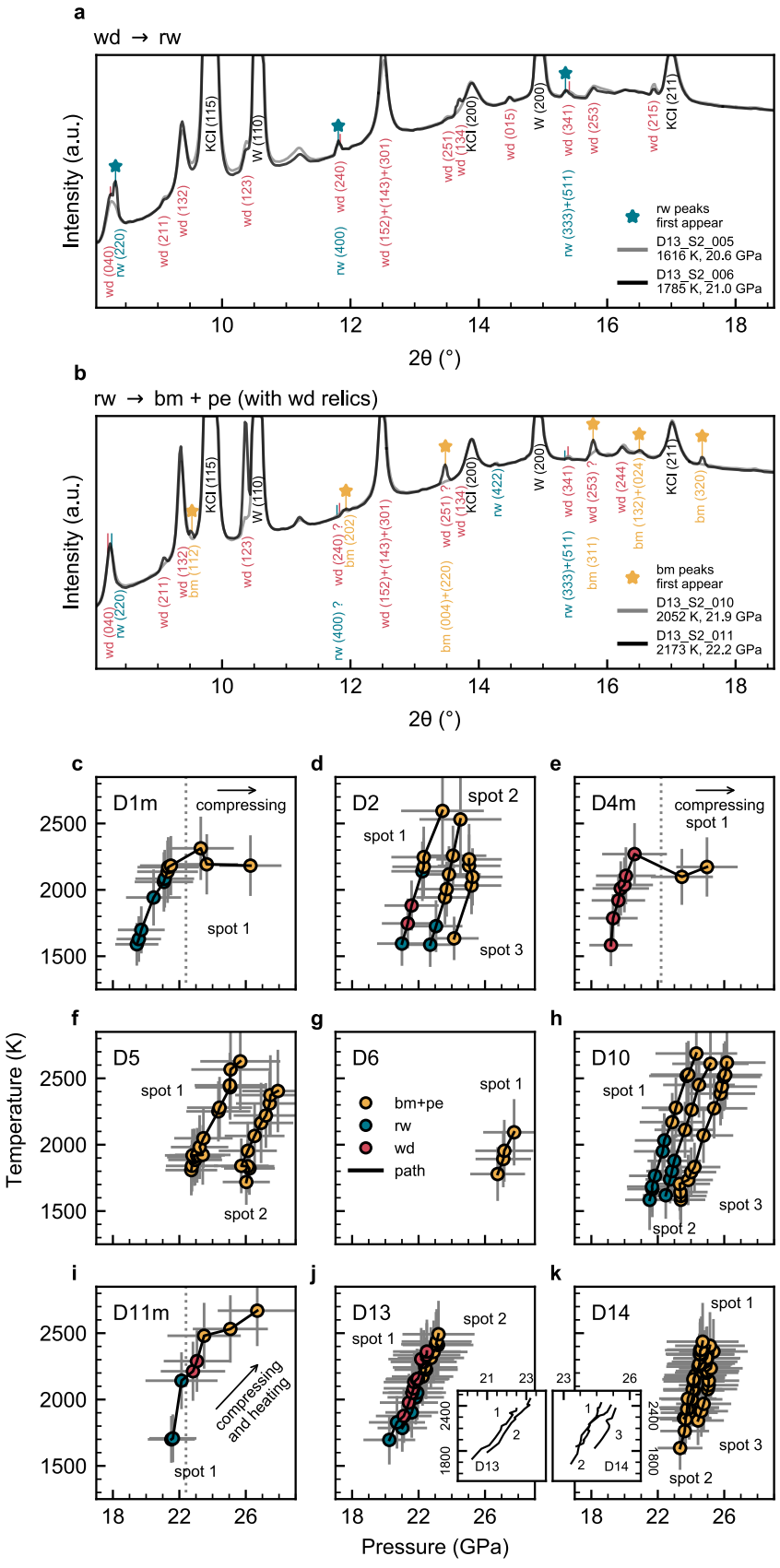
4.2.2 Phase Boundary Detection

Here, we reported a new dataset of phase stability observations for Mg_2SiO_4 between 16 and 28 GPa and between 1573 and 2723 K (Fig. 4.1). These in situ phase stability observations were collected upon heating and/or compression from 9 LH-DAC experiments with 17 laser-heated spots. The P–T path of each experiment is shown in Fig. 4.1c–i, and further details (including unit cell parameters and uncertainties) are available in Table C.1. In a typical experiment with the short symmetric cell (Fig. 4.1, d, f, g, h, j, and k), we first compressed the sample to a target pressure (usually 16–22 GPa) and then pre-heated the sample to 1200–1500 K until the diffraction peaks of either *wd* or *rw* became clear. After that, we began the heating cycle by increasing temperature slowly while continuously taking diffraction patterns. Three of our experiments, D1m, D4m, and D11m, were conducted in a gas-membrane cell; they were first heated up to 2000–2200 K at some pressures lower than 20–21 GPa, and then very small incremental

loads were applied from a gas membrane system to increase the pressure remotely while the sample was being heated (Fig. 4.1, c, e and i). In Fig. 4.1, we showed two examples of our in situ phase stability observations in which phase transitions were detected between two consecutive diffraction patterns upon heating. Figure 1a shows the $wd \leftrightarrow rw$ transition: all visible diffraction peaks of D13_S2_005 can be attributed to *wd*, and *wd* is the only stable phase at 1616 K, 20.6 GPa. In the next diffraction pattern, D13_S2_006, the *rw* peaks appeared in the heating cycle for the first time, and

---

Figure 4.1 *(following page)*: **In situ phase stability observations in Mg_2SiO_4 collected in LH-DAC experiments with synchrotron XRD from this study.** (a–b) Representative diffraction patterns from run D13 demonstrating the first appearance of the peaks of a new phase (marked by colored stars), from *wd* to *rw* (a), and then from *rw* to *bm* (+ *pe*) (b). All visible diffraction peaks of D13_S2_005 can be attributed to *wd*, including prominent peaks (040), (132), (152), (143), and (301), and minor peaks (211), (123), (240), (251) (?), (015), (341), (253), and (215), and *wd* is the only stable phase at 1616 K, 20.6 GPa. In D13_S2_006, the *rw* peaks appeared for the first time, (220), (400), and (341), and *wd* began transforming into *rw* at 1785 K, 21.0 GPa. The *rw* peaks of D13_S2_010 at 2052 K, 21.9 GPa continued to grow from D13_S2_006 at 1785 K, 21.0 GPa but became increasingly overlapped with the *wd* peaks at high temperatures (e.g., *wd* (040) and *rw* (220)). In D13_S2_011, the *bm* peaks appeared for the first time (112), (202), (311), (132), (024), and (320), and *rw* began transforming into *bm* (+ *pe*) at 2173 K, 22.2 GPa. All peaks are identified and labeled by (hkl). (c–k) *P*–*T* paths of phase stability observations in each experimental run (solid black line) with uncertainties (grey crosses). Phases are color coded as follow: *wd* in red, *rw* in blue, *bm* + *pe* in yellow.


a
wd → rw
Intensity (a.u.)
2θ (°)
rw peaks first appear
D13_S2_005 1616 K, 20.6 GPa
D13_S2_006 1785 K, 21.0 GPa
b
rw → bm + pe (with wd relics)
bm peaks first appear
D13_S2_010 2052 K, 21.9 GPa
D13_S2_011 2173 K, 22.2 GPa
c
D1m
compressing
spot 1
d
D2
spot 1
spot 2
spot 3
e
D4m
compressing
spot 1
f
D5
spot 1
spot 2
g
D6
bm+pe
rw
wd
path
spot 1
h
D10
spot 1
spot 2
spot 3
i
D11m
compressing and heating
spot 1
j
D13
spot 1
spot 2
k
D14
spot 1
spot 2
spot 3
Temperature (K)
Pressure (GPa)

wd began transforming into *rw* at 1785 K, 21.0 GPa. Fig. 4.1b shows the $rw \leftrightarrow bm + pe$ post-spinel transition near the triple point. Here, the *rw* peaks of D13_S2_010 at 2052 K, 21.9 GPa continued to grow from D13_S2_006 at 1785 K, 21.0 GPa but became increasingly overlapped with the *wd* peaks at high temperatures (e.g., *wd* (040) and *rw* (220)). In the next diffraction pattern, D13_S2_011, the *bm* peaks appeared in the heating cycle for the first time, and *rw* began transforming into *bm* (+ *pe*) at 2173 K, 22.2 GPa. The relics of the *wd* phase remained in the diffraction pattern, and a few peaks grew significantly (123) or reappeared (211) upon heating. The *pe* peaks were rarely found in the diffraction patterns at the first appearance of the *bm* peaks due to their overlap with silicate peaks. Additional details of phase identification and phase boundary detection can be found in Supplementary Text S2.

4.3 In Situ Phase Stability Observations in Mg_2SiO_4 Compiled From Literature and Their Pressure and Temperature Corrections

To compare our experimental observations (Section 2) with literature datasets, we searched and compiled all available in situ experimental data on the phase stability of *wd*, *rw*, and *bm*+*pe* available (Table C.2), corrected the temperatures and pressures originally reported in each study (Table C.3), and performed a comprehensive analysis of their inter-run and inter-lab uncertainties (Section 4). These previous in situ high-pressure experiments on Mg_2SiO_4 were conducted with either MA or DAC. Additional details of our data compilation can be found in Appendix C.3.

One source of discrepancy among the literature datasets is the use of different pressure scales (MgO, Au, Pt, etc.). Pressure estimates have often been incompatible with each other due to the lack of cross-calibrated equations of state (EoS) for those pressure scales used (e.g., Fei et al. 2007). Fortunately, most recent studies either reported the unit cell parameters of the pressure scales directly or provided the estimated pressure and the EoS references on which their pressure estimates were based. Therefore, we can recalculate the pressures based on some internally consistent pressure scales (Sokolova et al. 2016; Tateno et al. 2019).

Another source of discrepancy is the use of different temperature-measuring techniques: temperature is determined with a spectroradiometer in DAC experiments and with thermocouples in MA. Thermocouples provide higher precision temperature measurements (smaller random errors) than the spectroradiometer in the DAC experiment, but the pressure effects on the temperature–electromotive force (emf) relationship in commonly-used thermocouples had not been systematically investigated until very recently (Nishihara et al. 2020b,a). We used the two abovementioned studies published by Nishi hara and others to correct the nominal temperatures originally reported by the type D ($W_{97}Re_3$–$W_{75}Re_{25}$) and type S ($Pt_{90}Rh_{10}$–Pt) thermocouples from MA experiments. These models for thermocouple pressure effects were obtained at relatively low temperatures (<1173K), the temperature corrections we made here, therefore, are provisional (Table C.3).

4.4 Global Analysis of Phase Stability Observations in Mg_2SiO_4

4.4.1 Multi-Class Logistic Model for High Pressure Phase Diagram Determination

In principle, to precisely determine the location of a phase boundary from experiments, a pair of phase stability observations, one on each side of the boundary, would be required. However, such experimental brackets become increasingly difficult to obtain at higher pressures, and the results reported from different runs and different laboratories may not be fully consistent with each other. Thus far, most experimental studies determined the phase boundary based on free-hand drawing across their own experimental brackets, without quantitatively considering the inter-run and inter-lab uncertainties among the literature datasets. This common approach does not get a maximum of information from all the experimental constraints available for phase diagram determination, despite the fact that these high pressure experiments are often expensive and time-consuming; it also does not allow for a comprehensive assessment of the reliability and accuracy of the experimental datasets. Here, we proposed a machine learning framework for the global analysis of phase stability observations with multiple (more than two) stable phases or phase assemblage fields. This analytical methodology consists of multi-class logistic regression (this section) and supervised learning (Section 4.2). We performed a global analysis of the Mg_2SiO_4 phase diagram data, compiled from Section 4.2 and 4.3, as a case study to demonstrate our proposed analytical methodology for evaluating and selecting models for a phase diagram as well as estimating the uncertainties associated with each

phase boundary.

To build a statistical model to describe the stability fields of a high-pressure phase diagram, the response variable (stable phase) must be categorical instead of numerical, and hence determining the location of a phase boundary should be considered a "classification problem" (e.g., Bishop 2006; James et al. 2013) since it involves assigning the observations to one stable mineral phase (discrete and categorical response) at a specific P–T condition (numerical predictor). Kavner and Jeanloz (1998); Kavner et al. (2000) pioneered a similar but much simpler analysis of phase stability observations through binary logistic regression and tested it on the melting curve of platinum (Pt). However, their implementation 1) is limited to two stable phases with one phase boundary, 2) requires additional assumptions on the shape of the phase boundary, and 3) does not include necessary procedures to prevent overfitting. For the Mg_2SiO_4 phase diagram, with three stable phases or stability fields, wd, rw, and $bm + pe$ at transition zone conditions, we need to generalize the simple binary logistic model and estimate the probabilities of observing multiple stable phases, $\hat{p}(Y|P,T)$ simultaneously ($Y = k$, where k can be wd, rw, or $bm + pe$) at a given P–T condition. In the multi-class logistic model we propose here, the scenarios that Y belongs (or does not belong) to one specific phase stability field, k, can be modeled as:

$$\hat{p}(Y|P,T) = \begin{cases} 0 & \text{, if } Y = k \\ 1 & \text{, if } Y \neq k \end{cases} \tag{4.1}$$

To describe the probability that gives outputs between 0 and 1, we can write the probability of observing phase $Y = k$, $\hat{p}(Y = k|P,T)$ at a given P–T condition as a logistic function, $\frac{e^{f(X)}}{1+e^{f(X)}}$, where $f(X)$ is a nth degree polynomial function with two

variables, $f(P,T)$:

$$\hat{p}(Y=k|P,T)=\frac{e^{\sum_{i,j=0}^{n}\beta_{i,j}^{k}P^{i}T^{j}}}{1+e^{\sum_{i,j=0}^{n}\beta_{i,j}^{k}P^{i}T^{j}}} \tag{4.2}$$

Alternatively, Eq. 4.2 can be rewritten as:

$$\ln\frac{\hat{p}(Y=k|P,T)}{1-\hat{p}(Y=k|P,T)}=\ln\frac{\hat{p}(Y=k|P,T)}{\hat{p}(Y\neq k|P,T)}=\sum_{i,j=0}^{n}\beta_{i,j}^{k}P^{i}T^{j}=f(P,T) \tag{4.3}$$

The quantities $\ln\frac{\hat{p}(Y=k|P,T)}{\hat{p}(Y\neq k|P,T)}$ and $\ln\frac{\hat{p}(Y=k|P,T)}{1-\hat{p}(Y=k|P,T)}$ are called log-odds and logit, respectively. We can interpret the logistic model as fitting the log-odds or logit as a polynomial function of P and T, $f(P,T)$.

We can then convert probability estimates from three separate models (when k = wd, rw or $bm+pe$, $K=3$) to one set of probability estimates using a multi-class generalization of the logistic function, which is also known as the normalized exponential or the *softmax* function:

$$\hat{p}(Y=k|P,T)=\frac{e^{\sum_{i,j=0}^{n}\beta_{i,j}^{k}P^{i}T^{j}}}{\sum_{h=1}^{K}e^{\sum_{i,j=0}^{n}\beta_{i,j}^{h}P^{i}T^{j}}} \tag{4.4}$$

The rescaled probability estimates add up to 1. We attribute the stable phase as the class with the largest probability, and the tripe point is recovered at which $\hat{p}(Y=wd)=\hat{p}(Y=rw)=\hat{p}(Y=bm+pe)=\frac{1}{3}$. The coefficients, $\beta_{i,j}^{k}$, are estimated by minimizing a combined negative log-likelihood function, or total cross entropy, $-L$ (Bishop 2006):

$$-L=-\frac{1}{M}\sum_{m=1}^{M}\sum_{k=1}^{K}\left\{t_{m,k}(y_m=k)\cdot\ln\left[p_m(y_m=k)\right]+t_{m,l}(y\neq k)\cdot\ln\left[1-p_m(y_m\neq k)\right]\right\} \tag{4.5}$$

where $t_{m,l}(y_i=k)$ is 1 if and only if the observation m belongs to phase k , $p_m(y_m=k)$ is the output probability that the observation belongs to phase k, and vice versa; M is the total number of observations. Unlike the binary case (e.g., Kavner et al. 2000),

the multi-class logistic model does not produce a simple, easy-to-interpret analytic solution, therefore the phase boundaries between the three phases and their triple point in Mg_2SiO_4 are determined numerically with a Python package, scikit-learn (Pedregosa et al. 2011). A comprehensive review of the multi-class logistic model can be found in James et al. (2013).

4.4.2 Toward a Nonlinear Post-spinel Transition in Mg_2SiO_4

Thermodynamics of the Clapeyron Slope for the Post-spinel Transition

The Clapeyron slope of a coexistence curve, either a phase transition or a reaction, is uniquely determined by the entropy change (ΔS) of the phase transition/reaction divided by its volume change (ΔV); when P and T are constant and the change in the Gibbs free energy, $\Delta G_{P,T=\text{constant}} = 0$, we have $T\Delta S = \Delta H$, and then γ can be written as:

$$\gamma = \frac{\partial P}{\partial T} = \frac{\Delta S}{\Delta V} = \frac{\Delta H}{T\Delta V} \tag{4.6}$$

Previous studies (e.g., Ito and Takahashi 1989; Irifune et al. 1998; Shim et al. 2001; Katsura et al. 2003; Fei et al. 2004; Ishii et al. 2011; Ghosh et al. 2013) often adopted a linear approximation for the post-spinel transition in Mg_2SiO_4, with visual inspection and free-hand drawing. This assumption of a linear boundary was a reasonable choice, given the considerable inter-run and inter-lab uncertainties in existing experimental datasets and the lack of a robust statistical analysis; this linear assumption has often been justified by the semi-empirical interpretation that the changes in $\Delta S_{\text{post-spinel}}$ and $\Delta V_{\text{post-spinel}}$ along the reaction boundary between *rw* and *bm*+*pe* are small, gradual, and

comparable. However, if we take a closer look at recent empirical thermodynamic models of Mg_2SiO_4 that examined and extrapolated the low-temperature thermodynamic data carefully (e.g., Fabrichnaya 2008; Kojitani et al. 2016, 2017), some of their calculated transitions in Mg_2SiO_4, the post-spinel transition in particular, have a small but non-negligible nonlinearity. A recent first-principles calculation suggested an increasingly negative post-spinel Clapeyron slope in Mg_2SiO_4 with higher temperatures (Hernández et al. 2015). This predicted nonlinearity of the post-spinel transition implies that the thermal expansion coefficient (α_{rw}) of *rw* increases slower than that of bm (α_{bm}) and the volume difference between *rw* and *bm+pe* ($\Delta V_{\text{post-spinel}}$) would hence decrease with temperature (Hernández et al. 2015; Belmonte et al. 2022); assuming $\Delta S_{\text{post-spinel}}$ remains approximately constant, $\gamma_{\text{post-spinel}}$ is expected to become more negative with increasing temperature. Such nonlinearity may be small enough to be ignored if we are only interested in an averaged value for the Clapeyron slope within 100–200 K, and evidently, earlier studies indeed focused on bracketing the transition near 1700–1900 K, a temperature range only pertinent to warm slabs and the average temperature in ambient mantle across the "660-km" discontinuity. However, we need to take into account the nonlinearity of the post-spinel transition when we consider it across a range of several hundreds of kelvins because $\Delta V_{\text{post-spinel}}$ may change substantially over the entire mantle temperature range, from cold slabs to the ambient mantle and then to hot plumes. Chanyshev et al. (2022) have revisited the post-spinel transition recently with the state-of-the-art MA technique and reported the first experimental evidence of a nonlinear post-spinel transition. Its estimated nonlinearity, however, is based on the experimentalists' visual inspection and free-hand drawing only, the robustness of their reported Clapeyron slope and its compatibility with other experimental data needs to be

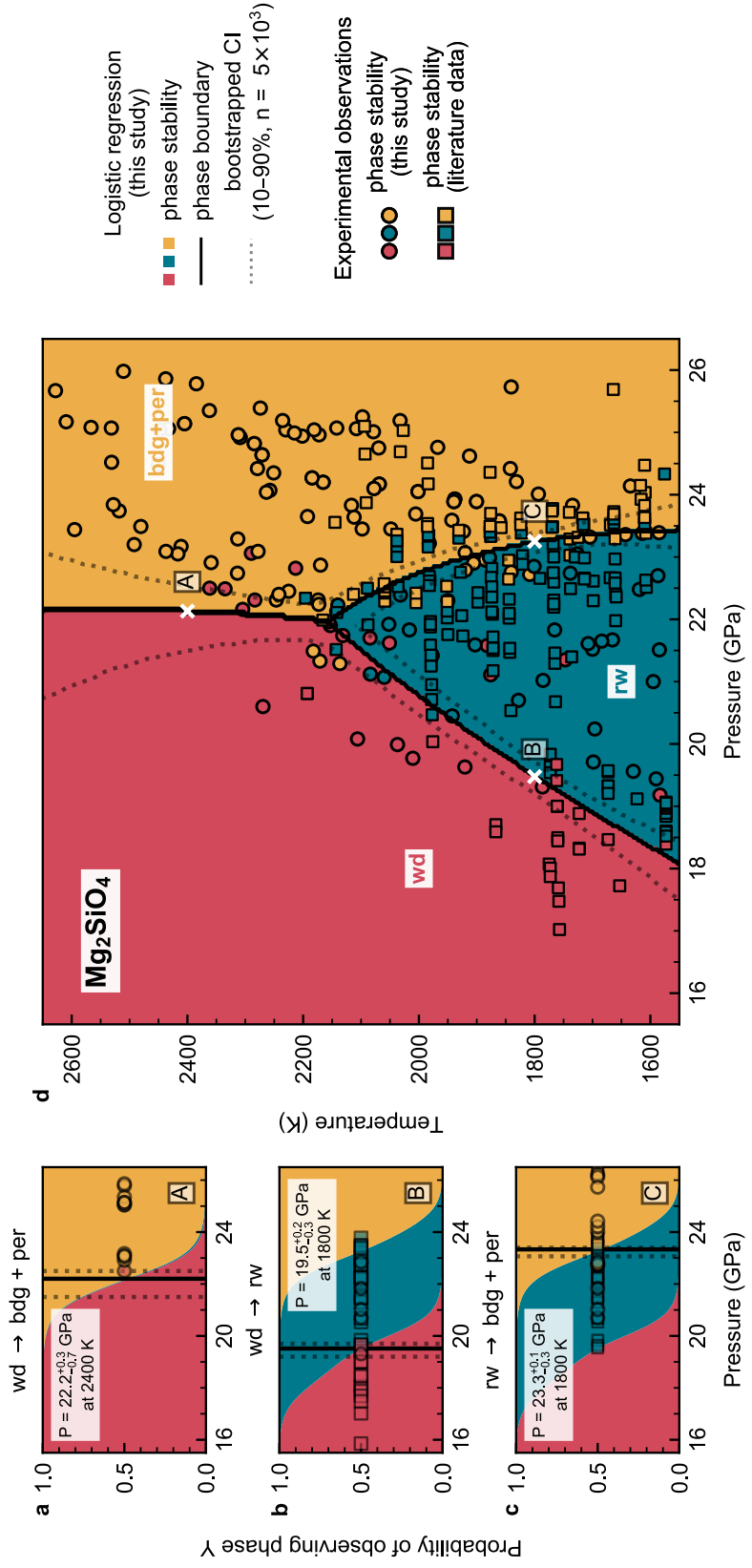
assessed.

A Machine Learning Framework for the Nonlinearity of Phase Boundary

In the multi-class logistic model we proposed for phase diagram determination in Section 4.1, a nonlinear phase boundary can be implemented in the log-odd/logit function (Eq. 4.3), and it is mathematically simplified as a polynomial function of P and T. Ideally, a phase boundary should be described by a function of thermoelastic properties such as thermal expansion coefficient, entropy, heat capacity, etc., which can then be converted into a function of pressure, temperature, and chemical composition. However, it would be cumbersome to obtain analytic approximation of these thermodynamic functions

---

Figure 4.2 *(following page)*: **Machine learned phase diagram of Mg_2SiO_4 at transition zone conditions.** (a–c) Probabilities of observing the (a) $wd \leftrightarrow bm + pe$, (b) $wd \leftrightarrow rw$, and (c) $rw \leftrightarrow bm + pe$ phase transition are predicted at (a) 2400 K and (b–c) 1800 K, respectively, with multiple logistic regression and supervised learning algorithms. Experimental observations made within 100 K of those prediction temperatures are shown with the predicted probability curves in (a–c). The phase transition pressure at the prediction temperature is the vertical solid line in each plot with uncertainties in the vertical grey dashed lines. (d) Phase stability fields of wd, rw and $bm + pe$ are predicted between 1500 and 2700 K and between 15 and 27 GPa with a bootstrapped confidence interval (CI) of 10–90% in the grey dashed lines. Experimental observations (circles: this study; squares: literature data) are shown with the predicted phase stability fields. P–T conditions for (a–c) are indicated by point A, B and C in (d) with a white cross. Phases are color coded as follow: wd in red, rw in blue, and $bm + pe$ in yellow.


Logistic regression
(this study)
phase stability
phase boundary
bootstrapped CI
(10–90%, n = 5×10³)
Experimental observations
phase stability
(this study)
phase stability
(literature data)
Mg2SiO4
bdg+per
wd
rw
A
B
C
d
Temperature (K)
Pressure (GPa)
a
wd → bdg + per
P = 22.2+0.3−0.7 GPa
at 2400 K
b
wd → rw
P = 19.5+0.2−0.3 GPa
at 1800 K
c
rw → bdg + per
P = 23.3+0.1−0.3 GPa
at 1800 K
Probability of observing phase γ

because such conversion would require solving a number of inexplicit functions in the EoS for each phase. For simplicity, we used polynomials (Eq. 4.3) to capture the nonlinearity of the phase boundary without the mathematical burdens to extract a complex analytic solution from physical thermodynamics directly.

Overfitting is often the primary argument against using a polynomial in regression models. The high degree of freedom we introduce to a conventional analysis would allow the model to capture not only the location of the phase boundary, but also the noise in the experimental dataset. As the degree of the polynomial keeps increasing, we would begin to fit a squiggle that matches more data points, despite the fact that only a smooth curve is expected for a phase boundary thermodynamically. On the contrary, this proposed machine learning framework is a robust way to identify the shape of a phase transition and to estimate its magnitude. Here, we applied a set of supervised learning algorithms from common machine learning practices to avoid overfitting, accompanied with regularization and bootstrapping: 1) we first split the compiled dataset into a train set and a test set (70% and 30%). The train set is further divided into k-fold (k = 3–5) for cross validation as well as (hyper-)parameter tuning to produce an optimized model for a series of polynomial functions with different degrees (n = 1–5), while the test set remained unseen to the models. Then, we used the test set to make the final selection of the best degree of polynomials based on the classification scores of the test set, F_1 score, a harmonic mean of precision and recall, where an F_1 score reaches its best value at 1 and worst score at 0. To further limit the behavior of the high-order polynomials, we applied L_1 regularization method (*lasso*) to allow the coefficients of some high-order terms to shrink to zero (truncation of high-order terms) when necessary. Finally, we used the selected model with the best degree of polynomials (regularized) to fit the entire

dataset (Fig. 4.2).

During model selection, we used grid search to exhaustively consider all parameter and hyperparameter combinations for the multi-class logistic model, including the degree of polynomials (n), regularization strength (C), and optimization solvers. The regularized 3rd order polynomial (with $C = 1000$ and some high-order terms truncated by L_1 regularization) is found to be the best model to describe the Mg_2SiO_4 phase diagram, with the highest F1 scores of 0.78 for the test set and 0.82 for the train set. In Fig. 4.3, the linear and 2nd order polynomial phase boundaries (polynomial with degrees 1 and 2) are insufficient to fit the training data (underfitting). For higher degrees, the models become stabilized but overfit the training data (with high F1 scores for the training data and lower F1 scores for the unseen testing data). Definitions and additional details of parameter tuning, regularization, and model selection can be found in Appendix C.4. A schematic diagram of the model selection procedures is shown in Fig. C.2; nevertheless, a full description of supervised learning algorithms cannot be done here as comprehensively as in textbooks, for example, James et al. (2013).

With the selected best model, we estimated the uncertainty in our predicted phase boundaries using bootstrapping. We resampled the compiled dataset with replacement (67%) and created 5×10^3 copies of the bootstrapped dataset. We then fit the best model to each resampled copy of the dataset, resulting in 5×10^3 sets of phase boundaries. We reported 10–90% confidence intervals of the simulated distributions as the allowed P–T regions (or uncertainty) for the phase boundaries.

Figure 4.3 *(following page)*: **Model selection and evaluation for the Mg_2SiO_4 phase diagram.** (a–e) Hyperparameter optimized predictions for phase stability fields of *wd*, *rw* and $bm + pe$ with different degree of polynomial functions (n = 1–5) using multi-class logistic model and supervised learning. Legend is the same as in Fig. 4.2. (f) Model performance (bias and variance measured by F1 score) as a function of degree of polynomials. As the degree of the polynomial function increases, the performance of the model over the train set (solid grey circles) increases continuously. On the other hand, the performance over the test set (solid black circles) increases initially but after degree 2 ($n = 3$), the classification score of the test set starts to decrease. Among the degree of the polynomial (n = 1–5) we tested in the study, $n = 3$ (highlighted in gold) is selected as the best parameter to balance the bias- variance trade-off in the model.

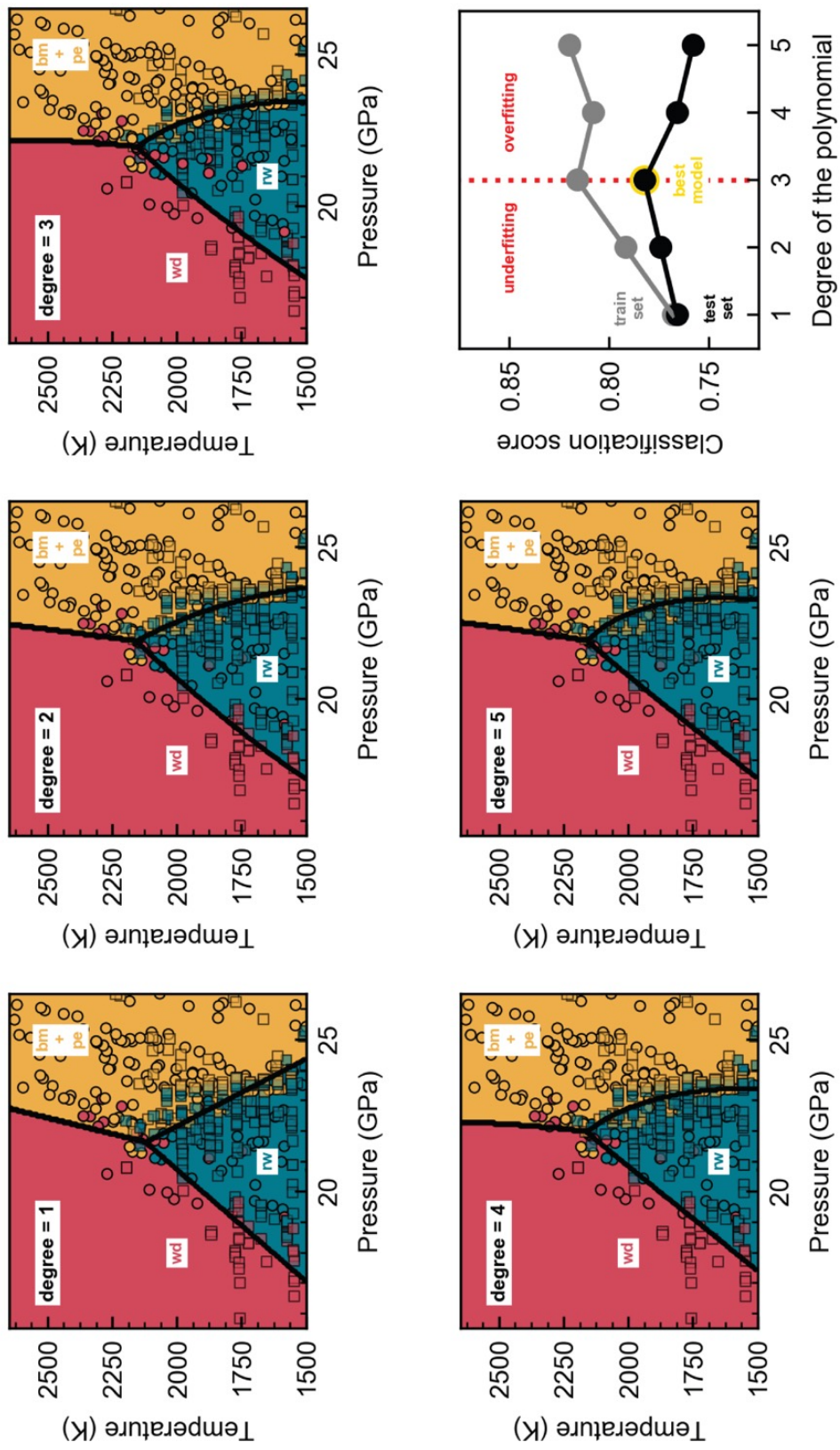
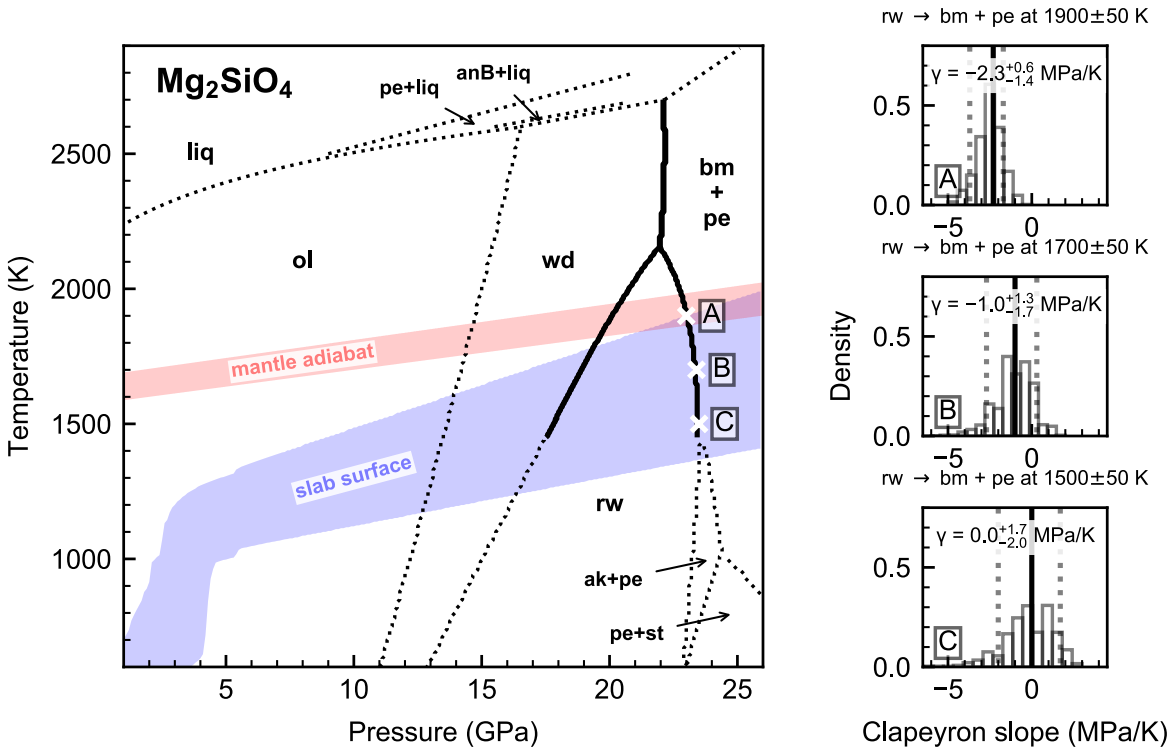

degree = 1
degree = 2
degree = 3
degree = 4
degree = 5
bm + pe
rw
wd
Temperature (K)
Pressure (GPa)
Classification score
Degree of the polynomial
underfitting
overfitting
best model
train set
test set

Figure 4.4 *(following page)*: **Temperature-dependent Clapeyron slope in the post-spinel transition in Mg_2SiO_4.** (a) Phase diagram for Mg_2SiO_4 up to 26 GPa. Three phase boundaries, $wd \leftrightarrow rw$, $wd \leftrightarrow bm + pe$, and $rw \leftrightarrow bm + pe$, at the transition zone conditions are statistically optimized from this study (solid black lines). The melting boundaries and the $ol \leftrightarrow wd$, $ak \leftrightarrow bm$, and $pe + st \leftrightarrow bm$ (dashed black lines) are adapted from Li et al. (2022) and Stixrude and Lithgow-Bertelloni (2022), respectively. (b–d) The distributions of the estimated Clapeyron slopes of the $rw \leftrightarrow bm+pe$ post-spinel transition at (b) 1900 K, (c) 1700 K, and (d) 1500 K are produced with bootstrap resampling (n = 5×10^3), and the local Clapeyron slope for the post-spinel transition is averaged within 50 K of its prediction temperatures (in the vertical solid line in each plot) with a bootstrapped confidence interval (CI) of 10–90% in the vertical grey dashed lines. P–T conditions for (b–d) are indicated by point A, B and C in (a) with a cross. The present-day ambient mantle adiabats were estimated based on Stixrude and Lithgow-Bertelloni (2011) with mantle potential temperatures between 1550–1650 K. The slab surface temperatures were extrapolated from a global compilation of subduction zone thermal models reported by Syracuse et al. (2010).


Mg2SiO4
pe+liq
anB+liq
liq
ol
wd
bm
+
pe
mantle adiabat
slab surface
rw
ak+pe
pe+st
A
B
C
Temperature (K)
Pressure (GPa)
rw → bm + pe at 1900±50 K
γ = −2.3+0.6−1.4 MPa/K
rw → bm + pe at 1700±50 K
γ = −1.0+1.3−1.7 MPa/K
rw → bm + pe at 1500±50 K
γ = 0.0+1.7−2.0 MPa/K
Density
Clapeyron slope (MPa/K)

4.4.3 Machine Learned Phase Diagram of Mg_2SiO_4 At Transition Zone Conditions

From the machine-learned phase diagram of Mg_2SiO_4 (Fig. 4.2), we found that the Clapeyron slope of the $rw \leftrightarrow bm + pe$ post-spinel transition varies locally from $-2.3^{+0.6}_{-1.4}$ MPa/K at 1900±50 K, to $-1.0^{+1.3}_{-1.7}$ MPa/K at 1700±50 K, and to $0.0^{+1.7}_{-2.0}$ MPa/K at 1500±50 K, and that the $wd \leftrightarrow rw$ boundary and the $wd \leftrightarrow bm + pe$ boundary are approximately linear, with estimated slopes of $6.2^{+1.6}_{-1.1}$ MPa/K at 1800±200 K and $0.4^{+1.8}_{-2.9}$ MPa/K at 2400±200 K, respectively (Fig. 4.2e–g,). The location of the triple point is estimated to be ∼22 GPa and ∼2155 K. The probabilities of observing each phase, $\hat{p}(Y|P,T)$, $k = wd$, rw, or $bm + pe$, are shown as a function of P with a constant T of 1800 K and 2400 K, respectively (Fig. 4.2a–c).

The nonlinear post-spinel boundary (more negative with increasing temperature) agrees visually with the corrected experimental data compilation (Fig. 4.2d). It is also in general consistent with that reported by Chanyshev et al. (2022); However, their post-spinel slope is on average slightly less negative (varies from 0.9 MPa/K at 2000 K to 0.1 MPa/K at temperatures <1700 K) and increasingly deviates from our estimate with increasing temperature. Except for Chanyshev et al. (2022) , all previous studies on the post-spinel transition assumed a linear boundary and determined it with visual inspection and free-hand drawing; hence those estimates are incommensurate with the nonlinear post-spinel Clapeyron slope we reported here. Nevertheless, we performed additional tests on the literature data using the simple binary logistic model with a linear boundary for benchmarking the methodology with these previous studies. A more detailed discussion on the comparison can be found in Appendix C.5 and Figs. C.3–C.5.

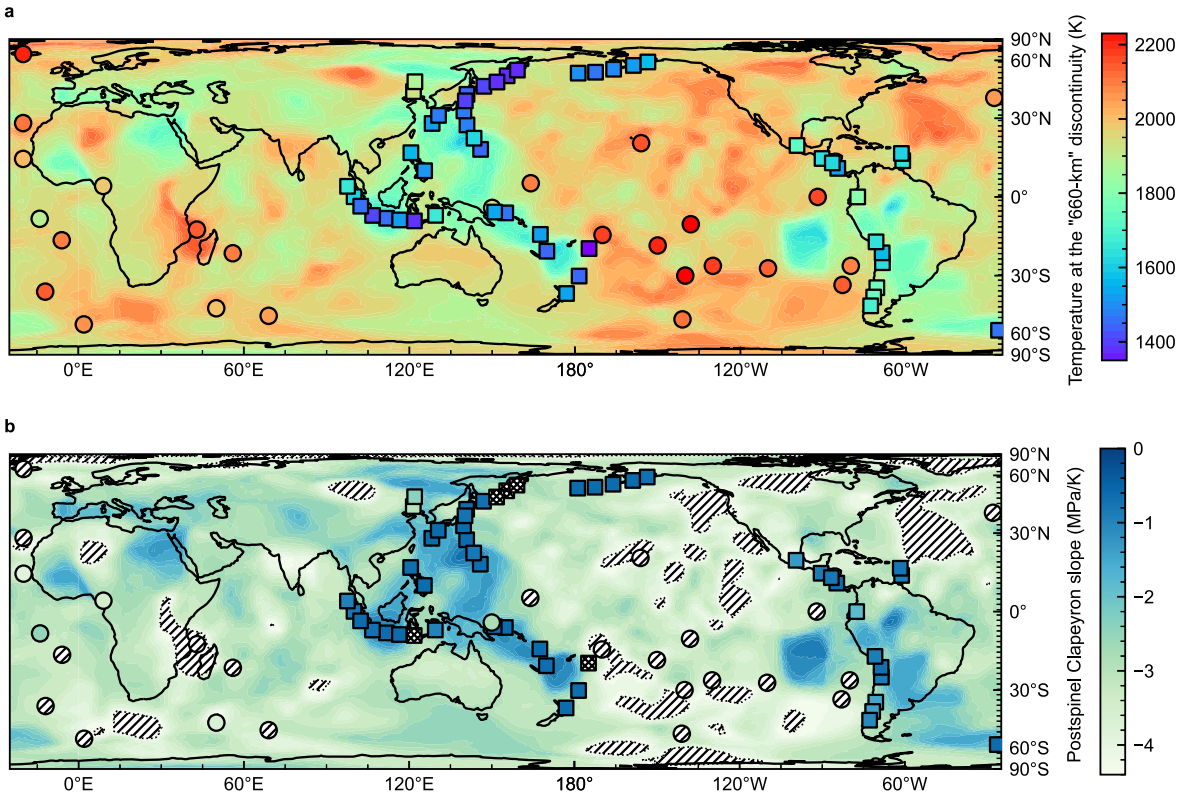
The $rw \leftrightarrow bm + pe$ post-spinel boundary has a considerable nonlinearity while the $wd \leftrightarrow rw$ boundary remains virtually constant over the same temperature range. This marked difference is generally consistent with the temperature- and pressure-dependent thermal expansivity trends in the Mg_2SiO_4 polymorphs, and more specifically, the divergent trends in $\Delta V_{wd \leftrightarrow rw}$ and $\Delta V_{\text{post-spinel}}$: 1) α_{rw} and α_{wd} increase at a similar rate with increasing temperature but α_{rw} increases slower than α_{bm} at high temperatures (Hernández et al. 2015); 2) the temperature-dependent thermal expansivity in rw becomes more pronounced at higher pressures (Belmonte et al. 2022). Therefore, $\Delta V_{wd \leftrightarrow rw}$ is expected to vary much less than $\Delta V_{\text{post-spinel}}$ at their relevant P–T conditions. In the meantime, the shape of the $wd \leftrightarrow bm + pe$ boundary remains underdetermined because the experimental constraints on the fields of wd and $bm + pe$ above the triple point remain sparse. Our global analysis with regularization/model selection chose a relatively simple linear boundary for the $wd \leftrightarrow bm + pe$ boundary when the data is insufficient to fit a more complex, nonlinear boundary, and it demonstrates the effectiveness of our proposed machine learning framework in avoiding overfitting.

The major limitation of all previous studies is that they focused on determining one phase boundary at a time: for example, if the primary task of the study was to determine the $rw \leftrightarrow bm + pe$ post-spinel boundary, the information contained in the phase stability observations of wd was typically ignored. The analytical methodology we proposed here concerns the exact opposite, and the task of determining the $wd \leftrightarrow rw$ and $wd \leftrightarrow bm + pe$ boundaries is not ancillary to determining the post-spinel boundary—the two tasks are one and the same. In other words, the post-spinel boundary here is statistically optimized from and consistent with the phase stability observations of all three phases/phase assemblages around the corresponding triple point, not just a simple

inversion of the phase observations of rw and $bm + pe$ only.

Last but not least, our discussion is so far limited to determining the Mg_2SiO_4 phase diagram. However, this analytical methodology with multi-class logistic regression and supervised learning can be applied generally to the inversion of any phase diagram data (e.g., P–T, P–X, T–X, etc.). Many widely-used thermodynamic datasets for modeling the Earth's mantle followed the general strategy in selecting the minimal possible set of phase stability studies that constrain the relevant phase diagrams based on least-squares inversions (Holland and Powell 1990; Stixrude and Lithgow-Bertelloni 2011). Such approach is susceptible to significant errors if the experimental dataset selected a posteriori were systematically biased. In addition, the least-squares fits used to create the abovementioned databases are unstable with the presence of experimental outliers. Our proposed analytical methodology can get a maximum of information from all existing phase diagram data without overfitting them and is less susceptible to both systematic bias and significant outliers, which help improve our ability to directly estimate thermodynamic quantities (such as high-temperature entropy) for which experimental measurements do not exist from the relevant phase boundaries, as well as to indirectly invert other thermochemical parameters (e.g., free energy, characteristic vibrational temperature, interaction parameters).

Figure 4.5 *(following page)*: **Global mapping of mantle temperature and post-spinel Clapeyron slope at the "660-km" discontinuity with superimposed subducting slabs and plume-fed hotspots locations.** (a) Composite temperature map of the "660-km" discontinuity for ambient mantle (color-coded background, based on globally compiled S660S observations from Waszek et al. (2021), subducting slabs (color-coded square, based on 2D kinematic models from Syracuse et al. (2010) and plume-fed hotspots (color-coded circle, based on global shear velocity constraints from Bao et al. (2022) The temperature variation patterns in these three independently constrained thermal models are consistent with each other; for example, temperature is the lowest around the Western Pacific subduction zones while the plume-fed hotspots coincide with the positive T660 anomalies in the ambient mantle. (b) Composite post-spinel Clapeyron slope map of the "660-km" discontinuity based on the nonlinearity of the post-spinel transition (Fig. 4.4 and Fig. C.5 from this study). A more negative post-spinel Clapeyron slope would produce stronger hindrance to the passage of mantle flow, both upwelling and downwelling. The subducting slabs (colored square) and plume-fed hotspots (colored circle) dominated by the post-spinel transition are color-coded based on the magnitude of Clapeyron slope, while those dominated by the $rw \leftrightarrow ak+pe$ transition (<1400 K in slabs) and post-garnet transition (>2050 K in plumes) are highlighted with hatched square and circle, respectively. Lateral variations of the post-spinel Clapeyron slope at the "660-km" discontinuity in the ambient mantle are shown as the color-coded background, and the potential regions of the ambient mantle influenced by the post-garnet transition (>2050 K) are hatched and outlined in thin dotted black lines. The name and location of each subducting slabs or plume-fed hotspot are listed with its post-spinel Clapeyron slope in Tables C.5–C.6.


a
90°N
60°N
30°N
0°
30°S
60°S
90°S
0°E
60°E
120°E
180°
120°W
60°W
Temperature at the "660-km" discontinuity (K)
2200
2000
1800
1600
1400
b
Postspinel Clapeyron slope (MPa/K)
0
−1
−2
−3
−4

4.5 Mantle Expression of Nonlinear Postspinel Boundary in Slabs and Plumes Worldwide

Our understanding of how phase transition Clapeyron slopes interact with mantle flow, both upwelling and downwelling, can be briefly summarized as follows: an endothermic transition/reaction with negative Clapeyron slope (latent heat is absorbed, i.e., $\Delta H > 0$ in (Eq. 4.6) impedes the passage of mantle flow, whereas an exothermic transition/reaction with positive Clapeyron slope ($\Delta H < 0$) enhances it (e.g., Christensen 1995). In particular, the endothermic post-spinel transition can cause localized and transient deflection to downwelling slabs and upwelling plumes. In this section, we explored the mantle expression of the nonlinearity of the post-spinel transition. First, we assembled a composite temperature map of the "660-km" discontinuity (referred to as T660) that includes individual slabs and plumes across the globe as well the ambient mantle (Fig. 4.5a). For consistency, T660 is defined as the temperature at 23 GPa (slightly shallower than the depth where the post-spinel transition is expected to occur) along the adiabatic geotherm of its respective mantle potential temperature (T_{p}). We derived the lateral variations in T660 from the T_{p} estimates based on 2D kinematic models for subducting slabs (Syracuse et al. 2010), global shear velocity constraints for plume-fed hotspots (Bao et al. 2022), and globally compiled S660S observations for the ambient mantle (Waszek et al. 2021). Further details of this composite T660 model can be found in Appendix C.6. The mantle temperature variation patterns in these three independently-constrained thermal models are consistent with each other; for example, mantle temperature is the lowest around the Western Pacific subduction zones while the plume-fed hotspots coincide with the positive T660 anomalies in the ambient mantle.

The ambient mantle has a global average T660 of 1955±74 K (one standard deviation, same hereafter). The post-spinel transition is the predominant bm-forming reaction when T660 is between 1400 K and 2050 K near 23 GPa (Stixrude and Lithgow-Bertelloni 2011). The "660-km" seismic discontinuity coincides with the post-spinel transition, and it contains the sharpest changes in seismic properties. Equally significant changes in temperature, rheology, and buoyancy are also accompanied by the post-spinel transition. The Clapeyron slope of the post-spinel transition, $\gamma_{\text{post-spinel}}$, hence, becomes one of the most important constraints on mantle convection.

A nonlinear post-spinel transition means that its Clapeyron slope is temperature dependent. To visualize this, we produced a global map of post-spinel Clapeyron slope at the "660-km" discontinuity (Fig. 4.5b) based on the composite T660 map where the post-spinel transition is predominant (Fig. 4.5a). The ambient mantle has a global average $\gamma_{\text{post-spinel}}$ of –3.1±0.6 MPa/K (∼91% of the total surface of the "660-km" layer), which is consistent with the seismically derived post-spinel Clapeyron slope of ∼–3 MPa/ K for the ambient mantle structure of the western half of the continental U.S. (Tauzin and Ricard 2014). The slabs accompanied by the post-spinel transition have an average T660 of 1569±125 K and an average $\gamma_{\text{post-spinel}}$ of –0.9±0.5 MPa/K (45 of 50 slabs considered here), while the hotspot-associated plumes have an average T660 of 2030±71 K and an average $\gamma_{\text{post-spinel}}$ slope of –3.3±0.6 MPa/K (5 of 26 plume-fed hotpots considered here). We found that the post-spinel Clapeyron slopes associated with the plumes (upwelling) are nearly three times more negative than those associated with the slabs (downwelling).

The temperature-dependent post-spinel Clapeyron slope renders a varying degree of hindrance to subducting slabs. Qualitatively speaking, the majority of the subducting

slabs are cold (mostly clustered around the West Pacific with T660 = 1400-1600 K) and have a slightly negative post-spinel Clapeyron slope of –0.6—0.7 MPa/K; these cold slabs are expected to encounter little to moderate hinderance from the post-spinel transition across the "660-km" depth. On the contrary, several hot slabs near Colombia/Ecuador (T660 = ∼1810 K), Central Cascadia (T660 = ∼1880 K), and North Cascadia (T660 = 1930 K) have much more negative post-spinel Clapeyron slopes of –1.8—2.9 MPa/K and are expected to encounter much greater hinderance to subduction from the post-spinel transition. We caution that any quantitative interpretation of the observed morphologies of subducting slabs must take into account other factors including (1) the viscosity and/or compositional contrasts between the upper and lower mantle and (2) the configuration and subduction history of the specific subduction zone (e.g., shape, strength trench motion) (e.g., Goes et al. 2017). Therefore, we advocate a reassessment of global subduction zone dynamics with the temperature-dependent post-spinel Clapeyron slope, which would help elucidate the diverse range of observed slab morphologies: some slabs remain neutrally buoyant temporarily (stagnation) at the base of the transition zone while others penetrate the lower mantle. Furthermore, if we consider the temporal evolution of one single slab, the effects of rheology and buoyancy driven by the temperature-dependent post-spinel transition may vary its dynamics and morphology over its lifetime as the slab becomes thermally equilibrated with the surrounding ambient mantle.

For the hotspot-associated mantle plumes accompanied primarily by the post-spinel transition near the "660-km" depth (T660 = 1870–2050 K in the compilation of global volcanic hotspots by Bao et al. (2022), 5 plumes in total considered here), the post-spinel Clapeyron slope is estimated to range from –2.5 MPa/K at T660 = 1890 K (Ascension)

to –3.8 MPa/K at T660 = 2010 K (Cape Verde). According to geodynamic modeling (e.g., Bossmann and Keken 2013), the post-spinel transition tends to trap plume heads at $\gamma = <\sim$–3.4 MPa/K while plumes ascend into the upper mantle at $\gamma = >\sim$–2.8 MPa/K; ring-shaped secondary plumes may form when γ is between –3.4 and –2.8 MPa/K. Therefore, the "660 km" depth is expected to hinder the passage of three post-spinel dominated plumes, Cameroon ($\gamma_{\text{post-spinel}}$ = –3.5 MPa/K at T660 = 1980 K), Crozet ($\gamma_{\text{post-spinel}}$ = –3.6 MPa/K at T660 = ∼1995 K), and Cape Verde ($\gamma_{\text{post-spinel}}$ = –3.8 MPa/K at T660 = ∼2010 K); while the plumes in two locations, Ascension ($\gamma_{\text{post-spinel}}$ = –2.5 MPa/K at T660 = ∼1890 K) and Manus Basin ($\gamma_{\text{post-spinel}}$ = –2.8 MPa/K at T660 = ∼1920 K), ascend across the "660 km" depth without much impediment. In addition, the dynamic topography of large igneous provinces above the post-spinel dominated plumes is influenced by $\gamma_{\text{post-spinel}}$ and can be used to estimate the T660: the dynamic subsidence decreases and lasts shorter as γ becomes more positive, from 100 m and 14 Ma at γ = –3.0 MPa/K to 200 m and 20 Ma at γ = –3.2 MPa/K ((Leng and Zhong 2010), and such change in surface subsidence can be attributed to a difference of 20 K in mantle temperature (from 1940 to 1960 K).

If the Earth's mantle is made of the simplified Mg_2SiO_4 system only, a *bm*-forming reaction, $wd \leftrightarrow bm + pe$ with the Clapeyron slope of ∼0 MPa/K, would replace the post-spinel transition when T660 is above ∼2155 K (above the *wd–rw–bm/pe* triple point). In a more realistic mantle composition (e.g., pyrolite), however, wd becomes increasingly less stable than majorite garnet (*gt*) (Stixrude and Lithgow-Bertelloni 2011). The post-garnet transition, $gt \leftrightarrow bm$, rather than the post-spinel transition or the $wd \leftrightarrow bm + pe$ transition, is expected to dominate some hotspot locations (hatched symbols in Fig. 4.5b) where T660 is above ∼2050 K (Stixrude and Lithgow-Bertelloni

2011), such as the Eastern and Southern Pacific; it is expected to affect less than 2% of the total surface of the "660-km" depth of the ambient mantle (hatched areas in Fig. 5b, the areal fraction distorted visually due to projection). This post-garnet transition is analogous to the one in the $MgSiO_3$ system and displays a positive Clapeyron slope of 1–4 MPa/K (e.g., Hirose 2002; Ishii et al. 2011), with opposite sign to the post-spinel transition; the magnitude of the post-garnet Clapeyron slope currently remains underdetermined by existing experimental constraints.

Another *bm*-forming reaction, *akimotoite* (ak) $\leftrightarrow$ bm may replace the post-spinel transition in a small number of extremely cold slabs when T660 is below 1400 K, such as Tonga (T660 = $\sim$1320 K) as well as Kamchatka, Kurile, and West Banda Sea (T660 = $\sim$1380 K). The presence of $ak \leftrightarrow bm$ has been seismically observed in the coldest Tonga slab. The $rw \leftrightarrow ak + pe$ transition in Mg_2SiO_4 is nearly identical to the same transition in pyrolite and has a negative Clapeyron slope of -8.1 MPa/K at low temperatures up to 1300 K (Chanyshev et al. 2022) and hence significantly hinder the passage of subducting slabs towards the lower mantle. The extremely cold condition for the $ak \leftrightarrow bm$ transition is unlikely to be present in the ambient mantle today based on our temperature estimates.

The global map of lateral variations in the post-spinel Clapeyron slope along with the identified regions of the post-garnet and $rw \leftrightarrow ak + pe$ transitions provides a spatial guide for us to study subducting slabs and hotpot-associated plumes worldwide (buoyancy-driven, active upwelling and downwelling) in their specific Clapeyron slope magnitude. In addition, the temperature-dependent post-spinel Clapeyron slope also permits a varying degree of convective layering and hence an evolving temperature contrast across the "660-km" depth through time. These nonlinear effects ultimately

depend on T660 and remain virtually unexplored in geodynamical models. It is therefore critical to model the thermal and dynamical evolution of slabs, plumes and the ambient mantle consistent with the temperature-dependent post-spinel Clapeyron slope.

4.6 Summary and Conclusions

The phase diagrams of mantle minerals have been investigated experimentally in the past several decades thanks to developments in high pressure techniques. Of these, the Mg_2SiO_4 phase diagram is the most extensively studied, because the Clapeyron slope of its post-spinel boundary represents one of the most important constraints on mantle dynamics. Yet the existing experimental datasets on the Mg_2SiO_4 phase diagram still show notable discrepancies in the location and Clapeyron slope of the post-spinel transition as well as the triple point of *wd*, *rw*, and *bm* + *pe*. The lack of rigorous analysis on inter-run and inter-lab uncertainties in the experimental results has motivated us to develop a machine learning framework with multi-class logistical regression and supervised learning algorithms for the determination of high-pressure phase diagrams. As a proof of concept, we have applied such analytical methodology to the Mg_2SiO_4 phase diagram data, including the new dataset reported by this study and previously-published datasets with redetermined P and T. Among our findings are that the post-spinel Clapeyron slope varies locally from $-2.3^{+0.6}_{-1.4}$ MPa/K at 1900±50 K, to $-1.0^{+1.3}_{-1.7}$ MPa/K at 1700±50 K, and to $0.0^{+1.7}_{-2.0}$ MPa/K at 1500±50 K and that the location of the triple point is statistically optimized at ∼22 GPa and ∼2155 K. Our proposed analytical methodology with machine learning can be applied generally for data inversion in phase diagram data and provides a tool to accurately predict thermodynamic

modeling parameters.

Most importantly, the polymorphic phase transitions and solid-state reactions in Mg_2SiO_4 have been historically conceived to be linear, but we found that the post-spinel boundary is noticeably nonlinear and its Clapeyron slope temperature dependent. To explore the mantle expression of the nonlinearity, we first presented a composite temperature map of the "660-km" discontinuity with which the post-spinel transition coincides and then estimated the lateral variation of the post-spinel Clapeyron slope, in subducting slabs and hotpot-associated plumes worldwide, as well as most of the ambient mantle. The nonlinearity of the post-spinel transition shifts our conceptual scheme of its role in mantle convection: its geodynamical effects are temperature dependent and the existing models of mantle flow across the "660-km" discontinuity, both upwelling and downwelling, need to be reassessed with the temperature-dependent Clapeyron slope.

Acknowledgments

J. Dong was supported by a James Mills Peirce Fellowship from the Graduate School of Arts and Sciences at Harvard University. R. A. Fischer was supported by the Henry Luce Foundation. L.P. Stixrude was supported by the National Science Foundation (EAR-1853388). M.C. Brennan was supported by a National Science Foundation Graduate Research Fellowship (DGE-1745303). We thank Andrew J. Campbell for loaning us the use of his short symmetric cell for a portion of these gas membrane experiments. The experimental part of this work was performed at GeoSoilEnviroCARS (Sector 13) and HPCAT (Sector 16), Advanced Photon Source (APS), Argonne National Laboratory. The Advanced Photon Source is a U.S. Department of Energy (DOE) Office

of Science User Facility operated for the DOE Office of Science by Argonne National Laboratory under Contract No. DE-AC02-06CH11357. GeoSoilEnviroCARS is supported by the National Science Foundation (EAR – 1634415) and DOE (DE-FG02-94ER14466). HPCAT operations are supported by the National Nuclear Security Administration (DOE-NNSA)'s Office of Experimental Sciences. The data analysis part of this work was inspired by a Harvard class, CS109a: Introduction to Data Science, taught by Pavlos Protopapas, Kevin A. Rader, and Chris Tanner in Fall 2020, and this work benefited from its course materials.

Chapter 5

Afterword: A Critical Reflection

> *A building is not finished when its foundation is laid; and just as little is the attainment of a general notion of a whole the whole itself. [...] In the same way, science, the crowning glory of a spiritual world, is not found complete in its initial stages.*
>
> —G. W. F. Hegel, *The Phenomenology of Spirit*

5.1 The Case for a Flooded Early Earth

Paul Voosen has written a news article in *Science* discussing our research presented in Chapter 2, which focuses on the evidence for Archean "water worlds"—an early Earth with completely submerged continents (Voosen 2021; Dong et al. 2021). While I won't go into the geological evidence for this hypothesis in this section, you can find a comprehensive summary in my Chapter 2 or in Paul's article, which explains it in plain

language. Instead, I'll provide a conceptual analysis of the term "water world" through a series of thought experiments, even if some might dismiss them as mere speculation. My goal is not to argue that any of the conjectures I present are definitively correct. Instead, my goal is to outline my thoughts on the interplay between water and land on the early Earth's surface, and to explore possible ways to test these ideas in the future, whenever possible.

Paul and I used the term "water worlds" to describe a rocky planet that has a significant amount of water on its surface, even though water is only a small percentage of its total mass. This water forms a thin layer that covers all the rocky layers. In my Chapter 2, I explore some possible configurations of early Earth's oceans and continents that could lead to an Archean water world. However, since we don't know much about the Archean Earth, such as whether there were continents, the density of the crust and mantle, or the height of its mountains, I had to make some assumptions to create a quantitative model. I followed the approach of Flament et al. (2008); Korenaga et al. (2017), who used a modified version of modern hypsometry to represent the early Earth's surface. While this approach may not accurately represent the actual surface of the Archean Earth, it is still useful for generating insights. The fact that this model is admittedly flawed makes it profoundly heuristic—it helps us understand the concept of "water worlds" and the factors that might lead to their formation.

In Chapter 2, I presented an Archean Earth configuration that imposed a dichotomy between the oceanic and continental columns. This model included implicit assumptions about the existence of a differentiated continental crust and, to some extent, a subduction-driven plate tectonic system, which was necessary to create the oceanic basins in the model. It is important to note, however, that none of these assumptions

have been confirmed for the early Earth. In the following thought experiments, we will explore what might happen if we deviate from these implicit assumptions, which could be problematic.

Let's start by considering an extreme hypothetical scenario where there is no dichotomy in the Earth's crust. Instead of having a lighter continental column and a denser oceanic column creating the topographic relief that forms the ocean basins, we'll imagine a uniform layer of mafic crust covering the Earth's surface. In this case, we wouldn't need much water to flood the surface of a rocky planet. Unlike today's Earth, where water must fill the ocean basins before it can reach the land, we could easily cover the Earth with a thin layer of water without ocean basins due to the density contrast between the oceanic and continental columns. This hypothetical scenario is not factual, but it illustrates how little water is needed to create a "water world" planet. This thought experiment also shows that determining whether the surface of a rocky planet is covered by water is not as simple as having more water. It involves finding the right balance between the amount of water on the surface and the amount of topographic relief that the density contrast within the crust can support to sustain an ocean basin.

Let's then examine the hypothetical case of a uniform mafic crust and explore its inaccuracies and insights. To physically have a uniform global mafic crust, the crust would have to have a uniform density. This would have been a challenge for the early Earth. Some argue that the continental crust was more mafic in the Archean than it is today, which would result in similar densities for the oceanic and continental columns. However, this is only true if the temperature is constant.

Therefore, we need to further investigate the temperature of the early Earth. In

modeling Earth's thermal history, we tend to simplify and construct a 0-D model as a function of time. While this theoretical representation is essential for understanding planetary cooling, it is inadequate for capturing the spatial distribution of mantle temperature and how these changes have affected the temperature of the continental and oceanic columns. The temperature distribution is not the average calculated in the model; it was quite heterogeneous.

Today, the Earth's interior has large lower mantle structures that cannot be explained by temperature anomalies alone. In addition, there are hotspots and large igneous provinces that are significantly hotter than the average mantle. Considering this complex 3-D view of temperature distribution inside the Earth, the solid mantle temperature of the early Earth may have been even more heterogeneous, resembling the "heat pipe" Earth that other researchers have proposed (Moore and Webb 2013). Now, one may ask, "why does this temperature matter?"

Let's return to the hypothetical case where the Earth has a uniform density mafic crust. The heat pipe scenario suggests that a uniform density crust is impossible to achieve due to temperature differences. Even if the composition is the same, some parts of the Earth's crust would become hotter and lighter. This excess heat not only heats the mafic crust, but also melts it. The resulting silica-enriched melt would move upward and form a slightly lighter crust, resembling oceanic islands or plateaus with distinct topographic features. An important caveat here is that these melts are not necessarily immediately light enough to be considered felsic.

Let's bring water back into the discussion. Imagine that the Earth initially had enough water on its surface to form a thin layer of water and an ocean over a crust that

was mostly uniform in density. In some areas, excessive heat would cause the crust to lighten and even melt, causing the crust to rise. This seems to be a plausible physical account of what might have happened. The total amount of water on the Earth's surface then becomes relevant again, as it would determine how long it would take for these areas of lighter crust and higher topography to rise out of the water.

Our conclusion in Chapter 2 about the Archean ocean is significant regardless of the surface continents we assume. A vast ocean would make it difficult for continents to rise above the water, which provides another valuable insight: the formation and growth of the initial continents may be different from their eventual emergence from the water. The question that remains is, what geochemical signatures could we look for to distinguish these two events? This fascinating challenge is left to our almighty geologist colleague to find a rock in the field.

5.2 A Wider View of Water Worlds

In the last year of my Ph.D., my interest shifted to a different type of "water world" that has been gaining attention in the exoplanet community. Thanks to more precise radius and mass measurements provided by telescopes in space and on the ground, a growing number of planets have been found to have densities lighter than rock but denser than pure gas. At present, their structure is still uncertain, as these planets are presumed to be composed of rocky layers and H_2/He, or to have a thick water shell with rocky layers. The constraints we have on their mass and radius are not sufficient to resolve this uncertainty at this time. However, we can still consider potential testable hypotheses that may allow us to rule out some cases with observations in the near future.

Planetary scientists and astronomers have been investigating the formation mechanisms for these planets, which is one direction to differentiate water worlds and sub-Neptunes—focusing on testing the proposed mechanisms to form the "radius valley" that separates conventional terrestrial-type planets from the lighter water-rich or sub-Neptunes on the other side. For water worlds, it has been proposed that sub-Neptunes form outside the water-ice line of the protoplanetary disc and migrate inside in orbits where their gas shells are blown off, resulting in the formation of water worlds. However, since I do not study orbital dynamics, I will not speculate further on the formation of these planets.

Another direction of distinguishing water worlds and sub-Neptunes that has not yet been sufficiently explored by planetary scientists is from the perspective of material properties and the type of structure that makes the most sense for these planets. For the sake of simplicity, the majority of the exoplanet community treats sub-Neptunes and water worlds as two distinct species—one with a gas envelope and a rocky core, and the other with a water envelope and a rocky core. However, if they were to examine what we have in the solar system, namely Uranus and Neptune, they would see that neither falls into either of these categories. In fact, Uranus has a transition from a layer of gas, to a layer of ice and water, to a rocky core. Of course, we will not know for sure until NASA's next flagship mission to Uranus.

Uranus is essentially a hybrid of a sub-Neptune and a water world, which has been a topic of interest for many. In the simplest picture astronomers have of these planets, they have layered structures with distinct boundaries, one layer of gas/water and one layer of rock. They use equations of state for H_2/H_2O and $MgSiO_3$ to build interior structures. However, these mock planets are quite inaccurate in the eyes of any

high-pressure physicist studying these materials. As pressure increases, especially in the megabar range, the valence electrons that define the chemical behavior of an element are squeezed into a small space, and electron degeneracy becomes more pronounced, rendering the chemical distinctiveness of these species less and less significant. The macroscopic manifestation of this is that the miscibility of these chemical species, which is distinct at ambient pressure, becomes much higher—gas will mix with water and water with rock.

From the point of view of material properties, the arbitrary boundary between sub-Neptunes and water worlds becomes quite unnecessary. Astronomers often use the mass-radius relation to determine the structure of exoplanets with observed masses and radii. However, the problem is that these lines, derived from pure H_2O or pure $MgSiO_3$, are unlikely to be informative in determining the structure of these planets. In fact, it's more accurate to say that a pure water or rock layer probably doesn't exist anywhere, but rather in some new phases whose chemical composition is a mixture of both.

It would be challenging, but not impossible, to use quantum mechanical simulations such as DFT to build a unit cell of some combination of atoms with this mixture and test its stability. However, DFT has the fallacy of not always predicting the stable phase. One possible solution to this problem would be to look to the ice giants, inclduing Uranus, in our solar system. If the upcoming ice giant mission takes a polar orbit, as the Juno mission did for Jupiter, we would soon get a moment of inertia measurement that will give us much better constraints on the density distribution in ice giants (Movshovitz and Fortney 2022). We would know at the first order whether the water-rock layer is continuous or has a sharp boundary.

Such a discovery would have profound implications for Uranus as well as exoplanets. If the boundary is distinct, with water, then ice, and then rock layers, there will be a thermal boundary between water and ice that traps significant heat inside the planet. Alternatively, if the water/ice and rock layers form a more continuous profile in density, we might expect to see something that looks more like a double-diffusive connection, such as something we see in our ocean or inside Jupiter, sustained by this gradient. Once we distinguish between these two scenarios, we can compare the density to the density of the ice-rock mix phase we found in DFT and significantly narrow down which mineral/phase is actually allowed in Uranus and more broadly speaking, in sub-Neptunes or water worlds.

This may seem like a tangent, but it is actually an essential step in understanding exoplanet structures. Just as climate models often use incorrect scaling laws to describe raindrops and clouds, many exoplanet models use oversimplified equations of state to approximate the internal structures of these planets. To truly understand these exoplanets and how their structures differ from one another, we need to dig deeper and study the microphysics of the materials that actually exist inside them and how they change with depth and temperature over time.

Many of the ideas presented here about this different kind of water world were derived from many insightful conversations I had with Lars and Robin. In the spring of 2023, Planetary Journal Club (PJC), a joint journal club between EPS and the Center for Astrophysics, dedicated a semester to discussing this topic, and I borrowed the title of this section from PJC, which I believe was originally suggested by Robin.

5.3 The Philosophy of Drawing a Phase Boundary

Mike Walter, the director of Carnegie's Earth and Planets Laboratory, asked a thought-provoking question during my interview for their postdoctoral fellowship about my phase boundary work (Chapter 4). He asked, "JJ, your machine learning approach to determining a global inversion of the phase boundary is interesting, but what if some or even most of our previous experiments were wrong? How will we ever know the true phase boundaries?" I was initially stumped by this question and couldn't come up with a convincing answer.

Mike astutely highlighted the philosophical challenge present in my work. Here, I will take some space to share my thoughts, which have accumulated over the five years I spent on this phase transition project. The immediate goal of Chapter 4 is to establish a boundary for the post-spinel transition in Mg_2SiO_4. A number of experimental datasets have been produced by different groups at various times, with each work drawing its own post-spinel phase boundary based on the respective dataset. This would not pose a problem if all the boundaries were consistent; however, the reality is that these studies have produced vastly different results. While I have no intention of challenging the expertise of the experimenters who produced the existing results, I am, in fact, humbled by the effort and meticulousness in their work. The time devoted by many of these experimenters to their own experiments is several orders of magnitude greater than the time I spent on my two visits to Argonne. Although I believe each group has tried their best to produce the "best" boundary based on their experience, we are still faced with the practical question of whose boundary to trust.

Historically, attempts have been made to reconcile these experiments through the

intercalibration of different pressure scales. Initially, all experimental observations used to draw boundaries were measured using different pressure scales, such as gold, platinum, magnesium oxide, and sometimes salts. When comparing phase stability observations measured with these different pressure scales, inconsistencies among them might introduce significant systematic errors to the perceived phase boundaries of each group. If pressure calibration was the only source of significant systematic errors, correcting historical data should resolve the issue, and any remaining errors in the dataset could be assumed to be random. Consequently, these random errors should and can be addressed using some statistical method (and devising such statistical method is what I am committed to in Chapter 4). Several brilliant experimentalists devoted nearly a decade to finding a unified, intercalibrated scale across various metals, oxides, and salts. However, even with the best available cross-calibration to correct historical data, we can only resolve most, but not all discrepancies among the existing dataset. Are the remaining discrepancies between datasets suggesting that some fraction of data is wrong? Or is there still an unknown systematic error that we could correct to resolve the last bit of discrepancy?

The issue now revolves around the tension between systematic errors and random errors. It seems that some additional systematic error is obstructing our attempts to find a consistent post-spinel boundary. Thus, to rephrase Mike's question slightly, he is essentially expressing concern about these additional unknown systematic errors, asking, "How can we ever know the true phase boundaries if some of our previous experiments are wrong or alternatively they suffer from some additional systematic errors?" So the ultimate philosophical challenge arises here: in either case, how can we draw a "true" phase boundary when we still have these unknowns?

Months later, in March 2023, I attended a roundtable discussion called "Stylistic Pluralism and Objectivity in the Sciences" with two of my favorite philosophers of science, Hasok Chang and Peter Galison. Although this discussion was, at face value, unrelated to Mike's question, philosophically it touched on the heart of Mike's concern.

In the roundtable, Peter raised an important point shared by Hasok and many philosophers of science today—there is a difference between "styles of reasoning" or "systems of practice" in science, and the metaphysical binary of truth and falsity in epistemology. Scientific objectivity may first appear to be ontological prima facie, but it actually has had multiple meanings in its history; an "objective" way of doing science in practice is not as transcendent as the metaphysical sense of the word "truth". When doing science, instead of focusing on whether something is true or not, we often focus on developing pragmatic methodological tactics that help us solve problems. After all, most practitioners of science are less interested in metaphysical questions and more interested in finding practical solutions. This procedural (instead of propositional) notion of knowledge can be traced back to Percy Bridgman's operationalism, who declared that the meaning of a concept consisted solely in the method of its measurements. Hasok brought back Bridgman's empiricist doctrine and summarized it elegantly: "knowledge resides in activities."

We have already learned from the history of science that the "true" nature of an object or its ontology is an unmanageable concept to work with. As we gain more access to the inner workings of an object, our understanding of its "true" nature constantly shifts, resulting in a complex and disjointed empirical world that lacks a unified ontology. For example, we once believed that all particles behaved classically according to Newtonian mechanics, but now we know that small particles like electrons

and hydrogen atoms can also behave like waves. Each such modification changes the ontology of the particle as we once knew it. Although I acknowledge the potential existence of the ontology of the world, we may only gain clarity about it at "the end of the inquiry." We are not yet at the point in science where we can approach ontology in a constructive way.

Once again, a pragmatic scientist would not be concerned with the issues mentioned above; they often show little to no interest in the so-called ontology of the object they're studying. Instead, their main focus is on developing ad hoc methodological tactics to solve immediate problems in their daily investigations in the lab or on the computer.

So, I will use Peter's comment to explain the rationale of my work. Instead of falling into the metaphysical trap of contemplating the unknowns and asking how we know where the phase boundaries really are, it's better to first understand and improve our approach to finding a phase boundary. In the past, experimentalists would simply look at a boundary and draw it by hand after making a series of phase stability observations. The experimenter's subjective judgment dictated how they perceived, quite literally, the location of a phase boundary through their own visual analysis. Compared with the remaining "unknown" systematic errors and a subset of potentially wrong data, the eye-balling approach to drawing a phase boundary poses a much bigger existential threat to our ability to determine where a phase boundary is from empirical evidence.

Similar to the scientist in Peter's analogy, I'm not committed to the ultimate ontology of the object I'm studying, which in this case is the "true" location of a phase boundary. Instead, I'm interested in developing a robust methodological tactic for determining a phase boundary from existing empirical evidence. In this work, more

specifically, my goal is to use statistical optimization to extract and utilize all of the available data to draw a phase boundary and to maximize coherence with the global inversion strategy based on all of our empirical knowledge about a given phase boundary.

Now, finally returning to Mike's question, "What if some of the existing experiments are wrong, [or suffer from unknown systematic errors]?" My response would be that we would simply need more empirical evidence to show they are either wrong or suffer from systematic errors. The less likely counterfactual scenario where most of our existing experiments were wrong or suffered from unknown systematic errors, as well as our ultimate concerns about our inability to know anything, are in fact external to the methodology I'm designing here. I might even feel comfortable stating that even if some of the existing phase observation data I include are likely to be "wrong," the phase boundary we provided from the global inversion is still faithful to all of our current empirical evidence about the relevant phase relations. If additional empirical evidence in the future suggests that a particular phase transition occurs at a different location than the one presented in the figures in Chapter 4, I wouldn't be surprised, because I never make any guarantees about the ontology of a phase boundary from my work.

However, since we have developed a robust method based on our prior, potentially incorrect empirical evidence, we can quickly incorporate new empirical evidence into our phase diagram investigation using the same methodology when needed. Any potential contradictory empirical evidence to the phase boundary I have produced here in my dissertation cannot be known a priori by the method itself. Nevertheless, as long as the method is robust and coherent, it can easily be used to provide a different, yet still faithful, representation of our new empirical landscape as critical new evidence emerges. Therefore, I am not suggesting that the specific phase boundaries I produced

in Chapter 4 is "objective" and "true." Instead, like Peter, Hasok, and Bridgman, I am not interested in such metaphysical exercises. My focus is on creating a method that remains viable regardless of the empirical evidence at the time and has the potential to provide a robust representation of the object as new empirical evidence emerges.

Appendix A

Supplementary Materials for Chapter 2

A.1 Thermodynamic Model of Water Storage Capacities in Nominally Anhydrous Minerals

Water is dissolved in nominally anhydrous minerals (NAMs) as hydroxyl groups (OH), and the water storage capacity is primarily controlled by the amount of point defects and at which sites they substitute with OH- groups. The thermodynamics of water storage capacity can be generalized by considering the following reaction (Keppler and Bolfan-Casanova 2006):

$$\frac{n}{2}\mathrm{H_2O} + \frac{n}{2}\mathrm{O^{2-}} = (\mathrm{OH^-})_n \tag{A.1}$$

for which the equilibrium constant is:

$$K = \frac{a_{(\mathrm{OH}^-)_n}}{f_{\mathrm{H_2O}}^{\frac{n}{2}} \cdot a_{\mathrm{O}^{2-}}^{\frac{n}{2}}} \tag{A.2}$$

where $a_{\mathrm{O}^{2-}}$ and $a_{(\mathrm{OH}^-)_n}$ are the activities of the unprotonated oxygens and hydroxyls, respectively; $f_{\mathrm{H_2O}}$ is the water fugacity; and n is the fugacity exponent. Assuming that the unprotonated oxygens have an activity of approximately unity and remain constant throughout the reaction ($a_{\mathrm{O}^{2-}} \sim 1$) and that OH^- is a dilute species, and its activity equals its concentration ($a_{(\mathrm{OH}^-)_n} \sim c_{(\mathrm{OH}^-)_n} \sim n \cdot c_{\mathrm{OH}^-}$), the hydroxyl concentration in NAMs can be expressed as:

$$c_{\mathrm{OH}^-} = \frac{1}{n} \cdot f_{\mathrm{H_2O}}^{\frac{n}{2}} \cdot K \tag{A.3}$$

For a given Mg endmember mineral, the equilibrium constant K can be described by:

$$\Delta G^*(P,T) = -\mathrm{R}T \ln K = \Delta H^* - T\Delta S^* + \Delta V^*(P - \mathrm{P}_0) \tag{A.4}$$

where ΔG^* is the Gibbs free energy of hydration, ΔH^* and ΔS^* are the hydration enthalpy and entropy, respectively, at a reference pressure P_0, ΔV^* is the volume change in the solid upon hydration, and R is the universal gas constant.

The Gibbs free energy of the concentration of hydroxyl defects (i.e., water storage capacity) in NAMs, ΔG, is a function of the solid solution composition (e.g., the mole fraction of iron, X_{Fe}). In ideal (Mg,Fe) solid solutions with minor amounts of Fe^{2+}, the Gibbs free energy of hydration may be approximated as a MacLaurin series (Schmalzried 1994; Zhao et al. 2004):

$$\Delta G^*(P,T,X_{\mathrm{Fe}}) \sim \Delta G^*(P,T) + X_{\mathrm{Fe}} \cdot \Delta G^*(P,T)' + \text{high-order terms} \tag{A.5}$$

where $X_{\mathrm{Fe}} \cdot \Delta G^*(P,T)'$ represents the deviation of the Gibbs free energy of hydration from that of the Mg endmember due to the presence of iron. For a small amount of

Fe, as in mantle silicates, the higher-order terms may be neglected. By combining Eq. A3–A5, we can express the water concentration $c_{\mathrm{OH^-}}$ in moles as:

$$c_{\mathrm{OH^-}} = \frac{1}{n} \cdot f_{\mathrm{H_2O}}^{\frac{n}{2}} \cdot e^{\frac{\Delta S^*}{\mathrm{R}} - \frac{\Delta H^*}{\mathrm{R}T} - \frac{\Delta V^* \cdot (P - \mathrm{P_0})}{\mathrm{R}T} - \frac{\Delta G^*(P,T)' \cdot X_{\mathrm{Fe}}}{\mathrm{R}T}} \tag{A.6}$$

$$c_{\mathrm{H_2O}} = \frac{1}{2} c_{\mathrm{OH^-}} \tag{A.7}$$

which, under water-saturated conditions, is equal to the water storage capacity. Eq. A6 can be further simplified into Eq. 1 of the main text in wt.% or ppm wt.:

$$\ln(c_{\mathrm{H_2O}}) = \ln(\frac{1}{2n}) + a + \frac{n}{2} \cdot \ln(f_{\mathrm{H_2O}}) + \frac{b + c \cdot P + d \cdot X_{Fe}}{T} \tag{A.8}$$

where a, b, and c are constants related to the changes in entropy, enthalpy, and volume of the hydration reaction, respectively, and d is related to the compositional effect. At mantle-relevant conditions where $P \gg P_0$, P_0 (typically 1 bar) becomes negligible (i.e., $P - P_0 \sim P$). The water fugacity was calculated by parameterizing the modified Redlich-Kwong (MRK) equation of state (Frost and Wood 1997; Holland and Powell 1991; Otsuka and Karato 2011).

A.2 Selection and Correction of Experimental Data on Water Storage Capacities in NAMs

It is possible that one of our criteria for selecting experimental data on water storage capacity, the presence of a liquid phase, is not sufficient to ensure that water storage capacities in NAMs have been established, especially at higher pressures when the liquid phase is hydrous melt if the NAMs of interest coexisted with water-undersaturated melt.

However, the water contents in the coexisting melt are often not reported in literature. Thus, we did not exclude any dataset based on water content in the melt.

Moreover, for wadsleyite and ringwoodite, we excluded experiments at temperatures less than 1673 K. At lower temperatures than this, their water concentrations approach the structural limit for water storage capacity (Kudoh et al. 1996); i.e., there are no/few available unprotonated oxygen atoms, which likely causes the water storage capacity to become temperature-independent and deviate from the trend predicted from the thermodynamic model (Demouchy et al. 2005).

Quantitative determination of water storage capacities in NAMs has often made use of FTIR spectroscopy. Earlier FTIR measurements were based on two empirical calibrations of the strength of frequency-dependent OH absorption bands that are generic to all water-/hydroxyl-bearing minerals (Paterson 1982; Libowitzky and Rossman 1997), which bear uncertainties as high as 30–50% and are inconsistent with one another. In addition, these infrared absorption calibrations may cause unsystematic errors in water concentration determination with the use of unpolarized light, and the associated uncertainty remains difficult to assess. Several independent and more accurate infrared absorption calibrations were later established specifically for OH in olivine, including Bell et al. (2003) (cross-calibrated with ^{15}N nuclear reaction analysis) and Withers et al. (2012) (cross-calibrated with ERDA). The Bell et al. (2003) calibration revises the water measurements upward based on the Paterson (1982) or Libowitzky and Rossman (1997) calibrations by a factor of 2–4, and the Withers et al. (2012) calibration gives water concentrations of $\sim$2/3 of the value from the Bell et al. (2003) calibration. To ensure the compiled water storage capacity measurements are internally consistent, we have corrected all the FTIR measurements for olivine to the Withers et al. (2012) calibration.

Though no independent infrared absorption calibration has been established specifically for OH in either wadsleyite or ringwoodite, it has been shown that the Paterson (1982) calibration underestimates water concentrations in wadsleyite and ringwoodite by approximately 55% relative to the ERDA technique (Bolfan-Casanova et al. 2018). Here, we corrected those water concentrations in wadsleyite and ringwoodite determined by FTIR based on the Paterson (1982) calibration by this amount.

Some water storage capacity measurements considered in this study were made using another method, SIMS, which was often calibrated against standards whose water concentrations were determined from FTIR. It has been shown that the SIMS measurements are typically in good agreement with the ERDA measurements (an absolute method for water measurement), at least for olivine (Bolfan-Casanova et al. 2018), so SIMS data in the compilation remain uncorrected. It would be ideal if the regressions were performed with the sub-dataset of either FTIR measurements or SIMS measurements exclusively, to avoid any potential systematic error from mixed-use of measurements obtained by two different techniques. At the moment, both FTIR and SIMS measurements are, however, required to encompass the P–T conditions of both the present-day and early mantle. The possible errors arising from the mixed-use of the two techniques are included in the variances of the regression coefficients, which have been incorporated in the Monte Carlos simulation (Table S4).

A.3 Parametrization of the Earth's Hypsometric Curve

To reconstruct the bathymetry curve (ocean floor topography from the ridge axis), a hybrid area–age distribution of the seafloor was assumed, evolving from a rectangular distribution to a triangular distribution as a linear function of $\chi = \frac{A_{\mathrm{cc}}}{A^*_{\mathrm{cc}}}$, where χ is the ratio of Archean (A_{cc}) to present-day (A^*_{cc}) continental area. The age–area distribution of the ocean floor can be parametrized as (Flament et al. 2008):

$$\frac{\mathrm{d}A}{\mathrm{d}\tau} = \upsilon \cdot (1 - \chi \frac{\tau}{\tau_{\max}}) \tag{A.9}$$

$$\tau_{\max} = \upsilon \cdot \frac{2A_{\mathrm{oc}}}{2 - \chi} \tag{A.10}$$

where υ is the global rate of seafloor spreading, A_{oc} is the surface area of Earth's oceanic crust ($A_{\mathrm{oc}} = A_{\mathrm{Earth}} - A_{\mathrm{cc}}$), and τ and $\tau_{\max}$ are the age of the oceanic floor and its maximum value, respectively. It has been suggested that the observed triangular distribution of the present-day seafloor age is a deviation from the theoretical rectangular distribution due to the presence of continents (Coltice et al. 2013).

A classical half-space cooling model was used to describe the subsidence of oceanic plates, and the depth to the ocean floor from the sea level (d) can be parameterized as (Korenaga et al. 2017):

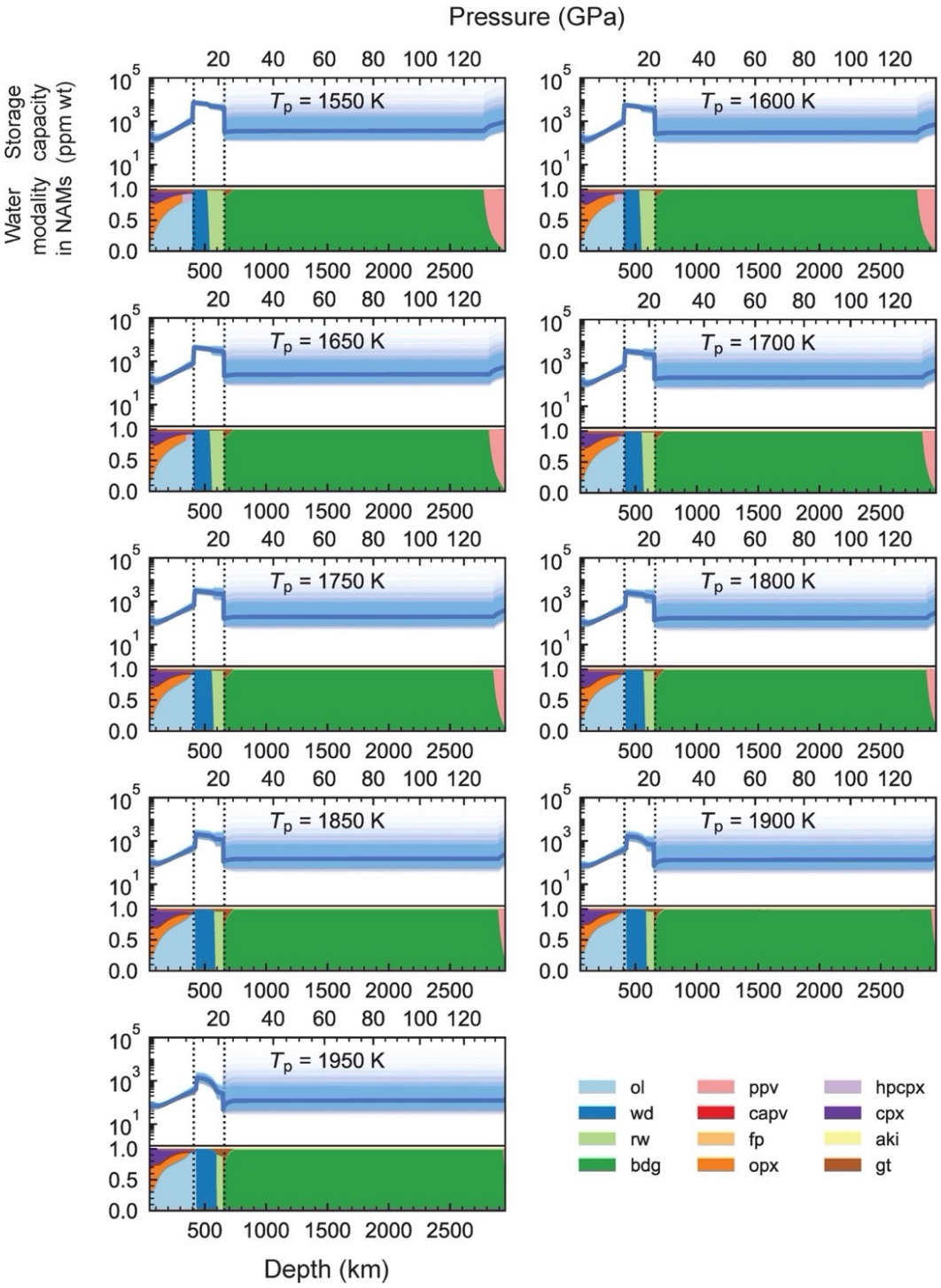
$$d\left(\tau, T_{\mathrm{p}}\right) = d_0\left(T_{\mathrm{p}}\right) + b\left(T_{\mathrm{p}}\right) \cdot \sqrt{\tau} \tag{A.11}$$

$$b\left(T_{\mathrm{p}}\right) = b_0 \cdot \frac{T_{\mathrm{p}}}{T_{\mathrm{p},0}} \tag{A.12}$$

where the zero-age depth of mid-ocean ridges $d_0(T_{\mathrm{p}})$ and the subsidence rate $b(T_{\mathrm{p}})$ depend on mantle potential temperature T_{p} (with modern value $T_{\mathrm{p},0} = 1627$ K), and b_0

$= 0.323$ km/$\sqrt{\text{Ma}}$ (Korenaga and Korenaga 2008). In fact, the volumes of ocean basins (from ocean floor to sea level) are not only associated with ridge spreading rate but also influenced by dynamic topography (Gurnis 1992). The global rate of seafloor spreading is taken as its present-day value, $v = v_0 \sim 3$ cm/yr (Rowan and Rowley 2016), consistent with the recent paleomagnetic evidence for modern-like plate motion velocities at 3.2 Ga (>2.50 cm/yr Brennan et al. 2020) as well as the scaling law for plate velocity adopted in Korenaga (2013) and Korenaga et al. (2017) (cf. the slower plate tectonic scenario in Korenaga et al., 2017). The bathymetry model described here remains kinematic but serves as a first-order estimation on time scales of $>10^9$ years (Conrad 2013).

Figure A.1 *(following page)*: **Water storage capacity profiles for T_p = 1550–1950 K generated from the Monte Carlo sampling.** In the upper panels, the thick blue curves correspond to the optimal water storage capacity profiles through a series of mantle geotherms at T_p = 1550–1950 K. These optimal profiles were calculated with the combination of the best fit parameters listed in the Supplementary Information and Table S4. The light blue curves correspond to 104 samples in a representative set of Monte Carlo simulations. In the lower panels, the contributions of individual NAMs to bulk water storage capacity are shown.


Pressure (GPa)
Water modality in NAMs
Storage capacity (ppm wt)
T_p = 1550 K
T_p = 1600 K
T_p = 1650 K
T_p = 1700 K
T_p = 1750 K
T_p = 1800 K
T_p = 1850 K
T_p = 1900 K
T_p = 1950 K
ol
wd
rw
bdg
ppv
capv
fp
opx
hpcpx
cpx
aki
gt
Depth (km)

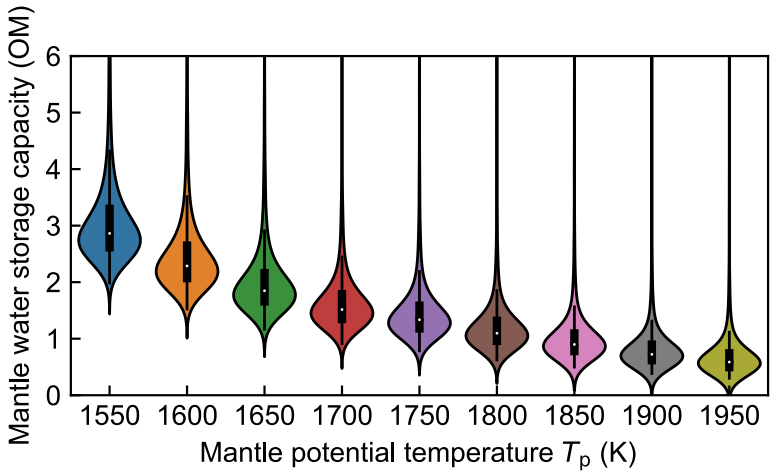


Figure A.2: **Distributions and differences in bulk mantle water storage capacities for T_p = 1550–1950 K generated from the Monte Carlo sampling.** The sampling results are drawn as violin plots for the temperature-dependent storage capacity scenarios. Each histogram shows the statistical distribution of the sampled bulk mantle water storage capacities. The white dots and bold black lines in the histograms represent the medians and interquartile ranges, respectively.

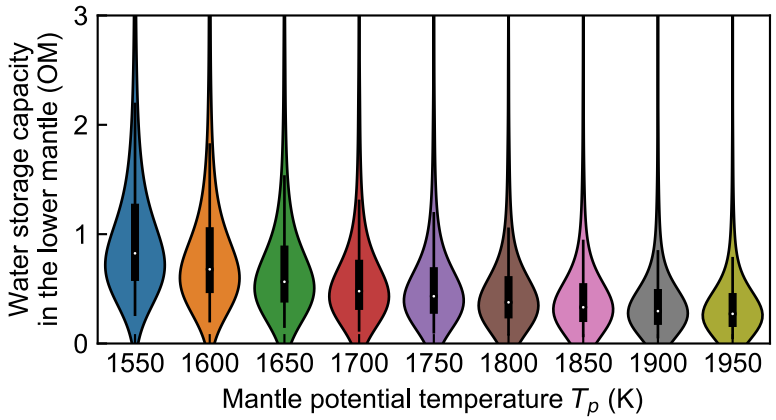


Figure A.3: **Distributions and differences in lower mantle water storage capacities for T_p = 1550–1950 K generated from the Monte Carlo sampling.** The sampling results are drawn as violin plots for the temperature-dependent storage capacity scenarios. Each histogram shows the statistical distribution of the sampled lower mantle water storage capacities. The white dots and bold black lines in the histograms represent the medians and interquartile ranges, respectively.

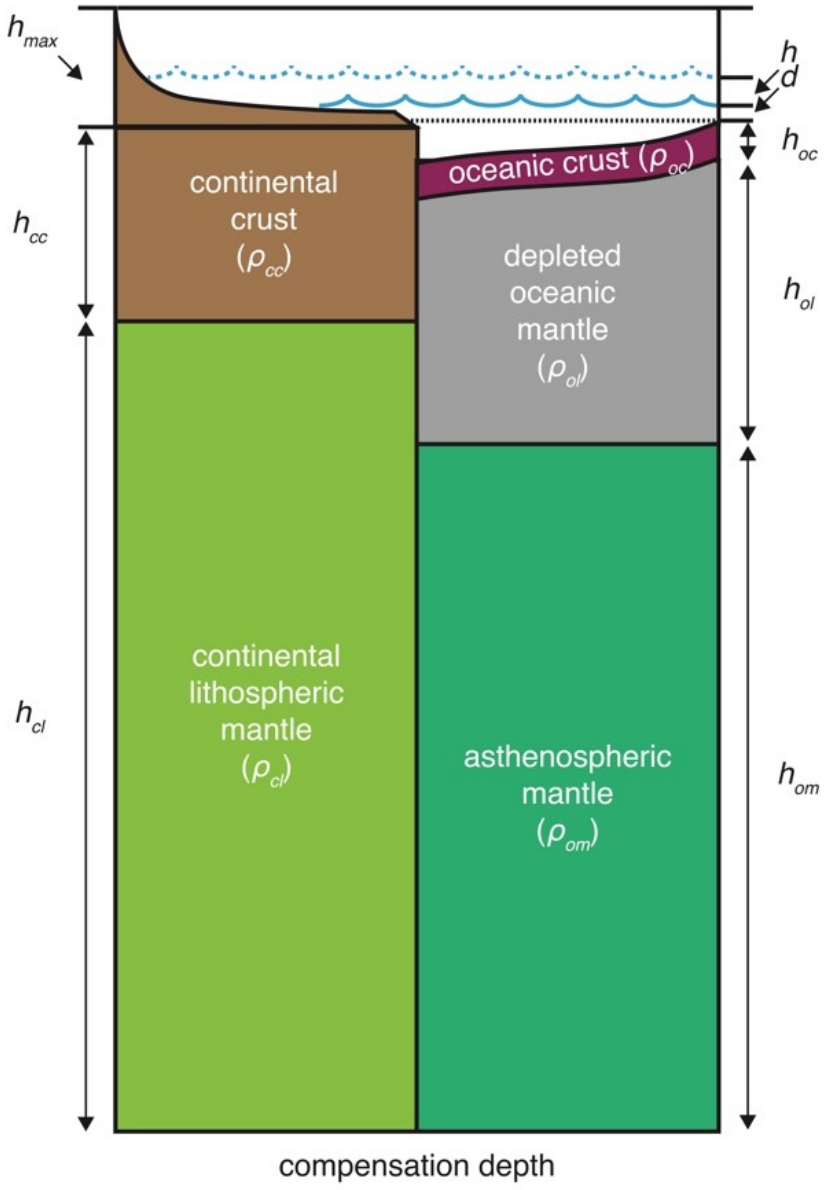


Figure A.4: **Isostacy schematic for the continental freeboard modeling.** The present-day sea level (d) is flush with the top of the continental column. A sea level increase (h ¿ 0) would cause additional flooding of the continents, and the flooded fraction is determined by the ocean volume and hypsometric curve.

Table A.1:: Summary of Experimental Data on Water Storage Capacity in Olivine.

Ref.	**Exp.#**	**P (GPa)**	**T (°C)**	**T (K)**	**Phases present**	**Fe/(Mg+Fe)***	**Method**	**$H_2O_{uncorr.}$ (ppm wt)**	**$H_2O_{corr.}$ (ppm wt)**
M06	R056	1.8	1300	1573	ol+l	0.000	FTIR	375	250
B08	591	2.5	1100	1373	ol+px+l	0.000	FTIR	51	34
F12	955	2.5	1175	1448	ol+px+l	0.074	FTIR	126	84
F12	962	2.5	1250	1523	ol+px+l	0.074	FTIR	54	36
B08	589	2.5	1250	1523	ol+px+l	0.000	FTIR	51	34
F12	956	2.5	1325	1598	ol+px+l	0.068	FTIR	32	21
B08	556	2.5	1325	1598	ol+px+l	0.000	FTIR	111	74
B08	534	2.5	1400	1673	ol+l	0.000	FTIR	173	115
W11†	A641	3.0	1200	1473	ol+px+l	0.197	SIMS	290	193
W11	B217	3.0	1200	1473	ol+px+l	0.096	SIMS	230	153
W11	A647	3.0	1200	1473	ol+px+l	0.000	SIMS	170	113
W11	B223	3.0	1500	1773	ol+px+l	0.052	SIMS	190	127
F12	893b	5.0	1175	1448	ol+px+l	0.071	FTIR	263	175

F12	895b	5.0	1250	1523	ol+px+l	0.078	FTIR	286	191
F12	907	5.0	1400	1673	ol+px+l	0.043	FTIR	18	12
A12	M446	5.0	1400	1673	ol+px+gt+l	0.060	SIMS	130	130
A12	M435	5.0	1400	1673	ol+px+gt+l	0.070	SIMS	103	103
A12	M439	5.0	1400	1673	ol+px+gt+l	0.070	SIMS	145	145
A12	M453	5.0	1450	1723	ol+px+gt+l	0.070	SIMS	57	57
A12	M462	5.0	1500	1773	ol+px+gt+l	0.060	SIMS	106	106
M06	ww296	5.7	1000	1273	ol+px+l	∼0.1	FTIR	2113	1409
M06	ww329	6.0	1000	1273	ol+px+l	∼0.1	FTIR	1705	1137
B08	565	6.0	1000	1273	ol+px+l	0.000	FTIR	548	365
B08	563	6.0	1175	1448	ol+px+l	0.000	FTIR	780	520
W11	M397	6.0	1200	1473	ol+px+l	0.179	SIMS	1010	673
W11	M406	6.0	1200	1473	ol+px+l	0.100	SIMS	790	527
W11	M398	6.0	1200	1473	ol+px+l	0.000	SIMS	530	353
B08	559	6.0	1250	1523	ol+px+l	0.000	FTIR	607	405
B08	586	6.0	1325	1598	ol+l	0.000	FTIR	551	367
B08	570	6.0	1400	1673	ol+px+l	0.000	FTIR	489	326

A12	M454	6.0	1450	1723	ol+px+gt+l	0.090	SIMS	207	207
A12	M466	6.0	1450	1723	ol+px+gt+l	0.080	SIMS	262	262
A12	M464	6.0	1450	1723	ol+px+gt+l	0.090	SIMS	289	289
A12	M456	7.0	1450	1723	ol+px+gt+l	0.080	SIMS	111	111
F12	949	7.5	1175	1448	ol+px+l	0.073	FTIR	2072	1381
F12	945b	7.5	1250	1523	ol+px+l	0.077	FTIR	1262	841
F12	948b	7.5	1325	1598	ol+px+l	0.066	FTIR	964	643
F12	1033	7.5	1400	1673	ol+px+l	0.073	FTIR	830	553
M06	ww317	8.0	1000	1273	ol+px+l	0.061	FTIR	3032	2021
W11	M300	8.0	1000	1273	ol+px+l	0.113	SIMS	3300	2200
M06	ww323	8.0	1100	1373	ol+px+l	~0.1	FTIR	1657	1105
M06	ww325	8.0	1200	1473	ol+px+l	0.047	FTIR	2398	1599
W11	M266	8.0	1200	1473	ol+px+l	0.000	SIMS	2300	1533
W11	M268	8.0	1400	1673	ol+px+l	0.000	SIMS	1600	1067
W11	M280	8.0	1400	1673	ol+px+l	0.067	SIMS	1400	933
W11	M281	8.0	1400	1673	ol+px+l	0.069	SIMS	1700	1133
W11	M287	8.0	1400	1673	ol+px+l	0.059	SIMS	1600	1067

W11	M283	8.0	1400	1673	ol+fp+l	0.078	SIMS	2200	1467
W11	M286	8.0	1400	1673	ol+fp+l	0.076	SIMS	2000	1333
W11	M292	8.0	1400	1673	ol+px+l	0.081	SIMS	1200	800
W11	M293	8.0	1400	1673	ol+px+l	0.078	SIMS	1300	867
A12	M460	8.0	1450	1723	ol+px+gt+l	0.040	SIMS	237	237
A12	M473	8.0	1450	1723	ol+px+gt+l	0.070	SIMS	272	272
W11	M298	8.0	1500	1773	ol+px+l	0.071	SIMS	1000	667
W11	M288	8.0	1520	1793	ol+px+l	0.062	SIMS	1200	800
W11	M303	8.0	1550	1823	ol+px+l	0.064	SIMS	900	600
W11	M297	8.0	1600	1873	ol+px+l	0.059	SIMS	680	453
B08	689	9.0	1100	1373	ol+px+l	0.000	FTIR	1223	815
F12	1043b	9.0	1175	1448	ol+px+l	0.082	FTIR	4690	3127
B08	663	9.0	1175	1448	ol+px+l	0.000	FTIR	1567	1045
F12	1044b	9.0	1250	1523	ol+px+l	0.083	FTIR	2805	1870
B08	613	9.0	1250	1523	ol+px+l	0.000	FTIR	1984	1323
B08	641	9.0	1325	1598	ol+px+l	0.000	FTIR	1158	772
F12	1050b	9.0	1400	1673	ol+px+l	0.068	FTIR	46	31

B08	650	9.0	1400	1673	ol+px+l	0.000	FTIR	386	257
M06	ww263	10.0	1200	1473	ol+l	~0.1	FTIR	5055	3370
T12	M455	10.0	1450	1723	ol+px+gt+l	0.070	SIMS	410	410
W11	M255	10.2	1200	1473	ol+px+l	0.000	SIMS	3900	2600
W11	M262	10.2	1400	1673	ol+px+l	0.000	SIMS	1800	1200
T12	M461	11.0	1450	1723	ol+px+gt+l	0.086	SIMS	330	330
W11	M273	11.6	1400	1673	ol+px+l	0.000	SIMS	2500	1667
S06	SZ0409B	12.0	1100	1373	ol+hu+l	0.000	FTIR	5560	3707
S06	SZ0411B	12.0	1100	1373	ol+px+l	0.000	FTIR	5770	3847
S06	SZ0407A	12.0	1250	1523	ol+px+l	~0.03	FTIR	4883	3255
S06	SZ0407B	12.0	1250	1523	ol+hu+l	~0.03	FTIR	8000	5333
S06	SZ0408A	12.0	1250	1523	ol+px+l	0.000	FTIR	8900	5933
S06	SZ0408B	12.0	1250	1523	ol+hu+l	0.000	FTIR	8500	5667
T12	M468	12.0	1350	1623	ol+px+gt+l	0.091	SIMS	1140	1140
T12	M474	12.0	1350	1623	ol+px+gt+l	0.085	SIMS	920	920
S06	SZ0410B	12.0	1400	1673	ol+hu+l	0.000	FTIR	4503	3002
S06	SZ0501B	12.0	1400	1673	ol+px+l	0.000	FTIR	4400	2933

S06	SZ0501B	12.0	1400	1673	ol+px+l	0.000	FTIR	3400	2267
T12	M467	12.0	1400	1673	ol+px+gt+l	0.088	SIMS	760	760
T12	M471	12.0	1400	1673	ol+px+gt+l	0.078	SIMS	1190	1190
T12	M476	12.0	1400	1673	ol+px+gt+l	0.079	SIMS	860	860
T12	M463	12.0	1450	1723	ol+px+gt+l	0.083	SIMS	600	600
T12	M470	12.0	1450	1723	ol+px+gt+l	0.075	SIMS	720	720
S06	H2296	12.0	1600	1873	ol+l	0.000	FTIR	1000	667
L07	K338	12.5	1100	1373	ol+px+l	∼0.12	FTIR	4720	3147
C02	2850	13.0	1200	1473	ol+l	0.030	SIMS	2900	2900
T12	M465	13.0	1450	1723	ol+px+gt+l	0.090	SIMS	470	470
C02	3064	13.1	1200	1473	ol+l	0.029	SIMS	5500	5500
F12	1064b	13.5	1400	1673	ol+px+l	0.062	FTIR	1680	1120
C02	2623	13.7	1200	1473	ol+l	0.000	SIMS	7600	7600
L07	K332	14.0	1200	1473	ol+px+l	∼0.12	FTIR	6250	4167
L07	K310	14.0	1400	1673	ol+px+l	∼0.12	FTIR	5770	3847
L07	K333	14.0	1500	1773	ol+px+l	∼0.12	FTIR	3707	2471
L07	K307	14.0	1600	1873	ol+l	∼0.12	FTIR	1364	909

L07	K287	14.0	1700	1973	ol+l	∼0.12	FTIR	418	279
L07	K346	14.0	1800	2073	ol+anhyB+l	∼0.12	FTIR	241	161
L07	K349	14.5	2000	2273	ol+l	∼0.12	FTIR	158	105

ol, olivine; px, pyroxene; gt, garnet; hu, humite; fp, ferropericlase; anhyB, anhydrous phase B; l, fluid/melt.

*Fe contents (Fe/(Mg+Fe)) of all recovered samples are listed in mole fraction. No Fe content measurement was reported on some of the recovered samples in M06, S06 and L07, and the initial Fe content of the starting material is listed instead.

†Water concentrations in W11 were measured using SIMS and a set of new standards that have been corrected to the calibration of Bell et al. (2003) specifically. We corrected these SIMS measurements to the calibration of Withers et al. (2013).

A12: Ardia, P., Hirschmann, M. M., Withers, A. C., & Tenner, T. J. H_2O storage capacity of olivine at 5–8 GPa and consequences for dehydration partial melting of the upper mantle. *Earth Planet. Sci. Lett.* **345**, 104-116 (2012); B08: Bali, E., Bolfan-Casanova, N., & Koga, K. T. Pressure and temperature dependence of H solubility in forsterite: an implication to water activity in the Earth interior. *Earth Planet. Sci. Lett.* **268**, 354-363 (2008); C02: Chen, J.,

Inoue, T., Yurimoto, H., & Weidner, D. J. Effect of water on olivine-wadsleyite phase boundary in the $(Mg,Fe)_2SiO_4$ system. *Geophys. Res. Lett.* **29** (2002); F12: Ferot, A., & Bolfan-Casanova, N. Water storage capacity in olivine and pyroxene to 14 GPa: Implications for the water content of the Earth's upper mantle and nature of seismic discontinuities. *Earth Planet. Sci. Lett.* **349**, 218-230 (2012); L07: Litasov, K. D., Ohtani, E., Kagi, H., Jacobsen, S. D., & Ghosh, S. Temperature dependence and mechanism of hydrogen incorporation in olivine at 12.5–14.0 GPa. *Geophys. Res. Lett.* **34** (2007); M06: Mosenfelder, J. L., Deligne, N. I., Asimow, P. D., & Rossman, G. R. Hydrogen incorporation in olivine from 2–12 GPa. *Am. Mineral.* **91**, 285-294 (2006); S06: Smyth, J. R., Frost, D. J., Nestola, F., Holl, C. M., & Bromiley, G. Olivine hydration in the deep upper mantle: Effects of temperature and silica activity. *Geophys. Res. Lett.* **33** (2006); T12: Tenner, T. J., Hirschmann, M. M., Withers, A. C., & Ardia, P. H_2O storage capacity of olivine and low-Ca pyroxene from 10 to 13 GPa: Consequences for dehydration melting above the transition zone. *Contributions Mineral. Petrol.* **163** 297-316 (2012); W11: Withers, A. C., Hirschmann, M. M., & Tenner, T. J. The effect of Fe on olivine H_2O storage capacity: Consequences for H_2O in the martian mantle. *Am. Mineral.* **96**, 1039-1053 (2011).

Table A.2:: Summary of Experimental Data on Water Storage Capacity in Wadsleyite at Temperatures Above 1673 K.

Ref.	**Exp.#**	**P (GPa)**	**T (°C)**	**T (K)**	**Phases present**	**Fe/(Mg+Fe)***	**Method**	**$H_2O_{uncorr.}$ (ppm wt)**	**$H_2O_{corr.}$ (ppm wt)**
K96	5	13.5	1425	1698	wd+gt+cen+phE+l	∼0.217	SIMS	2.890	2.890
L11	A1033/5	14.0	1400	1673	wd+per+l	0.000	FTIR	0.810	1.473
L08	K-310	14.5	1400	1673	wd+ol+l	0.133	FTIR	1.600	2.909
L08	K-341	14.5	1600	1873	wd+l	0.031	FTIR	0.330	0.600
D05	H2045	15.0	1400	1673	wd+cen+l	0.000	SIMS	0.930	0.930
L08	K-306	15.2	1400	1673	wd+l	0.060	FTIR	1.370	2.491
L08	K-309	15.2	1600	1873	wd+l	0.040	FTIR	0.310	0.564
L11	A970/5	15.5	1400	1673	wd+l	0.000	FTIR	0.580	1.055
K96	7	15.5	1450	1723	wd+gt+l	∼0.217	SIMS	1.950	1.950
K96	1	15.5	1500	1773	gt+cen+wd+l	∼0.217	SIMS	1.520	1.520
K96	2	15.5	1500	1773	gt+cen+wd+l	∼0.217	SIMS	1.520	1.520
J05	wz292	16.0	1400	1673	wd+phE+cpx+l	0.000	FTIR	0.960	1.745
J05	wz336	16.0	1400	1673	wd+phE+cpx+l	0.000	FTIR	1.060	1.927

L03	K-1	16.0	1400	1673	wd+gt+cpx+l	0.000	FTIR	0.720	1.309
BC18	226a	16.0	1500	1773	wd+l	0.160	ERDA	0.467	0.467
L11	K312	16.0	1500	1773	wd+l	0.000	FTIR	0.550	1.000
L11	K301	16.0	1600	1873	wd+cen+l	0.000	FTIR	0.370	0.673
L03	K-2	16.0	1600	1873	wd+gt+l	0.000	FTIR	0.700	1.273
L08	K-348	16.0	1800	2073	wd+anhyB+l	0.052	FTIR	0.180	0.327
I10	E1760-1	16.5	1400	1673	wd+rw+cen+l	0.121	SIMS	2.280	2.280
I10	E1760-2	16.5	1400	1673	wd+rw+cen+l	0.121	SIMS	2.240	2.240
I10	E1751-1	16.5	1400	1673	wd+rw+cen+l	0.111	SIMS	1.880	1.880
I10	E1751-2	16.5	1400	1673	wd+rw+cen+l	0.111	SIMS	1.790	1.790
K96	6	16.5	1400	1673	wd+gt+stv+phE+l	∼0.217	SIMS	2.610	2.610
L11	K299	16.5	1800	2073	wd+anhyB+l	0.000	FTIR	0.390	0.709
L08	K-347	16.5	2000	2273	wd+anhyB+l	0.051	FTIR	0.070	0.127
I10	E1788-1†	17.0	1400	1673	wd+rw+cen+l	0.200	SIMS	3.720	3.720
L08	K-375	17.0	1400	1673	wd+l	0.059	FTIR	0.630	1.145
S97	S97-1	17.0	1400	1673	wd+gt+l	0.054	SIMS	2.240	2.240
L03	K-3	17.0	1750	2023	wd+gt+l	0.000	FTIR	0.330	0.600

Y12	Y12-1	18.0	1400	1673	wd‡	0.000	FTIR	1.500	2.727
L11	K295	18.0	1900	2173	wd+anhyB+l	0.000	FTIR	0.240	0.436
L11	K293	18.5	1400	1673	wd+l	0.000	FTIR	0.720	1.309
L03	K-6	18.5	1400	1673	wd+gt+l	0.000	FTIR	0.460	0.836
L11	K313	18.5	1600	1873	wd+cen+l	0.000	FTIR	0.370	0.673
L03	K-5	18.5	1600	1873	wd+gt+l	0.000	FTIR	0.290	0.527
BC18	268	19.0	1450	1723	wd+l	0.000	ERDA	0.846	0.846
BC18	267	19.0	1650	1923	wd+l	0.001	ERDA	0.347	0.347
L11	A756/1	20.0	1500	1773	wd+l	0.000	FTIR	0.520	0.945
L11	K300	20.0	1600	1873	wd+l	0.000	FTIR	0.440	0.800
L08	K-350	20.0	1800	2073	wd+fp+l	0.070	FTIR	0.150	0.273
L11	K298	20.0	1900	2173	wd+l	0.000	FTIR	0.220	0.400
L08	K-392	20.0	1900	2173	wd+fp+l	0.055	FTIR	0.120	0.218

ol, olivine; wd, wadsleyite; rw, ringwoodite; cen, clinoenstatite; gt, garnet; cpx, clinopyroxene; per, periclase; fp, ferropericlase; stv, stishovite; phE, phase E; anhyB, anhydrous phase B; l, fluid/melt.

*Fe contents (Fe/(Mg+Fe)) of all recovered samples are listed in mole fraction. No Fe content measurement was reported on some of the recovered samples in K96, and the initial Fe content of the starting material is listed instead.

†Pressure reported for e1788-1 may have a relatively large uncertainty according to I10.

‡No phase assemblage information was reported in Y12.

BC18: Bolfan-Casanova, N. et al. Examination of water quantification and incorporation in transition zone minerals: wadsleyite, ringwoodite and phase D using ERDA (Elastic recoil detection Analysis). *Front. Earth Sci.* **6**, 75. (2018); D05: Demouchy, S., Deloule, E., Frost, D. J., & Keppler, H. Pressure and temperature-dependence of water solubility in Fe-free wadsleyite. *Am. Mineral.* **90**, 1084-1091 (2005); I10: Inoue, T., Wada, T., Sasaki, R., & Yurimoto, H. Water partitioning in the Earth's mantle. *Phys. Earth Planet. Inter.* **183**, 245-251 (2010); J05: Jacobsen, S. D., Demouchy, S., Frost, D. J., Ballaran, T. B., & Kung, J. A systematic study of OH in hydrous wadsleyite from polarized FTIR spectroscopy and single-crystal X-ray diffraction: Oxygen sites for hydrogen storage in Earth's interior. *Am. Mineral.* **90**, 61-70 (2005); K96: Kawamoto, T. Experimental constraints on differentiation and H_2O abundance of calc-alkaline magmas. *Earth Planet. Sci. Lett.* **144**, 577-589 (1996); L11:Litasov, K. D., Shatskiy, A., Ohtani, E., & Katsura, T. Systematic study of hydrogen incorporation into Fe-free wadsleyite. *Phys. Chem. Miner.* **38**, 75-84 (2011); L03: Litasov, K., & Ohtani, E. Stability of various hydrous phases in CMAS pyrolite-H_2O system up to 25 GPa. *Phys. Chem. Miner. 30*, 147-156 (2003); L08: Litasov, K., & Ohtani, E. Systematic study of hydrogen incorporation into Fe-bearing wadsleyite

and water storage capacity of the transition zone. *AIP Conf. Proc.* **987**, 113-118 (2008); S97: Smyth, J. R., & Kawamoto, T. Wadsleyite II: A new high pressure hydrous phase in the peridotite-H_2O system. *Earth Planet. Sci. Lett.* **146**, E9-E16 (1997); Y12: Yang, X., Dubrovinsky, L., Manthilake, M. A. G. M., & Wei, Q. High-pressure and high-temperature Raman spectroscopic study of hydrous wadsleyite (β-Mg_2SiO_4). *Phys. Earth Planet. Inter.* **39**, 57-64 (2012).

Table A.3:: Summary of Experimental Data on Water Storage Capacity in Ringwoodite at Temperatures Above 1673 K.

Ref.	**Exp.#**	**P (GPa)**	**T (°C)**	**T (K)**	**Phases present**	**Fe/(Mg+Fe)***	**Method**	**$H_2O_{uncorr.}$ (wt%)**	**$H_2O_{corr.}$ (wt%)**
I10	e1788-1†	17.0	1400	1673	wd+rw+cen+l	0.157	SIMS	1.69	1.69
I10	e1760-1	16.5	1400	1673	wd+rw+cen+l	0.189	SIMS	1.11	1.11
I10	e1760-2	16.5	1400	1673	wd+rw+cen+l	0.189	SIMS	1.25	1.25
I10	e1751-1	16.5	1400	1673	wd+rw+cen+l	0.196	SIMS	1.00	1.00
I10	e1751-2	16.5	1400	1673	wd+rw+cen+l	0.196	SIMS	1.10	1.10
S03	sz0107	19.0	1400	1673	wd+rw+gt+l	0.103	FTIR	0.86	1.56
S03	sz0002	20.0	1400	1673	rw+stv+l	0.108	FTIR	0.79	1.44
S03	sz9901	20.0	1400	1673	rw+stv+l	0.115	FTIR	0.93	1.69
S03	sz0104	18.0	1400	1673	wd+rw+gt+l	0.129	FTIR	1.07	1.95
O00	F11H06-1	23.0	1450	1723	rw+l	0.000	SIMS	1.60	1.60
O00	F11H06-2	23.0	1450	1723	rw+l	0.000	SIMS	1.70	1.70
O00	F11H06-3	23.0	1450	1723	rw+l	0.000	SIMS	1.50	1.50
BC18	271	19.0	1550	1823	rw+l	0.069	ERDA	0.43	0.43

BC18	253	19.0	1550	1823	rw+l	0.001	ERDA	1.16	1.16
BC18	362	21.0	1550	1823	rw+l	0.001	ERDA	1.04	1.04
I10	e1784	23.0	1600	1873	rw+bdg+l	0.199	SIMS	0.76	0.76
I10	e1730	23.1	1600	1873	rw+bdg+l	0.188	SIMS	0.71	0.71
I10	e1695	23.2	1600	1873	rw+bdg+l	0.178	SIMS	0.63	0.63
O00	F5H15	23.0	1680	1953	rw+l	0.000	SIMS	0.20	0.20
BC18	385	21.0	1700	1973	rw+l	0.003	ERDA	0.89	0.89
O00	F5H26	23.0	1800	2073	rw+bdg+l	0.000	SIMS	0.30	0.30

wd, wadsleyite; rw, ringwoodite; bdg, bridgmanite; cen, clinoenstatite; gt, garnet; stv, stishovite; l, fluid/melt.

*Fe contents (Fe/(Mg+Fe)) of all recovered samples are listed in mole fraction.

†Pressure reported for e1788-1 may have a relatively large uncertainty according to I10.

BC18: Bolfan-Casanova, N. et al. Examination of water quantification and incorporation in transition zone minerals: wadsleyite, ringwoodite and phase D using ERDA (Elastic recoil detection Analysis). *Front. Earth Sci.* **6**, 75.

(2018); I10: Inoue, T., Wada, T., Sasaki, R., & Yurimoto, H. Water partitioning in the Earth's mantle. *Phys. Earth Planet. Inter.* **183**, 245-251 (2010); O00: Ohtani, E., Mizobata, H., & Yurimoto, H. Stability of dense hydrous magnesium silicate phases in the systems Mg_2SiO_4-H_2O and $MgSiO_3$-H_2O at pressures up to 27 GPa. *Phys. Earth Planet. Inter.* **27**, 533-544 (2000); S03: Smyth, J. R. et al. Structural systematics of hydrous ringwoodite and water in Earth's interior. *Am. Mineral.* **88**, 1402-1407 (2003)

Table A.4:: Coefficients and Covariance Matrices of Parameterizations for the Water Storage Capacity Model, as Applied to Olivine, Wadsleyite, and Ringwoodite at High Pressure and Temperature.

Phase	**Coefficients (SE)***		**Covariance matrix**		
	n	**b**		**n**	**b**
olivine	0.6447 (0.0483)	4905.5403 (416.2888)	**n**	0.002336626	-19.08137476
			b	-19.08137476	173296.3502
	a	**b**		**a**	**b**
wadsleyite	-7.6356 (0.8952)	13739.5371 (1602.2032)	**a**	0.8012935	-1428.74358
			b	-1428.74358	2567055.173
	a	**b**		**a**	**b**
ringwoodite	-6.8856 (1.3651)	12206.2676 (2400.7947)	**a**	1.863515	-3271.070854
			b	-3271.070854	5763815.154

*Regression coefficients are shown with standard errors (SE) in parentheses.

Table A.5:: Tabulated Parameters for Water Partition Coefficient Calculations in Eq. 2.2

Partition coefficient	**A** (**ppm/bar^n**)	**n**	**ΔV** (**cm^3/mol**)	**ΔH** (**kJ/mol**)	**Ref.**
olivine	0.0066	1	10.6	—	K96
Al-free orthopyroxene	0.01354	0.5	12.1	−4.563	M07
Al-bearing orthopyroxene*	0.042	0.5	11.3	−79.685	M07
clinopyroxene	7.144	0.5	8.019	—	B04
garnet	0.679	0.5	5.71	—	LK97

*The total water storage capacity in orthopyroxene is the sum of the water storage capacity in $MgSiO_3$ enstatite (Al-free orthopyroxene) and the additional water storage capacity contributed from its Al^{3+}-coupled substitution (Al-bearing orthopyroxene).

K96: Kohlstedt, D. L., Keppler, H., & Rubie, D. C. Solubility of water in the α, β and γ phases of $(Mg,Fe)_2SiO_4$. *Contributions Mineral. Petrol.* **123(4)**, 345-357 (1996); M07: Mierdel, K., Keppler, H., Smyth, J. R., & Langenhorst, F. Water solubility in aluminous orthopyroxene and the origin of Earth's asthenosphere. *Science* **315(5810)**, 364-368 (2007); B04: Bromiley, G. D., Keppler, H., McCammon, C., Bromiley, F. A., & Jacobsen, S. D. Hydrogen solubility and speciation in natural, gem-quality chromian diopside. *Am. Mineral.* **89(7)**, 941-949 (2004); LK97: Lu, R., & Keppler, H. Water solubility in pyrope to 100 kbar. *Contributions Mineral. Petrol.* **129(1)** 35-42 (1997).

Appendix B

Supplementary Materials for Chapter 3

B.1 Density–Pressure Profiles for the Martian Mantle

Conversion from pressure to depth was performed using a thin shell calculation based on the density–pressure profiles pertinent to the potential temperature and bulk composition:

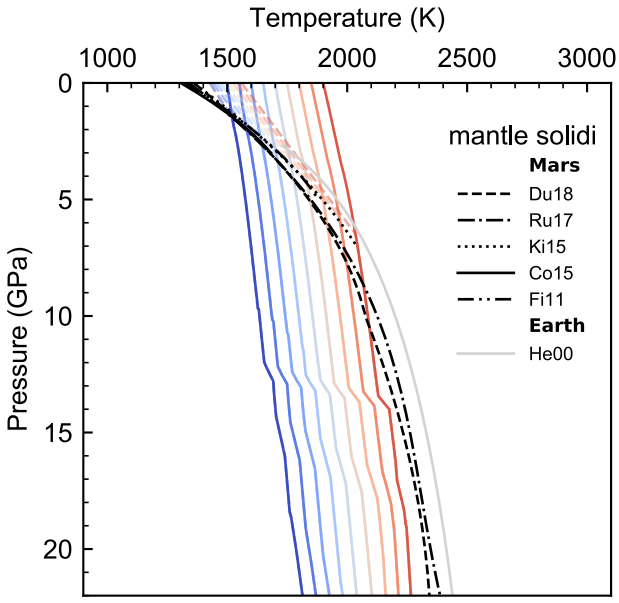
$$h_{i+1} = \frac{P_{i+1} - P_{i+1}}{\frac{(\rho_{i+1}+\rho_i)\cdot g_i}{2}} = r_i - r_{i+1} \tag{B.1}$$

$$V_{i+1} = \frac{4\pi}{3}[r_i^3 - (r_i - h_{i+1})^3] = \frac{4\pi}{3}(r_i^3 - r_{i+1}^3) \tag{B.2}$$

$$g_{i+1} = \frac{\mathrm{G}(\mathrm{M} - \sum_i^n V_{n+1}\frac{\rho_{n+1}+\rho_n}{2})}{(r_i - h_{i+1})^2} = \frac{\mathrm{G}(\mathrm{M} - \sum_i^n V_{n+1}\frac{\rho_{n+1}+\rho_n}{2})}{r_{i+1}^2} \tag{B.3}$$

where G is the gravitational constant ($G = 6.67408 \times 10^{-11} m^3/kg/s^2$); the mass M and radius R_0 of Mars are 6.4171×10^{23} kg (Konopliv et al. 2011) and 3390 km, respectively; and the fictitious density of Martian surface rock ρ_0 is 3 kg/m^3.

Figure B.1 *(following page)*: **Adiabatic temperature gradients (colored solid lines) of the "T13" Martian mantle computed with HeFESTo (Stixrude and Lithgow-Bertelloni 2005, 2011).** Adiabats are shown for potential temperatures of 1500–1900 K, with a spacing of 50 K. When adiabats of the convective solid mantle intersect its solidus, the actual mantle temperature will either continue to follow the adiabats if the melts remain within the source rocks (e.g., in a deep mantle upwelling), or the temperature will be deflected to follow the mantle solidus (e.g., in the case of lithospheric thinning) as the primary melts produced at the solidus temperature are extracted and ascend along their respective adiabats (colored dashed lines Collinet et al. 2021). Which of these two cases will arise depends on the geodynamic setting of mantle melting (cf. Rey 2015). The geodynamics of Martian mantle melting remain poorly constrained, and in this study the solid mantle adiabats are taken as a first-order approximation to the temperature gradients of the shallow mantle where the adiabats exceed the solidus. A temperature variation of ∼100 K (e.g., between the solid mantle adiabats and the melt adiabats) in the shallow mantle contributes an uncertainty of ¡0.1% of one Earth's ocean mass (¡0.001 OM) and is negligible. Only the unmelted portion of the shallow mantle is included in the bulk mantle water storage capacity calculations. The respective melt fraction at a specific P–T is estimated based on Collinet et al. (2021). Several Martian mantle solidi from the literature are shown as black curves: Duncan et al. (2018) (dashed), Ruedas and Breuer (2017) (dashdotted), Kiefer et al. (2015) (dotted), Collinet et al. (2021) (solid), and Filiberto and Dasgupta (2011) (dot-dot-dashed). The solid grey curve is the solidus for Earth's mantle from Herzberg et al. (2000).


Temperature (K)
1000
1500
2000
2500
3000
0
5
10
15
20
Pressure (GPa)
mantle solidi
Mars
Du18
Ru17
Ki15
Co15
Fi11
Earth
He00

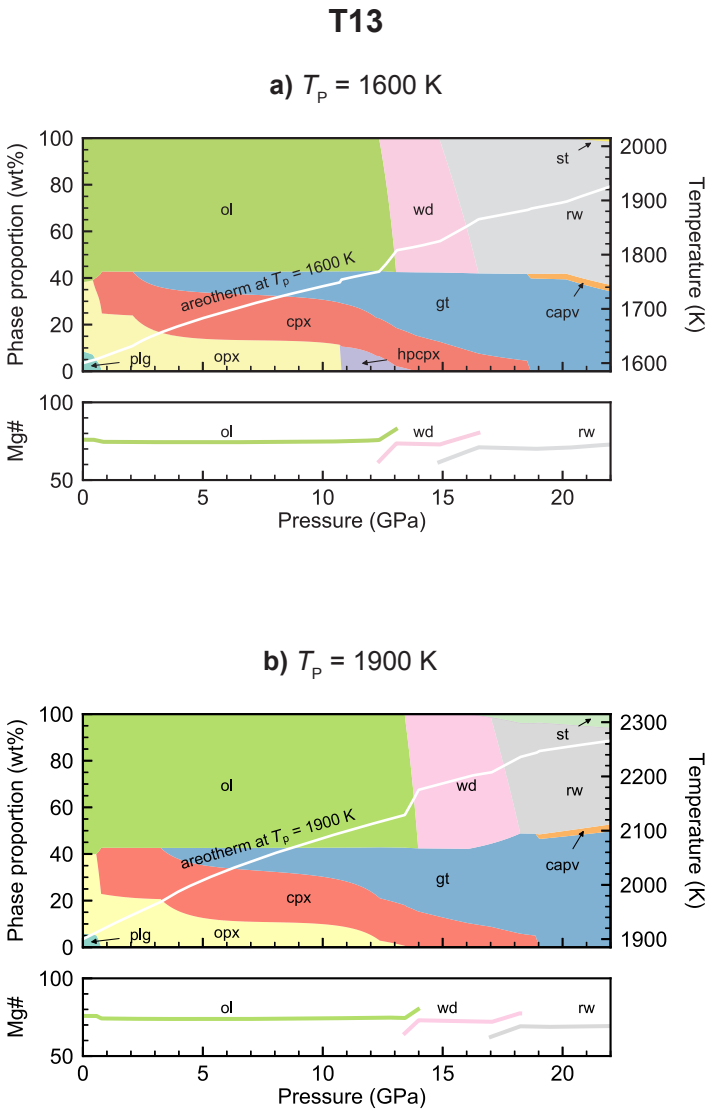


Figure B.2: **Examples of calculated phase assemblages for the "T13" Martian mantle along the 1600 K (a) and 1900 K (b) adiabats.** The upper panels show modal phase proportions along the adiabats (colored regions, left axes) and the temperature along the adiabat (white curves, right axes). The lower panels show the Mg of olivine, wadsleyite, and ringwoodite along the adiabats.

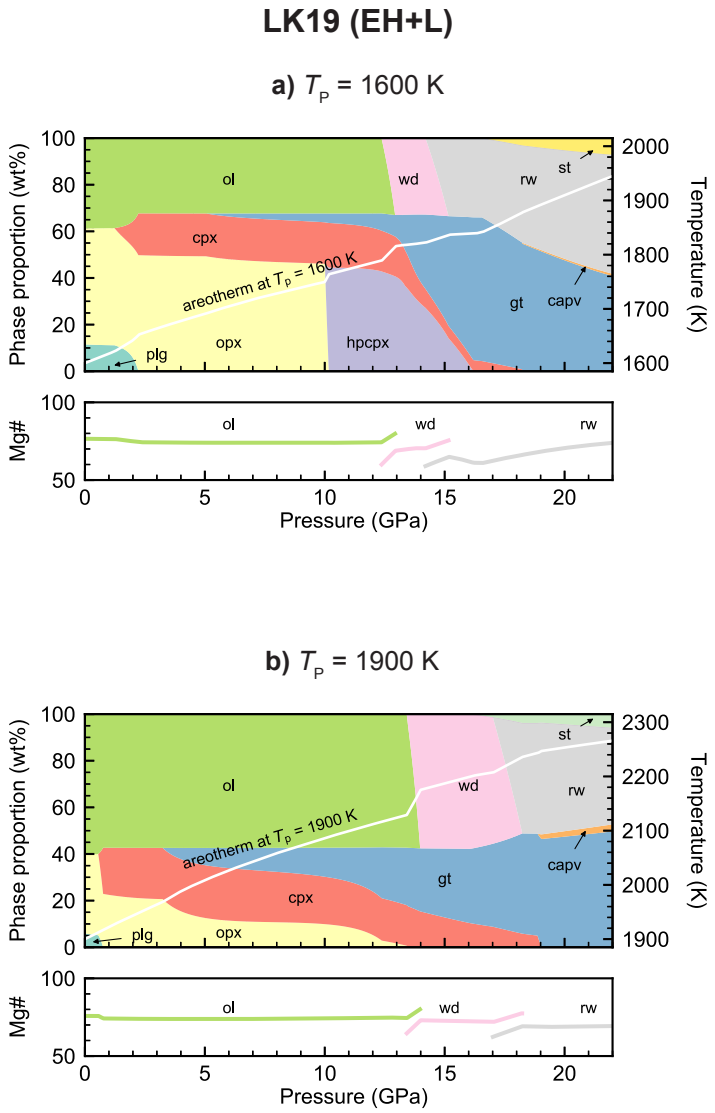


Figure B.3: **Examples of calculated phase assemblages for the "LK19 (EH+L)" Martian mantle along the 1600 K (a) and 1900 K (b) adiabats.** The upper panels show modal phase proportions along the adiabats (colored regions, left axes) and the temperature along the adiabat (white curves, right axes). The lower panels show the Mg of olivine, wadsleyite, and ringwoodite along the adiabats.

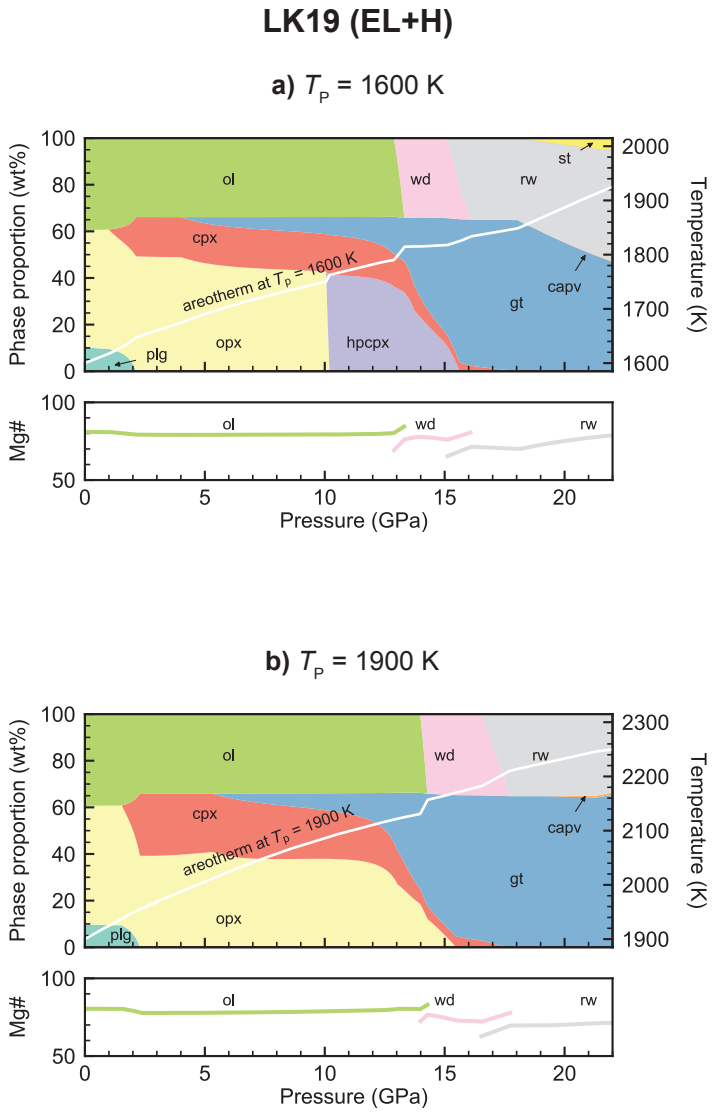


Figure B.4: **Examples of calculated phase assemblages for the "LK19 (EL+H)" Martian mantle along the 1600 K (a) and 1900 K (b) adiabats.** The upper panels show modal phase proportions along the adiabats (colored regions, left axes) and the temperature along the adiabat (white curves, right axes). The lower panels show the Mg of olivine, wadsleyite, and ringwoodite along the adiabats.

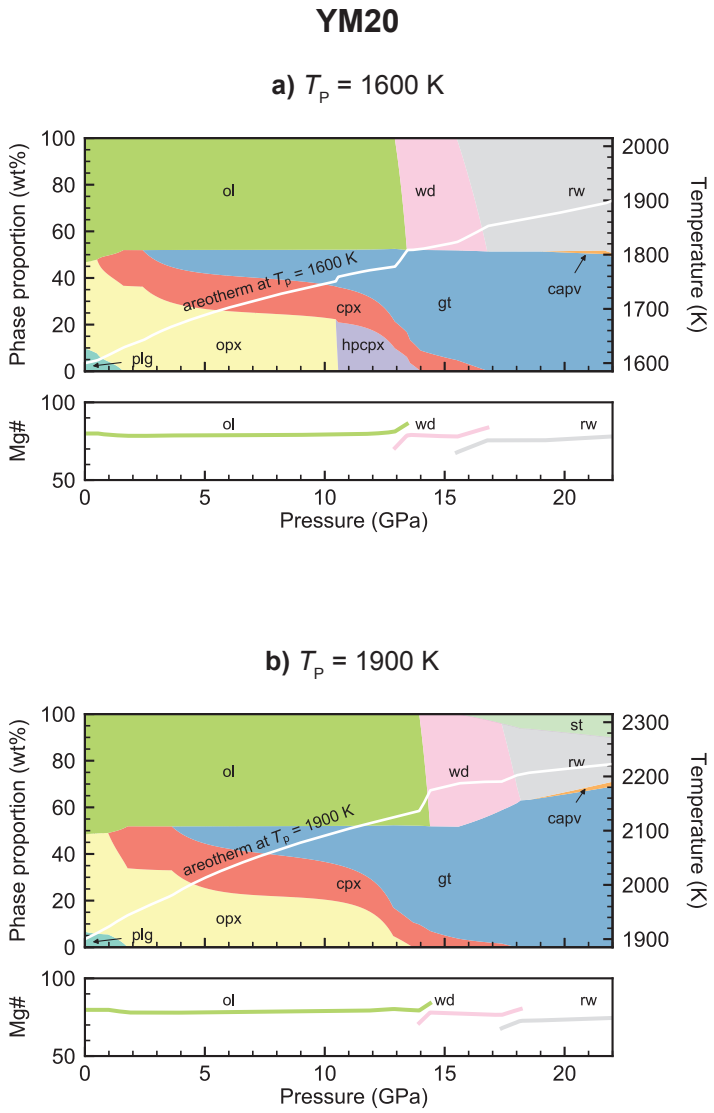


Figure B.5: **Examples of calculated phase assemblages for the "YM20" Martian mantle along the 1600 K (a) and 1900 K (b) adiabats.** The upper panels show modal phase proportions along the adiabats (colored regions, left axes) and the temperature along the adiabat (white curves, right axes). The lower panels show the Mg of olivine, wadsleyite, and ringwoodite along the adiabats.

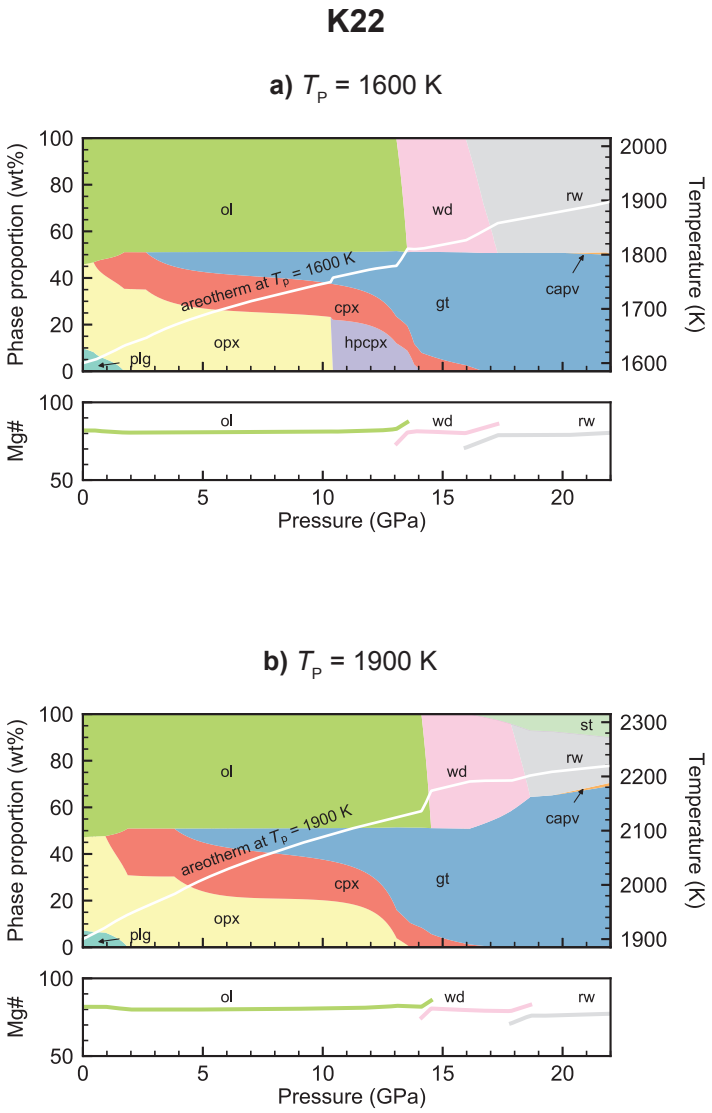
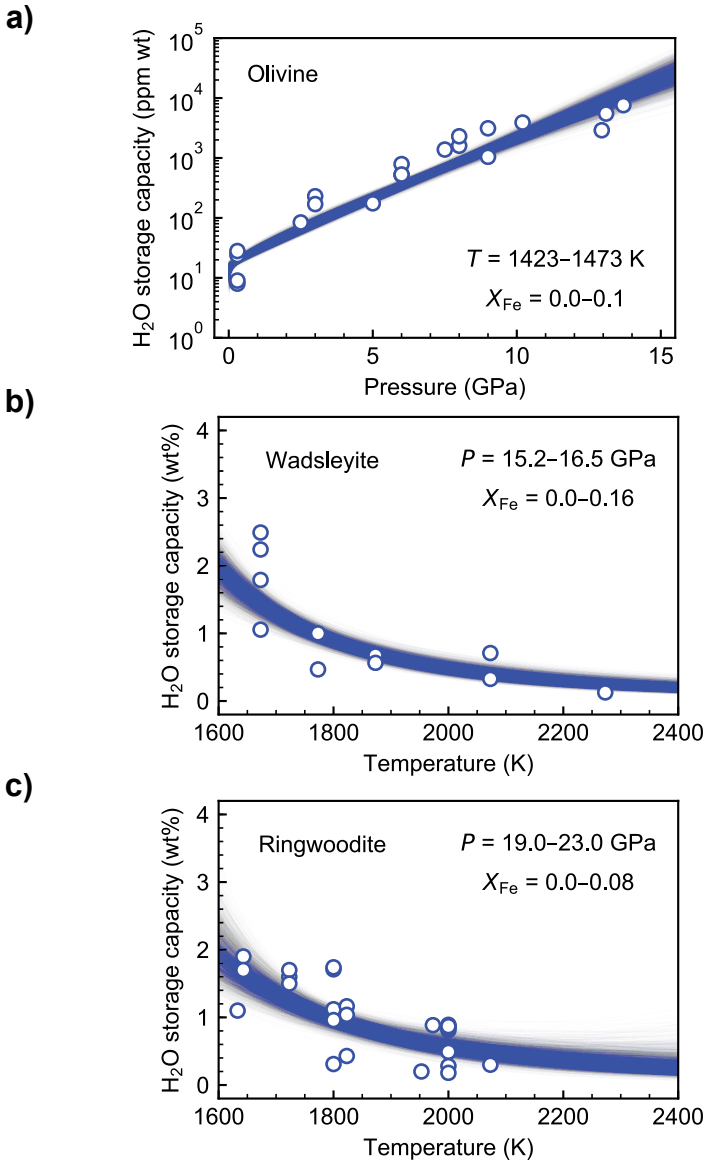


Figure B.6: Examples of calculated phase assemblages for the "K22" Martian mantle along the 1600 K (a) and 1900 K (b) adiabats. The upper panels show modal phase proportions along the adiabats (colored regions, left axes) and the temperature along the adiabat (white curves, right axes). The lower panels show the Mg of olivine, wadsleyite, and ringwoodite along the adiabats.

Figure B.7 *(following page)*: **Pressure or temperature effects on the water storage capacities of (a) olivine, (b) wadsleyite, and (c) ringwoodite at selected** P–T **conditions.** The open circles are a subset of the experimentally-determined water storage capacity data, at these P–T. Their associated error bars are not displayed for clarity. The blue curves correspond to 104 regressions in a representative set of bootstrapping (see Section 2 of the main text for details).


a)
Olivine
T = 1423–1473 K
X_Fe = 0.0–0.1
H2O storage capacity (ppm wt)
Pressure (GPa)
b)
Wadsleyite
P = 15.2–16.5 GPa
X_Fe = 0.0–0.16
H2O storage capacity (wt%)
Temperature (K)
c)
Ringwoodite
P = 19.0–23.0 GPa
X_Fe = 0.0–0.08
H2O storage capacity (wt%)
Temperature (K)

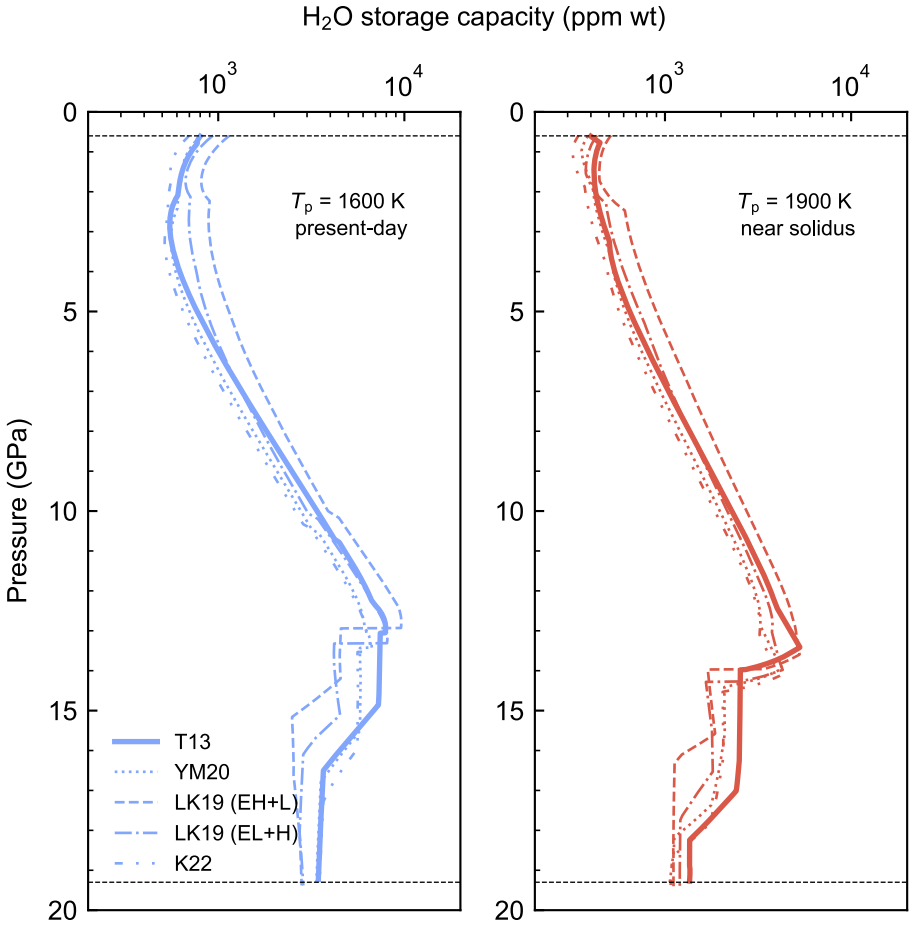


Figure B.8: **Best-fit water storage capacity profiles along mantle adiabats for five BSM compositions at (a) T_p = 1600 K in blue and (b) T_p = 1900 K in red.** "T13": bold solid, "YM20": dotted, "LK19 (EH+L)": dashed, "LK19 (EL+H)": dot-dashed, and "K22": dot-dot-dashed.

Table B.1:: Bulk Silicate Mars Composition Based on Taylor (2013)

Component	**Oxide (wt%)**	**Component**	**Cations (10 atoms)**
MgO	30.5	Mg	4.07714
Al_2O_3	3	Al	0.32128
SiO_2	43.7	Si	3.91862
CaO	2.4	Ca	0.23347
TiO_2	0.1	Ti	-
FeO	18.1	Fe	1.35735
Na_2O	0.5	Na	0.09214
P_2O_5	0.2	P	-
Cr_2O_3	0.7	Cr	-
MnO	0.4	Mn	-
Total	99.8		10
Mg# (molar)	75	**Mg/Si (wt)**	0.9

Table B.2:: Bulk Silicate Mars Composition Based on Liebske and Khan (2019) ("EH+L")

Component	**Oxide (wt%)**	**Component**	**Cations (10 atoms)**
MgO	27.9	Mg	3.68255
Al_2O_3	2.8	Al	0.29218
SiO_2	49.9	Si	4.41816
CaO	2.1	Ca	0.19922
FeO	16	Fe	1.18474
Na_2O	1.3	Na	0.22316
Total	100		10
Mg# (molar)	76	**Mg/Si (wt)**	0.72

Table B.3:: Bulk Silicate Mars Composition Based on Liebske and Khan (2019) (2019) ("El+H")

Component	**Oxide (wt%)**	**Component**	**Cations (10 atoms)**
MgO	30.5	Mg	3.96081
Al_2O_3	3.1	Al	0.31827
SiO_2	50	Si	4.35563
CaO	2.1	Ca	0.196
FeO	13.5	Fe	0.9835
Na_2O	1.1	Na	0.18578
Total	100.3		10
Mg# (molar)	80	**Mg/Si (wt)**	0.79

Table B.4:: Bulk Silicate Mars Composition Based on Yoshizaki and McDonough (2020)

Component	**Oxide (wt%)**	**Component**	**Cations (10 atoms)**
MgO	31	Mg	4.06275
Al_2O_3	3.59	Al	0.43313
SiO_2	45.5	Si	4.02396
CaO	2.88	Ca	0.27128
TiO_2	0.17	Ti	-
FeO	14.7	Fe	1.10832
Na_2O	0.59	Na	0.10056
P_2O_5	0.17	P	-
Cr_2O_3	0.88	Cr	-
MnO	0.37	Mn	-
Total	99.85		10
Mg# (molar)	79	**Mg/Si (wt)**	0.88

Table B.5:: Bulk Silicate Mars Composition Based on Khan et al. (2022)

Component	**Oxide (wt%)**	**Component**	**Cations (10 atoms)**
MgO	32.81	Mg	4.24162
Al_2O_3	3.49	Al	0.3567
SiO_2	46.66	Si	4.04638
CaO	2.66	Ca	0.24716
FeO	13.68	Fe	0.99213
Na_2O	0.69	Na	0.11601
Total	99.99		10
Mg# (molar)	81	**Mg/Si (wt)**	0.91

Table B.6:: Bulk Water Storage Capacity in the Solid Martian Mantle With the "T13" Composition (km GEL*)

T_p	Best-fit (mean)	1-st %tile	5-th %tile	10-th %tile	50-th %tile (median)	90-th %tile	95-th %tile	99-th %tile
1500	11.9	7.9	8.8	9.3	11.6	14.8	15.7	17.7
1550	10.3	6.9	7.7	8.1	10.1	12.7	13.4	15.1
1600	9	6	6.8	7.2	8.9	11.1	11.8	13.1
1650	8.1	5.3	6	6.4	7.9	9.8	10.5	11.7
1700	7.3	4.7	5.4	5.7	7.2	8.9	9.4	10.6
1750	6.6	4.2	4.8	5.2	6.6	8.1	8.6	9.6
1800	6.1	3.8	4.4	4.7	6	7.6	8	9
1850	5.6	3.4	4	4.3	5.6	7	7.5	8.4
1900	4.9	2.9	3.4	3.7	4.8	6.2	6.6	7.5

*Thickness of an H_2O layer if it were spread evenly over the Martian surface in kilometers, referred to as a global equivalent layer (GEL)

Table B.7:: Bulk Water Storage Capacity in the Solid Martian Mantle With the "LK19 (EH+L)" Composition (km GEL*)

T_p	Best-fit (mean)	1-st %tile	5-th %tile	10-th %tile	50-th %tile (median)	90-th %tile	95-th %tile	99-th %tile
1600	8.6	5.8	6.5	6.9	8.5	10.3	10.9	12.1
1900	5	2.8	3.3	3.7	4.9	6.4	6.9	7.8

*Thickness of an H_2O layer if it were spread evenly over the Martian surface in kilometers, referred to as a global equivalent layer (GEL)

Table B.8:: Bulk Water Storage Capacity in the Solid Martian Mantle With the "LK19 (El+H)" Composition (km GEL*)

T_p	Best-fit (mean)	1-st %tile	5-th %tile	10-th %tile	50-th %tile (median)	90-th %tile	95-th %tile	99-th %tile
1600	7.5	5.2	5.8	6.1	7.4	8.9	9.3	10.2
1900	4.2	2.4	2.9	3.2	4.2	5.4	5.8	6.5

*Thickness of an H_2O layer if it were spread evenly over the Martian surface in kilometers, referred to as a global equivalent layer (GEL)

Table B.9:: Bulk Water Storage Capacity in the Solid Martian Mantle With the "YM20" Composition

T_p	Best-fit (mean)	1-st %tile	5-th %tile	10-th %tile	50-th %tile (median)	90-th %tile	95-th %tile	99-th %tile
1600	7.7	5.4	6	6.4	7.7	9.2	9.6	10.5
1900	4.4	2.6	3	3.3	4.3	5.5	5.8	6.6

*Thickness of an H_2O layer if it were spread evenly over the Martian surface in kilometers, referred to as a global equivalent layer (GEL)

Table B.10:: Bulk Water Storage Capacity in the Solid Martian Mantle With the "K22" Composition (km GEL*)

T_p	Best-fit (mean)	1-st %tile	5-th %tile	10-th %tile	50-th %tile (median)	90-th %tile	95-th %tile	99-th %tile
1600	7.5	5.3	5.9	6.2	7.4	8.8	9.3	10.1
1900	4	2.3	2.7	3	3.9	5	5.3	6

*Thickness of an H_2O layer if it were spread evenly over the Martian surface in kilometers, referred to as a global equivalent layer (GEL)

Table B.11:: Additional Literature Data on the Water Storage Capacity of Olivine, an Update to the Compilation of Dong et al. (2021)

Method	**Cali.**	**Ref.**	**Exp.#**	**P (GPa)**	**T (K)**	**Initial bulk H_2O (wt%)**	**Phases present**	**Fe (mol%)**	**H_2O (ppm wt)**
FTIR	P82+B03	Z04	Fa0	0.3	1273	a few drops	water-saturated	0	5
FTIR	P82+B03	Z04	Fa0	0.3	1323	a few drops	water-saturated	0	6
FTIR	P82+B03	Z04	Fa0	0.3	1373	a few drops	water-saturated	0	7
FTIR	P82+B03	Z04	Fa0	0.3	1423	a few drops	water-saturated	0	8
FTIR	P82+B03	Z04	Fa0	0.3	1473	a few drops	water-saturated	0	9
FTIR	P82+B03	Z04	Fa0	0.3	1523	a few drops	water-saturated	0	10
FTIR	P82+B03	Z04	Fa0	0.3	1573	a few drops	water-saturated	0	12
FTIR	P82+B03	Z04	Fa8.5	0.3	1273	a few drops	water-saturated	0.085	14
FTIR	P82+B03	Z04	Fa8.5	0.3	1323	a few drops	water-saturated	0.085	16
FTIR	P82+B03	Z04	Fa8.5	0.3	1373	a few drops	water-saturated	0.085	20
FTIR	P82+B03	Z04	Fa8.5	0.3	1423	a few drops	water-saturated	0.085	24
FTIR	P82+B03	Z04	Fa8.5	0.3	1473	a few drops	water-saturated	0.085	28

FTIR	P82+B03	Z04	Fa8.5	0.3	1523	a few drops	water-saturated	0.085	29
FTIR	P82+B03	Z04	Fa8.5	0.3	1573	a few drops	water-saturated	0.085	35
FTIR	P82+B03	Z04	Fa12	0.3	1273	a few drops	water-saturated	0.12	20
FTIR	P82+B03	Z04	Fa12	0.3	1323	a few drops	water-saturated	0.12	28
FTIR	P82+B03	Z04	Fa12	0.3	1373	a few drops	water-saturated	0.12	29
FTIR	P82+B03	Z04	Fa12	0.3	1423	a few drops	water-saturated	0.12	30
FTIR	P82+B03	Z04	Fa12	0.3	1473	a few drops	water-saturated	0.12	37
FTIR	P82+B03	Z04	Fa12	0.3	1523	a few drops	water-saturated	0.12	43
FTIR	P82+B03	Z04	Fa12	0.3	1573	a few drops	water-saturated	0.149	46
FTIR	P82+B03	Z04	Fa14.9	0.3	1273	a few drops	water-saturated	0.149	24
FTIR	P82+B03	Z04	Fa14.9	0.3	1323	a few drops	water-saturated	0.149	31
FTIR	P82+B03	Z04	Fa14.9	0.3	1373	a few drops	water-saturated	0.149	32
FTIR	P82+B03	Z04	Fa14.9	0.3	1423	a few drops	water-saturated	0.149	42
FTIR	P82+B03	Z04	Fa14.9	0.3	1473	a few drops	water-saturated	0.149	43
FTIR	P82+B03	Z04	Fa14.9	0.3	1523	a few drops	water-saturated	0.149	48
FTIR	P82+B03	Z04	Fa14.9	0.3	1573	a few drops	water-saturated	0.149	56
FTIR	P82+B03	Z04	Fa15.3	0.3	1273	a few drops	water-saturated	0.153	24

FTIR	P82+B03	Z04	Fa15.3	0.3	1323	a few drops	water-saturated	0.153	34
FTIR	P82+B03	Z04	Fa15.3	0.3	1373	a few drops	water-saturated	0.153	34
FTIR	P82+B03	Z04	Fa15.3	0.3	1423	a few drops	water-saturated	0.153	41
FTIR	P82+B03	Z04	Fa15.3	0.3	1473	a few drops	water-saturated	0.153	46
FTIR	P82+B03	Z04	Fa15.3	0.3	1523	a few drops	water-saturated	0.153	48
FTIR	P82+B03	Z04	Fa15.3	0.3	1573	a few drops	water-saturated	0.153	54
FTIR	P82+B03	Z04	Fa16.8	0.3	1273	a few drops	water-saturated	0.168	27
FTIR	P82+B03	Z04	Fa16.8	0.3	1323	a few drops	water-saturated	0.168	36
FTIR	P82+B03	Z04	Fa16.8	0.3	1373	a few drops	water-saturated	0.168	40
FTIR	P82+B03	Z04	Fa16.8	0.3	1423	a few drops	water-saturated	0.168	50
FTIR	P82+B03	Z04	Fa16.8	0.3	1473	a few drops	water-saturated	0.168	55
FTIR	P82+B03	Z04	Fa16.8	0.3	1523	a few drops	water-saturated	0.168	58
FTIR	P82+B03	Z04	Fa16.8	0.3	1573	a few drops	water-saturated	0.168	64
FTIR	P82+B03	Z04	Fa16.9	0.3	1273	a few drops	water-saturated	0.169	26
FTIR	P82+B03	Z04	Fa16.9	0.3	1323	a few drops	water-saturated	0.169	36
FTIR	P82+B03	Z04	Fa16.9	0.3	1423	a few drops	water-saturated	0.169	48
FTIR	P82+B03	Z04	Fa16.9	0.3	1473	a few drops	water-saturated	0.169	57

FTIR	P82+B03	Z04	Fa16.9	0.3	1523	a few drops	water-saturated	0.169	59
FTIR	P82+B03	Z04	Fa16.9	0.3	1573	a few drops	water-saturated	0.169	65
FTIR	B03	G07	ALB5	1.5	1568	7	ol+en+sp+melt	0	22
FTIR	B03	G07	ALB6	1.5	1593	7	fo+en+melt	0	23
FTIR	B03	G07	ALB8	2	1612	7	fo+en+melt	0	36
FTIR	B03	G07	ALB10	1	1593	7	fo+sp+melt	0	37

FTIR: Fourier-transform infrared spectroscopy.

P82: Paterson, M. (1982). The determination of hydroxyl by infrared absorption in quartz, silicate glasses and similar materials. *Bulletin de Minéralogie*, **105(1)**, 20–29; B03: Bell, D. R., Rossman, G. R., Maldener, J., Endisch, D., and Rauch, F. (2003). Hydroxide in olivine: A quantitative determination of the absolute amount and calibration of the IR spectrum. *Journal of Geophysical Research Solid Earth*, **108(B2)**, 672; W12: Withers, A. C., Bureau, H., Raepsaet, C., and Hirschmann, M. M. (2012). Calibration of infrared spectroscopy by elastic recoil detection analysis of H in synthetic olivine. *Chemical Geology*, **334**, 92–98; Z04: Zhao, Y. H., Ginsberg, S. B., and Kohlstedt, D. L. (2004). Solubility of hydrogen in olivine: dependence on temperature and iron content. *Contributions to Mineralogy and Petrology*,

147(2), 155–161; G07: Grant, K. J., Brooker, R. A., Kohn, S. C., and Wood, B. J. (2007). The effect of oxygen fugacity on hydroxyl concentrations and speciation in olivine: Implications for water solubility in the upper mantle. *Earth and Planetary Science Letters*, **261(1–2)**, 217–229.

Table B.12:: Additional Literature Data on the Water Storage Capacity of Wadsleyite, an Update to the Compilation of Dong et al. (2021)

Method	**Cali.**	**Ref.**	**Exp.#**	**P (GPa)**	**T (K)**	**Initial bulk H_2O (wt%)**	**Phases present**	**Fe (mol%)**	**H_2O (ppm wt)**
FTIR	B18	F21	S7114Ol	17.5	2100	15	wd+melt	0.042	
FTIR	B18	F21	H4817Ol	17.5	1700	15	wd+en+melt	0.057	
FTIR	B18	F21	H4898Ol	17.5	1500	15	wd+PhB+melt	0.066	
FTIR	B18	F21	H4841Ol	17.5	1900	15	wd+melt	0.051	
FTIR	B18	F21	H4821Ol	17.5	1900	15	wd+en+melt	0.124	
FTIR	B18	F21	H4821Fo	17.5	1900	15	wd+en+melt	0	
FTIR	B18	F21	H4898Fo	17.5	1500	15	wd+PhB+melt	0	
FTIR	B18	F21	H4790Fo	21	2000	5	wd+en+melt	0	

FTIR: Fourier-transform infrared spectroscopy.

B18: Bolfan-Casanova, N., Schiavi, F., Novella, D., Bureau, H., Raepsaet, C., Khodja, H., and Demouchy, S.

(2018). Examination of water quantification and incorporation in transition zone minerals: wadsleyite, ringwoodite and phase D using ERDA (Elastic recoil detection Analysis). *Frontiers in Earth Science*, **6**, 75; F21: Fei, H. and Katsura, T. (2021). Water solubility in Fe-bearing wadsleyite at mantle transition zone temperatures. *Geophysical Research Letters*, **48**, e2021GL092836.

Table B.13:: Additional Literature Data on the Water Storage Capacity of Ringwoodite, an Update to the Compilation of Dong et al. (2021)

Method	Cali.	Ref.	Exp.#	P (GPa)	T (K)	Initial bulk H_2O (wt%)	Phases present	Fe (mol%)	H_2O (ppm wt)
FTIR	B18	F20	H4720	23	1600	15	rw+aki+melt+st	0.066	1.09
FTIR	B18	F20	H4784L	23	1800	5	rw+melt	0	1.12
FTIR	B18	F20	H4800	23	1800	5	rw+aki+melt	0	1.71
FTIR	B18	F20	H4784H	23	1800	15	rw+aki+melt	0	1.74
FTIR	B18	F20	H4723	23	1800	15	rw+aki+melt	0.0584	0.96
FTIR	B18	F20	S6985	23	1800	5	rw+aki+melt	0.08	0.31
FTIR	B18	F20	H4775	23	2000	5	rw+melt	0	0.49
FTIR	B18	F20	H4793	23	2000	5	rw+aki+melt	0	0.89
FTIR	B18	F20	H4805	23	2000	15	rw+melt	0	0.87
FTIR	B18	F20	S7051	23	2000	22	rw+aki?+melt	0.0322	0.81
FTIR	B18	F20	S7011	23	2000	15	rw+aki+melt	0.0501	0.84
FTIR	B18	F20	H4711	23	2000	5	rw+aki+melt	0.0663	0.28

FTIR	B18	F20	H4698	23	2000	15	rw+aki+melt	0.0682	0.87
FTIR	B18	F20	H4754	23	2000	1.5	rw+aki+melt	0.0845	0.18
FTIR	B18	F20	H4762	23	2000	15	rw+melt+st	0.1109	0.84

FTIR: Fourier-transform infrared spectroscopy.

B18: Bolfan-Casanova, N., Schiavi, F., Novella, D., Bureau, H., Raepsaet, C., Khodja, H., and Demouchy, S. (2018). Examination of water quantification and incorporation in transition zone minerals: wadsleyite, ringwoodite and phase D using ERDA (Elastic recoil detection Analysis). *Frontiers in Earth Science*, **6**, 75; F20: Fei, H. and Katsura, T. (2020). Pressure dependence of proton incorporation and water solubility in olivine. *Journal of Geophysical Research: Solid Earth*, **125(2)**, e2019JB018813.

Appendix C

Supplementary Materials for Chapter 4

C.1 Experimental Procedures

Short symmetric cells and a gas-membrane cell were used with 300 µm culet diamonds anvils to generate high pressure. Re gaskets were pre-indented to 20–28 GPa using the ruby fluorescence pressure and diamond anvil Raman (Akahama and Kawamura 2006; Dewaele et al. 2008), and the Re gaskets were drilled to form a sample chamber with 120 µm diameter.

Starting material was powdered synthetic forsterite Mg_2SiO_4 (Alfa Aesar, synthetic, 99%). W powder (Alfa Aesar, puratronic, 99.999%) was ground and mixed in with the sample material in a ratio of ∼1:3 by volume using a ball mill. The bulk composition and homogeneity of the starting material were confirmed by energy-dispersive X-ray

spectroscopy (EDS). The powder mixtures were compressed between two diamond anvils to form a flake ∼10 µm thick, then loaded between two layers of KCl. The KCl powder was oven-dried for at least 6 hours before sample loading. The samples were handled under clean, dry conditions at all stages of preparation and baked at 393–413 K (120–140 °C) under vacuum for 1–7 hours to remove residual moisture after loading but before closing the cell.

During laser heating, the sample was heated from both sides by two identical Yb fiber lasers (λ = 1064 nm). The X-ray beam was monochromatized to a wavelength of 0.3344 Å and focused to an area of 5.3 µm × 4.4 µm at GESCARS, and to a wavelength of 0.4066 Å and focused to an area of 2.9 µm × 4.8 µm at HPCAT. Diffraction images were recorded with X-ray exposure times of 3–60 seconds and then were integrated into 1-D patterns using Dioptas (Prescher and Prakapenka 2015).

Backgrounds of the integrated XRD patterns were identified using the least-squares fit of the Chebyshev series to data (implemented with the NumPy package in Python, Harris et al., 2020) and then subtracted. The peaks of W and KCl were identified and fitted with a combination of Gaussians, Lorentzians, and Voigt functions (implemented with the lmfit package in Python, Newville et al., 2014; Ostrouchov, 2018), and their 2θ values (related to the angles of diffraction) were estimated and used to calculate the unit cell parameters of W and KCl. Typically, the diffraction lines of (110), (200), (211), (220), (310) and (321) were used to determine the unit cell volume of W; (110), (200), (211) and (220) for the unit cell volume of KCl. The diffraction lines, their precision, and the propagated error to pressure were reported with the estimated pressure for each data point in Table S1

C.2 Phase Identification and Phase Boundary Detection

In general, 1) we used the first appearance of the peaks from the newly formed phase(s) between two consecutive diffraction patterns to detect phase transition, and 2) we tracked the trend of the peak intensity of the existing phase(s) between the phase boundaries detected in each heating cycle. The downside of the second criterion is that changes in peak intensity may also result from the non-random orientation of a small number of newly formed crystal grains and/or peak sharpening upon heating (e.g., Chanyshev et al. 2022). Therefore, as an additional criterion, we relied on the "spottiness" of Debye rings in the 2D XRD images to track the stability of existing phase(s) when the intensity of their diffraction peaks does not change in the same direction. In addition, to avoid mistaking variations in peak intensity and location caused by temperature drop for phase transitions, we excluded any diffraction pattern with a temperature drop of >50 K in the heating path.

One of the goals of this study is to explore the location of the Mg_2SiO_4 triple point as well as the high-temperature area between the triple point and the solidus. To reach this target P–T range (∼21–23 GPa and 1900–2300 K), we started some of our experiments 3–4 GPa lower than this target pressures to account for the thermal pressure upon heating (from ∼17–20 GPa and 1300–1600 K). This choice means that the newly formed *rw* and the relic *wd* often coexist throughout most of the experiment because the P–T conditions are close to the $wd \leftrightarrow rw$ phase boundary (with a lower reaction rate when approaching the boundary, Chanyshev et al., 2022). *wd* with the orthorhombic structure has a much higher density of diffraction peaks than *rw* with the

cubic structure, most of which are located near corresponding cubic features in the XRD patterns, which makes the detection of the first appearance of *rw* peaks particularly challenging.

Ideally, we would want to reverse the P–T path and observe the phase transitions again upon cooling. In practice, however, it is difficult to completely recombine the dissociated *bm* + *pe* back to one single phase upon cooling for the time frame allowed for fast-paced synchrotron experiments due to a slow diffusion rate (Shimojuku et al. 2014) and the separation of the *bm* and *pe* grains (Ishii et al. 2018). Reversed experiments are often only feasible in multi-anvil experiments because the compression-decompression cycle and heating-cooling cycle can be controlled simultaneously and in small increments by a resistance heater and a hydraulic ram. However, the accuracy of temperature measurements in a multi-anvil press is limited by the thermocouple calibrations, and the pressure effects on emf remains unconstrained experimentally at $> \sim$1000 K and, for example, would introduce a systematic temperature error of > 80 K at 1773 K for the type D thermocouple, which significantly affects the determination of Clapeyron slopes (Nishihara et al. 2020b). Therefore, LH-DAC experiments provide an effective way to collect a relatively large dataset with less systematic errors (at the cost of larger random errors) in temperature measurements.

C.3 Selection of Phase Stability Observations From Literature

Historically, experimental studies determined the P–T conditions of a phase transition using the ex situ method, and these ex situ studies (e.g., Ito and Takahashi 1989; Ishii et al. 2011) reported pressures based on "fixed point" calibrations (typically with one at room temperature and one at high temperature, e.g. Irifune et al. 2014). In these ex situ experiments, however, pressure usually varies with temperature, and this temperature dependence of pressure is a complex function of thermal pressure and material relaxation and depends on the P–T path of the run (Fei et al. 2004). It is difficult to compare and correct the pressures of these ex situ datasets, and we hence excluded them from the compilation. For temperature correction, one in situ study, Fei et al. (2004), used the type C ($W_{95}Re_5$–$W_{74}Re_{26}$) thermocouple; No extrapolatable calibration of its pressure effects is available for the type C thermocouple (Li et al. 2003). Therefore, we also excluded the Fei et al. (2004) dataset from the compilation. These excluded datasets represent only a very small fraction of total data points of our data compilation, and they had minimal effects on the location and slope of the post-spinel boundary when they were included in the global analysis.

C.4 Supervised Learning Procedures

In the framework of supervised learning (Fig. S2), the data compilation was first split into a train set (70%) and a test set (30%). The multi-class logistic model for the Mg_2SiO_4 phase boundaries would be eventually evaluated on both the train set and

test set because the model could overfit the train set to predict perfect responses but fail to perform well in the unseen test set. In this study, we used the polynomials of P and T by degree 1 to 5 to describe a phase boundary. Overfitting might occur without supervised learning if the degree of the polynomial we chose is too large, and to prevent overfitting, we applied a regularization method called *Lasso*, or L_1 regularization. The regularization method constrains or regularizes the coefficient estimates, β_j, by modifying the least-squares loss function, $L(\beta)$, into a regularized loss function, $L_{Lasso}(\beta) = L(\beta) + \lambda \sum_{i,j=1}^{n} |\beta_{i,j}|$, where λ is a scaler that assigns weights to the regularization term, or the regularization strength, $\lambda \sum_{i,j=1}^{n} |\beta_{i,j}|$. We then used λ to discourage/penalize extreme values of β_j to avoid overfitting: when λ is sufficiently large, the regularized loss function $L_{Lasso}(\beta)$ becomes increasingly sensitive to $\lambda \sum_{i,j=1}^{n} |\beta_{i,j}|$; in such scenario, a successful convergence would shrink β_{Lasso} to zero, or close to zero.

The hyperparameter (C), or the inverse of regularization strength ($\lambda = \frac{1}{C}$), along with other parameter choices in the scikit-learn package including "multi_class" (classification strategies) and "solver" (algorithms to use in the optimization problem), need to be tuned to optimize the multi-class logistic models. We performed (hyper-)parameter tuning using grid search with k-fold cross-validation, in which the train set was further split into k folds (k = 3–5): the model was trained using k–1 of the small folds, and the resulting model was validated on the reminder of the train set, a single fold held out as the validation set. The final evaluation of the parameters was based on the average over the k folds.

The next step was to choose an evaluation metric. Two common metrics are precision ($\frac{\text{true positive}}{\text{true positive + false positive}}$) and recall ($\frac{\text{true positive}}{\text{true positive + false negative}}$): for example, if we were to draw a phase boundary between *rw* and *bm* + *pe*, precision describes the

proportion of the data points the estimated phase boundary identified as *rw* actually were *rw*; while recall describes the proportion of all *rw* data points the estimated phase boundary actually identified as *rw*. The precision and recall of a model are inversely corelated, and in phase diagram determination, we need to maximize both precision and recall. So, their harmonic mean is used as the evaluation metric, F_1 score ($2 \times \frac{\text{precision} \times \text{recall}}{\text{precision} + \text{recall}}$) and it has the advantage of penalizing extreme values. A high F_1 score means a better balance between precision and recall. The hyperparameter-tuned model was then fit to the train set and test set, and the degree of polynomial that has the maximum F_1 score on the test set became the best-fit model. Then, we used the multi-class logistic regression with the selected degree of polynomial to fit the original data set (the train and test set recombined) and produced a statistically-optimized phase diagram.

C.5 A Brief Review of Previous Data and Their Comparison With This Study

To benchmark the logistic model used in this study, we applied the simple binary logistic model (Kavner et al., 2011) with the assumption of a linear boundary to the individual uncorrected literature dataset. The phase boundaries redetermined by on the logistic models in general agree with the free-hand drawn boundaries, which validates the logistic functions as a model to describe phase stability observations. We now review previous individual experimental datasets and compare it with our global analysis.

The Clapeyron slope of the post-spinel transition in Mg_2SiO_4 has been studied

extensively because of its relevance to the "660-km" seismic discontinuity, and except for Chanyshev et al. (2022), the majority of the literature assumed a linear boundary. Earlier experimental studies usually report a more negative Clapeyron slope for the post-spinel boundary, −3–−4 MPa/K (Ito 1982; Ito and Takahashi 1989; Ito et al. 1990; Akaogi and Ito 1993; Chopelas et al. 1994; Irifune et al. 1998); the pressures reported by these earlier studies were determined ex situ based on "fixed-point" calibrations, so they were more susceptible to systematic biases than in situ pressure scales (Li et al. 2022). More recent work with improved experimental techniques (e.g., pressure determination, phase identification, etc.) suggest the post-spinel slope is less negative, from −1–−2 to virtually 0 MPa/K (Katsura et al. 2003; Fei et al. 2004; Ghosh et al. 2013; Ishii et al. 2011; Chanyshev et al. 2022). The estimates on the post-spinel Clapeyron slope have become less negative over several decades of experimental investigation. This trend suggests inadequate assumption of the linear boundary that would cause overestimation of the post-spinel Clapeyron slope magnitude if it was averaged over a larger temperature range: indeed, earlier experimental studies that reported the slopes of −3–−4 MPa/K typically averaged their slopes between 1200 to 2100 K while more recent works averaged their slopes of −1–−2 MPa/K over 1600 to 2100 K. The nonlinearity we introduced in this study rendered the multi-class logistic model to capture the increasing negative post-spinel slope that the linear assumption was insufficient to describe.

We also found a nearly vertical $wd \leftrightarrow bm + pe$ boundary of $0.4^{+1.8}_{2.9}$ MPa/K at 2400±200 K, which is generally consistent with the dataset reported by Chudinovskikh and Boehler (2001) and Hirose (2002). The Chudinovskikh and Boehler (2001) dataset is uncorrectable due to the lack of the EoS information about its pressure scales, so it is not included in our compilation and therefore can be considered as an independent test.

Hirose (2002) suggested a slightly negative $wd \leftrightarrow bm + pe$ slope (∼–2 MPa/K), but its slope was only implied by a single pair of experimental brackets at 2273 K, so its slope was not effectively constrained. In general, the $wd \leftrightarrow bm + pe$ slope remains less well constrained even with the compiled dataset, due to the increasingly scattered data above the triple point.

Lastly, we found a $wd \leftrightarrow rw$ slope of $6.2^{+1.6}_{-1.1}$ MPa/K at 1800±200 K, which is consistent with the free-hand drawn slopes reported by Katsura and Ito (1989) and Suzuki et al. (2000) (∼7 MPa/K) and slightly more positive than the free-hand drawn slopes from Kuroda et al. (2000) and Inoue et al. (2006) (∼3–4 MPa/K). A relatively more positive slope between 1500 and 2100 K is more consistent with the corrected experimental observations and it is also more consistent with the phase diagram globally because a relatively linear $wd \leftrightarrow rw$ slope of ∼3–4 MPa/K would intersect and form at a triple point that does not agree with the majority of the $wd \leftrightarrow bm + pe$ boundary observations (Chudinovskikh and Boehler 2001; Hirose 2002, this study). We noticed that the redetermined $wd \leftrightarrow rw$ slope (∼1 MPa/K) from the Suzuki et al. (2000) data is significantly smaller than the values originally reported (∼7 MPa/K); it implies that the $wd \leftrightarrow rw$ boundary may become much more nonlinear when temperature is lower than 1500 K. Unfortunately, the low-temperature constraints on the $wd \leftrightarrow rw$ boundary are still lacking; our speculation on the nonlinearity of the $wd \leftrightarrow rw$ boundary below 1500 K requires future experimental evidence to confirm.

C.6 A Composite Mantle Temperature Model for the "660-km" Discontinuity

The composite mantle temperature model for the "660-km" discontinuity estimates the lateral variations in the mantle temperature at the "660-km" depths, T660 (Fig. 5a). It combines three existing thermal models derived from seismic, geophysical and geodynamical constraints: 1) 2D kinematic models for subducting slabs (Syracuse et al. 2010), 2) global shear velocity constraints for plume-fed hotspots (Bao et al. 2022), and 3) globally compiled S660S observations for the ambient mantle (Waszek et al. 2021).

To extrapolate slab temperatures to the "660-km" depth, we used the P–T paths of the slab surface for all arc segments from the W1300 case of Syracuse et al. (2010) (up to 250 km). The gradients of most subduction temperature profiles become virtually constant after 150 km (∼5 GPa) and vary between 0.3 and 0.5 K/km (Shirey et al. 2021). We, therefore, calculated the average slope of each subduction temperature profile between 150–250 km (∼5–8 GPa) and then estimated the T660 for each subduction segment by extrapolating their P–T paths to the 660-km depth with their respective temperature gradient.

Our estimates of the T660 for plume-fed oceanic hotspots were obtained based on their mantle potential temperature estimates reported by Bao et al. (2022) (Table S6). We first calculated the mantle adiabats for each plume-fed oceanic hotspot with their respective mantle potential temperature using HeFESTo, assuming a depleted MORB mantle (DMM). We then took the mantle temperature at the "660-km" depth along the respective mantle adiabat as the T660 for that specific hotspot.

Similarly, our estimates of the T660 for the ambient mantle were extrapolated from the global mantle potential temperature map reported by Waszek et al. (2021). We calculated the mantle adiabats for each geographical location based on their respective mantle potential temperature using HeFESTo, assuming a mechanically mixed (MM) mantle of 20% basalt and 80% harzburgite. We then took the mantle temperature at the "660-km" depth along the respective mantle adiabat as the T660 for that specific geographical location.

The simple extrapolations we used here to estimate T660 may introduce significant errors. For example, slab geometry may vary significantly beyond 250 km for some arc segments, and our assumption of the constant temperature gradient for all slab segments is likely unrealistic. The actual mantle temperatures for some slab segments at the "660-km" depths may deviate from our estimates. With that being said, this composite T660 model serves as reasonable first-order approximations for the lateral variation of mantle temperature across the "660-km" discontinuity.

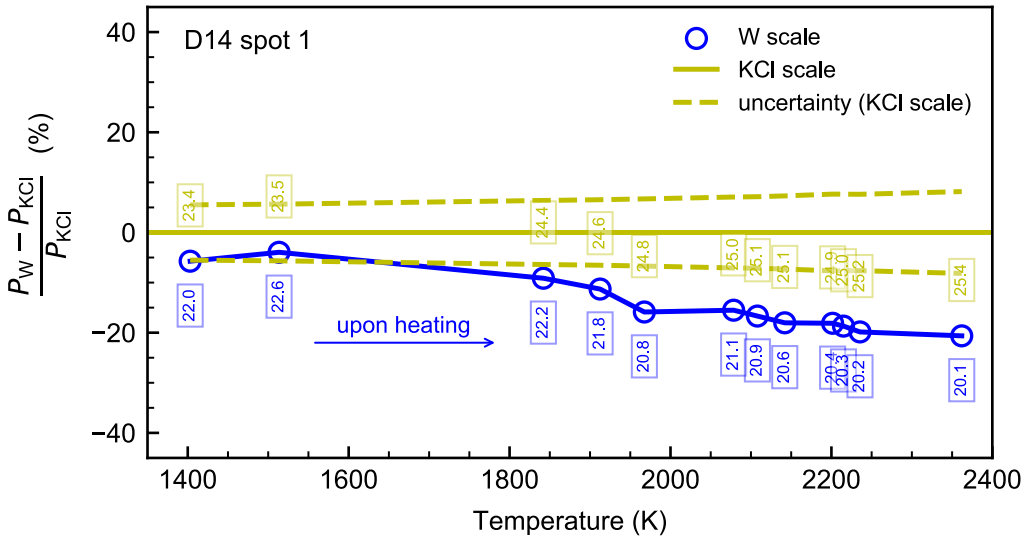


Figure C.1: **Difference between pressures (in GPa) calculated based on the W scale (Sokolova et al. 2016) and pressures based on the KCl scale (Tateno et al. 2019).** The PW estimates deviate significantly from those of P_{KCl} at high temperatures, likely due to lack of thermal EoS data on W at $>\sim$1673 K (Litasov et al. 2013; Sokolova et al. 2016). Therefore, we chose KCl as our primary pressure scale, and all pressures reported in the main text are based on the EoS of P_{KCl} from Tateno et al. (2019) The P_{W} estimates upon heating in D14 spot 1 are plotted in blue circles; their respective P_{KCl} estimates are plotted in a solid yellow line with the uncertainty range in dashed yellow lines.

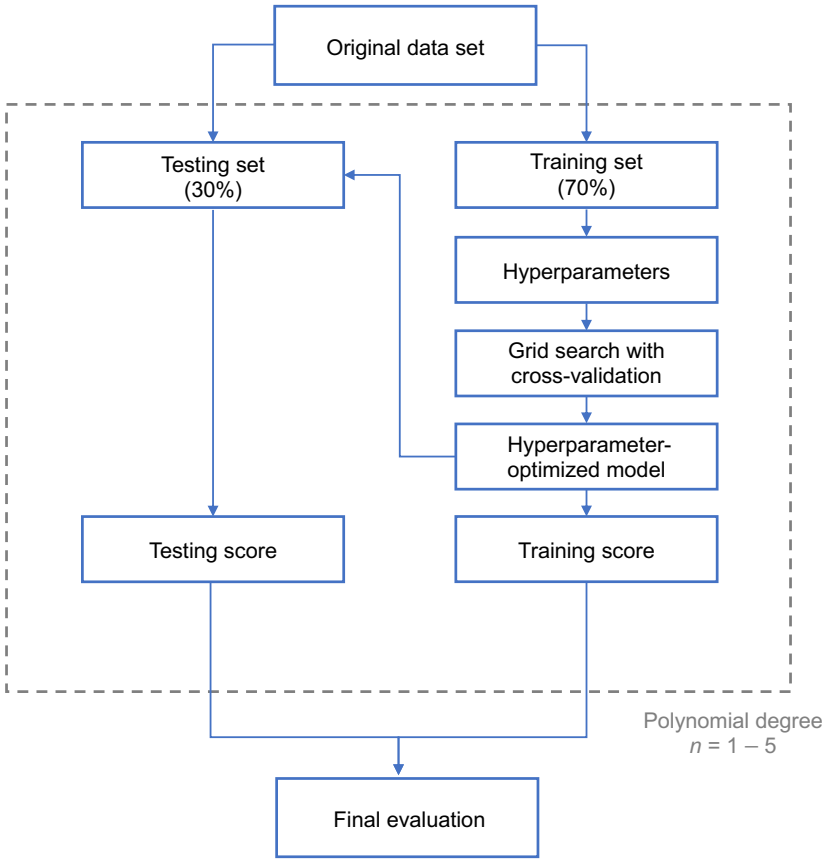
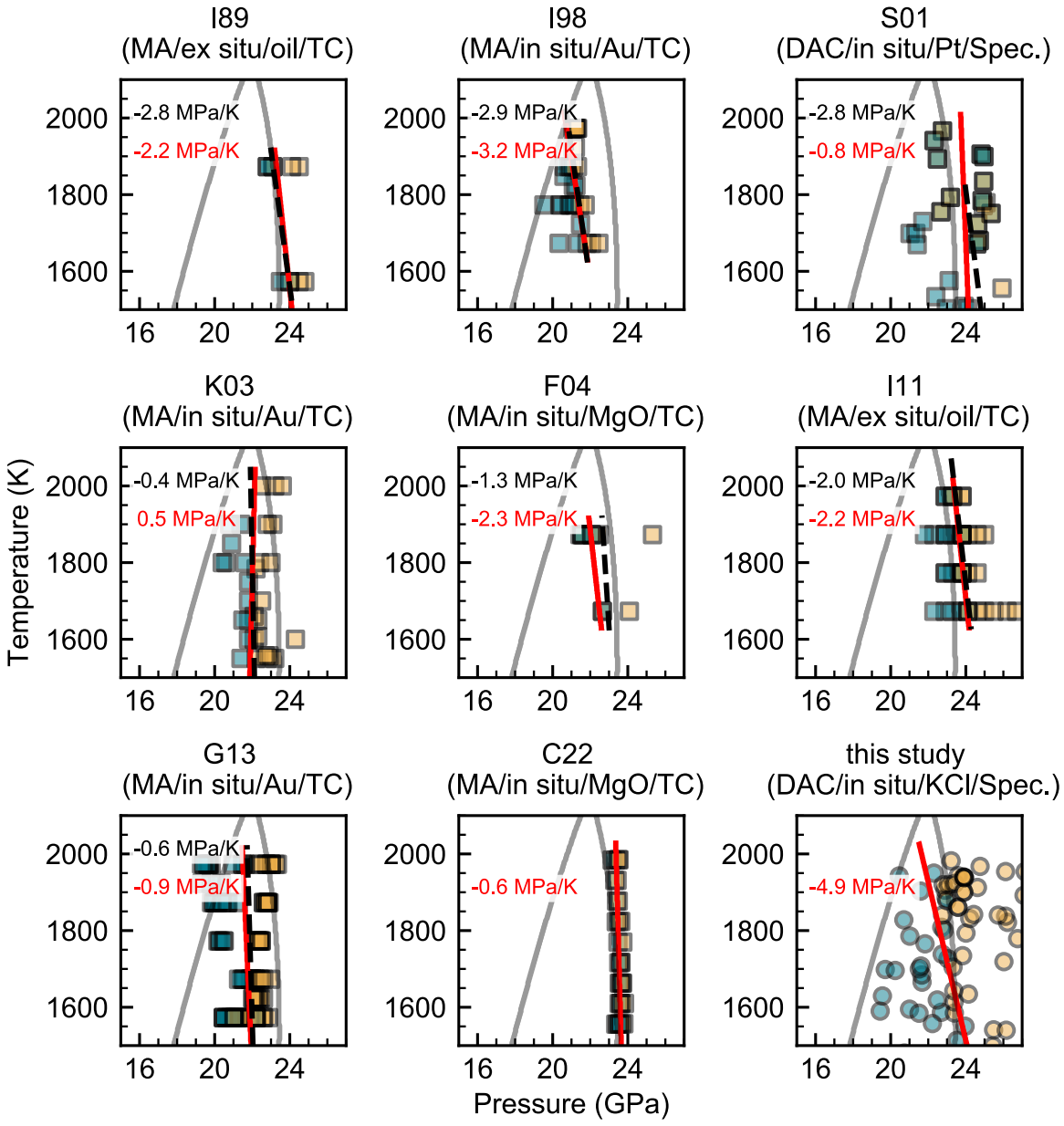


Figure C.2: **Flow chart of machine learning procedure.** The original dataset is split into two sets: a training set (70%) and a testing set (30%). With the training dataset, hyperparameters in the multi-class logistic model are optimized using grid searching with cross-validation. The F1 scores are estimated for the hyperparameter-optimized multi-class logistic models of the polynomials by degree 1 to 5 on the train set and test set, respectively; The best model is selected based on the F1 score of the testing set in the final evaluation.

Figure C.3 *(following page)*: **Benchmarks on the $rw \leftrightarrow bm + pe$ post-spinel transition with the simple binary logistic model for each literature dataset.** Phase stability observations on rw and bm + pe are color-coded in blue and yellow, respectively. Phase boundaries predicted by the simple binary logistic models are plotted as solid red lines while the free-hand drawn phase boundaries previously reported by their respective studies are plotted as dashed black lines. Clapeyron slopes estimated by the simple binary logistic models and free-hand drawing are shown in red and black, respectively. Additional information about the literature dataset is listed above each subplot, including the abbreviations for the relevant study, the type of high pressure techniques used, whether the data was collected in situ or ex situ, the type of pressure scale or calibration used, and the type of temperature measurement. The following abbreviations are used: I89, Ito Takahashi (1989); I98, Irifune et al. (1998); S01, Shim et al. (2001); K03, Katsura et al. (2003); F04, Fei et al. (2004); I11, Ishii et al. (2011); G13, Ghosh et al. (2013); C22, Chanyshev et al. (2022); MA, multi-anvil press; DAC, diamond anvil cell; TC, thermocouple; Spec., spectroradiometer.


I89
(MA/ex situ/oil/TC)
-2.8 MPa/K
-2.2 MPa/K
I98
(MA/in situ/Au/TC)
-2.9 MPa/K
-3.2 MPa/K
S01
(DAC/in situ/Pt/Spec.)
-2.8 MPa/K
-0.8 MPa/K
K03
(MA/in situ/Au/TC)
-0.4 MPa/K
0.5 MPa/K
F04
(MA/in situ/MgO/TC)
-1.3 MPa/K
-2.3 MPa/K
I11
(MA/ex situ/oil/TC)
-2.0 MPa/K
-2.2 MPa/K
G13
(MA/in situ/Au/TC)
-0.6 MPa/K
-0.9 MPa/K
C22
(MA/in situ/MgO/TC)
-0.6 MPa/K
this study
(DAC/in situ/KCl/Spec.)
-4.9 MPa/K
Temperature (K)
Pressure (GPa)
2000
1800
1600
16
20
24

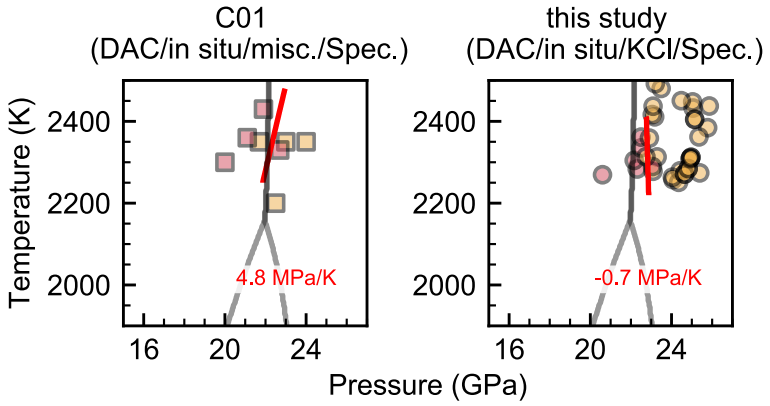


Figure C.4: **Benchmarks on the $wd \leftrightarrow bm+pe$ transition with the simple binary logistic model for each literature dataset.** Phase stability observations on wd and bm + pe are color-coded in red and yellow, respectively. Phase boundaries predicted by the simple binary logistic models are plotted as solid red lines. Clapeyron slopes estimated by the simple binary logistic models are shown in red. Additional information about the literature dataset is listed above each subplot, including the abbreviations for the relevant study, the type of high pressure techniques used, whether the data was collected in situ or ex situ, the type of pressure scale or calibration used, and the type of temperature measurement. The following abbreviations are used: C01, Chudinovskikh & Boehler (2001); DAC, diamond anvil cell; Spec., spectroradiometer; misc., miscellaneous pressure scales.

Figure C.5 *(following page)*: **Benchmarks on the $wd \leftrightarrow rw$ transition with the simple binary logistic model for each literature dataset.** Phase stability observations on wd and rw are color-coded in red and blue, respectively. Phase boundaries predicted by the simple binary logistic models are plotted as solid red lines while the free-hand drawn phase boundaries previously reported by their respective studies are plotted as dashed black lines. Clapeyron slopes estimated by the simple binary logistic models and free-hand drawing are shown in red and black, respectively. Additional information about the literature dataset is listed above each subplot, including the abbreviations for the relevant study, the type of high pressure techniques used, whether the data was collected in situ or ex situ, the type of pressure scale or calibration used, and the type of temperature measurement. The following abbreviations are used: S00, Suzuki et al. (2000); I06, (Inoue et al., 2006); I11, Ishii et al. (2011); MA, multi-anvil press; DAC, diamond anvil cell; TC, thermocouple; Spec., spectroradiometer.

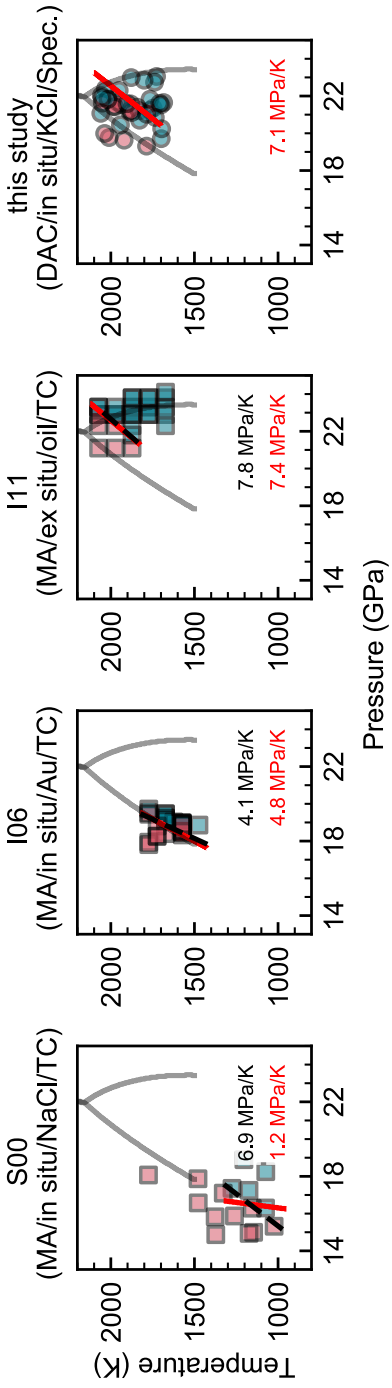

S00
(MA/in situ/NaCl/TC)
I06
(MA/in situ/Au/TC)
I11
(MA/ex situ/oil/TC)
this study
(DAC/in situ/KCl/Spec.)
6.9 MPa/K
1.2 MPa/K
4.1 MPa/K
4.8 MPa/K
7.8 MPa/K
7.4 MPa/K
7.1 MPa/K
Temperature (K)
Pressure (GPa)
2000
1500
1000
14
18
22

Table C.1:: New in situ experimental dataset on the Mg_2SiO_4 phase diagram.

Run #	T (K)	P_W (GPa)	P_W error (GPa)	T error (K)	P_{KCl} (GPa)	P_{KCl} error (GPa)	Phase
D1m	1590	19.8	0.0	184	19.4	1.3	rw
D1m	1630	19.6	0.0	218	19.6	1.3	rw
D1m	1699	18.0	0.1	220	19.7	1.4	rw
D1m	1943	18.0	0.4	278	20.5	1.7	rw
D1m	2060	18.3	0.5	293	21.1	1.8	rw
D1m	2084	18.3	0.5	270	21.1	1.8	rw
D1m	2137	18.3	0.6	311	21.3	1.8	bm
D1m	2171	18.2	0.7	280	21.3	1.9	bm
D1m	2183	18.7	0.6	265	21.5	1.9	bm
D1m	2313	20.5	0.6	290	23.3	2.0	bm
D1m	2193	21.1	0.4	277	23.7	1.9	bm
D1m	2183	23.9	0.1	286	26.3	1.9	bm
D2_spot_1	1595	20.2	0.0	210	21.0	1.5	rw
D2_spot_1	1747	20.3	0.0	244	21.4	1.6	wd

D2_spot_1	1882	20.5	0.0	192	21.6	1.6	wd
D2_spot_1	2140	21.3	0.1	281	22.2	1.9	rw
D2_spot_1	2174	21.5	0.1	251	22.3	1.9	bm
D2_spot_1	2247	21.8	0.1	273	22.3	2.0	bm
D2_spot_1	2595	22.9	0.3	594	23.4	2.5	bm
D2_spot_2	1587	22.0	0.0	212	22.7	1.5	rw
D2_spot_2	1727	22.2	0.0	264	23.1	1.6	rw
D2_spot_2	1943	22.4	0.0	254	23.6	1.7	bm
D2_spot_2	2006	22.6	0.0	254	23.7	1.8	bm
D2_spot_2	2117	22.7	0.0	230	23.8	1.9	bm
D2_spot_2	2258	23.1	0.1	229	24.1	2.0	bm
D2_spot_2	2531	24.1	0.2	580	24.5	2.5	bm
D2_spot_3	1635	22.8	0.0	169	24.1	1.5	bm
D2_spot_3	2033	24.1	0.0	277	25.2	1.8	bm
D2_spot_3	2098	24.1	0.0	260	25.3	1.8	bm
D2_spot_3	2181	24.4	0.0	307	25.0	1.9	bm
D2_spot_3	2230	24.5	0.0	369	25.0	2.0	bm

D4m	1584	17.2	0.0	160	19.2	1.3	wd
D4m	1787	17.2	0.1	200	19.3	1.5	wd
D4m	1921	17.4	0.1	233	19.6	1.6	wd
D4m	2011	17.2	0.1	240	19.8	1.7	wd
D4m	2037	16.8	0.1	238	20.0	1.7	wd
D4m	2106	16.4	0.2	254	20.1	1.8	wd
D4m	2270	17.3	0.2	281	20.6	2.0	wd
D4m	2098	19.8	0.1	230	23.5	1.9	bm
D4m	2173	21.2	0.1	269	25.0	1.9	bm
D5_spot_1	1809	20.8	0.0	240	22.7	1.6	bm
D5_spot_1	1841	20.3	0.0	243	22.8	1.6	bm
D5_spot_1	1886	20.6	0.0	222	23.0	1.6	bm
D5_spot_1	1906	20.2	0.1	291	22.9	1.6	bm
D5_spot_1	1920	20.8	0.0	245	22.8	1.7	bm
D5_spot_1	1920	20.9	0.0	268	23.1	1.7	bm
D5_spot_1	1923	19.4	0.1	308	23.4	1.7	bm
D5_spot_1	1982	20.0	0.1	334	23.2	1.7	bm

D5_spot_1	2049	19.1	0.1	293	23.5	1.8	bm
D5_spot_1	2251	19.0	0.1	256	24.4	1.9	bm
D5_spot_1	2279	19.9	0.1	271	24.4	2.0	bm
D5_spot_1	2433	20.3	0.1	266	25.1	2.1	bm
D5_spot_1	2448	21.1	0.1	249	25.0	2.1	bm
D5_spot_1	2567	20.8	0.3	449	25.1	2.4	bm
D5_spot_1	2628	19.5	0.4	517	25.7	2.4	bm
D5_spot_2	1719	24.1	0.1	177	26.0	1.4	bm
D5_spot_2	1822	23.2	0.0	263	26.2	1.5	bm
D5_spot_2	1838	23.6	0.0	257	26.1	1.6	bm
D5_spot_2	1841	20.5	0.0	278	25.7	1.7	bm
D5_spot_2	1954	19.7	0.1	294	26.1	1.8	bm
D5_spot_2	2066	19.6	0.1	327	26.5	1.8	bm
D5_spot_2	2164	19.8	0.2	427	26.9	1.9	bm
D5_spot_2	2220	21.0	0.1	324	27.2	1.9	bm
D5_spot_2	2311	20.2	0.1	302	27.4	2.0	bm
D5_spot_2	2374	19.9	0.2	422	27.5	2.1	bm

D5_spot_2	2405	19.6	0.3	437	27.9	2.2	bm
D6_spot_1	1609	17.9	0.0	207	20.8	1.5	wd
D6_spot_1	1766	18.4	0.1	268	21.2	1.6	wd
D6_spot_1	1842	18.6	0.1	294	21.4	1.7	wd
D6_spot_1	1883	18.2	0.1	283	21.2	1.7	wd
D6_spot_1	1889	17.0	0.1	288	21.2	1.7	wd
D6_spot_1	1984	17.5	0.1	274	21.4	1.8	wd
D6_spot_1	2050	16.9	0.2	334	21.8	1.9	bm
D6_spot_1	2140	17.2	0.2	328	21.9	1.9	bm
D6_spot_1	2198	17.0	0.2	369	22.4	2.0	bm
D6_spot_1	2238	17.2	0.2	372	22.6	2.1	bm
D6_spot_1	2378	17.0	0.3	440	22.8	2.3	bm
D6_spot_1	2420	17.1	0.3	461	22.9	2.3	bm
D10_spot_1	1585	20.7	0.0	322	21.5	1.5	rw
D10_spot_1	1666	20.7	0.0	297	21.7	1.5	rw
D10_spot_1	1684	20.6	0.0	261	21.7	1.5	rw
D10_spot_1	1766	20.4	0.0	229	21.8	1.6	rw

D10_spot_1	1950	21.3	0.0	258	22.3	1.7	rw
D10_spot_1	2032	22.4	0.0	228	22.4	1.8	rw
D10_spot_1	2170	23.1	0.0	253	22.9	2.0	bm
D10_spot_1	2278	24.2	0.0	242	23.1	2.1	bm
D10_spot_1	2518	24.7	0.1	252	23.7	2.3	bm
D10_spot_1	2528	25.2	0.1	273	23.8	2.3	bm
D10_spot_1	2687	26.3	0.1	270	24.3	2.5	bm
D10_spot_2	1619	21.9	0.0	234	22.5	1.4	rw
D10_spot_2	1739	22.3	0.0	223	22.7	1.5	rw
D10_spot_2	1801	22.6	0.0	198	22.9	1.5	rw
D10_spot_2	1878	22.4	0.0	247	23.0	1.6	rw
D10_spot_2	2112	24.2	0.0	219	23.6	1.8	bm
D10_spot_2	2264	25.3	0.0	235	24.0	2.0	bm
D10_spot_2	2451	26.8	0.0	268	24.5	2.2	bm
D10_spot_2	2610	27.7	0.1	326	25.2	2.3	bm
D10_spot_3	1585	22.7	0.1	256	23.4	1.5	bm
D10_spot_3	1614	22.8	0.1	293	23.4	1.6	bm

D10_spot_3	1643	22.7	0.1	292	23.4	1.6	bm
D10_spot_3	1705	22.8	0.0	280	23.3	1.8	bm
D10_spot_3	1735	22.7	0.0	251	23.8	1.5	bm
D10_spot_3	1794	22.9	0.0	229	24.0	1.5	bm
D10_spot_3	1832	22.9	0.0	190	24.2	1.6	bm
D10_spot_3	2070	23.2	0.0	215	24.8	1.8	bm
D10_spot_3	2274	25.5	0.0	233	25.4	2.0	bm
D10_spot_3	2385	25.9	0.0	256	25.8	2.1	bm
D10_spot_3	2438	25.6	0.0	260	25.9	2.1	bm
D10_spot_3	2511	25.7	0.1	281	26.0	2.2	bm
D10_spot_3	2526	25.6	0.1	283	26.1	2.2	bm
D10_spot_3	2619	25.8	0.1	355	26.2	2.3	bm
D11m	1700	19.0	0.0	217	21.5	1.4	rw
D11m	1708	19.0	0.0	229	21.6	1.4	rw
D11m	2142	19.6	0.1	218	22.1	2.2	rw
D11m	2213	18.7	0.1	245	22.8	1.9	wd
D11m	2290	18.2	0.1	263	23.1	2.0	wd

D11m	2481	19.8	0.2	255	23.5	2.2	bm
D11m	2532	21.3	0.1	272	25.1	2.3	bm
D11m	2670	22.8	0.2	271	26.7	2.4	bm
D13_spot_1	1696	19.0	0.0	245	20.2	1.6	rw
D13_spot_1	1828	18.7	0.1	258	20.7	1.7	rw
D13_spot_1	1876	18.2	0.1	266	21.1	1.7	wd
D13_spot_1	1977	18.3	0.1	288	21.4	1.8	wd
D13_spot_1	2051	17.8	0.1	293	21.6	1.8	wd
D13_spot_1	2085	18.4	0.1	286	21.7	1.8	wd
D13_spot_1	2132	18.0	0.1	282	21.7	1.8	wd
D13_spot_1	2153	18.0	0.1	294	21.9	1.9	wd
D13_spot_1	2156	17.6	0.1	280	22.0	1.9	wd
D13_spot_1	2284	18.0	0.2	301	22.3	2.0	wd
D13_spot_1	2305	17.9	0.2	276	22.2	2.0	wd
D13_spot_1	2335	17.6	0.2	292	22.5	2.0	wd
D13_spot_1	2362	18.0	0.2	282	22.5	2.0	wd
D13_spot_2	1786	18.8	0.0	187	21.0	1.5	rw

D13_spot_2	1903	18.6	0.1	205	21.6	1.6	rw
D13_spot_2	2017	18.8	0.1	236	21.8	1.7	rw
D13_spot_2	2052	18.6	0.1	218	21.9	1.7	rw
D13_spot_2	2173	18.6	0.1	252	22.2	1.9	bm
D13_spot_2	2225	18.3	0.1	226	22.5	1.9	bm
D13_spot_2	2242	18.2	0.1	247	22.4	2.0	bm
D13_spot_2	2314	18.3	0.1	240	22.7	2.0	bm
D13_spot_2	2359	18.4	0.2	252	22.9	2.0	bm
D13_spot_2	2411	18.9	0.2	262	23.2	2.1	bm
D13_spot_2	2417	18.3	0.2	269	23.1	2.1	bm
D13_spot_2	2437	18.4	0.2	257	23.1	2.1	bm
D13_spot_2	2492	18.5	0.2	284	23.2	2.2	bm
D14_spot_1	1842	22.2	0.0	203	24.4	1.6	bm
D14_spot_1	1913	21.8	0.0	220	24.6	1.6	bm
D14_spot_1	1968	20.8	0.0	221	24.8	1.7	bm
D14_spot_1	2079	21.1	0.1	229	25.0	1.8	bm
D14_spot_1	2108	20.9	0.1	236	25.1	1.8	bm

D14_spot_1	2142	20.6	0.1	239	25.1	1.8	bm
D14_spot_1	2202	20.4	0.1	288	24.9	1.9	bm
D14_spot_1	2215	20.3	0.1	264	25.0	1.9	bm
D14_spot_1	2236	20.2	0.1	260	25.2	1.9	bm
D14_spot_1	2362	20.1	0.1	299	25.4	2.1	bm
D14_spot_2	1861	21.2	0.0	222	23.6	1.7	bm
D14_spot_2	1901	20.9	0.0	259	23.9	1.7	bm
D14_spot_2	1938	20.6	0.0	254	23.9	1.8	bm
D14_spot_2	1940	20.6	0.0	242	23.9	1.8	bm
D14_spot_2	2002	20.5	0.1	241	24.1	1.8	bm
D14_spot_2	2069	20.4	0.1	261	24.2	1.8	bm
D14_spot_2	2078	20.0	0.1	271	24.1	1.8	bm
D14_spot_2	2166	20.1	0.1	251	24.2	1.9	bm
D14_spot_2	2185	20.0	0.1	276	24.3	1.9	bm
D14_spot_2	2271	20.7	0.1	306	24.6	2.0	bm
D14_spot_2	2285	20.2	0.1	296	24.8	2.0	bm
D14_spot_2	2309	20.6	0.1	285	24.9	2.0	bm

D14_spot_2	2312	20.4	0.1	293	25.0	2.0	bm
D14_spot_2	2405	20.0	0.2	320	25.1	2.1	bm
D14_spot_3	1635	23.9	0.1	179	23.3	1.4	bm
D14_spot_3	1763	24.1	0.0	184	23.6	1.5	bm
D14_spot_3	1852	24.2	0.0	189	23.7	1.6	bm
D14_spot_3	1928	24.4	0.0	207	23.8	1.6	bm
D14_spot_3	2007	24.5	0.0	213	23.8	1.7	bm
D14_spot_3	2137	24.5	0.0	251	24.2	1.8	bm
D14_spot_3	2153	24.4	0.0	254	24.1	1.9	bm
D14_spot_3	2248	24.5	0.0	254	24.5	1.9	bm
D14_spot_3	2266	24.7	0.0	281	24.5	2.0	bm
D14_spot_3	2267	24.5	0.0	230	24.5	2.0	bm
D14_spot_3	2339	24.9	0.0	261	24.6	2.1	bm
D14_spot_3	2344	24.7	0.0	277	24.5	2.1	bm
D14_spot_3	2372	24.9	0.0	244	24.6	2.1	bm
D14_spot_3	2376	24.6	0.1	315	24.6	2.1	bm
D14_spot_3	2436	24.7	0.1	405	24.7	2.2	bm

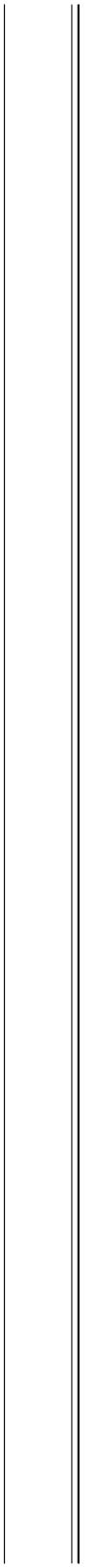


Table C.2:: In situ phase stability observations in Mg_2SiO_4 compiled from literature with corrected pressures and temperatures.

Exp #	**T (K)**	**P (GPa)**	**Phase**
C22	1238	22.9	rw
C22	1238	23.0	rw
C22	1239	23.3	rw
C22	1240	24.2	bm
C22	1292	23.5	rw
C22	1344	23.4	rw
C22	1345	23.7	bm
C22	1397	23.6	rw
C22	1450	23.6	rw
C22	1450	23.7	bm
C22	1450	23.5	rw
C22	1451	23.9	bm
C22	1556	23.4	rw
C22	1556	23.4	rw
C22	1556	23.5	rw
C22	1557	23.8	bm
C22	1557	23.7	bm
C22	1557	23.6	rw
C22	1610	23.6	rw
C22	1610	23.8	bm

C22	1610	23.5	rw
C22	1610	23.6	bm
C22	1663	23.7	bm
C22	1663	23.5	rw
C22	1663	23.6	rw
C22	1663	23.7	bm
C22	1716	23.5	rw
C22	1717	23.6	bm
C22	1717	23.6	bm
C22	1770	23.5	rw
C22	1770	23.7	bm
C22	1823	23.4	rw
C22	1824	23.6	bm
C22	1824	23.5	bm
C22	1877	23.4	rw
C22	1877	23.5	bm
C22	1931	23.3	rw
C22	1931	23.4	bm
C22	1984	23.2	rw
C22	1984	23.4	rw
C22	1985	23.5	bm
C22	1985	23.5	bm
C22	2038	23.0	rw

C22	2038	23.2	rw
C22	2038	23.4	bm
C22	2038	23.3	rw
G13	1273	21.0	rw
G13	1273	21.2	rw
G13	1273	21.3	rw
G13	1273	21.3	rw
G13	1273	21.4	rw
G13	1273	21.4	rw
G13	1273	21.9	rw
G13	1273	20.9	rw
G13	1273	21.1	rw
G13	1273	21.2	rw
G13	1273	21.3	rw
G13	1273	22.2	bm
G13	1273	22.3	bm
G13	1273	22.3	bm
G13	1273	22.3	bm
G13	1273	22.3	bm
G13	1273	22.5	bm
G13	1273	22.5	bm
G13	1273	22.4	bm
G13	1273	22.5	bm

G13	1273	22.5	bm
G13	1273	23.9	rw
G13	1273	23.9	rw
G13	1273	23.9	rw
G13	1273	23.9	rw
G13	1273	23.9	bm
G13	1273	23.9	bm
G13	1273	23.9	bm
G13	1273	23.9	bm
G13	1373	24.1	bm
G13	1373	24.0	bm
G13	1373	24.1	bm
G13	1373	21.8	rw
G13	1373	21.9	rw
G13	1373	21.9	rw
G13	1373	22.0	rw
G13	1373	22.0	rw
G13	1373	22.6	bm
G13	1373	22.7	bm
G13	1373	22.7	bm
G13	1373	22.8	bm
G13	1373	22.7	bm
G13	1373	22.6	bm

G13	1373	22.5	bm
G13	1373	22.6	bm
G13	1473	22.1	rw
G13	1473	22.1	rw
G13	1473	22.1	rw
G13	1473	22.5	bm
G13	1473	22.5	bm
G13	1473	22.6	bm
G13	1473	22.5	bm
G13	1473	22.6	bm
G13	1473	22.7	bm
G13	1473	22.7	bm
G13	1473	22.7	bm
G13	1473	22.7	bm
G13	1473	22.5	bm
G13	1473	22.6	bm
G13	1473	22.3	bm
G13	1473	21.7	rw
G13	1473	21.8	rw
G13	1473	22.0	rw
G13	1573	22.9	bm
G13	1573	22.6	bm
G13	1573	22.6	bm

G13	1573	21.3	rw
G13	1573	21.2	rw
G13	1573	21.1	rw
G13	1573	21.2	rw
G13	1573	21.1	rw
G13	1573	21.2	rw
G13	1573	21.1	rw
G13	1573	20.7	rw
G13	1573	20.9	rw
G13	1573	20.8	rw
G13	1573	20.6	rw
G13	1573	20.5	rw
G13	1573	20.5	rw
G13	1573	20.5	rw
G13	1573	22.2	bm
G13	1573	22.2	bm
G13	1573	21.9	bm
G13	1573	21.9	bm
G13	1573	22.2	rw
G13	1573	21.0	rw
G13	1573	22.2	bm
G13	1573	21.0	bm
G13	1623	22.6	bm

G13	1623	22.4	bm
G13	1623	22.2	bm
G13	1623	22.4	bm
G13	1623	22.1	bm
G13	1623	22.2	bm
G13	1623	22.0	bm
G13	1623	22.1	bm
G13	1673	22.2	bm
G13	1673	22.0	bm
G13	1673	21.9	bm
G13	1673	22.1	bm
G13	1673	22.0	bm
G13	1673	21.9	bm
G13	1673	21.9	bm
G13	1673	23.0	bm
G13	1673	22.2	bm
G13	1673	22.0	bm
G13	1673	22.4	bm
G13	1673	22.5	bm
G13	1673	22.6	bm
G13	1673	21.6	rw
G13	1673	21.5	rw
G13	1673	21.5	rw

G13	1673	21.3	rw
G13	1773	20.2	rw
G13	1773	20.3	rw
G13	1773	20.2	rw
G13	1773	22.3	bm
G13	1773	22.3	bm
G13	1773	22.4	bm
G13	1773	22.4	bm
G13	1773	22.3	bm
G13	1773	22.3	bm
G13	1773	22.5	bm
G13	1773	22.5	bm
G13	1773	20.5	rw
G13	1773	20.5	rw
G13	1873	19.9	rw
G13	1873	20.2	rw
G13	1873	20.1	rw
G13	1873	20.0	rw
G13	1873	20.2	rw
G13	1873	20.0	rw
G13	1873	19.8	rw
G13	1873	22.6	bm
G13	1873	22.6	bm

G13	1873	22.9	bm
G13	1873	22.8	bm
G13	1873	22.8	bm
G13	1873	22.8	bm
G13	1873	22.7	bm
G13	1873	22.8	bm
G13	1873	22.8	bm
G13	1873	20.7	rw
G13	1873	20.7	rw
G13	1873	20.6	rw
G13	1873	21.3	rw
G13	1873	20.4	rw
G13	1923	20.4	rw
G13	1923	19.8	rw
G13	1923	19.3	rw
G13	1973	19.8	rw
G13	1973	19.7	rw
G13	1973	19.7	rw
G13	1973	19.7	rw
G13	1973	19.6	rw
G13	1973	19.4	rw
G13	1973	19.5	rw
G13	1973	22.8	bm

G13	1973	22.8	bm
G13	1973	23.0	bm
G13	1973	23.2	bm
G13	1973	23.3	bm
G13	1973	23.0	bm
G13	1973	23.0	bm
G13	1973	22.3	bm
G13	1973	22.5	bm
G13	1973	21.7	rw
G13	1973	21.5	rw
G13	1973	21.5	rw
G13	1973	21.0	rw
G13	1973	19.3	rw
G13	2023	23.3	bm
G13	2023	23.1	bm
I11	1673	24.6	bm
I11	1673	25.0	bm
I11	1673	25.5	bm
I11	1673	23.8	rw
I11	1673	23.3	rw
I11	1673	22.9	rw
I11	1673	24.1	rw
I11	1673	24.1	bm

I11	1673	22.3	rw
I11	1673	26.2	bm
I11	1673	26.7	bm
I11	1773	22.9	rw
I11	1773	23.3	rw
I11	1773	22.9	rw
I11	1773	24.6	bm
I11	1773	24.1	bm
I11	1773	23.8	rw
I11	1773	23.8	bm
I11	1773	23.8	rw
I11	1773	23.8	bm
I11	1873	25.0	bm
I11	1873	24.1	bm
I11	1873	24.6	bm
I11	1873	23.8	rw
I11	1873	23.8	bm
I11	1873	22.3	rw
I11	1873	22.9	rw
I11	1873	23.3	rw
I11	1873	21.1	wd
I11	1873	23.8	rw
I11	1873	23.8	bm

I11	1873	22.9	rw
I11	1873	21.8	rw
I11	1973	22.9	rw
I11	1973	22.3	wd
I11	1973	22.9	rw
I11	1973	23.8	bm
I11	1973	23.8	bm
I11	1973	23.3	rw
I11	1973	23.3	bm
I11	1973	21.1	wd
I11	2073	22.9	wd
I11	2073	22.9	bm
I11	2073	23.3	rw
I11	2073	23.3	bm
I11	2073	22.9	wd
I11	2073	22.9	bm
I11	2073	22.3	wd
I11	2073	25.0	bm
I11	2073	23.8	bm
I11	2073	23.3	rw
I11	2073	23.3	bm
I11	2073	28.0	bm
I11	2073	27.0	bm

I11	2073	26.2	bm
I11	2073	25.5	bm
I11	2073	21.1	wd
I06	300	13.9	wd
I06	300	15.2	wd
I06	300	15.3	wd
I06	1473	18.9	rw
I06	1573	18.8	rw
I06	1573	19.0	rw
I06	1573	19.0	rw
I06	1573	18.5	rw
I06	1573	18.5	rw
I06	1573	18.8	rw
I06	1573	18.8	rw
I06	1573	19.0	rw
I06	1573	19.0	rw
I06	1573	18.9	rw
I06	1573	18.3	wd
I06	1573	18.5	wd
I06	1573	18.5	wd
I06	1573	18.9	wd
I06	1623	19.0	rw
I06	1673	19.2	rw

I06	1673	19.5	rw
I06	1673	19.5	rw
I06	1673	19.2	rw
I06	1673	19.1	rw
I06	1673	18.4	wd
I06	1723	18.8	wd
I06	1723	18.3	wd
I06	1723	18.3	wd
I06	1773	19.7	rw
I06	1773	19.5	rw
I06	1773	17.9	wd
I06	1773	17.8	wd
I06	1773	19.4	wd
F04	1673	23.4	bm
F04	1673	23.4	rw
F04	1673	24.6	bm
F04	1873	22.1	rw
F04	1873	22.1	rw
F04	1873	22.7	rw
F04	1873	22.4	rw
F04	1873	23.1	bm
F04	1873	25.6	bm
F04	2023	22.6	rw

F04	2023	23.0	bm
F04	2173	21.6	wd
F04	2173	22.5	wd
F04	2173	22.8	wd
F04	2173	22.8	rw
F04	2173	22.8	bm
K03	1200	24.8	bm
K03	1350	24.4	bm
K03	1550	23.2	bm
K03	1550	22.8	bm
K03	1550	22.2	bm
K03	1550	21.4	rw
K03	1557	22.9	bm
K03	1557	22.7	bm
K03	1600	24.3	bm
K03	1600	22.1	bm
K03	1600	21.8	rw
K03	1607	22.3	bm
K03	1650	22.3	bm
K03	1650	21.8	rw
K03	1650	21.5	rw
K03	1660	22.1	bm
K03	1700	22.5	bm

K03	1700	21.8	rw
K03	1750	21.8	rw
K03	1784	22.2	bm
K03	1800	22.4	bm
K03	1800	23	bm
K03	1800	20.6	rw
K03	1800	20.4	rw
K03	1800	21.6	rw
K03	1850	20.9	rw
K03	1900	23.1	bm
K03	1900	22.8	bm
K03	1900	21.4	rw
K03	1900	20.8	rw
K03	2000	23.2	bm
K03	2000	22.5	bm
K03	2000	23.6	bm
K03	2050	22.2	bm
K03	2050	20.9	rw
K03	2100	21.1	rw
S01	1699	21.0	rw
S01	1699	21.3	rw
S01	1670	21.4	rw
S01	1534	22.4	rw

S01	1576	23.1	rw
S01	1502	23.0	rw
S01	1509	23.9	rw
S01	1502	24.1	rw
S01	1730	21.7	rw
S01	1466	30.4	bm
S01	1731	29.7	bm
S01	1879	30.0	bm
S01	1461	27.4	bm
S01	1591	27.7	bm
S01	1701	28.3	bm
S01	1809	28.5	bm
S01	1869	28.4	bm
S01	1882	28.6	bm
S01	1964	28.0	bm
S01	2145	27.5	bm
S01	2135	27.0	bm
S01	2233	26.3	bm
S01	2195	25.6	bm
S01	2218	24.9	bm
S01	2235	24.9	bm
S01	1779	25.1	bm
S01	1771	24.9	bm

S01	1556	25.9	bm
S01	1461	24.7	bm
S01	2027	23.6	bm
S01	2032	23.2	bm
C01	1800	25.8	bm
C01	1800	22.6	rw
C01	1800	22.6	bm
C01	1880	23.0	bm
C01	1950	22.0	rw
C01	1950	24.0	bm
C01	2000	21.2	wd
C01	2000	21.2	rw
C01	2030	23.0	rw
C01	2030	23.0	bm
C01	2030	22.2	rw
C01	2050	21.1	rw
C01	2100	21.3	wd
C01	2100	21.3	rw
C01	2200	22.5	rw
C01	2200	22.5	bm
C01	2230	22.2	rw
C01	2300	20.0	wd
C01	2330	22.7	wd

C01	2350	23.0	bm
C01	2350	21.7	bm
C01	2350	24.0	bm
C01	2360	21.1	wd
C01	2430	21.9	wd
C01	2870	22.0	bm
S00	922	15.0	rw
S00	924	15.3	rw
S00	973	16.4	rw
S00	1075	16.3	rw
S00	1174	17.2	rw
S00	1275	17.4	rw
S00	1073	18.3	rw
S00	1204	18.9	rw
S00	973	19.5	rw
S00	1024	15.3	wd
S00	1146	15.0	wd
S00	1173	14.9	wd
S00	1372	14.9	wd
S00	1261	15.9	wd
S00	1154	16.3	wd
S00	1328	17.1	wd
S00	1376	15.8	wd

S00	1477	16.6	wd
S00	1479	17.9	wd
S00	1775	18.1	wd
I98	1673	20.3	rw
I98	1673	21.3	rw
I98	1673	21.8	bm
I98	1673	22.1	bm
I98	1673	22.5	bm
I98	1723	21.5	rw
I98	1773	19.5	rw
I98	1773	20.4	rw
I98	1773	20.4	rw
I98	1773	20.9	rw
I98	1773	21.0	rw
I98	1773	21.2	rw
I98	1773	21.5	bm
I98	1773	21.7	bm
I98	1823	21.1	rw
I98	1823	21.2	rw
I98	1848	20.6	rw
I98	1873	20.6	rw
I98	1873	20.9	rw
I98	1873	21.0	rw

I98	1873	21.3	bm
I98	1873	21.1	bm
I98	1923	21.1	bm
I98	1923	21.2	bm
I98	1973	21.1	bm
I98	1973	21.2	bm
I98	1973	21.2	bm
I98	1973	21.3	bm
I98	1973	21.3	bm
I98	2023	21.2	bm
I98	2053	20.4	rw
I98	2073	20.8	bm
I89	1273	25	bm
I89	1273	24.5	rw
I89	1273	24.8	rw
I89	1273	24.8	bm
I89	1373	25	bm
I89	1373	24.8	bm
I89	1373	24.5	rw
I89	1373	24.5	bm
I89	1373	24.2	rw
I89	1573	24.8	bm
I89	1573	24.5	bm

I89	1573	24	rw
I89	1573	24	bm
I89	1573	23.5	rw
I89	1873	24.5	bm
I89	1873	24.1	bm
I89	1873	22.8	rw
I89	1873	23.1	rw
I89	1873	23.1	bm
I89	1873	22.8	rw

The following abbreviations are used: [**C22**] Chanyshev, A., Ishii, T., Bondar, D., Bhat, S., Kim, E. J., Farla, R., Nishida, K., Liu, Z., Wang, L., Nakajima, A., Yan, B., Tang, H., Chen, Z., Higo, Y., Tange, Y., & Katsura, T. (2022). Depressed 660-km discontinuity caused by akimotoite–bridgmanite transition. Nature, 601(7891), 69–73. [**G13**] Ghosh, S., Ohtani, E., Litasov, K. D., Suzuki, A., Dobson, D., & Funakoshi, K. (2013). Effect of water in depleted mantle on post-spinel transition and implication for 660km seismic discontinuity. Earth and Planetary Science Letters, 371–372, 103–111. [**I11**] Ishii, T., Kojitani, H., & Akaogi, M. (2011). Post-spinel transitions in pyrolite and Mg_2SiO_4 and akimotoite-perovskite transition in $MgSiO_3$: Precise comparison by high-pressure high-temperature experiments with multi-sample cell technique. Earth and Planetary Science Letters, 309(3–4), 185–197. [**I06**] Inoue, T., Irifune, T., Higo, Y., Sanehira, T., Sueda, Y., Yamada, A., Shinmei, T., Yamazaki, D., Ando, J., Funakoshi,

K., & Utsumi, W. (2006). The phase boundary between wadsleyite and ringwoodite in Mg_2SiO_4 determined by in situ X-ray diffraction. Physics and Chemistry of Minerals, 33(2), 106–114. [**F04**] Fei, Y., van Orman, J., Li, J., van Westrenen, W., Sanloup, C., Minarik, W., Hirose, K., Komabayashi, T., Walter, M., & Funakoshi, K. (2004). Experimentally determined postspinel transformation boundary in Mg_2SiO_4 using MgO as an internal pressure standard and its geophysical implications. Journal of Geophysical Research: Solid Earth, 109(B2). [**K03**] Katsura, T., Yamada, H., Shinmei, T., Kubo, A., Ono, S., Kanzaki, M., Yoneda, A., Walter, M. J., Ito, E., Urakawa, S., Funakoshi, K., & Utsumi, W. (2003). Post-spinel transition in Mg_2SiO_4 determined by high P–T in situ X-ray diffractometry. Physics of the Earth and Planetary Interiors, 136(1–2), 11–24. [**S01**] Shim, S.-H., Duffy, T. S., & Shen, G. (2001). The post-spinel transformation in Mg_2SiO_4 and its relation to the 660-km seismic discontinuity. Nature, 411, 571–574. [**C01**] Chudinovskikh, L., & Boehler, R. (2001). High-pressure polymorphs of olivine and the 660-km seismic discontinuity. Nature, 411, 574–577. [**S00**] Suzuki, A., Ohtani, E., Morishima, H., Kubo, T., Kanbe, Y., Kondo, T., Okada, T., Terasaki, H., Kato, T., & Kikegawa, T. (2000). In situ determination of the phase boundary between wadsleyite and ringwoodite in Mg_2SiO_4. Geophysical Research Letters, 27(6), 803–806. [**I98**] Irifune, T., Nishiyama, N., Kuroda, K., Inoue, T., Isshiki, M., Utsumi, W., Urakawa, S., Uchida, T., & Ohtaka, O. (1998). The Postspinel Phase Boundary in Mg_2SiO_4 Determined by in Situ X-ray Diffraction. Science, 279(5357), 1698–1700. [**I89**] Ito, E., & Takahashi, E. (1989). Postspinel transformations in the system Mg_2SiO_4–Fe_2SiO_4 and some geophysical implications. Journal of Geophysical Research, 94(B8).

Table C.3:: In situ phase stability observations in Mg_2SiO_4 compiled from literature with uncorrected pressures and temperatures.

Exp #	**T (K)**	**P (GPa)**	**Phase**
C22	1238	22.9	rw
C22	1238	23.0	rw
C22	1239	23.3	rw
C22	1240	24.2	bm
C22	1292	23.5	rw
C22	1344	23.4	rw
C22	1345	23.7	bm
C22	1397	23.6	rw
C22	1450	23.6	rw
C22	1450	23.7	bm
C22	1450	23.5	rw
C22	1451	23.9	bm
C22	1556	23.4	rw
C22	1556	23.4	rw
C22	1556	23.5	rw
C22	1557	23.8	bm
C22	1557	23.7	bm
C22	1557	23.6	rw
C22	1610	23.6	rw
C22	1610	23.8	bm

C22	1610	23.5	rw
C22	1610	23.6	bm
C22	1663	23.7	bm
C22	1663	23.5	rw
C22	1663	23.6	rw
C22	1663	23.7	bm
C22	1716	23.5	rw
C22	1717	23.6	bm
C22	1717	23.6	bm
C22	1770	23.5	rw
C22	1770	23.7	bm
C22	1823	23.4	rw
C22	1824	23.6	bm
C22	1824	23.5	bm
C22	1877	23.4	rw
C22	1877	23.5	bm
C22	1931	23.3	rw
C22	1931	23.4	bm
C22	1984	23.2	rw
C22	1984	23.4	rw
C22	1985	23.5	bm
C22	1985	23.5	bm
C22	2038	23.0	rw

C22	2038	23.2	rw
C22	2038	23.4	bm
C22	2038	23.3	rw
K09	309	11.8	wd
K09	309	19.0	wd
K09	310	14.6	wd
K09	311	14.6	wd
K09	312	13.2	wd
K09	312	15.6	wd
K09	312	17.2	wd
K09	313	12.6	wd
K09	313	16.3	wd
K09	313	16.2	wd
K09	320	14.1	wd
K09	507	12.8	wd
K09	507	12.0	wd
K09	508	14.7	wd
K09	508	14.8	wd
K09	508	15.8	wd
K09	508	16.5	wd
K09	508	16.4	wd
K09	509	17.4	wd
K09	711	12.4	wd

K09	712	13.0	wd
K09	713	15.0	wd
K09	713	15.2	wd
K09	713	16.1	wd
K09	713	16.6	wd
K09	714	16.8	wd
K09	714	17.8	wd
K09	917	13.4	wd
K09	917	12.7	wd
K09	919	15.4	wd
K09	919	15.6	wd
K09	920	16.5	wd
K09	920	17.3	wd
K09	920	16.9	wd
K09	921	18.1	wd
K09	1123	13.2	wd
K09	1124	13.7	wd
K09	1126	15.8	wd
K09	1127	16.1	wd
K09	1128	17.1	wd
K09	1128	17.7	wd
K09	1128	17.2	wd
K09	1129	18.7	wd

K09	1332	14.1	wd
K09	1332	13.7	wd
K09	1335	16.2	wd
K09	1336	16.6	wd
K09	1337	17.6	wd
K09	1337	17.6	wd
K09	1338	18.3	wd
K09	1339	19.1	wd
K09	1437	14.3	wd
K09	1540	13.7	wd
K09	1541	13.9	wd
K09	1541	14.1	wd
K09	1542	14.5	wd
K09	1542	14.8	wd
K09	1545	16.6	wd
K09	1546	17.2	wd
K09	1546	17.1	wd
K09	1547	17.9	wd
K09	1547	17.7	wd
K09	1548	18.1	wd
K09	1548	18.1	wd
K09	1549	18.8	wd
K09	1645	13.7	wd

K09	1647	14.6	wd
K09	1647	14.5	wd
K09	1653	17.7	wd
K09	1752	14.7	wd
K09	1755	15.9	wd
K09	1757	17.0	wd
K09	1758	17.5	wd
K09	1759	17.7	wd
K09	1760	18.5	wd
K09	1760	18.4	wd
K09	1761	19.0	wd
K09	1761	19.0	wd
K09	1762	19.4	wd
K09	1762	19.7	wd
K09	1867	18.7	wd
K09	1867	18.6	wd
K09	1976	20.0	wd
K09	2193	20.8	wd
K09	2193	20.8	wd
I06	300	14.4	wd
I06	300	15.7	wd
I06	300	15.8	wd
I06	1473	19.0	rw

I06	1573	18.8	rw
I06	1573	18.4	wd
I06	1573	18.6	wd
I06	1573	18.6	wd
I06	1573	18.6	rw
I06	1573	18.5	rw
I06	1573	18.9	rw
I06	1573	18.9	rw
I06	1573	19.0	wd
I06	1573	19.1	rw
I06	1573	19.1	rw
I06	1573	19.0	rw
I06	1573	19.0	rw
I06	1573	19.1	rw
I06	1623	19.1	rw
I06	1673	18.5	wd
I06	1673	19.3	rw
I06	1673	19.6	rw
I06	1673	19.6	rw
I06	1673	19.3	rw
I06	1673	19.2	rw
I06	1723	18.9	wd
I06	1723	18.3	wd

I06	1723	18.3	wd
I06	1773	18.0	wd
I06	1773	17.9	wd
I06	1773	19.8	rw
I06	1773	19.6	rw
I06	1773	19.5	rw
K04	300	0.2	rw
K04	302	4.3	rw
K04	302	5.0	rw
K04	303	10.0	rw
K04	304	15.4	rw
K04	305	19.9	rw
K04	305	18.8	rw
K04	305	19.2	rw
K04	305	19.4	rw
K04	305	20.8	rw
K04	305	21.5	rw
K04	305	22.1	rw
K04	305	22.2	rw
K04	305	20.1	rw
K04	305	16.9	rw
K04	306	22.5	rw
K04	309	19.5	rw

K04	407	20.1	rw
K04	407	18.9	rw
K04	508	15.4	rw
K04	509	20.1	rw
K04	509	19.0	rw
K04	509	19.5	rw
K04	509	17.1	rw
K04	510	22.3	rw
K04	510	20.3	rw
K04	612	20.2	rw
K04	612	19.1	rw
K04	713	15.6	rw
K04	714	17.4	rw
K04	715	20.3	rw
K04	715	19.3	rw
K04	715	19.9	rw
K04	715	20.6	rw
K04	716	22.5	rw
K04	716	22.6	rw
K04	818	19.4	rw
K04	819	20.5	rw
K04	919	16.1	rw
K04	921	17.9	rw

K04	922	20.7	rw
K04	922	19.6	rw
K04	922	20.3	rw
K04	923	21.0	rw
K04	924	22.9	rw
K04	1026	19.8	rw
K04	1027	20.9	rw
K04	1127	16.6	rw
K04	1129	18.3	rw
K04	1130	20.0	rw
K04	1131	21.1	rw
K04	1131	21.2	rw
K04	1131	21.4	rw
K04	1133	23.2	rw
K04	1133	23.3	rw
K04	1235	20.2	rw
K04	1236	21.3	rw
K04	1338	18.8	rw
K04	1340	20.4	rw
K04	1342	21.6	rw
K04	1342	21.8	rw
K04	1342	21.9	rw
K04	1344	23.6	rw

K04	1344	23.7	rw
K04	1446	20.7	rw
K04	1447	21.9	rw
K04	1450	23.8	rw
K04	1550	19.3	rw
K04	1551	20.3	rw
K04	1551	20.0	rw
K04	1552	20.9	rw
K04	1552	20.9	rw
K04	1553	21.7	rw
K04	1554	22.6	rw
K04	1554	22.1	rw
K04	1554	22.2	rw
K04	1554	22.3	rw
K04	1555	23.4	rw
K04	1556	24.0	rw
K04	1556	24.0	rw
K04	1608	22.6	rw
K04	1658	21.1	rw
K04	1659	22.4	rw
K04	1660	22.4	rw
K04	1660	22.0	rw
K04	1661	22.7	rw

K04	1661	22.6	rw
K04	1714	22.6	rw
K04	1764	20.7	rw
K04	1765	21.3	rw
K04	1765	21.5	rw
K04	1767	22.6	rw
K04	1767	22.2	rw
K04	1767	22.3	rw
K04	1767	22.2	rw
K04	1767	22.2	rw
K04	1768	22.7	rw
K04	1768	23.2	rw
K04	1768	22.7	rw
K04	1769	23.8	rw
K04	1769	23.5	rw
K04	1821	22.9	rw
K04	1872	21.2	rw
K04	1872	21.5	rw
K04	1873	22.1	rw
K04	1874	22.5	rw
K04	1874	22.4	rw
K04	1874	22.1	rw
K04	1875	22.7	rw

K04	1876	23.3	rw
K04	1928	22.8	rw
K04	1977	20.5	rw
K04	1978	21.0	rw
K04	1978	20.7	rw
K04	1979	21.3	rw
K04	1979	21.4	rw
K04	1979	21.2	rw
K04	1980	21.9	rw
K04	1980	21.9	rw
K04	1980	21.6	rw
K04	1982	22.7	rw
K04	1982	22.6	rw
K04	1982	22.5	rw
K04	1983	23.3	rw
K04	2036	22.5	rw
K04	2088	21.9	rw
K04	2089	22.5	rw
K03	1240	26.0	bm
K03	1398	25.7	bm
K03	1607	22.5	rw
K03	1608	23.4	bm
K03	1609	24.0	bm

K03	1610	24.5	bm
K03	1616	23.9	bm
K03	1617	24.1	bm
K03	1661	23.3	bm
K03	1661	23.0	rw
K03	1664	25.7	bm
K03	1669	23.5	bm
K03	1714	23.0	rw
K03	1714	22.7	rw
K03	1715	23.5	bm
K03	1725	23.3	bm
K03	1767	23.0	rw
K03	1769	23.8	bm
K03	1821	23.0	rw
K03	1858	23.5	bm
K03	1872	21.7	rw
K03	1872	21.5	rw
K03	1874	22.8	rw
K03	1876	23.7	bm
K03	1877	24.4	bm
K03	1926	22.1	rw
K03	1980	22.0	rw
K03	1981	22.6	rw

K03	1984	24.2	bm
K03	1985	24.5	bm
K03	2091	23.9	bm
K03	2093	24.7	bm
K03	2094	25.1	bm
K03	2142	22.1	rw
K03	2145	23.6	bm
K03	2196	22.3	rw
S01	1461	28.6	bm
S01	1461	25.9	bm
S01	1466	31.6	bm
S01	1502	24.1	rw
S01	1502	25.3	rw
S01	1509	25.1	rw
S01	1534	23.6	rw
S01	1556	27.2	bm
S01	1576	24.3	rw
S01	1591	28.9	bm
S01	1670	22.7	rw
S01	1699	22.3	rw
S01	1699	22.6	rw
S01	1701	29.6	bm
S01	1730	23.0	rw

S01	1731	31.0	bm
S01	1771	26.3	bm
S01	1779	26.4	bm
S01	1809	29.9	bm
S01	1869	29.7	bm
S01	1879	31.4	bm
S01	1882	30.0	bm
S01	1964	29.5	bm
S01	2027	25.0	bm
S01	2032	24.7	bm
S01	2135	28.5	bm
S01	2145	29.1	bm
S01	2195	27.2	bm
S01	2218	26.5	bm
S01	2233	27.9	bm
S01	2235	26.5	bm
I98	1736	21.4	rw
I98	1738	22.5	rw
I98	1739	23.0	bm
I98	1739	23.3	bm
I98	1740	23.7	bm
I98	1791	22.7	rw
I98	1841	20.5	rw

I98	1843	21.5	rw
I98	1843	21.5	rw
I98	1844	22.0	rw
I98	1844	22.1	rw
I98	1844	22.3	rw
I98	1845	22.6	bm
I98	1845	22.9	bm
I98	1898	22.3	rw
I98	1898	22.4	rw
I98	1924	21.7	rw
I98	1950	21.8	rw
I98	1951	22.0	rw
I98	1951	22.1	rw
I98	1951	22.3	bm
I98	1952	22.5	bm
I98	2005	22.3	bm
I98	2005	22.4	bm
I98	2059	22.3	bm
I98	2059	22.4	bm
I98	2059	22.5	bm
I98	2059	22.5	bm
I98	2060	22.6	bm
I98	2113	22.4	bm

I98	2143	21.5	rw
I98	2166	22.0	bm

The following abbreviations are used: [**C22**] Chanyshev, A., Ishii, T., Bondar, D., Bhat, S., Kim, E. J., Farla, R., Nishida, K., Liu, Z., Wang, L., Nakajima, A., Yan, B., Tang, H., Chen, Z., Higo, Y., Tange, Y., & Katsura, T. (2022). Depressed 660-km discontinuity caused by akimotoite–bridgmanite transition. Nature, 601(7891), 69–73. [**K09**] Katsura, T., Shatskiy, A., Manthilake, M. A. G. M., Zhai, S., Yamazaki, D., Matsuzaki, T., Yoshino, T., Yoneda, A., Ito, E., Sugita, M., Tomioka, N., Nozawa, A., & Funakoshi, K. I. (2009). P-V-T relations of wadsleyite determined by in situ X-ray diffraction in a large-volume high-pressure apparatus. Geophysical Research Letters, 36(11). [**I06**] Inoue, T., Irifune, T., Higo, Y., Sanehira, T., Sueda, Y., Yamada, A., Shinmei, T., Yamazaki, D., Ando, J., Funakoshi, K., & Utsumi, W. (2006). The phase boundary between wadsleyite and ringwoodite in Mg_2SiO_4 determined by in situ X-ray diffraction. Physics and Chemistry of Minerals, 33(2), 106–114. [**K04**] Katsura, T., Yokoshi, S., Song, M., Kawabe, K., Tsujimura, T., Kubo, A., Ito, E., Tange, Y., Tomioka, N., Saito, K., Nozawa, A., & Funakoshi, K. I. (2004). Thermal expansion of Mg_2SiO_4 ringwoodite at high pressures. Journal of Geophysical Research: Solid Earth, 109(12), 1–10. [**K03**] Katsura, T., Yamada, H., Shinmei, T., Kubo, A., Ono, S., Kanzaki, M., Yoneda, A., Walter, M. J., Ito, E., Urakawa, S., Funakoshi, K., & Utsumi, W. (2003). Post-spinel transition in Mg_2SiO_4 determined by high P-T in situ X-ray diffractometry. Physics of the Earth and Planetary Interiors, 136(1–2), 11–24. [**S01**] Shim, S.-H., Duffy,

T. S., & Shen, G. (2001). The post-spinel transformation in Mg_2SiO_4 and its relation to the 660-km seismic discontinuity. Nature, 411, 571–574. [**I98**] Irifune, T., Nishiyama, N., Kuroda, K., Inoue, T., Isshiki, M., Utsumi, W., Urakawa, S., Uchida, T., & Ohtaka, O. (1998). The Postspinel Phase Boundary in Mg_2SiO_4 Determined by in Situ X-ray Diffraction. Science, 279(5357), 1698–1700. Journal of Geophysical Research, 94(B8).

Table C.4:: Model selection results.

Degree of polynomials	Micro F1 score (test)	Micro F1 score (train)	Hyperparameter C
1	0.766	0.768	100
2	0.774	0.792	100
3	0.782	0.816	1000
4	0.766	0.808	0.01
5	0.758	0.820	0.0001

Table C.5:: Subducting slabs and their T660 and $\gamma_{\text{post-spinel}}$.

Name	Lat.	Lon.	T660 (K)	$\gamma_{\text{post-spinel}}$ (MPa/K)
Subducting slabs accompanied by the post-spinel transntion				
NC_Chile	-24.72	-68.53	1637	-0.9
Solomon	-5.83	154.93	1466	-0.6
Ryukyu	27.85	128.25	1522	-0.6
Scotia	-57.78	-26.45	1468	-0.6
Java	-7.81	111.76	1461	-0.6
C_Sumatra	0.08	99.98	1611	-0.8
S_Antilles	13.33	-61.18	1649	-0.9
N_Chile	-20.83	-68.63	1568	-0.7
Sunda_Strait	-6.75	106.68	1404	-0.7
N_Phil	16.33	120.55	1565	-0.7
C_Chile	-35.24	-70.57	1762	-1.5
S_Vanuatu	-20.2	169.83	1448	-0.6
Bonin	27.24	140.88	1483	-0.6
Alaska_Peninsula	56.53	-158.8	1520	-0.6
New_Zealand	-37.86	176.98	1532	-0.6
Kermadec	-30.2	-178.47	1451	-0.6
Hokkaido	44.62	147	1409	-0.7
S_Marianas	17.6	145.83	1448	-0.6
S_Sumatra	-3.38	102.37	1462	-0.6
New_Britain	-5.53	150.9	1537	-0.6

Alaska	58.87	-153.55	1573	-0.7
North_Cascadia	42	121.5	1932	-2.9
N_Marianas	21.93	143.44	1622	-0.8
N_Vanuatu	-13.8	167.47	1528	-0.6
Kyushu	31.22	130.57	1475	-0.6
GuatElSal	14.15	-90.42	1640	-0.9
Peru	-16.61	-70.85	1646	-0.9
S_Phil	9.59	125.52	1512	-0.6
Costa_Rica	10.47	-84.73	1528	-0.6
E_Banda_Sea	-6.73	129.5	1668	-1.0
Mexico	19.1	-99.5	1737	-1.3
N_Sumatra	3.87	97.6	1662	-0.9
Central_Cascadia	47	122	1877	-2.4
W_Aleut	51.78	-178.8	1507	-0.6
Colombia_Ecuador	0	-77.5	1813	-1.8
N_Antilles	16.05	-61.67	1615	-0.8
S_Chile	-39.5	-71.7	1750	-1.4
E_Aleut	54.13	-165.97	1493	-0.6
Izu	33.13	139.77	1475	-0.6
Nicaragua	12.5	-86.7	1623	-0.8
SC_Chile	-43.75	-72.8	1687	-1.1
N_Honshu	40.65	140.88	1450	-0.6
Bali_Lombok	-8.42	116.47	1521	-0.6

C_Aleut	52.32	-172.52	1467	-0.6
C_Honshu	37.62	140.28	1401	-0.7
Subducting slabs accompanied by the ak↔bm transntion				
Tonga	-174.87	-19.18	1324	
N_Kurile	155.43	50.25	1378	
S_Kurile	151.75	46.83	1379	
Kamchatka	159.15	53.59	1376	
W_Banda_Sea	121.83	-8.76	1382	

Notes: Subduction sections and their thermal models are based on the compilation of [**S10**]; When a subdcuting slab has a T660 of $\sim$ 1400 K, its passage across the "660-km" depth is expected to be primaily accompancyed by the post-spinel transntion.

[**S10**]: Syracuse, E. M., van Keken, P. E., & Abers, G. A. (2010). The global range of subduction zone thermal models. Physics of the Earth and Planetary Interiors, 183(1–2), 73–90.

Table C.6:: Hotspot-associated plumes and their T660 and $\gamma_{\text{post-spinel}}$.

ID	Hotpsot	Lat.	Lon.	T_p (K)	T_{660} (K)	$\gamma_{\text{post-spinel}}$ (MPa/K)
	Plume-fed oceanic hotspots accompanied by the post-spinel transntion					
11	Cape Verde	14	-20	1711	2011	-3.8
13	Manus Basin	-4	150	1632	1919	-2.8
17	Crozet	-45	50	1697	1994	-3.6
27	Cameroon	4	9	1688	1984	-3.5
29	Ascension	-8	-14	1607	1890	-2.5
	Plume-fed oceanic hotspots accompanied by the post-garnet transntion					
1	Iceland	65	-20	1882	2209	
2	Hawaii	20	-156	1832	2151	
3	Samoa	-14	-170	1850	2172	
4	Galapagos	0	-92	1846	2168	
5	Easter	-27	-110	1816	2133	
6	Azores	39	-28	1754	2061	
7	Kerguelen/Heard	-49	69	1746	2051	

8	Juan Fernandez	-34	-83	1822	2140
9	Societies	-18	-150	1878	2205
10	Macdonald	-30	-140	1915	2248
14	Bouvet	-54	2	1760	2068
15	Marquesas	-10	-138	1918	2251
18	Reunion	-21	56	1786	2098
19	Pitcairn	-26	-130	1853	2176
20	Caroline	5	164	1784	2096
23	Louisville	-51	-141	1797	2111
24	Canary	28	-20	1795	2108
31	Comores	-12	43	1824	2142
32	San Felix	-26	-80	1782	2093
33	Tristan/Gough/Walvis Ridge	-37	-12	1823	2141
36	St Helena	-16	-6	1784	2096

Notes: Hotspot IDs are based on the compilation of [**B22**]; When a mantle plume has a T660 of $\leq$2050 K, its passage

across the "660-km" depth is expected to be primaily accompancyed by the post-spinel transntion. [**B22**]: Bao, X., Lithgow-Bertelloni, C. R., Jackson, M. G., & Romanowicz, B. (2022). On the relative temperatures of Earth's volcanic hotspots and mid-ocean ridges. Science, 375(6576), 57–61.

References

Abe, Y., Ohtani, E., Okuchi, T., Righter, K., and Drake, M. (2000). Water in the early Earth. In *Origin of the Earth and Moon*, volume 1, pages 413–433. University of Arizona Press Tucson.

Akahama, Y. and Kawamura, H. (2006). Pressure calibration of diamond anvil Raman gauge to 310 GPa. *Journal of Applied Physics*, 100:043516.

Akaogi, M. and Ito, E. (1993). Refinement of enthalpy measurement of $MgSiO_3$ perovskite and negative pressure-temperature slopes for perovskite-forming reactions. *Geophysical Research Letters*, 20:1839–1842.

Amante, C. and Eakins, B. (2009). ETOPO1 1 arc-minute global relief model: procedures, data sources and analysis. Technical Report V5C8276M, National Geophysical Data Center, NOAA.

Andrault, D., Petitgirard, S., Lo Nigro, G., Devidal, J.-L., Veronesi, G., Garbarino, G., and Mezouar, M. (2012). Solid–liquid iron partitioning in Earth's deep mantle. *Nature*, 487(7407):354–357.

Ardia, P., Hirschmann, M. M., Withers, A. C., and Tenner, T. J. (2012). H_2O storage capacity of olivine at 5-8 GPa and consequences for dehydration partial melting of the upper mantle. *Earth and Planetary Science Letters*, 345:104–116.

Arndt, N. T. and Nisbet, E. G. (2012). Processes on the young Earth and the habitats of early life. *Annual Review of Earth and Planetary Sciences*, 40:521–549.

Aulbach, S. and Arndt, N. T. (2019). Eclogites as palaeodynamic archives: evidence for warm (not hot) and depleted (but heterogeneous) Archaean ambient mantle. *Earth and Planetary Science Letters*, 505:162–172.

Bao, X., Lithgow-Bertelloni, C. R., Jackson, M. G., and Romanowicz, B. (2022). On the relative temperatures of Earth's volcanic hotspots and mid-ocean ridges. *Science*, 375:57–61.

Baratoux, D., Toplis, M. J., Monnereau, M., and Gasnault, O. (2011). Thermal history of Mars inferred from orbital geochemistry of volcanic provinces. *Nature*, 472:338–341.

Barnes, J. J., McCubbin, F. M., Santos, A. R., Day, J. M. D., Boyce, J. W., Schwenzer, S. P., Ott, U., Franchi, I. A., Messenger, S., Anand, M., and Agee, C. B. (2020). Multiple early-formed water reservoirs in the interior of Mars. *Nature Geoscience*, 13:260–264.

Bebout, G. E. (1996). Volatile transfer and recycling at convergent margins: mass-balance and insights from high-P/T metamorphic rocks. In *Subduction Top to Bottom*, volume 96, pages 179–193. American Geophysical Union.

Bell, D. R., Rossman, G. R., Maldener, J., Endisch, D., and Rauch, F. (2003). Hydroxide in olivine: A quantitative determination of the absolute amount and calibration of the IR spectrum. *Journal of Geophysical Research-Solid Earth*, 108(B2).

Belmonte, D., Fortezza, M. L., and Menescardi, F. (2022). Ab initio thermal expansion and thermoelastic properties of ringwoodite (γ-Mg_2SiO_4) at mantle transition zone conditions. *European Journal of Mineralogy*, 34:167–182.

Bercovici, D. and Karato, S. (2003). Whole-mantle convection and the transition-zone water filter. *Nature*, 425:39–44.

Bertka, C. M. and Fei, Y. W. (1997). Mineralogy of the Martian interior up to core-mantle boundary pressures. *Journal of Geophysical Research: Solid Earth*, 102:5251–5264.

Bishop, C. M. (2006). *Pattern Recognition and Machine Learning*. Springer.

Bolfan-Casanova, N., Keppler, H., and Rubie, D. C. (2003). Water partitioning at 660 km depth and evidence for very low water solubility in magnesium silicate perovskite. *Geophysical Research Letters*, 30(17).

Bolfan-Casanova, N., Mackwell, S., Keppler, H., McCammon, C., and Rubie, D. C. (2002). Pressure dependence of H solubility in magnesiowustite up to 25 GPa: Implications for the storage of water in the Earth's lower mantle. *Geophysical Research Letters*, 29(10).

Bolfan-Casanova, N., Schiavi, F., Novella, D., Bureau, H., Raepsaet, C., Khodja, H., and Demouchy, S. (2018). Examination of water quantification and incorporation in transition zone minerals: Wadsleyite, ringwoodite and phase D using ERDA (Elastic Recoil Detection Analysis). *Frontiers in Earth Science*, 6:75.

Bossmann, A. B. and Keken, P. E. V. (2013). Dynamics of plumes in a compressible mantle with phase changes: Implications for phase boundary topography. *Physics of the Earth and Planetary Interiors*, 224:21–31.

Bouhifd, M. A., Andrault, D., Fiquet, G., and Richet, P. (1996). Thermal expansion of forsterite up to the melting point. *Geophysical Research Letters*, 23:1143–1146.

Brasser, R. (2013). The formation of Mars: Building blocks and accretion time scale. *Space Science Reviews*, 174:11–25.

Brennan, M. C., Fischer, R. A., and Irving, J. C. E. (2020). Core formation and geophysical properties of Mars. *Earth and Planetary Science Letters*, 530:115923.

Breuer, D., Plesa, A. C., Tosi, N., and Grott, M. (2016). Water in the Martian interior: The geodynamical perspective. *Meteoritics and Planetary Science*, 51:1959–1992.

Brown, M., Johnson, T., and Gardiner, N. J. (2020). Plate tectonics and the Archean Earth. *Annual Review of Earth and Planetary Sciences*, 48:291–320.

Campbell, A. J., Danielson, L., Righter, K., Seagle, C. T., Wang, Y., and Prakapenka, V. B. (2009). High pressure effects on the iron–iron oxide and nickel–nickel oxide oxygen fugacity buffers. *Earth and Planetary Science Letters*, 286:556–564.

Carr, M. H. (1996). *Water on Mars*. Oxford University Press.

Carr, M. H. and Head, J. W. (2003). Oceans on Mars: An assessment of the observational evidence and possible fate. *Journal of Geophysical Research: Planets*, 108(E5).

Carr, M. H. and Head, J. W. (2015). Martian surface/near-surface water inventory: Sources, sinks, and changes with time. *Geophysical Research Letters*, 42:726–732.

Cawood, P. A., Hawkesworth, C. J., Pisarevsky, S. A., Dhuime, B., Capitanio, F. A., and Nebel, O. (2018). Geological archive of the onset of plate tectonics. *Philosophical Transactions of the Royal Society A: Mathematical, Physical and Engineering Sciences*, 376(2132):20170405.

Chanyshev, A., Ishii, T., Bondar, D., Bhat, S., Kim, E. J., Farla, R., Nishida, K., Liu, Z., Wang, L., Nakajima, A., Yan, B., Tang, H., Chen, Z., Higo, Y., Tange, Y., and Katsura, T. (2022). Depressed 660-km discontinuity caused by akimotoite–bridgmanite transition. *Nature*, 601:69–73.

Chassefiere, E., Langlais, B., Quesnel, Y., and Leblanc, F. (2013). The fate of early Mars' lost water: The role of serpentinization. *Journal of Geophysical Research: Planets*, 118:1123–1134.

Chen, H., Leinenweber, K., Prakapenka, V., Prescher, C., Meng, Y., Bechtel, H., Kunz, M., and Shim, S.-H. (2020). Possible H_2O storage in the crystal structure of $CaSiO_3$ perovskite. *Physics of the Earth and Planetary Interiors*, 299:106412.

Chopelas, A., Boehler, R., and Ko, T. (1994). Thermodynamics and behavior of γ–Mg_2SiO_4 at high pressure: Implications for Mg_2SiO_4 phase equilibrium. *Physics and Chemistry of Minerals*, 21:351–359.

Christensen, U. (1995). Effects of phase transitions on mantle convection. *Annual Review of Earth and Planetary Sciences*, 23:65–87.

Chudinovskikh, L. and Boehler, R. (2001). High-pressure polymorphs of olivine and the 660-km seismic discontinuity. *Nature*, 411:574–577.

Civet, F. and Tarits, P. (2014). Electrical conductivity of the mantle of mars from MGS magnetic observations. *Earth, Planets and Space*, 66:1–7.

Clesi, V., Bouhifd, M. A., Bolfan-Casanova, N., Manthilake, G., Schiavi, F., Raepsaet, C., Bureau, H., Khodja, H., and Andrault, D. (2018). Low hydrogen contents in the cores of terrestrial planets. *Science Advances*, 4(3):e1701876.

Clifford, S. M., Lasue, J., Heggy, E., Boisson, J., McGovern, P., and Max, M. D. (2010). Depth of the martian cryosphere: Revised estimates and implications for the existence and detection of subpermafrost groundwater. *Journal of Geophysical Research: Planets*, 115(E7).

Clifford, S. M. and Parker, T. J. (2001). The evolution of the Martian hydrosphere: Implications for the fate of a primordial ocean and the current state of the northern plains. *Icarus*, 154:40–79.

Collinet, M., Plesa, A.-C., Grove, T. L., Schwinger, S., Ruedas, T., and Breuer, D. (2021). Magmars: A melting model for the Martian mantle and FeO-rich peridotite. *Journal of Geophysical Research: Planets*, 126(12):e2021JE006985.

Coltice, N., Seton, M., Rolf, T., Muller, R. D., and Tackley, P. J. (2013). Convergence of tectonic reconstructions and mantle convection models for significant fluctuations in seafloor spreading. *Earth and Planetary Science Letters*, 383:92–100.

Condie, K. C., Aster, R. C., and Van Hunen, J. (2016). A great thermal divergence in the mantle beginning 2.5 Ga: Geochemical constraints from greenstone basalts and komatiites. *Geoscience Frontiers*, 7(4):543–553.

Conrad, C. P. (2013). The solid Earth's influence on sea level. *GSA Bulletin*, 125(7-8):1027–1052.

Craddock, R. A. and Greeley, R. (2009). Minimum estimates of the amount and timing of gases released into the Martian atmosphere from volcanic eruptions. *Icarus*, 204:512–526.

Crowley, J. W., Gérault, M., and O'Connell, R. J. (2011). On the relative influence of heat and water transport on planetary dynamics. *Earth and Planetary Science Letters*, 310(3-4):380–388.

Dauphas, N. and Morbidelli, A. (2014). Geochemical and planetary dynamical views on the origin of Earth's atmosphere and oceans. In *Treatise on Geochemistry*, pages 1–35. Elsevier, 2nd edition.

Demouchy, S., Deloule, E., Frost, D. J., and Keppler, H. (2005). Pressure and temperature-dependence of water solubility in fe-free wadsleyite. *American Mineralogist*, 90:1084–1091.

Deuss, A., Andrews, J., and Day, E. (2013). Seismic observations of mantle discontinuities and their mineralogical and dynamical interpretation. In Karato, S.-i., editor, *Physics and Chemistry of the Deep Earth*, pages 295–323. Wiley-Blackwell.

Dewaele, A., Torrent, M., Loubeyre, P., and Mezouar, M. (2008). Compression curves of transition metals in the Mbar range: Experiments and projector augmented-wave calculations. *Physical Review B*, 78:104102.

Dong, J., Fischer, R. A., Stixrude, L., Brennan, M. C., Daviau, K., Suer, T.-A., Turner, K. M., Meng, Y., and Prakapenka, V. B. (2022a). Nonlinearity of the post-spinel transition and its expression in slabs and plumes worldwide. *arXiv preprint*, (https://doi.org/10.48550/arXiv.2208.08975).

Dong, J., Fischer, R. A., Stixrude, L. P., Lithgow-Bertelloni, C. R., Eriksen, Z. T., and Brennan, M. C. (2022b). Water storage capacity of the martian mantle through time. *Icarus*, 385:115113.

Dong, J., Fischer, R. A., Stixrude, L. P., and Lithgow-Bertelloni, C. R. (2021). Constraining the volume of Earth's early oceans with a temperature-dependent mantle water storage capacity model. *AGU Advances*, 2(1):e2020AV000323.

Dreibus, G. and Wänke, H. (1989). Supply and loss of volatile constituents during the accretion of terrestrial planets. In Atreya, S. and Pollack, J.B.and Matthews, M., editors, *Origin and Evolution of Planetary and Satellite Atmospheres*, pages 268–288. Arizona.

Druzhbin, D., Fei, H. Z., and Katsura, T. (2021). Independent hydrogen incorporation in wadsleyite from oxygen fugacity and non-dissociation of h2o in the reducing mantle transition zone. *EARTH AND PLANETARY SCIENCE LETTERS*, 557.

Duncan, M. S., Schmerr, N. C., Bertka, C. M., and Fei, Y. W. (2018). Extending the solidus for a model iron-rich Martian mantle composition to 25 GPa. *Geophysical Research Letters*, 45(19):10211–10220.

Eakins, B. and Sharman, G. (2010). Volumes of the world's oceans from ETOPO1. Technical report, NOAA National Geophysical Data Center.

Ehlmann, B. L. and Edwards, C. S. (2014). Mineralogy of the Martian surface. *Annual Review of Earth and Planetary Sciences*, 42:291–315.

Elkins-Tanton, L. T. (2008). Linked magma ocean solidification and atmospheric growth for Earth and Mars. *Earth and Planetary Science Letters*, 271(1):181–191.

Errandonea, D. (2005). Improving the understanding of the melting behaviour of Mo, Ta, and W at extreme pressures. *Physica B: Condensed Matter*, 357(3-4):356–364.

Fabrichnaya, O. (2008). Calculation of the phase diagrams of the MgO–FeO–Al_2O_3–SiO_2 system at high pressures and temperatures: Application to the mineral structure of the Earth's mantle transition zone. In Hack, K., editor, *The SGTE Casebook*, pages 132–143. Woodhead Publishing, 2nd edition.

Fei, H. Z. and Katsura, T. (2020). Pressure dependence of proton incorporation and water solubility in olivine. *Journal of Geophysical Research: Solid Earth*, 125(2):e2019JB018813.

Fei, H. Z. and Katsura, T. (2021). Water solubility in Fe-bearing wadsleyite at mantle transition zone temperatures. *Geophysical Research Letters*, 48(9):e2021GL092836.

Fei, H. Z., Yamazaki, D., Sakurai, M., Miyajima, N., Ohfuji, H., Katsura, T., and Yamamoto, T. (2017). A nearly water-saturated mantle transition zone inferred from mineral viscosity. *Science Advances*, 3(6):e1603024.

Fei, Y., Orman, J. V., Li, J., van Westrenen, W., Sanloup, C., Minarik, W., Hirose, K., Komabayashi, T., Walter, M., and Funakoshi, K. (2004). Experimentally determined postspinel transformation boundary in Mg_2SiO_4 using MgO as an internal pressure standard and its geophysical implications. *Journal of Geophysical Research: Solid Earth*, 109(B2).

Fei, Y., Ricolleau, A., Frank, M., Mibe, K., Shen, G., and Prakapenka, V. (2007). Toward an internally consistent pressure scale. *Proceedings of the National Academy of Sciences*, 104:9182–9186.

Ferot, A. and Bolfan-Casanova, N. (2012). Water storage capacity in olivine and pyroxene to 14 GPa: Implications for the water content of the Earth's upper mantle and nature of seismic discontinuities. *Earth and Planetary Science Letters*, 349:218–230.

Filiberto, J. (2017). Geochemistry of Martian basalts with constraints on magma genesis. *Chemical Geology*, 466:1–14.

Filiberto, J. and Dasgupta, R. (2011). Fe^{2+}–Mg partitioning between olivine and basaltic melts: Applications to genesis of olivine-phyric shergottites and conditions of melting in the Martian interior. *Earth and Planetary Science Letters*, 304:527–537.

Filiberto, J. and Dasgupta, R. (2015). Constraints on the depth and thermal vigor of melting in the Martian mantle. *Journal of Geophysical Research: Planets*, 120(1):109–122.

Filiberto, J., McCubbin, F. M., and Taylor, G. J. (2019). Volatiles in Martian magmas and the interior: Inputs of volatiles into the crust and atmosphere. In Filiberto, J. and Schwenzer, S. P., editors, *Volatiles in the Martian Crust*, pages 13–33.

Flament, N., Coltice, N., and Rey, P. F. (2008). A case for late-Archaean continental emergence from thermal evolution models and hypsometry. *Earth and Planetary Science Letters*, 275(3-4):326–336.

Fraeman, A. A. and Korenaga, J. (2010). The influence of mantle melting on the evolution of Mars. *Icarus*, 210(1):43–57.

Frost, D. J. and Dolejs, D. (2007). Experimental determination of the effect of H_2O on the 410-km seismic discontinuity. *Earth and Planetary Science Letters*, 256(1-2):182–195.

Frost, D. J. and Fei, Y. (1998). Stability of phase D at high pressure and high temperature. *Journal of Geophysical Research: Solid Earth*, 103(B4):7463–7474.

Frost, D. J. and Wood, B. J. (1997). Experimental measurements of the properties of H_2O–CO_2 mixtures at high pressures and temperatures. *Geochimica et Cosmochimica Acta*, 61(16):3301–3309.

Fu, S., Yang, J., ichiro Karato, S., Vasiliev, A., Presniakov, M. Y., Gavrilliuk, A. G., Ivanova, A. G., Hauri, E. H., Okuchi, T., Purevjav, N., and Lin, J. F. (2019). Water concentration in single-crystal (Al,Fe)-bearing bridgmanite grown from the hydrous melt: Implications for dehydration melting at the topmost lower mantle. *Geophysical Research Letters*, 46(17-18):10346–10357.

Gaetani, G. A., O'Leary, J. A., Koga, K. T., Hauri, E. H., Rose-Koga, E. F., and Monteleone, B. D. (2014). Hydration of mantle olivine under variable water and oxygen fugacity conditions. *Contributions to Mineralogy and Petrology*, 167(2):965.

Ganne, J. and Feng, X. (2017). Primary magmas and mantle temperatures through time. *Geochemistry, Geophysics, Geosystems*, 18(3):872–888.

Ganskow, G. and Langenhorst, F. (2014). Stability and crystal chemistry of iron-bearing dense hydrous magnesium silicates. *Chemie der Erde*, 74(3):489–496.

Ghosh, S., Ohtani, E., Litasov, K. D., Suzuki, A., Dobson, D., and Funakoshi, K. (2013). Effect of water in depleted mantle on post-spinel transition and implication for 660km seismic discontinuity. *Earth and Planetary Science Letters*, 371–372:103–111.

Goes, S., Agrusta, R., van Hunen, J., and Garel, F. (2017). Subduction-transition zone interaction: A review. *Geosphere*, 13(3):644–664.

Greber, N. D. and Dauphas, N. (2019). The chemistry of fine-grained terrigenous sediments reveals a chemically evolved paleo-Archean emerged crust. *Geochimica et Cosmochimica Acta*, 255:247–264.

Grott, M., Morschhauser, A., Breuer, D., and Hauber, E. (2011). Volcanic outgassing of co2 and h2o on mars. *Earth and Planetary Science Letters*, 308(3-4):391–400.

Guo, M. and Korenaga, J. (2020). Argon constraints on the early growth of felsic continental crust. *Science Advances*, 6(21):eaaz6234.

Gurnis, M. (1992). Rapid continental subsidence following the initiation and evolution of subduction. *Science*, 255(5051):1556–1558.

Hacker, B. R. (2008). H_2O subduction beyond arcs. *Geochemistry, Geophysics, Geosystems*, 9(3):Q03001.

Hallis, L. J., Huss, G. R., Nagashima, K., Taylor, G. J., Halldorsson, S. A., Hilion, D. R., Mottl, M. J., and Meech, K. J. (2015). Evidence for primordial water in Earth's deep mantle. *Science*, 350(6262):795–797.

Hansen, K. S. (1982). Secular effects of oceanic tidal dissipation on the Moon's orbit and the Earth's rotation. *Reviews of Geophysics*, 20(3):457–480.

Hauck, S. A. and Phillips, R. J. (2002). Thermal and crustal evolution of Mars. *Journal of Geophysical Research: Planets*, 107.

Hauri, E. H., Gaetani, G. A., and Green, T. H. (2006). Partitioning of water during melting of the Earth's upper mantle at H_2O-undersaturated conditions. *Earth and Planetary Science Letters*, 248(3–4):715–734.

Hernández, E. R., Brodholt, J., and Alfè, D. (2015). Structural, vibrational and thermodynamic properties of Mg_2SiO_4 and $MgSiO_3$ minerals from first-principles simulations. *Physics of the Earth and Planetary Interiors*, 240:1–24.

Herzberg, C. (2019). Origin of high-Mg bimineralic eclogite xenoliths in kimberlite: A comment on a paper by Aulbach and Arndt (2019). *Earth and Planetary Science Letters*, 510:231–233.

Herzberg, C., Condie, K., and Korenaga, J. (2010). Thermal history of the Earth and its petrological expression. *Earth and Planetary Science Letters*, 292:79–88.

Herzberg, C., Raterron, P., and Zhang, J. Z. (2000). New experimental observations on the anhydrous solidus for peridotite KLB-1. *Geochemistry Geophysics Geosystems*, 1(11).

Hirose, K. (2002). Phase transitions in pyrolitic mantle around 670-km depth: Implications for upwelling of plumes from the lower mantle. *Journal of Geophysical Research: Solid Earth*, 107(B4):2078.

Hirose, K., Tagawa, S., Kuwayama, Y., Sinmyo, R., Morard, G., Ohishi, Y., and Genda, H. (2019). Hydrogen limits carbon in liquid iron. *Geophysical Research Letters*, 46(10):5190–5197.

Hirschmann, M. M. (2018). Comparative deep Earth volatile cycles: The case for C recycling from exosphere/mantle fractionation of major (H_2O, C, N) volatiles and from H_2O/Ce, CO_2/Ba, and CO_2/Nb exosphere ratios. *Earth and Planetary Science Letters*, 502:262–273.

Hirschmann, M. M., Tenner, T., Aubaud, C., and Withers, A. C. (2009). Dehydration melting of nominally anhydrous mantle: The primacy of partitioning. *Physics of the Earth and Planetary Interiors*, 176:54–68.

Hirschmann, M. M., Withers, A. C., Ardia, P., and Foley, N. T. (2012). Solubility of molecular hydrogen in silicate melts and consequences for volatile evolution of terrestrial planets. *Earth and Planetary Science Letters*, 345-348:38–48.

Holland, T. and Powell, R. (1991). A Compensated-Redlich-Kwong (CORK) equation for volumes and fugacities of CO_2 and H_2O in the range 1 bar to 50 kbar and 100–1600 °C. *Contributions to Mineralogy and Petrology*, 109:265–273.

Holland, T. J. B. and Powell, R. (1990). An enlarged and updated internally consistent thermodynamic dataset with uncertainties and correlations: the system K_2O–Na_2O–CaO–MgO–MnO–FeO–Fe_2O_3–Al_2O_3–TiO_2–SiO_2–C–H_2–O_2.

Huang, Y., Chubakov, V., Mantovani, F., Rudnick, R. L., and McDonough, W. F. (2013). A reference Earth model for the heat-producing elements and associated geoneutrino flux. *Geochemistry, Geophysics, Geosystems*, 14:2003–2029.

Iizuka-Oku, R., Yagi, T., Gotou, H., Okuchi, T., Hattori, T., and Sano-Furukawa, A. (2017). Hydrogenation of iron in the early stage of Earth's evolution. *Nature Communications*, 8(1):14096.

Inoue, T., Irifune, T., Higo, Y., Sanehira, T., Sueda, Y., Yamada, A., Shinmei, T., Yamazaki, D., Ando, J., Funakoshi, K., and Utsumi, W. (2006). The phase boundary between wadsleyite and ringwoodite in Mg_2SiO_4 determined by in situ X-ray diffraction. *Physics and Chemistry of Minerals*, 33(2):106–114.

Inoue, T., Wada, T., Sasaki, R., and Yurimoto, H. (2010). Water partitioning in the Earth's mantle. *Physics of the Earth and Planetary Interiors*, 183(1-2):245–251.

Irifune, T., Isobe, F., and Shinmei, T. (2014). A novel large-volume Kawai-type apparatus and its application to the synthesis of sintered bodies of nano-polycrystalline diamond. *Physics of the Earth and Planetary Interiors*, 228:255–261.

Irifune, T., Nishiyama, N., Kuroda, K., Inoue, T., Isshiki, M., Utsumi, W., Urakawa, S., Uchida, T., and Ohtaka, O. (1998). The postspinel phase boundary in Mg_2SiO_4 determined by in situ x-ray diffraction. *Science*, 279(5357):1698–1700.

Ishii, T., Huang, R., Fei, H., Koemets, I., Liu, Z., Maeda, F., Yuan, L., Wang, L., Druzhbin, D., Yamamoto, T., Bhat, S., Farla, R., Kawazoe, T., Tsujino, N., Kulik, E., Higo, Y., Tange, Y., and Katsura, T. (2018). Complete agreement of the post-spinel transition with the 660-km seismic discontinuity. *Scientific Reports*, 8:6358.

Ishii, T., Huang, R., Myhill, R., Fei, H., Koemets, I., Liu, Z., Maeda, F., Yuan, L., Wang, L., Druzhbin, D., Yamamoto, T., Bhat, S., Farla, R., Kawazoe, T., Tsujino, N.,

Kulik, E., Higo, Y., Tange, Y., and Katsura, T. (2019). Sharp 660-km discontinuity controlled by extremely narrow binary post-spinel transition. *Nature Geoscience*, 12:869–872.

Ishii, T., Kojitani, H., and Akaogi, M. (2011). Post-spinel transitions in pyrolite and Mg_2SiO_4 and akimotoite-perovskite transition in $MgSiO_3$: Precise comparison by high-pressure high-temperature experiments with multi-sample cell technique. *Earth and Planetary Science Letters*, 309(3-4):185–197.

Ito, E. (1982). Stability relations of silicate spinels, ilmenites, and perovskite. In *High Pressure Research in Geophysics*, pages 405–419. Springer.

Ito, E., Akaogi, M., Topor, L., and Navrotsky, A. (1990). Negative pressure-temperature slopes for reactions foriing $MgSiO_3$ perovskite from calorimetry. *Science*, 249(4974):1275–1278.

Ito, E. and Takahashi, E. (1989). Postspinel transformations in the system Mg_2SiO_4–Fe_2SiO_4 and some geophysical implications. *Journal of Geophysical Research*, 94.

Iwamori, H. (2007). Transportation of H_2O beneath the Japan arcs and its implications for global water circulation. *Chemical Geology*, 239(3-4):182–198.

Jakosky, B. M. (2021). Atmospheric loss to space and the history of water on Mars. *Annual Review of Earth and Planetary Sciences*, 49:71–93.

James, G., Witten, D., Hastie, T., and Tibshirani, R. (2013). *An Introduction to Statistical Learning*. Springer.

Johnson, B. W. and Wing, B. A. (2020). Limited Archaean continental emergence reflected in an early Archaean ^{18}O-enriched ocean. *Nature Geoscience*, 13(3):243–248.

Johnson, C. L., Mittelholz, A., Langlais, B., Russell, C. T., Ansan, V., Banfield, D., Chi, P. T. J., Fillingim, M. O., Forget, F., Haviland, H. F., Golombek, M., Joy, S., Lognonne, P., Liu, X. P., Michaut, C., Pan, L., Quantin-Nataf, C., Spiga, A., Stanley, S., Thorne, S. N., Wieczorek, M. A., Yu, Y. N., Smrekar, S. E., and Banerdt, W. B. (2020). Crustal and time-varying magnetic fields at the InSight landing site on Mars. *Nature Geoscience*, (13):199–204.

Kaminsky, F. V. (2018). Water in the Earth's lower mantle. *Geochemistry International*, 56:1117–1134.

Karato, S. I., Karki, B., and Park, J. (2020). Deep mantle melting, global water circulation and its implications for the stability of the ocean mass. *Progress in Earth and Planetary Science*, 7(1):76.

Katsura, T. and Ito, E. (1989). The system Mg_2SiO_4–Fe_2SiO_4 at high pressures and temperatures: precise determination of stabilities of olivine, modified spinel, and spinel. *Journal of Geophysical Research*, 94(B11):15663–15670.

Katsura, T., Yamada, H., Shinmei, T., Kubo, A., Ono, S., Kanzaki, M., Yoneda, A., Walter, M. J., Ito, E., Urakawa, S., Funakoshi, K., and Utsumi, W. (2003). Post-spinel transition in Mg_2SiO_4 determined by high P–T in situ X-ray diffractometry. *Physics of the Earth and Planetary Interiors*, 136:11–24.

Kavner, A. and Jeanloz, R. (1998). High-pressure melting curve of platinum. *Journal of Applied Physics*, 83(12):7553–7559.

Kavner, A., Speed, T., and Jeanloz, R. (2000). Statistical analysis of phase boundary. In Aoki, H., Syono, Y., and Hemley, R., editors, *Physics Meets Mineralogy: Condensed Matter Physics in the Geosciences*, pages 71–80. Cambridge University Press.

Kelbert, A., Schultz, A., and Egbert, G. (2009). Global electromagnetic induction constraints on transition-zone water content variations. *Nature*, 460(7258):1003–1006.

Keppler, H. and Bolfan-Casanova, N. (2006). Water in nominally anhydrous minerals. In Keppler, H. and Smyth, J. R., editors, *Thermodynamics of water solubility and partitioning*, volume 62, pages 193–230.

Khan, A., Sossi, P., Liebske, C., Rivoldini, A., and Giardini, D. (2022). Geophysical and cosmochemical evidence for a volatile-rich Mars. *Earth and Planetary Science Letters*, 578:117330.

Kiefer, W. S., Filiberto, J., Sandu, C., and Li, Q. (2015). The effects of mantle composition on the peridotite solidus: Implications for the magmatic history of Mars. *Geochimica et Cosmochimica Acta*, 162:247–258.

Knapmeyer-Endrun, B., Panning, M. P., Bissig, F., Joshi, R., Khan, A., Kim, D., Lekic, V., Tauzin, B., Tharimena, S., Plasman, M., Compaire, N., Garcia, R. F., Margerin, L., Schimmel, M., Stutzmann, E., Schmerr, N., Bozdag, E., Plesa, A. C., Wieczorek, M. A., Broquet, A., Antonangeli, D., McLennan, S. M., Samuel, H., Michaut, C., Pan, L., Smrekar, S. E., Johnson, C. L., Brinkman, N., Mittelholz, A., Rivoldini, A., Davis, P. M., Lognonne, P., Pinot, B., Scholz, J. R., Stahler, S., Knapmeyer, M., van Driel, M., Giardini, D., and Banerdt, W. B. (2021). Thickness and structure of the martian crust from InSight seismic data. *Science*, 373(6553):438–443.

Kojitani, H., Inoue, T., and Akaogi, M. (2016). Precise measurements of enthalpy of postspinel transition in Mg_2SiO_4 and application to the phase boundary calculation. *Journal of Geophysical Research: Solid Earth*, 121(2):729–742.

Kojitani, H., Terata, S., Ohsawa, M., Mori, D., Inaguma, Y., and Akaogi, M. (2017). Experimental and thermodynamic investigations on the stability of $Mg_{14}Si_5O_{24}$ anhydrous phase B with relevance to Mg_2SiO_4 forsterite, wadsleyite, and ringwoodite. *American Mineralogist*, 102(10):2032–2044.

Konopliv, A. S., Asmar, S. W., Folkner, W. M., Karatekin, Ö., Nunes, D. C., Smrekar, S. E., Yoder, C. F., and Zuber, M. T. (2011). Mars high resolution gravity fields from MRO, Mars seasonal gravity, and other dynamical parameters. *Icarus*, 211(1):401–428.

Korenaga, J. (2006). Archean geodynamics and the thermal evolution of Earth. In K. Benn, J.-C. M. and Condie, K., editors, *Archean Geodynamics and Environments*, volume 164, pages 7–32. American Geophysical Union.

Korenaga, J. (2007). Thermal cracking and the deep hydration of oceanic lithosphere: A key to the generation of plate tectonics? *Journal of Geophysical Research: Solid Earth*, 112(B5).

Korenaga, J. (2013). Initiation and evolution of plate tectonics on Earth: theories and observations. *Annual Review of Earth and Planetary Sciences*, 41:117–151.

Korenaga, J., Planavsky, N. J., and Evans, D. A. D. (2017). Global water cycle and the coevolution of the Earth's interior and surface environment. *Philosophical Transactions of the Royal Society A: Mathematical Physical and Engineering Sciences*, 375:20150393.

Korenaga, T. and Korenaga, J. (2008). Subsidence of normal oceanic lithosphere, apparent thermal expansivity, and seafloor flattening. *Earth and Planetary Science Letters*, 268(1-2):41–51.

Kudoh, Y., Inoue, T., and Arashi, H. (1996). Structure and crystal chemistry of hydrous wadsleyite, $Mg_{1.75}SiH_{0.5}O_4$: Possible hydrous magnesium silicate in the mantle transition zone. *Physics and Chemistry of Minerals*, 23(7):461–469.

Kump, L. R. and Barley, M. E. (2007). Increased subaerial volcanism and the rise of atmospheric oxygen 2.5 billion years ago. *Nature*, 448(7157):1033–1036.

Kuroda, K., Irifune, T., Inoue, T., Nishiyama, N., Miyashita, M., Funakoshi, K., and Utsumi, W. (2000). Determination of the phase boundary between ilmenite and perovskite in $MgSiO_3$ by in situ x-ray diffraction and quench experiments. *Physics and Chemistry of Minerals volume*, 27:523–532.

Kurokawa, H., Foriel, J., Laneuville, M., Houser, C., and Usui, T. (2018). Subduction and atmospheric escape of Earth's seawater constrained by hydrogen isotopes. *Earth and Planetary Science Letters*, 497:149–160.

Kurokawa, H., Miura, Y. N., Sugita, S., Cho, Y., Leblanc, F., Terada, N., and Nakagawa, H. (2021). Mars' atmospheric neon suggests volatile-rich primitive mantle. *Icarus*, 370:114685.

Kurokawa, H., Sato, M., Ushioda, M., Matsuyama, T., Moriwaki, R., Dohm, J. M., and Usui, T. (2014). Evolution of water reservoirs on Mars: Constraints from hydrogen isotopes in martian meteorites. *Earth and Planetary Science Letters*, 394:179–185.

Latour, B. and Woolgar, S. (1986). *Laboratory Life: The Construction of Scientific Facts*. Princeton University Press.

Leng, W. and Zhong, S. (2010). Surface subsidence caused by mantle plumes and volcanic loading in large igneous provinces. *Earth and Planetary Science Letters*, 291:207–214.

Li, H. F., Oganov, A. R., Cui, H., Zhou, X. F., Dong, X., and Wang, H. T. (2022). Ultrahigh-pressure magnesium hydrosilicates as reservoirs of water in early Earth. *Physical Review Letters*, 128:035703.

Li, J., Hadidiacos, C., Mao, H. K., Fei, Y., and Hemley, R. J. (2003). Behavior of thermocouples under high pressure in a multi-anvil apparatus. *High Pressure Research*, 23(4):389–401.

Li, Y., Vočadlo, L., Sun, T., and Brodholt, J. P. (2020). The Earth's core as a reservoir of water. *Nature Geoscience*, 13(6):453–458.

Libowitzky, E. and Rossman, G. R. (1997). An IR absorption calibration for water in minerals. *American Mineralogist*, 82(11-12):1111–1115.

Liebske, C. and Khan, A. (2019). On the principal building blocks of Mars and Earth. *Icarus*, 322:121–134.

Lin, Y., Hu, Q., Walter, M. J., Yang, J., Meng, Y., Feng, X., Zhuang, Y., Cohen, R. E., and Mao, H. K. (2022). Hydrous SiO_2 in subducted oceanic crust and H_2O transport to the core-mantle boundary. *Earth and Planetary Science Letters*, 594:117708.

Litasov, K. (2010). The influence of Al_2O_3 on the H_2O content in periclase and ferropericlase at 25 GPa. *Russian Geology and Geophysics*, 51(6):644–649.

Litasov, K. and Ohtani, E. (2002). Phase relations and melt compositions in CMAS–pyrolite–H_2O system up to 25 GPa. *Physics of the Earth and Planetary Interiors*, 134(1-2):105–127.

Litasov, K. and Ohtani, E. (2008). Systematic study of hydrogen incorporation into Fe-bearing wadsleyite and water storage capacity of the transition zone. *AIP Conference Proceedings*, 987(1):113–118.

Litasov, K., Ohtani, E., Langenhorst, F., Yurimoto, H., Kubo, T., and Kondo, T. (2003). Water solubility in Mg-perovskites and water storage capacity in the lower mantle. *Earth and Planetary Science Letters*, 211(1-2):189–203.

Litasov, K. D., Gavryushkin, P. N., Dorogokupets, P. I., Sharygin, I. S., Shatskiy, A., Fei, Y., Rashchenko, S. V., Seryotkin, Y. V., Higo, Y., Funakoshi, K., and Ohtani, E. (2013). Thermal equation of state to 33.5 GPa and 1673 K and thermodynamic properties of tungsten. *Journal of Applied Physics*, 113(13).

Litasov, K. D., Shatskiy, A., Ohtani, E., and Katsura, T. (2011). Systematic study of hydrogen incorporation into Fe-free wadsleyite. *Physics and Chemistry of Minerals*, 38:75–84.

Luo, W., Howard, A. D., and Cang, X. Z. (2020). Comment on "the volume of water required to carve the Martian valley networks: Improved constraints using updated methods". *Icarus*, 336:113321.

Marty, B., Bekaert, D. V., Broadley, M. W., and Jaupart, C. (2019). Geochemical evidence for high volatile fluxes from the mantle at the end of the Archaean. *Nature*, 575(7783):485–488.

Matsuzaka, K., Akaogi, M., Suzuki, T., and Suda, T. (2000). Mg–Fe partitioning between silicate spinel and magnesiowustite at high pressure: experimental determination and calculation of phase relations in the system Mg_2SiO_4–Fe_2SiO_4. *Physics and Chemistry of Minerals*, 27(5):310–319.

Mazza, S. E., Gazel, E., Bizimis, M., Moucha, R., Béguelin, P., Johnson, E. A., McAleer, R. J., and Sobolev, A. V. (2019). Sampling the volatile-rich transition zone beneath Bermuda. *Nature*, 569(7756):398–403.

Meade, C., Reffner, J. A., Ito, E., Reffner, J. A., and Ito, E. (1994). Synchrotron infrared absorbance measurements of hydrogen in $MgSiO_3$ perovskite. *Science*, 264:1558–1560.

Meng, Y., Hrubiak, R., Rod, E., Boehler, R., and Shen, G. (2015). New developments in laser-heated diamond anvil cell with in situ synchrotron X-ray diffraction at High Pressure Collaborative Access Team. *Review of Scientific Instruments*, 86(7):072201.

Mibe, K., Fujii, T., and Yasuda, A. (2002). Composition of aqueous fluid coexisting with mantle minerals at high pressure and its bearing on the differentiation of the Earth's mantle. *Geochimica et Cosmochimica Acta*, 66(12):2273–2285.

Miller, K. G., Kominz, M. A., Browning, J. V., Wright, J. D., Mountain, G. S., Katz, M. E., Sugarman, P. J., Cramer, B. S., Christie-Blick, N., and Pekar, S. F. (2005). The Phanerozoic record of global sea-level change. *Science*, 310(5752):1293–1298.

Mocquet, A. and Menvielle, M. (2000). Complementarity of seismological and electromagnetic sounding methods for constraining the structure of the Martian mantle. *Planetary and Space Science*, 48(12-14):1249–1260.

Mookherjee, M., Stixrude, L., and Karki, B. (2008). Hydrous silicate melt at high pressure. *Nature*, 452(7190):983–986.

Moore, W. B. and Webb, A. A. G. (2013). Heat-pipe Earth. *Nature*, 501(7468):501–505.

Morbidelli, A., Chambers, J., Lunine, J. I., Petit, J. M., Robert, F., Valsecchi, G. B., and Cyr, K. E. (2000). Source regions and timescales for the delivery of water to the Earth. *Meteoritics and Planetary Science*, 35(6):1309–1320.

Morschhauser, A., Grott, M., and Breuer, D. (2011). Crustal recycling, mantle dehydration, and the thermal evolution of Mars. *Icarus*, 212(2):541–558.

Motoyama, M., Tsunakawa, H., and Takahashi, F. (2020). Tidal resonance of eigenmode oscillation in the early Earth's ocean and its acceleration effect on the Moon's orbital evolution. *Icarus*, 335:113382.

Movshovitz, N. and Fortney, J. J. (2022). The promise and limitations of precision gravity: Application to the interior structure of uranus and neptune. *Planetary Science Journal*, 3(4):88.

Muir, J. M. R. and Brodholt, J. P. (2018). Water distribution in the lower mantle: Implications for hydrolytic weakening. *Earth and Planetary Science Letters*, 484:363–369.

Murakami, M., Hirose, K., Yurimoto, H., Nakashima, S., and Takafuji, N. (2002). Water in Earth's lower mantle. *Science*, 295:1885–1887.

Mustard, J. F. (2019). Sequestration of volatiles in the Martian crust through hydrated minerals: A significant planetary reservoir of water. In Filiberto, J. and Schwenzer, S. P., editors, *Volatiles in the Martian Crust*, pages 247–263.

Nakagawa, T. and Iwamori, H. (2019). On the implications of the coupled evolution of the deep planetary interior and the presence of surface ocean water in hydrous mantle convection. *Comptes Rendus Geoscience*, 351(2-3):197–208.

Németh, P., Leinenweber, K., Ohfuji, H., Groy, T., Domanik, K. J., Kovács, I. J., Kovács, J. S., and Buseck, P. R. (2017). Water-bearing, high-pressure Ca-silicates. *Earth and Planetary Science Letters*, 469:148–155.

Nimmo, F. and Tanaka, K. (2005). Early crustal evolution of Mars. *Annual Review of Earth and Planetary Sciences*, 33:133–161.

Nishi, M., Irifune, T., Tsuchiya, J., Tange, Y., Nishihara, Y., Fujino, K., and Higo, Y. (2014). Stability of hydrous silicate at high pressures and water transport to the deep lower mantle. *Nature Geoscience*, 7(3):224–227.

Nishihara, Y., Doi, S., Hino, H., Higo, Y., and Tange, Y. (2020a). Pressure effect on the electromotive force of the type R thermocouple. *High Pressure Research*, 40(2):205–218.

Nishihara, Y., Doi, S., Kakizawa, S., Higo, Y., and Tange, Y. (2020b). Effect of pressure on temperature measurements using WRe thermocouple and its geophysical impact. *Physics of the Earth and Planetary Interiors*, 298.

Nomura, R., Ozawa, H., Tateno, S., Hirose, K., Hernlund, J., Muto, S., Ishii, H., and Hiraoka, N. (2011). Spin crossover and iron-rich silicate melt in the Earth's deep mantle. *Nature*, 473(7346):199–202.

Ogawa, M. (2021). The four-stage evolution of Martian mantle inferred from numerical simulation of the magmatism-mantle upwelling feedback. *Journal of Geophysical Research: Planets*, 126(12):e2021JE006997.

Ohtani, E., Amaike, Y., Kamada, S., Sakamaki, T., and Hirao, N. (2014). Stability of hydrous phase H $MgSiO_4H_2$ under lower mantle conditions. *Geophysical Research Letters*, 41(23):8283–8287.

Ohtani, E., Mizobata, H., and Yurimoto, H. (2000). Stability of dense hydrous magnesium silicate phases in the systems Mg_2SiO_4–H_2O and $MgSiO_3$–H_2O at pressures up to 27 GPa. *Physics and Chemistry of Minerals*, 27(8):533–544.

Okuchi, T. (1997). Hydrogen partitioning into molten iron at high pressure: Implications for Earth's core. *Science*, 278(5344):1781–1784.

Olson, P. and Sharp, Z. D. (2018). Hydrogen and helium ingassing during terrestrial planet accretion. *Earth and Planetary Science Letters*, 498:418–426.

O'Rourke, J. G. and Shim, S.-H. (2019). Hydrogenation of the Martian core by hydrated mantle minerals with implications for the early dynamo. *Journal of Geophysical Research: Planets*, 124(12):3422–3441.

Otsuka, K. and Karato, S. I. (2011). Control of the water fugacity at high pressures and temperatures: Applications to the incorporation mechanisms of water in olivine. *Physics of the Earth and Planetary Interiors*, 189(1-2):27–33.

Padrón-Navarta, J. A. and Hermann, J. (2017). A subsolidus olivine water solubility equation for the Earth's upper mantle. *Journal of Geophysical Research: Solid Earth*, 122(12):9862–9880.

Parai, R. and Mukhopadhyay, S. (2018). Xenon isotopic constraints on the history of volatile recycling into the mantle. *Nature*, 560(7717):223–227.

Paterson, M. S. (1982). The determination of hydroxyl by infrared adsorption in quartz, silicate glasses and similar materials. *Bulletin de Mineralogie*, 105:20–29.

Pearson, D. G., Brenker, F. E., Nestola, F., McNeill, J., Nasdala, L., Hutchison, M. T., Matveev, S., Mather, K., Silversmit, G., Schmitz, S., Vekemans, B., and Vincze, L. (2014). Hydrous mantle transition zone indicated by ringwoodite included within diamond. *Nature*, 507(7491):221–224.

Pedregosa, F., Varoquaux, G., Gramfort, A., Michel, V., Thirion, B., Grisel, O., Blondel, M., Prettenhofer, P., Weiss, R., Bubourg, V., Vanderplas, J., Passos, A., Cournapeau, D., Brucher, M., Perrot, M., and Édouard Duchesnay (2011). Scikit-learn: Machine learning in Python. *Journal of Machine Learning Research*, 12:2825–2830.

Phillips, R. J., Zuber, M. T., Solomon, S. C., Golombek, M. P., Jakosky, B. M., Banerdt, W. B., Smith, D. E., Williams, R. M. E., Hynek, B. M., Aharonson, O., and Hauck, S. A. (2001). Ancient geodynamics and global-scale hydrology on Mars. *Science*, 291(5513):2587–2591.

Pope, E. C., Bird, D. K., and Rosing, M. T. (2012). Isotope composition and volume of Earth's early oceans. *Proceedings of the National Academy of Sciences*, 109(12):4371–4376.

Prakapenka, V. B., Kubo, A., Kuznetsov, A., Laskin, A., Shkurikhin, O., Dera, P., Rivers, M. L., and Sutton, S. R. (2008). Advanced flat top laser heating system for high pressure research at GSECARS: Application to the melting behavior of germanium. *High Pressure Research*, 28(3):225–235.

Prescher, C. and Prakapenka, V. B. (2015). DIOPTAS: A program for reduction of two-dimensional X-ray diffraction data and data exploration. *High Pressure Research*, 35(3):223–230.

Price, M. G., Davies, J., and Panton, J. (2019). Controls on the deep-water cycle within three-dimensional mantle convection models. *Geochemistry, Geophysics, Geosystems*, 20(5):2199–2213.

Ptáček, M. P., Dauphas, N., and Greber, N. D. (2020). Chemical evolution of the continental crust from a data-driven inversion of terrigenous sediment compositions. *Earth and Planetary Science Letters*, 539:116090.

Rey, P. F. (2015). The geodynamics of mantle melting. *Geology*, 43(4):367–368.

Rey, P. F. and Coltice, N. (2008). Neoarchean lithospheric strengthening and the coupling of Earth's geochemical reservoirs. *Geology*, 36(8):635–638.

Righter, K. and Drake, M. J. (1999). Effect of water on metal-silicate partitioning of siderophile elements: a high pressure and temperature terrestrial magma ocean and core formation. *Earth and Planetary Science Letters*, 171(3):383–399.

Rosenberg, E. N., Palumbo, A. M., Cassanelli, J. P., Head, J. W., and Weiss, D. K. (2019). The volume of water required to carve the Martian valley networks: Improved constraints using updated methods. *Icarus*, 317:379–387.

Rosing, M. T., Bird, D. K., Sleep, N. H., and Bjerrum, C. J. (2010). No climate paradox under the faint early Sun. *Nature*, 464(7289):744–747.

Rowan, C. J. and Rowley, D. B. (2016). Preserved history of global mean spreading rate: 83 Ma to present. *Geophysical Journal International*, 208(2):1173–1183.

Ruedas, T. and Breuer, D. (2017). On the relative importance of thermal and chemical buoyancy in regular and impact-induced melting in a Mars-like planet. *Journal of Geophysical Research: Planets*, 122(7):1554–1579.

Ruedas, T. and Breuer, D. (2021). Electrical and seismological structure of the Martian mantle and the detectability of impact-generated anomalies. *Icarus*, 358:114176.

Ruedas, T., Tackley, P. J., and Solomon, S. C. (2013a). Thermal and compositional evolution of the Martian mantle: Effects of phase transitions and melting. *Physics of the Earth and Planetary Interiors*, 216:32–58.

Ruedas, T., Tackley, P. J., and Solomon, S. C. (2013b). Thermal and compositional evolution of the Martian mantle: Effects of water. *Physics of the Earth and Planetary Interiors*, 220:50–72.

Rüpke, L. H., Morgan, J. P., Hort, M., and Connolly, J. A. (2004). Serpentine and the subduction zone water cycle. *Earth and Planetary Science Letters*, 223(1-2):17–34.

Sakamaki, T., Suzuki, A., and Ohtani, E. (2006). Stability of hydrous melt at the base of the Earth's upper mantle. *Nature*, 439(7073):192–194.

Sandu, C. and Kiefer, W. S. (2012). Degassing history of Mars and the lifespan of its magnetic dynamo. *Geophysical Research Letters*, 39.

Sandu, C., Lenardic, A., and McGovern, P. (2011). The effects of deep water cycling on planetary thermal evolution. *Journal of Geophysical Research: Solid Earth*, 116(B12).

Scheller, E. L., Ehlmann, B. L., Hu, R. Y., Adams, D. J., and Yung, Y. L. (2021). Long-term drying of Mars by sequestration of ocean-scale volumes of water in the crust. *Science*, 372(6537):56–62.

Schmalzried, H. (1994). *Chemical Kinetics of Solids*. VCH.

Schmandt, B., Jacobsen, S. D., Becker, T. W., Liu, Z., and Dueker, K. G. (2014). Dehydration melting at the top of the lower mantle. *Science*, 344(6189):1265–1268.

Schmidt, M. and Poli, S. (2014). Devolatilization during subduction. In Holland, H. D. and Turekian, K. K., editors, *Treatise on Geochemistry*, pages 669–701. Elsevier, Oxford, 2nd edition.

Schulze, K., Marquardt, H., Kawazoe, T., Ballaran, T. B., McCammon, C., Koch-Müller, M., Kurnosov, A., and Marquardt, K. (2018). Seismically invisible water in Earth's transition zone? *Earth and Planetary Science Letters*, 498:9–16.

Seales, J. and Lenardic, A. (2020). Deep water cycling and the multi-stage cooling of the Earth. *Geochemistry, Geophysics, Geosystems*, 21(10):e2020GC009106.

Servali, A. and Korenaga, J. (2018). Oceanic origin of continental mantle lithosphere. *Geology*, 46(12):1047–1050.

Shen, G., Prakapenka, V. B., Eng, P. J., Rivers, M. L., and Sutton, S. R. (2005). Facilities for high-pressure research with the diamond anvil cell at GSECARS. *Journal of Synchrotron Radiation*, 12(5):642–649.

Shieh, S. R., Mao, H.-k., Hemley, R. J., and Ming, L. C. (1998). Decomposition of phase D in the lower mantle and the fate of dense hydrous silicates in subducting slabs. *Earth and Planetary Science Letters*, 159(1-2):13–23.

Shim, S.-H., Duffy, T. S., and Shen, G. (2001). The post-spinel transformation in Mg_2SiO_4 and its relation to the 660-km seismic discontinuity. *Nature*, 411:571–0574.

Shimojuku, A., Boujibar, A., Yamazaki, D., Yoshino, T., Tomioka, N., and Xu, J. (2014). Growth of ringwoodite reaction rims from $MgSiO_3$ perovskite and periclase at 22.5 GPa and 1800 °C. *Physics and Chemistry of Minerals*, 41(7):555–567.

Shirey, S. B., Wagner, L. S., Walter, M. J., Pearson, D. G., and van Keken, P. E. (2021). Slab transport of fluids to deep focus earthquake depths—thermal modeling constraints and evidence from diamonds. *AGU Advances*, 2:e2020AV000304.

Sholes, S. F., Dickeson, Z. I., Montgomery, D. R., and Catling, D. C. (2021). Where are Mars' hypothesized ocean shorelines? Large lateral and topographic offsets between different versions of paleoshoreline maps. *Journal of Geophysical Research: Planets*, 126(5):e2020JE006486.

Sobolev, A. V., Hofmann, A. W., Kuzmin, D. V., Yaxley, G. M., Arndt, N. T., Chung, S.-L., Danyushevsky, L. V., Elliott, T., Frey, F. A., Garcia, M. O., et al. (2007). The amount of recycled crust in sources of mantle-derived melts. *Science*, 316(5823):412–417.

Sokolova, T. S., Dorogokupets, P. I., Dymshits, A. M., Danilov, B. S., and Litasov, K. D. (2016). Microsoft excel spreadsheets for calculation of P–V–T relations and thermodynamic properties from equations of state of MgO, diamond and nine metals as pressure markers in high-pressure and high-temperature experiments. *Computers and Geosciences*, (94):162–169.

Stahler, S. C., Khan, A., Banerdt, W. B., Lognonne, P., Giardini, D., Ceylan, S., Drilleau, M., Duran, A. C., Garcia, R. F., Huang, Q. C., Kim, D., Lekic, V., Samuel, H., Schimmel, M., Schmerr, N., Sollberger, D., Stutzmann, E., Xu, Z. B., Antonangeli, D., Charalambous, C., Davis, P. M., Irving, J. C. E., Kawamura, T., Knapmeyer, M., Maguire, R., Marusiak, A. G., Panning, M. P., Perrin, C., Plesa, A. C., Rivoldini, A., Schmelzbach, C., Zenhausern, G., Beucler, E., Clinton, J., Dahmen, N., van Driel, M., Gudkova, T., Horleston, A., Pike, W. T., Plasman, M., and Smrekar, S. E. (2021). Seismic detection of the Martian core. *Science*, 373(6553):443–448.

Stalder, R., Ulmer, P., Thompson, A. B., and Gunther, D. (2001). High pressure fluids in the system $MgO–SiO_2–H_2O$ under upper mantle conditions. *Contributions to Mineralogy and Petrology*, 140(5):607–618.

Stixrude, L. and Lithgow-Bertelloni, C. (2005). Thermodynamics of mantle minerals: I. Physical properties. *Geophysical Journal International*, 162(2):610–632.

Stixrude, L. and Lithgow-Bertelloni, C. (2011). Thermodynamics of mantle minerals: II. Phase equilibria. *Geophysical Journal International*, 184(3):1180–1213.

Stixrude, L. and Lithgow-Bertelloni, C. (2022). Thermal expansivity, heat capacity and bulk modulus of the mantle. *Geophysical Journal International*, 228(2):1119–1149.

Suzuki, A., Ohtani, E., Morishima, H., Kubo, T., Kanbe, Y., Kondo, T., Okada, T., Terasaki, H., Kato, T., and Kikegawa, T. (2000). In situ determination of the phase boundary between wadsleyite and ringwoodite in Mg_2SiO_4. *Geophysical Research Letters*, 27(6):803–806.

Syracuse, E. M., van Keken, P. E., Abers, G. A., Suetsugu, D., Bina, C., Inoue, T., Wiens, D., and Jellinek, M. (2010). The global range of subduction zone thermal models. *Physics of the Earth and Planetary Interiors*, 183(1-2):73–90.

Tang, M., Chen, K., and Rudnick, R. L. (2016). Archean upper crust transition from mafic to felsic marks the onset of plate tectonics. *Science*, 351(6271):372–375.

Tateno, S., Hirose, K., and Ohishi, Y. (2014). Melting experiments on peridotite to lowermost mantle conditions. *Journal of Geophysical Research: Solid Earth*, 119(6):4684–4694.

Tateno, S., Komabayashi, T., Hirose, K., Hirao, N., and Ohishi, Y. (2019). Static compression of B2 KCl to 230 GPa and its P–V–T equation of state. *American Mineralogist*, 104(5):718–723.

Tauzin, B. and Ricard, Y. (2014). Seismically deduced thermodynamics phase diagrams for the mantle transition zone. *Earth and Planetary Science Letters*, 401:337–346.

Taylor, G. J. (2013). The bulk composition of Mars. *Chemie der Erde*, 73(4):401–420.

Tenner, T. J., Hirschmann, M. M., Withers, A. C., and Ardia, P. (2012). H_2O storage capacity of olivine and low-Ca pyroxene from 10 to 13 GPa: consequences for dehydration melting above the transition zone. *Contributions to Mineralogy and Petrology*, 163(2):297–316.

Terasaki, H., Ohtani, E., Sakai, T., Kamada, S., Asanuma, H., Shibazaki, Y., Hirao, N., Sata, N., Ohishi, Y., Sakamaki, T., Suzuki, A., and Funakoshi, K. (2012). Stability of Fe-Ni hydride after the reaction between Fe–Ni alloy and hydrous phase (delta-AlOOH) up to 1.2 Mbar: Possibility of H contribution to the core density deficit. *Physics of the Earth and Planetary Interiors*, 194:18–24.

Tikoo, S. M. and Elkins-Tanton, L. T. (2017). The fate of water within Earth and super-Earths and implications for plate tectonics. *Philosophical Transactions of the Royal Society A: Mathematical, Physical and Engineering Sciences*, 375(2094):20150394.

Townsend, J. P., Tsuchiya, J., Bina, C. R., and Jacobsen, S. D. (2016). Water partitioning between bridgmanite and postperovskite in the lowermost mantle. *Earth and Planetary Science Letters*, 454:20–27.

Tschauner, O., Huang, S., Greenberg, E., Prakapenka, V. B., Ma, C., Rossman, G. R., Shen, A. H., Zhang, D., Newville, M., Lanzirotti, A., and Tait, K. (2018). Ice–VII inclusions in diamonds: Evidence for aqueous fluid in Earth's deep mantle. *Science*, 359(6380):1136–1139.

van der Meer, D. G., Spakman, W., van Hinsbergen, D. J., Amaru, M. L., and Torsvik, T. H. (2010). Towards absolute plate motions constrained by lower-mantle slab remnants. *Nature Geoscience*, 3(1):36–40.

van Hunen, J. and Moyen, J. F. (2012). Archean subduction: Fact or fiction? *Annual Review of Earth and Planetary Sciences*, 40:195–219.

van Keken, P. E., Hacker, B. R., Syracuse, E. M., and Abers, G. A. (2011). Subduction factory: 4. Depth-dependent flux of H_2O from subducting slabs worldwide. *Journal of Geophysical Research: Solid Earth*, 116:B01401.

Verhoeven, O. and Vacher, P. (2016). Laboratory-based electrical conductivity at Martian mantle conditions. *Planetary and Space Science*, 134:29–35.

Villanueva, G. L., Mumma, M. J., Novak, R. E., Kaufl, H. U., Hartogh, P., Encrenaz, T., Tokunaga, A., Khayat, A., and Smith, M. D. (2015). Strong water isotopic anomalies in the Martian atmosphere: Probing current and ancient reservoirs. *Science*, 348(6231):218–221.

Voosen, P. (2021). Ancient Earth was a water world. *Science*, 371(6534):1088–1089.

Wade, J., Dyck, B., Palin, R. M., Moore, J. D. P., and Smye, A. J. (2017). The divergent fates of primitive hydrospheric water on Earth and Mars. *Nature*, 552(7685):391–394.

Wang, W., Walter, M. J., Peng, Y., Redfern, S., and Wu, Z. (2019). Constraining olivine abundance and water content of the mantle at the 410-km discontinuity from the elasticity of olivine and wadsleyite. *Earth and Planetary Science Letters*, 519:1–11.

Wasserstein, R. L. and Lazar, N. A. (2016). The asa's statement on p-values: Context, process, and purpose. *American Statistician*, 70(2):129–131.

Waszek, L., Tauzin, B., Schmerr, N. C., Ballmer, M. D., and Afonso, J. C. (2021). A poorly mixed mantle transition zone and its thermal state inferred from seismic waves. *Nature Geoscience*, 14:949–955.

Wernicke, L. J. and Jakosky, B. M. (2021). Martian hydrated minerals: A significant water sink. *Journal of Geophysical Research: Planets*, 126(3):e2019JE006351.

Windley, B. F. (1996). *The Evolving Continents*. Wiley, 3rd edition.

Withers, A. C., Bureau, H., Raepsaet, C., and Hirschmann, M. M. (2012). Calibration of infrared spectroscopy by elastic recoil detection analysis of H in synthetic olivine. *Chemical Geology*, 334:92–98.

Withers, A. C. and Hirschmann, M. M. (2008). Influence of temperature, composition, silica activity and oxygen fugacity on the H_2O storage capacity of olivine at 8 GPa. *Contributions to Mineralogy and Petrology*, 156:595–605.

Withers, A. C., Hirschmann, M. M., and Tenner, T. J. (2011). The effect of Fe on olivine H_2O storage capacity: Consequences for H_2O in the Martian mantle. *American Mineralogist*, 96(7):1039–1053.

Wordsworth, R. D. and Pierrehumbert, R. T. (2013). Water loss from terrestrial planets with CO_2-rich atmospheres. *Astrophysical Journal*, 778(2):154.

Workman, R. K. and Hart, S. R. (2005). Major and trace element composition of the depleted MORB mantle (DMM). *Earth and Planetary Science Letters*, 231(1-2):53–72.

Wu, J., Desch, S. J., Schaefer, L., Elkins-Tanton, L. T., Pahlevan, K., and Buseck, P. R. (2018). Origin of Earth's water: Chondritic inheritance plus nebular ingassing and storage of hydrogen in the core. *Journal of Geophysical Research: Planets*, 123(10):2691–2712.

Xu, W., Lithgow-Bertelloni, C., Stixrude, L., and Ritsema, J. (2008). The effect of bulk composition and temperature on mantle seismic structure. *Earth and Planetary Science Letters*, 275(1-2):70–79.

Yoshizaki, T. and McDonough, W. F. (2020). The composition of mars. *Geochimica et Cosmochimica Acta*, 273:137–162.

Yuan, H., Zhang, L., Ohtani, E., Meng, Y., Greenberg, E., and Prakapenka, V. B. (2019). Stability of Fe-bearing hydrous phases and element partitioning in the system MgO–Al_2O_3–Fe_2O_3–SiO_2–H_2O in Earth's lowermost mantle. *Earth and Planetary Science Letters*, 524:115714.

Yuan, L. and Steinle-Neumann, G. (2020). Strong sequestration of hydrogen into the Earth's core during planetary differentiation. *Geophysical Research Letters*, 47(15):e2020GL088303.

Zahnle, K. J., Gacesa, M., and Catling, D. C. (2019). Strange messenger: A new history of hydrogen on Earth, as told by xenon. *Geochimica et Cosmochimica Acta*, 244:56–85.

Zhao, Y. H., Ginsberg, S. B., and Kohstedt, D. L. (2004). Solubility of hydrogen in olivine: dependence on temperature and iron content. *Contributions to Mineralogy and Petrology*, 147(2):155–161.

Zhou, D., Dong, J., Si, Y., Zhu, F., and Li, J. (2020). Melting curve of potassium chloride from in situ ionic conduction measurements. *Minerals*, 10(3):250.

Zhu, F., Li, J., Liu, J. C., Dong, J. J., and Liu, Z. X. (2019). Metallic iron limits silicate hydration in earth's transition zone. *Proceedings of the National Academy of Sciences*, 116:22526–22530.